eman ta zabal zazu

Universidad del País Vasco
Euskal Herriko Unibertsitatea

Study of Crystal Structures and Phase Transitions in Perovskite-Type Oxides Using Powder-Diffraction Techniques and Symmetry-Mode Analysis

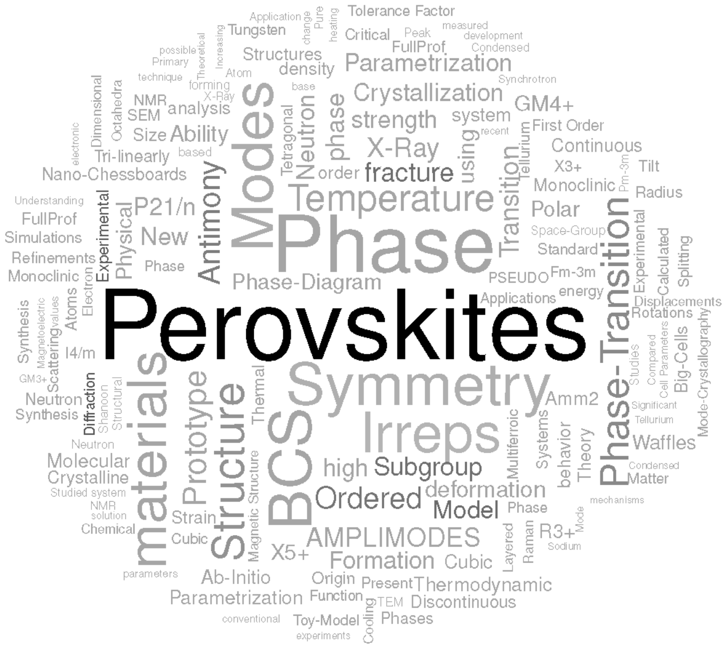

By

Brahim ORAYECH

A Dissertation Presented for the Degree Doctor of Physics
" International Doctor" mention

Leioa, July 2015

ZTF-FCT
Zientzia eta Teknologia Fakultatea
Facultad de Ciencia y Tecnología

eman ta zabal zazu
Universidad del País Vasco
Euskal Herriko Unibertsitatea

Applied Physics II Department

Study of Crystal Structures and Phase Transitions in Perovskite-Type Oxides Using Powder-Diffraction Techniques and Symmetry-Mode Analysis

$Na_{0.5}K_{0.5}NbO_3$, La_2MMnO_6,
Sr_2LnSbO_6 (Ln=Nd, Eu, Gd, Dy, Ho, Er, Tm and Yb)
Sr_2MSbO_6 (M=In, Y and Sc), Ca_2MSbO_6 (M=Ln, Y, In)
$Sr_2M_{1-x}M'_xTeO_6$ (M, M'= Co, Mn, Ni, Fe and Mg)
and
$NaLnMM'O_6$ (Ln=La, Nd, Pr; M=Co, Mn, Mg; M'= W and Te)

By

Brahim ORAYECH

Directed by Professor Dr. Josu Mirena Igartua Aldamiz

A Dissertation Presented for the Degree Doctor of Physics
" International Doctor" mention

Leioa, July 2015

eman ta zabal zazu

Universidad del País Vasco
Euskal Herriko Unibertsitatea

AUTORIZACION DEL/LA DIRECTOR/A DE TESIS PARA SU PRESENTACION

Dr **JOSU MIRENA IGARTUA ALDAMIZ** como Director/a de la Tesis Doctoral: **CRYSTAL STRUCTURE AND PHASE TRANSITION STUDIES IN PEROVSKITE-TYPE OXIDES USING POWDER-DIFFRACTION TECHNIQUES AND SYMMETRY-MODE ANALYSIS. $Na_{0.5}K_{0.5}NbO_3$, La_2MMnO_6, Sr_2MSbO_6 (M=Ln, Y, In), , Ca_2MSbO_6 (M=Ln, Y, In) $Sr_2M_{1-x}M'_xTeO_6$ (M, M'= Co, Mn, Ni, Fe and Mg), and $NaLnMM'O_6$ (Ln=La, Nd, Pr; M=Co, Mn, Mg; M'= W and Te)** realizada en el Departamento **FÍSICA APLICADA II** por el Doctorando Don. **BRAHIM ORAYECH**, autorizo la presentación de la citada Tesis Doctoral, dado que reúne las condiciones necesarias para su defensa.

En Leioa a 12 de Junio de 2015

EL/LA DIRECTOR/A DE LA TESIS

Fdo.: JOSU MIRENA IGARTUA ALDAMIZ

eman ta zabal zazu

Universidad del País Vasco
Euskal Herriko Unibertsitatea

CONFORMIDAD DEL DEPARTAMENTO

El Consejo del Departamento de **FÍSICA APLICADA II** en reunión celebrada el día 27 de Mayo de 2015 ha acordado dar la conformidad a la admisión a trámite de presentación de la Tesis Doctoral titulada: **CRYSTAL STRUCTURE AND PHASE TRANSITION STUDIES IN PEROVSKITE-TYPE OXIDES USING POWDER-DIFFRACTION TECHNIQUES AND SYMMETRY-MODE ANALYSIS. $\mathrm{Na_{0.5}K_{0.5}NbO_3}$, $\mathrm{La_2}\mathit{M}\mathrm{MnO_6}$, $\mathrm{Sr_2}\mathit{M}\mathrm{SbO_6}$ (M=Ln, Y, In), , $\mathrm{Ca_2}\mathit{M}\mathrm{SbO_6}$ (M=Ln, Y, In) $\mathrm{Sr_2}\mathit{M}_{1-x}\mathit{M'}_{x}\mathrm{TeO_6}$ (M, $\mathit{M'}$= Co, Mn, Ni, Fe and Mg), and $\mathrm{Na}\mathit{LnMM'}\mathrm{O_6}$ (Ln=La, Nd, Pr; M=Co, Mn, Mg; $\mathit{M'}$= W and Te)** dirigida por el Dr. **JOSU MIRENA IGARTUA ALDAMIZ** y presentada por Don. **BRAHIM ORAYECH** ante este Departamento.

En Leioa a 6 de Mayo de 2015

VºBº DIRECTOR/A DEL DEPARTAMENTO SECRETARIO/A DEL DEPARTAMENTO

Fdo.: CARLOS SANTAMARÍA SALAZAR Fdo.: IÑIGO ETXEBARRÍA ALTZAGA

eman ta zabal zazu

Universidad del País Vasco
Euskal Herriko Unibertsitatea

ACTA DE GRADO DE DOCTOR O DOCTORA
ACTA DE DEFENSA DE TESIS DOCTORAL

DOCTORANDO/A DON. **BRAHIM ORAYECH**

TITULO DE LA TESIS: **CRYSTAL STRUCTURE AND PHASE TRANSITION STUDIES IN PEROVSKITE-TYPE OXIDES USING POWDER-DIFFRACTION TECHNIQUES AND SYMMETRY-MODE ANALYSIS.** $Na_{0.5}K_{0.5}NbO_3$, La_2MMnO_6, Sr_2MSbO_6 **(**M**=Ln, Y, In), ,** Ca_2MSbO_6 **(**M**=Ln, Y, In)** $Sr_2M_{1-x}M'_xTeO_6$ **(**M, M'**= Co, Mn, Ni, Fe and Mg), and** $NaLnMM'O_6$ **(**Ln**=La, Nd, Pr;** M**=Co, Mn, Mg;** M'**= W and Te)**

El Tribunal designado por la Comisión de Postgrado de la UPV/EHU para calificar la Tesis Doctoral arriba indicada y reunido en el día de la fecha, una vez efectuada la defensa por el/la doctorando/a y contestadas las objeciones y/o sugerencias que se le han formulado, ha otorgado por___________________la calificación de:
unanimidad ó mayoría

SOBRESALIENTE / NOTABLE / APROBADO / NO APTO

Idioma/s de defensa (en caso de más de un idioma, especificar porcentaje defendido en cada idioma):
____

En ____________________a ______de _______________________de ______

EL/LA PRESIDENTE/A,

EL/LA SECRETARIO/A,

Fdo.:

Dr/a: ____________________

Fdo.:

Dr/a: ______________________

VOCAL 1º,

VOCAL 2º,

VOCAL 3º,

Fdo.:

Fdo.:

Fdo.:

Dr/a: __________________________

Dr/a:_____________________________

Dr/a:_________________________

EL/LA DOCTORANDO/A,

Fdo.: _____________________

À mes parents, Fatima et El Mostapha. Cette Réussite est la vôtre!
A Sawsane
A Rayane, Abdessamad y Fadwa
A toda mi familia
A todos mis amigos

Acknowledgments

Despite time flies, it is sometimes hard to realize how we change. Looking backwards is not an exercise that we often do, but when we are at the end of a stage it is crucial to train our memory and understand where we are coming from. It is only this way that we recognize the experience gained in this stage after all the effort. I started this adventure three years ago pushed by an ignorant hope. Now, I feel like a scientist. This would not have been possible without the help of many people. My fondest gratitude to all of them.

But first I would like to thank the basque country, this very place that hosted me during all this time. Before coming, I knew nothing on this place, I knew only Spain, but now, I know that there is Spain and there is the Basque country, the place of hospitality and very friendly people. I have really spent unforgettable moments here. Eskerrik asko Euskal Herria!

Tesi Doktoral hau amaitu izana nire zuzendariari, Josuri, zor diot. Gogoratzen naiz 2011ko martxoan, Bilbora lehendabiziko aldiz etorri nintzenean, tesia zurekin hastea proposatu zenidala. Nekez ezagutzen bazintudan ere, baietz esan nizun, erakutsi zenizkidan konfidantza eta pasioa zirela eta. Eta hau bai fisika interesgarria egin duguna urte hauetan zehar, zure gidaritza gogotsu horri esker. Zure ideiak eta aholkuak ezinbestekoak izan dira tesi hau ondo amaitzeko. Biziki miresten dut arazo berriei aurre egiteko duzun erraztasuna. Zurengandik ikasi dut edozer gerta edo egin daitekeela. Bestalde, hainbat azalpen emateko orduan izan duzun pazientzia handi hori eskertzen dizut. Halaber, gauza franko ere ikasi ditut zurengandik, eta oso berriketa interesgarriak izan ditugu, bai zientifikoak bai arruntak, leku frankotan: zure bulegoan, nire lekuan -hau da, zure bigarren bulegoa-, eta gure bidaia luzeetan zehar: (Grenoble, PSI, Segovia, Zurich...) Fisika ugari irakatsi didazu. Eskerrik asko Montxi!

I owe having finished this PhD thesis to my supervisor. I remember that in March 2011, when I came for the first time to Bilbao for an internship, Josu suggested me to start the thesis working with him. I barely knew you, but I guess I agreed due to the confidence and passion you showed me. We have done very interesting physics during these years, principally driven by your eagerness. Your ideas and suggestions were extremely useful to get this thesis to its final shape. I deeply admire your facility to face new problems. I learned from you that everything could be "possible"! and could be done. You had a great patience when you explained to me many things. I have learned many things from you, we had very interesting discussions, scientific and general ones, in many places: in your office, my place (your second office), during our long journeys (Grenoble, PSI, Segovia, Zurich...). You taught me lots of physics. Thank you Montxi!

Abdessamad, Faik (Abdo) deserve a special position here. Abdo showed me the mysteries of Perovskites and how to handle and treat many types of data. You have passed me the knowledge you have gained from Josu and from your experiences in material Science. We had many long interesting conversations in Vitoria during the weekends. You were always here when I needed you for professional or personal advices. Thank you so much for all your support in all this time. Sincerely, I would not have faced many interesting problems without your help.

The research of this thesis has been my work during these three years and half. However, a worker cannot work without a salary. Thus, I would like to acknowledge Prof. Juan Manuel Pérez-Mato and Prof. Gotzon Madariaga for contracting me during these years. I have been financially supported under the investigation projects funded by the Basque Government (IT-282-07 and IT-779) and the Ministry of Economy and Competitiveness (MINECO) (MAT2012-34740). Thank you very much to them as well.

All the calculations presented in this work have been performed using many programs from the Bilbao Crystallographic Server (http://www.cryst.ehu.es/), I know there is a big work behind, for that I would like to thank all the scientists who ensure the proper functioning of the server and for the quality of the programs they are providing us. Special thanks to Prof. Mois Aroyo, Dr. Luis Elcoro, Dr. Emre S. Tasci, Dr. Gemma de la Flor and Samuel V. Gallego.

I also want to thank all panel members who took their precious time to read and judge my thesis. First, Prof. José Antonio Alonso, who has agreed to the jury president, and showed much kindness.

Mes remerciements vont également à Dr. Damien Saurel, pour avoir accepté de faire partie de jury et apporté un regard critique sur ce travail.

Thank you Dr. Milen Gatheshki and Dr. Edurne Iturbe Zabalo, for the quality of the work you did during your PhDs on Perovskites. Your thesis reports were always a pertinent guide of my analysis and interpretations. Again, thank you Dr. Milen Gatheshki for accepting to be one of the members of my PhD panel.

I would like to thank Dr. Iñigo Etxebarria for his help at many occasions and for the Ab-initio calculations. Thank you for accepting to take part in the panel of my thesis.

This work would not be possible with out the support and multiple human, informatics, equipment, facilities... resources from Applied Physics II, Condensed Matter Physics departments. I would like to acknowledge Dr. Maite Insausti and Dr. Jorge Lago for their help for using different equipments at the Inorganic Chemistry department.

Special thanks to Dr. Aitor Larrañaga from XRD-SGIker General Services (UPV/EHU) (*By the way I have some more samples to pass for LT... I am joking!*), Dr. Iñaki Santos (NMR)

(*Mr.'Yes we can!'*) and Dr. Mariano Barrado (SEM/TEM) from SGIker General Services (UPV/EHU) San Sebastian.

Many thanks to Dr. Gabriel A. López for the SEM and TEM measurements, I know I was always pressing you to pass my samples as soon as possible *(but I was paying for that by many cups of Nespresso coffee!!)*, but... I had to do it! by the way, you were right when you were telling me that I have many samples from different system...I know, but this thesis is the fruit coming from all the work done on those samples!

I would like to express my deep gratitude to all the Diffraction Group people from Institut Laue-Langevin (ILL) in Grenoble (France), and in particular to Dr. Oscar Fabelo for his assistance during the experiments.

I would like to acknowledge the great welcome that Prof. Patrick Simon gave me in Orleans, and for receiving me in his group for two months on Raman spectroscopy. I think we will have some nice papers from that work we did. I am grateful to Dr. Aurélien Canizarès and Dr. Mohamed-Ramzi Ammar for their technical help during my experiments at the CEMHTI-CNRS.

I am grateful to Dr. Irene Urcelay-Olabarria for her time and nice contribution in our work by resolving the magnetic structure of some of our materials.

Thanks to all the people that helped me with all the paperwork of the visa procedure or my thesis, Prof. Carlos Santamaría from Applied Physics II department, Rosa, Marian and Marisa (Secretaries of both departments) and my friend Khalid Fikri who was my translator for long time in many places. Many thank to all of you! you made it easier for me.

How can I forget about my officemates, the PhD students and the Postdocs. There are some that left, others that arrived. I shared with many of you interesting discussions and you helped me to switch off. You made easier all these years. I would like to thank all of you, one by one: Julen and Roberto *(we spent great time in the shared flat in Sarriko, Julen, I really miss your amazing Pizzas)*, Iñaki (*Cómo te quedas Montx!*), Nora (*Ca va?*), Bea (*Latex expert!*), Peio (*with who I was practicing and maintaining my French, Thanks for the basque translation!*), Sofía (*Dont forget your promise to come to Casablanca!*), Laura (*Labas?*), Ion (*Sorry for the Tropela money!*), Ainhoa (*Profesora!*), Gemma (*I have a question about the BCS!*), Nerea, Urko (*The master of Ab-initio Calculations*), Patricia (*mi vecina*), Unai, Leire, Luis, Gerardo, Emre, Noelia, I cannot forget the veterans (Danel, Pablo and Txema), Paul, Telmo, José, Samuel...

A doctorate degree is not a work three or four years, but it is built based on eight years university studies. Deeply thank you to all Professors, but specially my friend El Bouari Abdeslam.

Of course I want to thank in all sincerity Rayane (*Brahim no sabe!*), my sister Fadwa (*Mama no sabe!*) and my brother Abdo (*Papa sabe!*), for all the family time you have offered me during all these years, thank you for your support, I am deeply touched.

I need to thank my friends for all their support when I was feeling stressed. Specially my brother Naji Simou, thank you for this wonderful friendship you gave me. Also, I am grateful to Aboufariss Simou and Ahmed Bachar.

Of course I want to thank in all sincerity my parents, Fatima and El Mostapha, for their comprehension, support and confidence. I know it is hard to understand what I am doing, to sense its value. That is why I am deeply touched.

when I feel that you strongly appreciate my work. If I have finished this thesis is because you always have encouraged me to follow my path. That is priceless, thus, thank you. In compensation, I think I transmitted you and all the family some passion towards Science.

And, finally, thanks to you, Sawsane, my life, dream, passion, tear, sorrow, journey and happiness fellow. Thanks for your great support. You listened to me when I needed it, you cheered me up when I was down, you cleared the future when I saw it dark. Therefore, this thesis is dedicated to you.

Regarding who I forgot to thank: I am sorry!!! I will make another Acknowledgments version 2.0, even longer!

Enjoy reading and thank you once more!

Brahim

My adventure in the world of Perovskites has started in 2011 when I was doing my internship, at the LPCES, Paris-sud 11 University, and one of the targets was to grow the simple perovskite $BaTiO_3$*. At that time I have learned that Dr. A. Faik has worked in his thesis on Double Perovskites, so I have proposed him to try to grow one him materials,* Sr_2MnWO_6*, which, at that time, no one has prepared before as even small signal crystals. After having tried it, it was successfully grown! I have succeeded to grow a signal crystal of 3 cm. Then I tried with* Sr_2MnSbO_6 *which was also successfully grown. After that Professor J. M. Igartua has learned about those promising results he proposed me an internship of two months in this group, which has been extended for another month, and then another three years and half, by joining the group as a PhD student.*

SCOPE OF THE THESIS

One of the main research fields of our group is structural phase transition of materials, mainly Perovskite. Many publications derived from those works, are experimental analysis dealing with synthesis and characterization of different families of double Perovskites. In the last years, many programs have been developed by the team of the Bilbao Crystallographic Server (http://www.cryst.ehu.es), this has opened for us a new path for the phase-transition analysis in a deep way in terms of symmetry-adapted modes, by using many of those programs.

When I got involved in the PhD Thesis proposed to me by Professor Dr. Josu M. Igartua, there were two main topics to be developed, at least, regarding the materials to be analyzed, all being double perovskites: continuation of the studies on the Sb family and extension of the analysis to a new very promising family, the layered double perovskites prone to show multiferroic properties.

For the first topic, the purpose was to prepare myself in structural determination and analysis. The work done in the research group I had incorporated to, had in some respects some gaps and my supervisor had in mind the possible way to fill them. The phase diagram proposed for the family of tungstate (Sr_2MWO_6),[1] extended to some materials of the antimony family (Sr_2MSbO_6, $SrCaLnSbO_6$,...) [2] and, then, also proposed for some other families of double perovskites ($SrLnMRuO_6$...),[3] could be analyzed using a more tight sieve and could be extended to more sophisticated families, solid solutions, for instance. One of the parameters used for classifying, labelling, analyzing perovskites, simple or double, is the *tolerance factor*. The mentioned phase diagram is constructed to show the phase-transition temperatures versus the tolerance factor. One of the main conclusions from the studies on the tungstate family, regarding the phase diagram, was that it showed two features: first, the more distorted the structure, that is, the lower the tolerance factor, the higher the phase-transition temperatures; and, second, the higher the tolerance factor the

---

[1] M. Gateshki. *Estudio, mediante métodos de difracción, de la estructura y las transiciones de fase en las perovskitas dobles Sr_2MWO_6 (M=Mn,Cu,Ni,Co,Fe,Zn,Mg) Y La_2NiRuO_6*. PhD thesis. Universidad del País Vasco/Euskal Herriko Unibertsitatea, 2003.

[2] A. Faik. *Estudio de las estructuras y de las transiciones de fase en nuevos materiales de wolframio ($Sr_2M^{2+}W^{6+}O_6$) y de antimonio ($A_2M^{3+}Sb^{5+}O_6$) con estructuras de perovskita doble*. PhD thesis. Universidad del País Vasco/Euskal Herriko Unibertsitatea, 2009.

[3] E. Iturbe Zabalo. *Crystal structure and phase transition studies in perovskite-type oxides using powder-diffraction techniques and symmetry-mode analysis. $SrLnMRuO_6$ (Ln=La,Pr,Nd; M=Zn,Co,Mg,Ni,Fe) and $ALn_2CuTi_2O_9$ (A=Ca,Ba; Ln=La,Pr,Nd,Sm)*. PhD thesis. Universidad del País Vasco/Euskal Herriko Unibertsitatea, 2012.

higher the interval of existence of the intermediate distorted phase. Among others, these two facts had also been observed in subsequently studied related families; families showing more rich phase-transition sequences and with different combinations of cations. Hence, the idea was the following:

- Fill the gaps, as marked in the figure, in the phase diagram, to make the lines more continuous: this point is not purely academic, as filling the gap puts all the materials on the same ground
- Fill the gaps analyzing different materials but with the same tolerance factor: clearly, they should be on the same vertical in the diagram, but should show the same characteristics if the tolerance factor is a suitable universal parameter to describe these systems
- Extend the phase diagram to combinations of cations in the B- and B′-sites in the double perovskites, but, also, in the A-site, to gain knowledge on the evolution of the properties and the phase-transition sequences as the cubo-octahedral volume between the corner-sharing octahedra of the perovskite framework, responsible in another view (changing the reference system) of the distortions, changes.

In the second topic, once I had gained some experience in the analysis, the idea was to enter into the layered double perovskites, in particular, those for which the prototype high-temperature phase shows a tetragonal space group, one of which the sub-groups is polar. I learned that this fact, combined with a careful selection of a couple of magnetic cations, could give rise, possibly, to multiferroic properties,[4] which turned out to be the main (starting) topic of the PhD work my supervisor proposed to me. The difficulties in this case were related, mainly, to the synthesis. The analysis was supposed to be easy, as some previous theoretical works had evened the path. Nevertheless, the path turned out to be tortuous, in both respects: at the beginning, the preparation become difficult and time consuming, with scarce results and, then, the analysis resulted to be *even* more time consuming and needed the assistance of more experimental techniques not thought of beforehand: SEM, TEM and NMR. I have to say that the preparation difficulties gave to me opportunity to refine the approach to obtained good materials: after some months, I mastered the preparation and I was able to obtain, on demand (for the neutron experiments, for instance) good quality and big quantities of the needed materials, the samples analyzed over three-day-at-home-laboratory-X-ray experiments.

But then, in the course of the analysis, as in life, many things appear and many things tend to disappear. The period of those events is not fixed and, sometimes, even more than one event happens to take part: superimposes to the existing one. In my case, I mean, that there could be more materials that could had become interesting as the ones started to analyze were studied, and some other, for many reasons, lose attention, not importance, but for priority changes, mainly, in my experience, due to experimental everyday facts.

The first case is the Te-family, I proposed to my supervisor the possibility to add another family to the analysis. My idea was to have another B-site 6+ oxidation-state

---

[4] T. Fukushima, A. Stroppa, S. Picozzi, and J. M. Perez-Mato. **13**: 12186–12190, 2011.

cation-family to compare to the Sb-family 5+, in the one hand. In the other, I had discovered a lot of work done and included in the manuscript of the PhD of Dr. Ortega-San Martin,[5] but not published. A lot of work similar to the one I was doing, worth publishing, but more importantly, worth including in the framework of the analysis I was performing, mainly because of the variety of cation-combinations, solid solutions and, hence, new and old intervals in the phase diagram could be involved, paving the path more solidly.

In the second case, the priorities of the technologically, perhaps, and theoretically, with no doubt, more interesting materials, decayed: The layered perovskites. I have the permission to say that *the were decayed*: my supervisor decided to conserve the analysis in the scientific fridge, to conserve and maintain without corruption. We did a lot work on these materials, work that has been complemented as I have been working on the rest of themes. We will resume it, after I obtain my doctor degree.

Nevertheless, I have been able to realize that the *method* itself could be regarded as the topic of the analysis. This is what happened in my case: I have turned some aspects of the refinement process the subject of part of the work I have done during these years, mainly, in the last months.

I have to say that this has been possible because the effort of and thanks to the work done by many people, many of them pertaining to the research group I have been working in during my PhD. I like to think that these things related to the refinement process are small contributions that my supervisor, myself and the collaborators involved in the works, are exposing to the community, in the one hand, to have an improved way of using and analyzing data and, in the other, to improve my own knowledge of the method.

One of the problems that people involved in material science has, as I have been able to see, is the difficulty to have access to sophisticated, because they have to be performed at big facilities, but otherwise routine, high-resolution experiments for structural determination, could be. To have access to powder diffraction data from a high-resolution instrument at the ILL, for instance, implies a very hard off-the-scenes work that starts, perhaps, six months before the experiment itself is held, if it happens. The clear, concise and convincing proposal has to be consciously prepared in advance, (having in mind that if it realizes it will be in a six-months period) and sent in time. It has to wait for its approval, which will happen not only if it is sounded scientifically, but if it is better than the other ones revised by the committee, competing during the same period...At the ILL, for instance, the ratio of approved proposals to the sent ones, in some of the instruments, is less than a third. Accessing those instruments has become a luxury not only because of the budget involved, but because of the time and effort 'budget' behind it. Among others, this has been one of the reasons to think and to try to rationalize the refinement-process, at least in the words of my supervisor. In his words also, as I have mentioned previously, the contribution is small, but it is interesting I think: make out all the possible information from not-so-hig-resolution-data making use of good data, from the literature, for instance, or from a carefully designed sole experiment. The analysis of the results from this experiment,

---

[5] L. Ortega San Martín. *Óxidos mixtos $Sr_2B_{1-x}Mg_xO_6$ (B = Co^{2+}, Ni^{2+} Mn^{2+} and Fe^{3+}) con estructura tipo perovskita doble. Estudio estructural, espectroscópico y magnético*. PhD thesis. Universidad del País Vasco/Euskal Herriko Unibertsitatea, 2005.

following the workflow we are contributing (if it could be applied, for sure), will even the analysis for X-ray diffraction data.

This contribution is based on the work by Professor Dr. Perez-Mato and collaborators .[6] We *adapted* that analysis to the simple perovskite $Na_{0.5}K_{0.5}NbO_3$ and, then we successfully applied at a reduced family of double perovskites (Ln_2MMnO_6). After, we extended its applicability to all the materials analyzed by me in the course of my PhD and by the preceding PhD students of my supervisor. We accompanied the extension by adding physical arguments, via a collaboration with the group leaded by the Professor Dr. Etxebarria: the analysis of the simulated ground states at zero kelvin for some of the good cases and for some 'pathological' ones, as pointed out by or enhanced analysis method, matched perfectly with predictions of the method. With those good results, during the last months, we have revised (redone) all the refinements previously done on all the materials I have analyzed, to adapt the refinement method, in the cases it could be done.

Finally, and before I enter to core of the manuscript, I would like to mention another started path, not yet paved, but with a promising future, as I guess: the Raman spectroscopy analysis initiated via the collaboration with the Professor Dr. Patrick Simon, at the CEMHTI-CNRS Orléans, of all the materials I have synthesized. The main idea of this project was to have reproducible fingerprints of the phases and phase transitions in this kind of materials. Having a statistically significant set of materials, grouped in families, with different solid solutions and in a big interval in the tolerance factor axis and showing different phase-transitions sequences, could it be possible to find reproducible features in the Raman spectra usable as indications for a particular phase to be present? In the context of the analysis I perform, Raman spectroscopy as a complementary technique, used to aid in the studies. But, it is quite easy to use it at extreme conditions of temperature, and pressure, for instance. And, it is quite usual to have access to very high external field values, i.e. temperature, in home-laboratory conditions. Hence, if the key features are already identified, it could be checked for the existence of very high-temperature distorted phases, for instance, or for the presence of the prototype expected cubic phase, not accessible, so easily in the laboratory diffractometers' set-ups. Indeed, acquisition time for these experiments is very competitive, once the appropriate measuring conditions for the sample have been found. As mentioned, after gaining the doctor degree, I will resume this interesting project.

In the manuscript you are reading I have gathered the analyzed materials and the results obtained not in chronological order, as I performed the work, but according to the (small) method contribution. In my opinion, this ordering scheme is more adequate. I introduce the mode-crystallography and applied it to a couple of examples, just to establish the refinement context. Then, I go step by step, adapting the method from Professor Dr. Perez-Mato ,[6] developing it for the applicable cases in my materials, I extend the method and complete it and, then, I applied it routinely to the Sb, Te families.

As the subject of the study, this thesis describes the crystal structure and temperature induced structural phase transitions in terms of symmetry-adapted modes of the high temperature prototype phase of some perovskite-related oxides, simple and doubles, which pertain to different families. The fruits of three and half years of work are presented in this

---

[6] B. Kocsis et al. *J. App. Crystallogr.* **47**: 1165–1179, 2014.

memory, which constitute my thesis, are presented in three parts:

- Part I: Introduction, Chemical Synthesis, Structural Determination and Symmetry-Mode Analysis Description
- Part II: Results and discussions
- Part III: Conclusions and Future work
- Appendices: Symmetry-mode decomposition of published perovskite structures and Instrumentation

The first part is devoted to the *Introduction, Chemical Synthesis, Structural Determination, and Symmetry-Mode Analysis* are described. This part brings together all the general features of the studied materials. The *Introduction* chapter is a concise review of the principal characteristics of the simple and double perovskites: structural defects, cation ordering configuration and distorted structures. There is a chapter dedicated to the *Synthesis* of the samples. A detailed description of the *Synthesis* process of each of the Perovskite family is described. *Structural Determination* chapter collects all the information depending on the structure characterization techniques, starting from a brief and general diffraction introduction and following with the techniques used along the thesis. In this memory the notation for classification of distorted perovskites proposed by Glazer will not be used, in general. There is a chapter dedicated to describe a more suitable notation based on Group Theory using symmetry-adapted modes. In that chapter two examples are giving developed to some external, to show the more suitable way of describing the perovskites systems.

From the second part, is settled in the results and discussions of the studied materials giving in six chapters: $Na_{0.5}K_{0.5}NbO_3$ as an entrance to the symmetry-mode analysis where many concepts of this kind of analysis are introduced and used. Second is settled in an experimental study in which we analyze the synthesized very pure and well crystallized sample of La_2CoMnO_6. The third chapter is devoted to a Statistical analysis of five different of double perovskite families $Sr_2MM'O_6$ (M'=W, Mo, Sb, Ru and Te).

The fourth chapter is related to crystal structures of Sr_2MSbO_6 (M= Nd, Eu , Gd, Dy, Ho, Y, Er, Tm, Yb and In) and their phase transition analysis. The fifth and sixth chapters are dedicated to different materials of tellurium family $Sr_2M_{1-x}M'_xTeO_6$ where a complete spectroscopic, magnetic, structural and the phase transitions studies using mode-crystallography are reported for two solid solutions.

The third part is dedicated to the principal conclusions of all the work of my PhD work, then to the future perspectives (non-finished work), which is about, M^{3+} Size effect in the Ca_2MSbO_6 (M = *Ln*, Y), the Nano-chessboards Layered Family Na*LnMM'*O$_6$ and Raman scattering studies on Double Perovskites.

The last part of the memory is dedicated to the appendices, gathering the Symmetry-mode decomposition of published perovskite structures and Instrumentation. The selected bibliography related to this memory is the chapter that brings this part to an end.

Contents

Abbreviations

APB	Anti-phase boundaries
AS	Antisite
a.u.	Arbitrary unit
BCS	Bilbao Crystallographic Server
BET	Burumauer-Emmott-Teller
ca.	*circa*, approximately
e.g.	*exempli gratia*, for example
HT	High temperature
i.e.	*id est*, in other words
Irrep	Irreducible representation
JT	Jahn-Teller
LT	Low temperature
NKN	$Na_{1-x}K_xNbO_3$
NPD	Neutron Powder Diffraction
PS	Phase transition
PZT	$PbZr_{1-x}Ti_xO_3$
RT	Room temperature
SOFC	Solid Oxide Fuel Cells
SXRPD	Synchrotron Powder Diffraction
XRPD	X-ray Powder Diffraction

Part I

General characteristics

Chapter 1

Introduction

The compositional and structural diversity of perovskites arises because of extreme flexibility of the structure with regard to cationic and anionic replacements, and tolerance to ion defects. Unlike other structural types, every element of the periodic table, with the exception of the nobles gases, can be found in some variant of the perovskite-structured materials.

The nature of these materials is due to the remarkable stability of the perovskite framework. It should be no surprise then, that perovskites and materials related to them, have provide entire series of technologically and theoretically important systems at the forefront of solid-state research.

1.1 The perovskite structure

The so-called 'perovskites' materials, constitute a large family of crystalline and inorganic compounds, which represent one of the most extensively studied structures in solid-state chemistry and physics material science and geology. Their name is derived from the mineral $CaTiO_3$, which presents the basic crystalline structure, the simple perovskite, to which are analogous the structures of the compounds pertaining to the mentioned family. The mineral perovskite ($CaTiO_3$) was discovered by the German chemist and mineralogist Gustav Rose in the Ural Mountains in 1839 and then it was named after the Russian nobleman and mineralogist Lev Aleksevich von Perovski .[7]

Since that time, perovskite materials have been the subject of great interest for the scientific community, due their considerable technological importance. In 1926, V.M. Goldschmidt made and studied the first synthetic perovskite, including $BaTiO_3$ (a fundamental dielectric material). In his work [8] he pioneered many principles, like the relationship between the radii of atoms and the structural features of the perovskite, known as *toleranace*

---

[7] G. Rose. *De novis quibusdam fossilibus, quae in montibus uraliis inveniuntur*. Scripsit. Ann. Phys., 1839.

[8] V. M. Goldschmidt. *Naturwissenschaften* **14**: 477–485, 1926.

factor, that remains applicable to the structure today.

The first step in an examination of a perovskite structure is to examine the basic perovskite structure and the ways in that it can distort. The most sensible place to begin such an examination is the ideal simple perovskite, which has cubic symmetry (space group $Pm\bar{3}m$) as depicted in Figure 1.1. Its general formula is ABX_3, where A is typically a large, low oxidation state cation, B is a smaller cation that can adopt octahedral coordination (normally a transition metal), and X is an anion such as F^- or O^{2-}. It is composed of a three dimensional network of regular corner-shared MX_6 octahedra. Historically the octahedra site (M cation) is designated the B-site. The terms B-site and octahedral cation M are used interchangeably in this text. In the ideal case, the B-site cations are at the center of the octahedra with the A cations centrally located in the body center of the cube formed by eight corner-shared octahedra (twelve coordination).

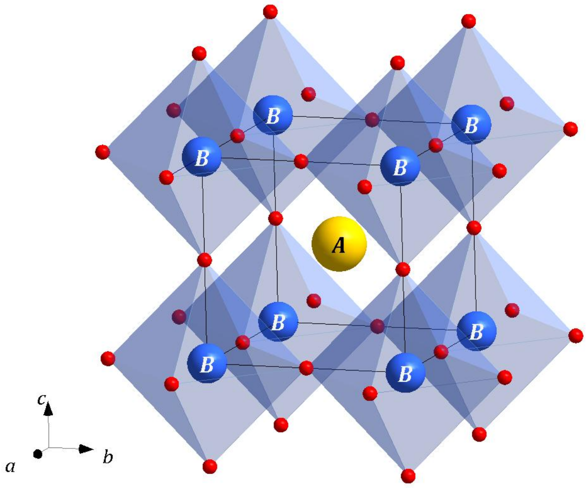

Figure 1.1: The schematic representation of the cubic simple perovskite structure ABO_3. The A and B cations are shown as yellow and blue spheres. The corners of the octahedra denote the oxygen atoms.

The perovskite structure has a high-degree of chemical versatility, allowing for numerous cation substitutions. Virtually nearly all the elements in the periodic table have been incorporated into the structure. The great part of the perovskite compounds are fluorides or oxides (type of materials in the present work), but the perovskite structure is also known for heavier halides ($LiGaCl_3$ [9] or $KMgF_3$ [10]), sulfides ($BaZrS_3$) ,[11] hydrides ($CsCaH_3$) [12]... The number of perovskites is further extended by the aptitude of this structure to support defects, particularly anion and cation vacancies.

The wide range of composition leads to diverse physical properties in perovskite type materials. These properties are known to be strongly linked to subtle structural variations. A good example of this is that varying the degree of octahedral tilting in a perovskite, changes the extent of orbital overlap through the BO_6 octahedral network, thereby affecting

---

[9] W. Hönle, G. Miller, and A. Simon. *J. Solid State Chem.* **75**: 147–155, 1988.

[10] V. Luaña, A. Costales, and A. M. Pendás. *Phys. Rev. B* **55**: 4285–4297, 1997.

[11] A. Clearfield. *Acta Crystallogr.* **16**: 135–142, 1963.

[12] F. Gingl, T. Vogt, E. Akiba, and K. Yvon. *J. Alloy. Compd.* **282**: 125–129, 1999.

3.2 Rietveld Refinement

In order to determine and refine the crystal structure of the studied materials in this work, the Rietveld method has been used. These method was developed in the late 1960s by Hugo Rietveld [54] and is widely used to refine crystal and magnetic structures from obtained X-ray or neutron diffraction data with a constant wavelength.

The Rietveld method is a refinement technique to minimis the residual S_y between the observed intensity $y_{i(\mathrm{obs})}$ (experimental) and the calculated intensity (based on a starting model) $y_{i(\mathrm{calc})}$ by the best least-square fits to all the steps:

$$S_y = \sum_i \frac{(y_{i(\mathrm{obs})} - y_{i(\mathrm{calc})})^2}{y_{i(\mathrm{obs})}} = \sum_i w_i (y_{i(\mathrm{obs})} - y_{i(\mathrm{calc})})^2 \tag{3.3}$$

where w_i is the statistical weight assigned to each point and $y_{i(\mathrm{calc})}$ is the intensity of each step which can be calculated by a mathematical expression that includes the factors related to both the structure and non-diffraction terms. During the refinement cycles, each of these terms and its parameters may be varied to improve the match between observed and calculated diffraction patterns, *i.e.* to minimize the S_y value. Therefore a good initial structure model is required including information about space group, unit cell parameters, atomic positions an instrumental details.

As a result of the fitting, a plot is given (prf file). The goodness of the fitting can be estimated by examining the plot of the difference between observed and calculated patterns. On the other hand, several numerical terms can be used to estimate the goodness of the least-square process. These residual values are defined as:

$$R_{\mathrm{p}}(\%) = 100 \times \frac{\sum_{i=1}^{n} |y_{i(\mathrm{obs})} - y_{i(\mathrm{calc})}|}{\sum_{i=1}^{n} y_{i(\mathrm{obs})}} \qquad \text{R-pattern} \tag{3.4}$$

$$R_{\mathrm{wp}}(\%) = 100 \times \sqrt{\frac{\sum_{i=1}^{n} w_i (y_{i(\mathrm{obs})} - y_{i(\mathrm{calc})})^2}{\sum_{i=1}^{n} w_i (y_{i(\mathrm{obs})})^2}} \qquad \text{R-weight pattern} \tag{3.5}$$

$$R_{\mathrm{exp}}(\%) = 100 \times \sqrt{\frac{N - P + C}{\sum_{i=1}^{n} w_i (y_{i(\mathrm{obs})})^2}} \qquad \text{R-expected pattern} \tag{3.6}$$

$$\chi^2 = \frac{R_{\mathrm{wp}}}{R_{\mathrm{exp}}} \qquad \text{Goodness of fit} \tag{3.7}$$

where N is the number of independent observations, P is the number of refined parameters and C is the number of constrains. A good fit with the refined structure model will accompany with a low residual value. The R_{wp} is commonly considered, since it contains S_y, the quantity to be minimized by the least-square refinements. The goodness of fit, χ^2, which is directly proportional to S_y, is also typically regarded and is ideally to be unity.

The Fullprof program [55] have been used to carried out the Rietveld refinements of all the reported structures, in this work,from X-ray and neutron powder diffraction patterns.

---

[54] H. M. Rietveld. *J. App. Crystallogr.* **2**: 65–71, 1969.

[55] J. Rodríguez-Carvajal. *Physica B* **192**: 55–69, 1993.

Chapter 4

Symmetry-Mode Analysis

Symmetry-mode analysis is a new description way to describe the distortion of the structures. This way, which is based Group Theory applied to Solid State Physics, has gain importance in the last years .[56–58] Thanks to their known phase transitions property , perovskite materials represent a best candidate to be studied using the symmetry-mode adapted method. This type of analysis gives the chance to refine the collective coordinates (distortion-mode amplitudes), instead of the individual atomic coordinates

In this framework, two programs based on the distortion-mode decomposition have been developed, in order to make easier *a priori* a very tedious procedure; AMPLIMODES [59,60] and ISODISTORT .[61]

The decomposition of the distorted structure could be performed by AMPLIMODES available in the Bilbao Crystallographic Server (BCS) [62,63] (http://www.cryst.ehu.es) or ISODISTORT (http://stokes.byu.edu/isotropy.html). The analysis presented in this work has mainly been done with AMPLIMODES, and therefore only the procedure used in AMPLIMODES is explained.

In the present chapter, an overview description and two example using these programs is given. For farther information the reader could have a look at [56–58] based on symmetry-

---

[56] H. T. Stokes, D. M. Hatch, and J. D. Wells. *Phys. Rev. B* **43**: 11010–11018, 1991.

[57] M. I. Aroyo and J. M. Perez-Mato. *Phase Transit.* **63**: 235–255, 1997.

[58] M. I. Aroyo and J. M. Perez-Mato. *Acta Crystallogr. A* **54**: 19–30, 1998.

[59] D. Orobengoa, C. Capillas, M. I. Aroyo, and J. M. Perez-Mato. *J. App. Crystallogr.* **42**: 820–833, 2009.

[60] D. Orobengoa. *Desarrollo de bases de datos cristalográficos on-line y de herramientas para el estudio grupo-teórico de materiales ferróicos y multiferróicos*. PhD thesis. Universidad del País Vasco/Euskal Herriko Unibertsitatea, 2010.

[61] B. J. Campbell, H. T. Stokes, D. E. Tanner, and D. M. Hatch. *J. App. Crystallogr.* **39**: 607–614, 2006.

[62] M. I. Aroyo et al. *Z. Kristallogr.* **221**: 15–27, 2006.

[63] M. I. Aroyo et al. *Acta Crystallogr. A* **62**: 115–128, 2006.

mode decomposition, and at [53,64–66] more particularly in perovskite distortions. distortions.

4.1 Symmetry-mode analysis of distorted structures

Many crystalline structures can be considered distorted with respect to a structure of higher symmetry. This higher-symmetry arrangement may be another phase of the compound (Real parent phase) or a virtual reference structure (virtual parent phase). By definition, a group-subgroup relation necessarily exists between the space groups of the parent structure and the observed one. This latter can then be qualified as a distorted structure and can be described as the parent crystalline structure plus a static symmetry-breaking structural distortion. If the distortion is sufficiently small, a thermally driven structural transition to the configuration of higher symmetry may take place at higher temperatures.

Let $\mathbf{r}_0(\mu)$ be the atomic positions of the μ atoms (μ=1,...,s) within the asymmetric unit of the reference (parent) structure with space group G. The asymmetric unit of the distorted structure (space group H, subgroup of G) will generally have more atoms, due to the high symmetry structure Wyckoff orbital splitting; and the atomic positions within the H asymmetric unit, can be expressed as

$$\mathbf{r}(\mu,i) = \mathbf{r}_0(\mu,i) + \mathbf{u}(\mu,i) \tag{4.1}$$

where $\mathbf{r}_0(\mu,i)$(μ=1,...,n_μ) denotes the atomic positions in the parent phase written in the low symmetry structure bases, with the i label enumerating the H space group Wyckoff orbitals arising from a unique orbital of G.

The magnitude of a displacive distortion can be measured by the amplitude of the displacement, and depends on the cell parameters values used in the scalar product (which generally corresponds to the parent phase cell), its variation will be minimum as long as the deformation of the cell is reasonable small. In general, any distortion can be expressed as the sum of the contributions of a set of symmetry-adapted modes. Each defined mode is compatible with an intermediate space group Z between G and H ($G \geq Z \geq H$), known as *isotropy* group and it is supergroup of H. This means that the symmetry-modes are restricted to the isotropy subgroup of the associated *irrep*.

The distortion present in a distorted structure (pseudo-symmetric) contains a primary component, corresponding to a mode or modes which are unstable in the parent high-symmetry configuration, and are fundamental for explaining the stability of the distorted structure. This primary distortion mode is enough to break totally the symmetry between the reference and the low symmetry phase. In addition, the distortion contains other secondary contributions of less importance, associated with modes which are allowed by symmetry and become frozen through coupling with the primary ones. The secondary modes, will break the symmetry into intermediate symmetries. Those distortion modes are

---

[53] C. J. Howard and H. T. Stokes. *Acta Crystallogr. B* **54**: 782–789, 1998.

[64] C. J. Howard, B. J. Kennedy, and P. M. Woodward. *Acta Crystallogr. B* **59**: 463–471, 2003.

[65] C. J. Howard and H. T. Stokes. *Acta Crystallogr. B* **60**: 674–684, 2004.

[66] C. J. Howard and H. T. Stokes. *Acta Crystallogr. A* **61**: 93–111, 2005.

associated with different irreducible representations (irreps) of the parent space group. The separation of the contributions of the different modes in a structural distortion is done using the symmetry-mode analysis. In this, two concepts have to be properly defined: (a) the structural distortion itself (displacement field) relating the parent and the distorted phases; which can be decomposed into two contributions: a homogeneous strain (elastic degrees of freedom) and an atomic displacement field (internal atomic degrees of freedom) given by the displacements of each atom in the low-symmetry structure with respect to its position in the parent structure. And (b) the basis with respect to which that displacement field can be decomposed and formed by the symmetry modes compatible with the symmetry break between the space groups of the parent phase and the analyzed phase.

To determine the amplitudes of the modes taking part in the symmetry-breaking, it is not necessary to know the *real* reference structure. The modes transforming according to the identity *irrep* are the unique amplitudes that depends on the specific atomic coordinates of the reference structure; those allowed in the reference structure, but who do not break the symmetry of the space group. Moreover, changes in the degrees of freedom of the atomic coordinates of the reference structure, means atomic displacements in those modes; leaving the rest of the modes, the ones involved in the symmetry-breaking untouched.

There are two versions of the program: AMPLIMODES and AMPLIMODES for FullProf. The initial structural information needed for the symmetry-mode analysis is shown in Section A.1, and consists of: the high symmetry phase (prototype phase); the low symmetry phase (the cell parameters and the space group); and, finally, the transformation matrix between both cells. It is important to empathized the possibility to make the analysis in non-standard settings. AMPLIMODES, apart from the above mentioned information, needs the low symmetry phase atomic coordinates and in the output provides the amplitudes corresponding to each distortion mode; nevertheless, AMPLIMODES for FullProf does not requires that information, but in the output file prepared to introduce in a .pcr file (input file for FullProf) all the mode amplitudes are null.

In the first step we obtain, using the room temperature (RT) cell parameter values from the XRPD data, a complete basis of symmetry-adapted distortion modes. It is worth noting that for the symmetry-mode analysis AMPLIMODES (AMPLIMODES for Fullprof) performs, it is not necessary to know a real parent structure. Starting from the distorted phase (H space group) one can construct an ideal parent structure whose symmetry group (G, with $G > H$) is determined by the structural pseudo-symmetry of the low symmetry phase. The structural differences between that ideal parent structure and any other possible parent structure of this symmetry are due only to contributions of symmetry-modes compatible with G, i.e. the totally symmetric modes. The contributions of the much more important symmetry-breaking distortion-modes present in the distorted phase do not depend on any choice of the atomic coordinates of the parent structure.

The pseudosymmetry search of a distorted structure could be done by PSEUDO [67] available in the BCS. If the atomic displacements relating the two structures are smaller than 1 Å, it is probable that the structure undergoes a temperature induced phase transition of Landau type into a high symmetry configuration. The program is designed to detect

---

[67] C. Capillas et al. *Z. Kristallogr.* **226(2)**: 186–196, 2011.

Table 4.1: Transformation of the Sr_2CoTeO_6 structure from the $P2_1/n$ monoclinic non-conventional structure to the conventional $P2_1/c$ setting by PSEUDO.

14 ($P\ 1\ 2_1/n\ 1$)
5.6437 5.6096 7.9271 90.00 90.06 90.00
6

Te	1	2a	0.0000	0.0000	0.0000
Co	1	2b	0.0000	0.0000	0.5000
Sr	1	4e	0.4999	0.0066	0.7493
O	1	4e	0.9499	0.0028	0.2376
O	2	4e	0.2751	0.2452	0.4721
O	3	4e	0.7536	0.2727	0.5224

14 ($P\ 1\ 2_1/c\ 1$)
7.9271 5.6096 9.7261 90.00 144.53 90.00
6

Te	1	2a	0.0000	0.0000	0.0000
Co	1	2b	0.5000	0.0000	0.0000
Sr	1	4e	0.2494	0.0066	-0.4999
O	1	4e	-0.7123	0.0028	-0.9499
O	2	4e	0.1970	0.2452	-0.2751
O	3	4e	-0.2312	0.2727	-0.7536

Transformation matrix $P2_1/n$ (No.14) – $P2_1/c$ (No.14)

$$(\mathbf{P},\mathbf{p})_0 = \left(\begin{array}{ccc|c} 0 & 0 & 0 & 0 \\ 0 & 1 & 0 & 0 \\ 1 & 0 & -1 & 0 \end{array}\right)$$

pseudosymmetry in any given structure, and derive a virtual parent high symmetry phase. The required initial information is the space group, cell parameters and atomic coordinates in the asymmetric unit and the structure has to be introduced using the conventional default setting of the space group. The information of all ready known equivalent structure can be used for this purpose. The tolerance factor which limits the maximal atomic displacements with respect to the high symmetry phase structure can be defined in each case.

4.2 Symmetry-Mode Analysis examples

4.2.1 Double perovskite example: Sr_2CoTeO_6

As an example for a double perovskite structure, the ordered Sr_2CoTeO_6 has been chosen. It has a monoclinic structure with the space group $P2_1/n$.[5] Since the structure is given in a non conventional setting, the AMPLIMODES programs needs to transform it into a conventional default setting, thereby SETSTRU in the BCS need to be used. Table 4.4 shows the input ($P2_1/n$ setting, left) and the Output ($P2_1/c$ setting, right) structures.

By PSEUDO, one can access the pseudosymmetry of a structure by checking the pseudosymmetry for the minimal supergroups of H, and if favorable for one of the results, repeat the process once more for its minimal supergroups, and so on, until the maximal

---

[5] L. Ortega San Martín. *Óxidos mixtos $Sr_2B_{1-x}Mg_xO_6$ (B = Co^{2+}, Ni^{2+} Mn^{2+} and Fe^{3+}) con estructura tipo perovskita doble. Estudio estructural, espectroscópico y magnético.* PhD thesis. Universidad del País Vasco/Euskal Herriko Unibertsitatea, 2005.

supergroup is reached. That process has been followed for the example of the monoclinic in the default setting ($P2_1/c$) structure. The unique possible chain of minimal supergroups reaching the cubic ($Fm\bar{3}m$) structure is shown below Figure 4.1. The reason to chose $Fm\bar{3}m$ space group for the parent phase is that the ideal ordered double perovskite is known to have that symmetry. In order to have the possibility to compare the different structure results, the same reference structure has been used for all the compounds (see Table 4.2).

- $P2_1/c$ (No.14) – $Pnnm$ (No.58): index=2

$$(\mathbf{P},\mathbf{p})_1 = \left(\begin{array}{ccc|c} 0 & 0 & -1 & 0 \\ 0 & 1 & 0 & 0 \\ 1 & 0 & -1 & 0 \end{array}\right)$$

- $Pnnm$ (No.58) – $Immm$ (No.71): index=2

$$(\mathbf{P},\mathbf{p})_2 = \left(\begin{array}{ccc|c} 1 & 0 & 0 & 0 \\ 0 & 1 & 0 & 0 \\ 0 & 0 & 1 & 0 \end{array}\right)$$

- $Immm$ (No.71) – $I4/mmm$ (No.139): index=2

$$(\mathbf{P},\mathbf{p})_3 = \left(\begin{array}{ccc|c} 1 & 0 & 0 & 0 \\ 0 & 1 & 0 & 0 \\ 0 & 0 & 1 & 0 \end{array}\right)$$

- $I4/mmm$ (No.139) – $Fm-3m$ (No.225): index=3

$$(\mathbf{P},\mathbf{p})_4 = \left(\begin{array}{ccc|c} 1/2 & 1/2 & 0 & 0 \\ -1/2 & 1/2 & 0 & 0 \\ 0 & 0 & 1 & 0 \end{array}\right)$$

Table 4.2: Reference structure (parent phase) for ordered ($Fm\bar{3}m$, No.225) perovskite structures. The same virtual reference structure has been used for all the compounds.

```
225
7.9209 7.9209 7.9209 90.00 90.00 90.00
6
Te  1  4a   0.00000  0.00000  0.00000
M   1  4b   0.50000  0.50000  0.50000
Sr  1  8c   0.25000  0.25000  0.25000
O   1  24e  0.24714  0.00000  0.00000
```

The transformation matrix (**P**,**p**) for the pair $Fm\bar{3}m > P2_1/n$ can be obtained from the product of the matrices $(\mathbf{P},\mathbf{p})_i$ of the gradual procedure along the supergroups chain (eq.(4.2 and eq.(4.3):

$$P2_1/n \xrightarrow{(\mathbf{P},\mathbf{p})_0} P2_1/c \xrightarrow{(\mathbf{P},\mathbf{p})_1} Pnnm \xrightarrow{(\mathbf{P},\mathbf{p})_2} Immm \xrightarrow{(\mathbf{P},\mathbf{p})_3} I4/mmm \xrightarrow{(\mathbf{P},\mathbf{p})_4} Fm\bar{3}m \qquad (4.2)$$

Table 4.3: Summary of the symmetry mode decomposition, with respect to the ideal cubic perovskite $Fm\bar{3}m$, of the room temperature monoclinic phase ($P2_1/n$), as given by AMPLIMODES. The primary mode, if existing, is written in bold letters. For each irrep the number of basis modes associated to the indicated atoms is shown in parenthesis. Atom labels refer to the $Fm\bar{3}m$ structure. The column headed *Dimension* refers to number of basis modes necessary in general to describe the corresponding irrep distortion; whereas the one headed as *Direction* indicates, in the convention of ISOTROPY [**ISOTROPY**], the direction in the irrep space corresponding to the irrep distortion. Mode amplitudes are given in the last column and their standard deviations in parenthesis.

Atoms	WP	Modes
O1	24*e*	GM^{1+}(1) GM^{3+}(1) GM^{4+}(1) GM^{5+}(2) X^{2+}(1) X^{3+}(1) X^{5+}(2)
Sr1	8*c*	GM^{5+}(2) X^{5+}(1)

K-vector	Irrep	Direction	Isotropy subgroup	Dimension	Amplitude (Å)
(0,0,0)	GM_1^+	(a)	$Fm\bar{3}m$ (ITA 225)	1	0.021(2)
(0,0,0)	GM_3^+	(a,0)	$I4/mmm$ (ITA 139)	1	0.033(2)
(0,0,0)	GM_4^+	(a,a,0)	$C2/m$ (ITA 12)	1	0.795(2)
(0,0,0)	GM_5^+	(-b,a,-a)	$C2/m$ (ITA 12)	4	0.022(1)
(0,1,0)	X_2^+	(0,a,0)	$P4_2/mnm$ (ITA 136)	1	0.006(1)
(0,1,0)	X_3^+	(0,a,0)	$P4/mnc$ (ITA 128)	1	0.314(1)
(0,1,0)	X_5^+	(a,a,0,0,a,-a)	$Pnnm$ (ITA 58)	3	0.101(4)
Global distortion: 0.8886 Å					

$$(\mathbf{P},\mathbf{p}) = (\mathbf{P},\mathbf{p})_0(\mathbf{P},\mathbf{p})_1(\mathbf{P},\mathbf{p})_2(\mathbf{P},\mathbf{p})_3(\mathbf{P},\mathbf{p})_4 = \left(\begin{array}{ccc|c} 1/2 & 1/2 & 0 & 0 \\ -1/2 & 1/2 & 0 & 0 \\ 0 & 0 & 1 & 0 \end{array}\right) \tag{4.3}$$

Now, since the virtual parent phase and the transformation matrix between the cubic and monoclinic cell are known, the distortion decomposition is obtained by AMPLIMODES (see Table 4.3). It can be observed that a single irrep distortion component is not enough to explain the full symmetry-break, there is not a unique primary mode. That means that more than one distortion mode will be necessary to break totally the symmetry from the cubic prototype phase into the monoclinic distorted phase. In this kind of examples were there is not a unique primary mode, one can deduce the importance of each mode checking the amplitude values; directly introducing the low symmetry phase in AMPLIMODES or refining the mode amplitudes by a refinement program. The last case is the optimum choice as different refinement attempts could be done (giving zero values to different mode amplitudes) and observed the best refinement result.

There are seven irreps of the $Fm\bar{3}m$ space group, that can take part in the symmetry-breaking from that space group to the RT $P2_1/n$ monoclinic space group: GM_1^+(1) (totally symmetric), GM_3^+(1), GM_4^+(1), GM_5^+(4), X_2^+(1), X_3^+(1) and X_5^+(3). The numbers in parenthesis (Table 4.3) indicate the number of modes transforming according to the corresponding irrep. Hence, there are 12 modes (one of them is the totally symmetric). In Table 4.3 there is part of the output from AMPLIMODES; the modes' labels indicate the atoms, with their corresponding Wyckoff position in the reference structure, involved in the modes. Therefore, from the twelve modes, 8 (+1) modes move only the oxygen atoms (24*e*) and the rest 3 modes, the Sr atoms (8*c*). As indicated in Table 4.3, the GM irreps have a (0,0,0) *k*-vector, they maintain the unit cell; and the X irreps have a (0,1,0) *k*-vector, they double the unit cell in the *b* direction. The isotropy groups stand for the possible intermediate groups, with a group-subgroup relation between the reference and the distorted symmetry phase (Figure 4.1). The atomic displacements involved in the modes imply the symmetry-breaking from the prototype symmetry to the isotropy group symmetry.

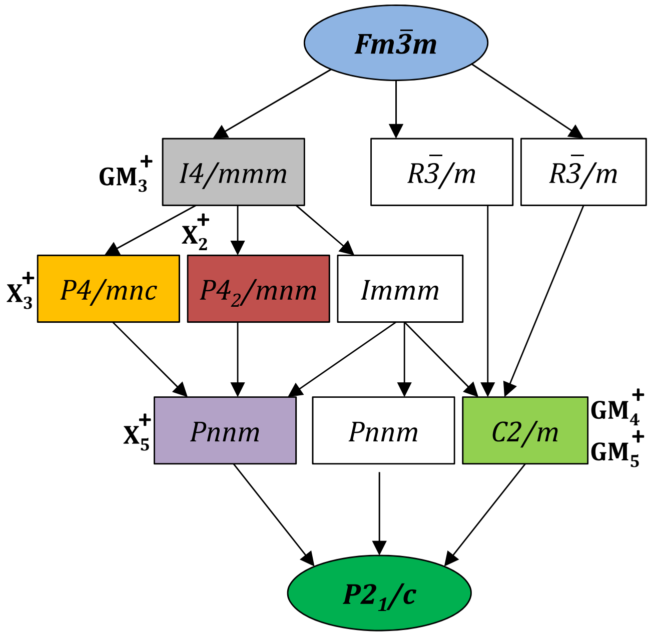

Figure 4.1: Graph of maximal subgroups relating the $Fm\bar{3}m$ and the $P2_1/c$ space groups of room temperature Sr_2MSbO_6 (M=Ln, Y, In and Sc) phases. For each space group, the irreducible representation of the distortion mode yielding this symmetry is indicated if existing.

The seven irreps that break the symmetry from the $Fm\bar{3}m$ to the $P2_1/n$ could be described in as the following: GM_3^+, expands the octahedra in the equatorial *ab* plane, while the apical (in the *c* axis) oxygens are moved along *c* axis to the center of the octahedra. GM_4^+, is essentially a rotation around the *b* axis; although it deforms a bit the octahedra (the displacement of the oxygens in the *ab* plane and the ones in *c* axis are not the same). GM_5^+ irrep is four dimensional, actuating on A/A'-site cations and oxygens. GM_5^+-A4 [1] and GM_5^+-A5 modes, displace the A/A'-site cations in *a* and *c* axes, respectively. GM_5^+-A6, moves the equatorial oxygens in the *ab* plane, transforming in a rectangle the square formed by the oxygens; while GM_5^+-A7, is a kind of rotation along *b* axis, with the apical oxygens displaced in the opposite direction of the rotation. The mode transforming according to X_3^+ is a pure rotation of the octahedra around the *c* axis. X_2^+ mode actuates on the equatorial oxygens, deforming into a rhombus the square formed by the oxygens. Finally, there are

---

[1] FullProf notation

three modes that transforms according to X_5^+ irrep. This mode actuates on the oxygens and on the A/A'-site cations. In the former case, it is a rotation around the *a* axis, although the amount of displacements in the *ac* plane and the ones in *b* are not the same. In the latter, displaces the A/A'-site cations along the *b* axis.

In collaboration with Dr. Juan Rodriguez-Carvajal with our group, a modified version of AMPLIMODES program has been implemented which: AMPLIMODES for Fullprof. In practice, when the virtual parent phase is obtained by pseudosymmetry search, that information together with the low symmetry phase cell parameters and space group (obtained by diffraction data indexation), and the transformation matrix are introduced in AMPLIMODES for FullProf. The program decomposes the distortion in terms of the basis of the symmetry-modes, but the amplitudes for each of the distortion modes are null (see below).

The results are displayed as text incorporating the results of the various parameters required by the Fullprof program so that this text can be copied directly into a .pcr file that serves as an Input for this program. These results are divided into three distinct parts. in the first part follows, the reference structure used in a format suitable for Fullprof. The second part includes the polarization vectors obtained, *i.e.* the new basis in which the refinements will be made, and finally the amplitudes obtained for each of the modes are indicated. Importantly, these amplitudes are the modes of symmetry parameters to refine and not the amplitudes of the distortions irrep. If you do not have a full .pcr file where you can enter all this information, the program provides a generic file .pcr adapted that can be read by Fullprof.

```
P121/N1                    <--Space group symbol
!Atom   Typ       X         Y         Z     Biso      Occ     In Fin N_t Spc /Codes
Te1    TE      0.000000  0.000000  0.000000 0.500000 0.500000  0   0   0    1
                   0.00      0.00      0.00      0.00      0.00
Co1    CO      0.000000  0.000000  0.500000 0.500000 0.500000  0   0   0    1
                   0.00      0.00      0.00      0.00      0.00
Sr1    SR      0.000000  0.500000  0.250000 0.500000 1.000000  0   0   0    1
                   0.00      0.00      0.00      0.00      0.00
O1     O      -0.752860  0.247140  0.000000 0.500000 1.000000  0   0   0    1
                   0.00      0.00      0.00      0.00      0.00
O1_2   O      -0.500000  0.500000 -0.252860 0.500000 1.000000  0   0   0    1
                   0.00      0.00      0.00      0.00      0.00
O1_3   O      -0.247140  0.247140  0.000000 0.500000 1.000000  0   0   0    1
                   0.00      0.00      0.00      0.00      0.00
! Polarisation Vectors of Symmetry Modes for each atom
V_MODES   30
! Nm Atm     Irrep      Vx        Vy        Vz         Coeff
  1 O1      GM1+    0.036445  0.036445  0.000000 1.00
  1 O1_2    GM1+    0.000000  0.000000  0.036445 1.00
  1 O1_3    GM1+   -0.036445  0.036445  0.000000 1.00
  2 O1      GM3+    0.025770  0.025770  0.000000 1.00
  2 O1_2    GM3+    0.000000  0.000000 -0.051541 1.00
  2 O1_3    GM3+   -0.025770  0.025770  0.000000 1.00
  3 O1      GM4+    0.000000  0.000000 -0.031562 1.00
  3 O1_2    GM4+    0.063124  0.000000  0.000000 1.00
```

```
  3 O1_3   GM4+    0.000000  0.000000  0.031562 1.00
  4 Sr1    GM5+    0.089271  0.000000  0.000000 1.00
  5 Sr1    GM5+    0.000000  0.000000 -0.063124 1.00
  6 O1     GM5+    0.044636 -0.044636  0.000000 1.00
  6 O1_2   GM5+    0.000000  0.000000  0.000000 1.00
  6 O1_3   GM5+   -0.044636 -0.044636  0.000000 1.00
  7 O1     GM5+    0.000000  0.000000 -0.031562 1.00
  7 O1_2   GM5+   -0.063124  0.000000  0.000000 1.00
  7 O1_3   GM5+    0.000000  0.000000  0.031562 1.00
  8 O1     X2+    -0.044636 -0.044636  0.000000 1.00
  8 O1_2   X2+     0.000000  0.000000  0.000000 1.00
  8 O1_3   X2+    -0.044636  0.044636  0.000000 1.00
  9 O1     X3+    -0.044636  0.044636  0.000000 1.00
  9 O1_2   X3+     0.000000  0.000000  0.000000 1.00
  9 O1_3   X3+    -0.044636 -0.044636  0.000000 1.00
 10 Sr1    X5+     0.000000  0.089271  0.000000 1.00
 11 O1     X5+     0.000000  0.000000  0.000000 1.00
 11 O1_2   X5+     0.000000 -0.089271  0.000000 1.00
 11 O1_3   X5+     0.000000  0.000000  0.000000 1.00
 12 O1     X5+     0.000000  0.000000  0.044636 1.00
 12 O1_2   X5+     0.000000  0.000000  0.000000 1.00
 12 O1_3   X5+     0.000000  0.000000  0.044636 1.00
!Amplitudes of Symmetry Modes
A_MODES    12   2
    A1_GM1+    0.000000     1.00
    A2_GM3+    0.000000     1.00
    A3_GM4+    0.000000     1.00
    A4_GM5+    0.000000     1.00
    A5_GM5+    0.000000     1.00
    A6_GM5+    0.000000     1.00
    A7_GM5+    0.000000     1.00
    A8_X2+     0.000000     1.00
    A9_X3+     0.000000     1.00
    A10_X5+    0.000000     1.00
    A11_X5+    0.000000     1.00
    A12_X5+    0.000000     1.00
```

4.2.2 Simple perovskite example: $Na_{0.5}K_{0.5}NbO_3$

Based on the explanations and the example given in the previous sections, the $Na_{0.5}K_{0.5}O_3$ example will be briefly explained. More detailed information about this material are reported in Chapter 5.

Let us consider as example the orthorhombic *Amm*2 structure of the distorted $Na_{0.5}K_{0.5}O_3$. As explained previously, the only data needed by AMPLIMODES are the parent structure and the distorted structure to be analyzed (both structures are described in standard settings). This, together with the transformation matrix relating the space groups of the two structures, is sufficient for running the program.

The *Amm*2 structure is polar along z direction, which means that the displacive distortion relation both structures (the distorted and the parent) may include some global translation of the structure as a whole, due to the arbitrary chose of the origin along z in the *Amm*2 structure. For polar structures, the program shifts its origin to eliminate this global displacement. If this shift is not desired, the (0, 0, 0) can be set (by the used) as the polar structure in second input menu (only appearing for polar structures).

The parent structure and the transformation matrix obtained using PSEUDO program (pseudosymmetry search), together with the orthorhombic structure, are listed in Table 4.4. The transformation between the conventional cell of the high- and that of the low-symmetry space groups is $(a+c, c, -a+c)(0,0,0)$: the former indicates the rotational part of the transformation relating the high and low symmetry lattices' cell parameters and the latter defines its origin shift between both.

Table 4.4: Input information for AMPLIMODES: high-symmetry phase information (virtual prototype structure), low-symmetry structure information and transformation matrix. *Amm*2 (ITA No.38, standard setting), and $Pm\bar{3}m$ (ITA No.221). Structures are given in the Server format, ready to be used.

High-symmetry structure						Low-symmetry structure					
221 ($Pm\bar{3}m$)						038 (*Amm*2)					
3.9551 3.9551 3.9551 90.00 90.00 90.00						3.9440 5.6423 5.6767 90.00 90.00 90.00					
3						4					
Na/Ka	1	1*a*	0	0	0	Na/K	1	2a	0	0	0.0447
Nb	1	1*b*	1/2	1/2	1/2	Nb	1	2b	1/2	0	0.5248
O	1	3*c*	1/2	0	1/2	O	1	2a	0	0	0.4730
						O	2	4e	1/2	0.7534	0.2287

Transformation matrix

$$\left(\begin{array}{rrr|r} 0 & 1 & 1 & 0 \\ 0 & -1 & 1 & 0 \\ 1 & 0 & 0 & 0 \end{array}\right)$$

Table 4.5 lists the number of basis symmetry modes and their irreps, that describe the

Table 4.5: Summary of the symmetry mode decomposition, with respect to the ideal cubic perovskite $Pm\bar{3}m$, of the room temperature orthorhombic phase ($Amm2$), as given by AMPLIMODES. The primary mode, if existing, is written in bold letters. For each irrep the number of basis modes associated to the indicated atoms is shown in parenthesis. Atom labels refer to the $Pm\bar{3}m$ structure. The column headed *Dimension* refers to number of basis modes necessary in general to describe the corresponding irrep distortion; whereas the one headed as *Direction* indicates, in the convention of ISOTROPY [**ISOTROPY**], the direction in the irrep space corresponding to the irrep distortion. Mode amplitudes are given in the last column and their standard deviations in parenthesis.

Atoms	WP	Modes
O1	3c	GM$_4^-$(2) GM$_5^-$(1)
Nb1	1b	GM$_4^-$(1)
Na1/K1	1a	GM$_4^-$(1)

K-vector	Irrep	Direction	Isotropy subgroup	Dimension	Amplitude (Å)
(0,0,0)	GM$_4^-$	(a,a,0)	$Amm2$ (ITA 38)	4	0.383(5)
(0,0,0)	GM$_5^-$	(0,a,-a)	$Amm2$ (ITA 38)	1	0.010(5)
Global distortion: 0.3832 Å					

atomic displacements of the atoms in each occupied Wyckoff orbit of the high symmetry phase. For each Wyckoff type, the table lists the relevant irreps and in parenthesis the number of basis modes corresponding to this irrep and this Wyckoff orbit. This information only depends on the type of Wyckoff orbit, therefore all atoms with the same type of orbit are included in a single row. There are a total of five modes, four corresponding to irrep GM$_4^-$ and one to irrep GM$_5^-$. The single mode GM$_5^-$ only involves displacements of the high symmetry orbit of atoms represented by O1. It is worth noting that the ideal number of modes must coincide with the total number of free structural parameters that are necessary to describe the structure. Indeed, if we inspect the original asymmetric unit of the $Amm2$ structure, it can be seen that there are five atomic components that are 'free' by symmetry (the ones should be freed in the refinements), although one of them has been arbitrarily chosen zero due to the polar character of the structure.

The second part of the Table 4.5, is the most important one, it shows the irreps present in the distortion and the absolute amplitudes of these two symmetry components of the global distortion. The table gives for each irrep its wave vector, the restricted direction within the irrep space that the modes fulfill, their isotropy subgroup, and the dimension of its subspace. The GM$_4^-$ subspace is four dimensional. To describe a GM$_4^-$ distortion, four components must be given corresponding to the four GM$_4^-$ (orthonormal) basis modes, one for the *Na* atoms, one for the *Nb* atoms and the other two for the oxygens. While, the GM$_5^-$ subspace is one dimensional as only basis mode of this symmetry exists.

The graph of maximal subgroups connecting the two space groups is displayed in Figure 4.2. In this case, the $Amm2$ distortion decomposes into two distortion modes of different symmetry, transforming according to the irreps GM$_4^-$ and GM$_5^-$. As reported in the Table 4.5, both irreps have *Amm*2 as isotropy subgroup ,[68] which means any of the two could be the active irrep. Thus, theory predicts that, in principle, no single irrep is sufficient to explain the full symmetry break for the transition from the cubic to the orthorhombic phase. That is, the *Amm*2 phase cannot be generated by a single mode distortion, but at least two distortion modes must be active. This fact is confirmed by the amplitudes presented in Table 4.5, where the amplitude corresponding to GM_5^- is more than 30 times smaller. In our case the GM_4^- is the most important irrep responsible for the symmetry-breaking from the cubic, while the GM_5^- is only a secondary effect allowed by symmetry.

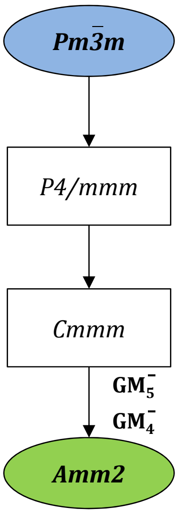

Figure 4.2: Graph of maximal subgroups relating the $Pm\bar{3}m$ and the *Amm*2 space groups of room temperature $Na_{0.5}K_{0.5}O_3$ phase. For each space group, the irreducible representation of the distortion mode yielding this symmetry is indicated if existing.

In order to make a Rietveld refinement of a experimental data, a mode decomposition is needed. The input information listed in Table 4.4 needed for AMPLIMODES for FullProf. The resulting decomposition list is shown below, the amplitudes for each of the distortion modes are null. The decomposition is given in format ready to be copied and pasted in the pcr file. Next step in the analysis consists on refining the amplitudes of the basis modes obtained in the former step. It is worth nothing, in the case where two atoms are sharing the same position, the polarization vectors corresponding to that position should be copied and pasted. For instance in the present example, the *Na* and the *K* atoms are sharing the same position, a second line for the polarization vectors (GM_4^- 0.000000 0.000000 0.170593 1.00) has been created by hand for the *K* atoms.

---

[68] J. M. Perez-Mato, D. Orobengoa, and M. I. Aroyo. *Acta Crystallogr. A* **66**: 558–590, 2010.

```
038                   <--Space group symbol
!Atom   Typ       X         Y         Z     Biso      Occ     In Fin N_t Spc /Codes
Na1    NA      0.000000  0.000000  0.000000 0.500000 0.125000  0   0   0    1
                   0.00      0.00      0.00     0.00     0.00
K1     K       0.000000  0.000000  0.000000 0.500000 0.125000  0   0   0    1
                   0.00      0.00      0.00     0.00     0.00
Nb1    NB      0.500000  0.000000  0.500000 0.500000 0.250000  0   0   0    1
                   0.00      0.00      0.00     0.00     0.00
O1     O       0.000000  0.000000  0.500000 0.500000 0.250000  0   0   0    1
                   0.00      0.00      0.00     0.00     0.00
O1_2   O       0.500000  0.750000  0.250000 0.500000 0.500000  0   0   0    1
                   0.00      0.00      0.00     0.00     0.00
! Polarisation Vectors of Symmetry Modes for each atom
V_MODES   9
! Nm Atm     Irrep      Vx        Vy        Vz         Coeff
  1 Na1    GM4-    0.000000  0.000000  0.170593 1.00
  1 K1     GM4-    0.000000  0.000000  0.170593 1.00
  2 Nb1    GM4-    0.000000  0.000000  0.170593 1.00
  3 O1     GM4-    0.000000  0.000000  0.120628 1.00
  3 O1_2   GM4-    0.000000 -0.060314  0.060314 1.00
  4 O1     GM4-    0.000000  0.000000  0.000000 1.00
  4 O1_2   GM4-    0.000000  0.085297  0.085297 1.00
  5 O1     GM5-    0.000000  0.000000  0.120628 1.00
  5 O1_2   GM5-    0.000000  0.060314 -0.060314 1.00
!Amplitudes of Symmetry Modes
A_MODES    5   2
    A1_GM4-    0.000000     1.00
    A2_GM4-    0.000000     1.00
    A3_GM4-    0.000000     1.00
    A4_GM4-    0.000000     1.00
    A5_GM5-    0.000000     1.00
```

Part II

Results and discussions

Introduction to $Na_{0.5}K_{0.5}NbO_3$ and $Ln_2\mathit{M}MnO_6$

The presence in some of the materials under study of light elements, the fact that the most accessible structural determination technique, X-rays, is not capable to discriminate between some elements, due to the absence of contrast for some elements, the not-so-easy-access to best suited high-resolution techniques for the structural determination, has lead us, among some other reasons, to think on a more efficient workflow for the refinement of the patterns of perovskite materials, simple and double.

The existence of the Bilbao Crystallographic Server, amongst others, with AMPLIMODES, and related Solid State Theory Applications and the Structure Utilities, has facilitated the path to elaborate a new structural analysis workflow, less expensive, more autonomous and independent, less time-consuming to reach the final solution and more efficient, at least when analyzing the kind of materials we are interested in.

It is based on a special parametrization, in the refinements, of some degrees of freedom. The parametrization is done guided by the experimental results from high-resolution data on the material (or on related materials). The parametrization is based on mode-crystallography, the structural degrees of freedom are not the atomic co-ordinates, but the amplitudes of symmetry-adapted-modes.

The method is based on the recent work .[6] We have applied it to $Na_{0.5}K_{0.5}NbO_3$ Chapter 5 and used, in La_2CoMnO_6 Chapter 6.

We show that among the studied set of materials there are a few outliers. They correspond, to the non-high-resolution data, so should be discarded. The structural solutions of the outliers from high-resolution data should be re-visited, in our view. We show that all the accepted solutions have a partial distortion that shares a common direction in the internal space. We show that the direction is unique, although they show up in both senses, corresponding to equivalent structural descriptions, energetically equal. The outliers correspond to non-equivalent descriptions, energetically different.

The method (workflow) gives a first approach to the final solution. It reduces consid-

---

[6] B. Kocsis et al. *J. App. Crystallogr.* **47**: 1165–1179, 2014.

erably the need to perform high-resolution experiments of the same kind in temperature, for instance. Makes more usable data from newly designed (not only as characterizing) preliminary X-ray diffraction experiments. Thus, home-made experiments have extended capabilities for research groups with no access to big facilities, but giving them reliable tools for their own systematic structural analysis or for suitable re-visit of cases subjected to controversy.

Chapter 5

Mode-crystallography analysis of the crystal structures and the low- and high-temperature phase-transitions in $Na_{0.5}K_{0.5}NbO_3$

Over the past few decades there has been a tremendous increase of research works on perovskite-type oxides and solid solutions among them, due to their fundamental interest and technological applications. Perovskite-type oxides have been potential candidates for piezoelectric ceramics used for sensors, actuators, transducers, buzzers and other electronic devices .[69–71] One of the best known and studied perovskite-type solid solutions is the $PbZr_{1-x}Ti_xO_3$ (PZT), which exhibits remarkable piezoelectric properties and a challenging richness of structural features .[72–75] However, these perovskites contain more than 60 wt.% Lead (Pb), well-known for its toxicity. Although there has been a concerted effort to develop lead-free piezoelectric ceramics, no effective alternative to PZT has yet

---

[69] M. Li et al. *Nat. Mater.* **13**: 31–35, 2014.

[70] S. Wada et al. *J. Appl. Phys.* **108**: 094–114, 2010.

[71] T. Tani and T. Kimura. *Adv. Appl. Ceram.* **105**: 55–65, 2006.

[72] E. Cross. *Nature* **432**: 24–25, 2004.

[73] G. A. Samara. *J. Phys-Condens. Mat.* **15**: R367, 2003.

[74] M. Kosec et al. *J. Mater. Res.* **19**: 1849–1853, 2004.

[75] J. Yoo et al. **58**: 3831–3835, 2004.

been found .[76–85]

Sodium Potassium Niobate $Na_{1-x}K_xNbO_3$ (NKN), and associated compounds containing various additional elements as dopants, are potential candidates for piezoelectric and ferroelectric applications. The potentiality of these materials is not only due to their high performance as promising piezoelectrics, but also to their lead-free nature. .[86–89]

$Na_{0.5}K_{0.5}NbO_3$ is one of the important Lead-free piezoelectric materials with perovskite structure. Studies on various aspects of phase transitions in $Na_{0.5}K_{0.5}NbO_3$ have been reported using a variety of experimental techniques, including X-ray absorption fine structure ,[90] transmission electron spectroscopy ,[91] electron paramagnetic resonance ,[92] nuclear magnetic resonance ,[93,94] Raman spectroscopy .[95]

X-ray diffraction (XRD) studies combined with neutron diffraction measurements have been already done on $Na_{0.5}K_{0.5}NbO_3$ in order to determine the room-temperature structure (RT) and the possible phase transitions at high temperature. At RT, it shows an orthorhombic symmetry *Amm*2 .[87,96,97] X-ray diffraction studies revealed that the $Na_{0.5}K_{0.5}NbO_3$ underwent orthorhombic-to-tetragonal and tetragonal-to-cubic phase transitions at 465 and 671 K during heating and 446 and 666 K during cooling, respectively. The temperature dependence of polarization in the temperature range from 300 to 700 K has been also studied by Ishizawa et al., .[97]

In spite of these studies at room- and high-temperature on $Na_{0.5}K_{0.5}NbO_3$, no previous studies at low temperature have been carried out neither on the crystallographic structure, nor on the possible temperature-dependent structural modifications of this material with this composition. No structural data for $Na_{0.5}K_{0.5}NbO_3$ at low temperature is available to

---

[76] R. J. Zeches et al. *Science* **326**: 977, 2009.

[77] H. Maiwa, N. Lizawa, D. Togawa, and T. Hayashi. *Appl. Phys. Lett.* **82**: 1760–1762, 2003.

[78] J.X. Zhang et al. *Nat. Nanotechnol.* **6**: 98–102, 2011.

[79] M. S. Kim, S. J. Jeong, and J.S. Song. *J. Am. Ceram. Soc.* **90**: 3338–3340, 2007.

[80] D. S. Tinberg and S. Trolier-Mckinstry. *J. Appl. Phys.* **101**: 024112, 2007.

[81] P. Wang, Y. Li, and Y. Lu. *J. Eur. Ceram. Soc.* **31**: 2005–2012, 2011.

[82] J. Kling et al. *J. Am. Ceram. Soc.* **93**: 2452–2455, 2010.

[83] C. Ma, H. Guo, S. P. Beckman, and X. Tan. *Phys. Rev. Lett.* **109**: 107602, 2012.

[84] D. Fu, K. Suzuki, K. Kato, and H Suzuki. *Appl. Phys. Lett.* **82**: 2130, 2003.

[85] P. Baettig et al. *Chem. Mater.* **17**: 1376–1380, 2005.

[86] N. Zhang, A. M. Glazer, D. Baker, and P. A. Thomas. *Acta Crystallogr. B* **65**: 291–299, 2009.

[87] T. Sakakura et al. *IOP Conf. Ser.: Mater. Sci. Eng.* **18**: 022006, 2011.

[88] Y. P. Guo, K. Kakimoto, and H. Ohsato. *Appl. Phys. Lett.* **85**: 4121–3, 2004.

[89] D. W. Baker, P. A. Thomas, N. Zhang, and A. M. Glazer. *Acta Crystallogr. B* **65**: 22–28, 2009.

[90] V. A. Shuvaeva et al. *J. Synchrotron Radiat.* **8**: 833, 2001.

[91] J. Chen and D. Feng. *Phys. Status Solidi A.* **109**: 427–434, 1988.

[92] A. Avogadro, G. Bonera, F. Borsa, and A. Rigamont. *Phys. Rev. B* **9**: 3905, 1974.

[93] G. D. Ariano, S. Aldrovandi, and A. Rigamonti. *Phys. Rev. B* **25**: 7044, 1982.

[94] S. E. Ashbrook et al. *Phys. Chem. Chem. Phys.* **8**: 3423, 2006.

[95] K. K. Mishra, V. Sivasubramanian, and A. K. Arora. *J. Raman Spectrosc.* **42**: 517–521, 2011.

[96] L. Liu et al. **68**: 300–302, 2012.

[97] N. Ishizawa et al. *J. Solid State Chem.* **183**: 2731–2738, 2010.

date in the inorganic crystal structure data-base .[98]

It is worth mentioning the importance of the structural phase transition studies in order to understand the physical properties observed in the materials. The present chapter on $Na_{0.5}K_{0.5}NbO_3$ is mainly focused on that aspect using the mode-crystallography analysis.

This chapter is presented as an entrance to the symmetry-mode analysis where many concepts of this kind of analysis are explained in details, and that are going to be cited in the rest of the chapters of this manuscript. This chapter has three main goals focused on the $Na_{0.5}K_{0.5}NbO_3$ material itself. First, to study this material at low temperature and determine the structures and possible phase transitions.

The second target is to re-investigate the structure and the phase transitions at high temperature using the symmetry adapted mode analysis for the first time for this material, a more suitable approach for the analysis of the phase-transition sequences .[40,68,99–103]

The third aim is to present the calculation of the spontaneous polarization in the whole temperature range of existence of the distorted structures. This, in turn, will be compared to the reported polarization in this material using an *a doc* (un-physical) model .[97] In this report we present, following .[6] a novel way of refining, a step forward in the use of the symmetry adapted modes as degrees of freedom in the refinement process: the parameterization of a direction in the internal space of the, in this case, sole irreducible representation, GM_4^-, responsible for the symmetry breaking from the parent cubic space group to the polar distorted low symmetry phases.

5.1 Overall morphology and characteristics of the $Na_{0.5}K_{0.5}NbO_3$ material

Figure 5.1a shows the general aspect of the powder sample. Two different types of particles can be observed: large particles of about 2-8 μm and the small fragments. The SEM shows the typical KNN morphology consisting of faceted grains with a bimodal grain size distribution. Abnormal grain growth tends to occur as a result of the high temperatures treatments. Such bimodal size distribution of grains was also observed in Li and Sb substituted KNN ceramics [104,105] The small fragments could also have been produced during grinding. The in-set presents an enlargement of a quite well facetted

---

[98] Germany Fachin formations zentrum Karlsruhe. *ICSD (Inorganic Crystal Structure Database)*. 2010.

[40] A. Faik, D. Orobengoa, E. Iturbe-Zabalo, and J. M. Igartua. *J. Solid State Chem.* **192**: 273–283, 2012.

[68] J. M. Perez-Mato, D. Orobengoa, and M. I. Aroyo. *Acta Crystallogr. A* **66**: 558–590, 2010.

[99] A. Faik, J. M. Igartua, M. Gateshki, and G. J. Cuello. *J. Solid State Chem.* **182**: 1717–1725, 2009.

[100] E. Iturbe-Zabalo et al. *J. Solid State Chem.* **198**: 24–38, 2013.

[101] E. Iturbe-Zabalo et al. *J. Phys-Condens. Mat.* **25**: 205401, 2013.

[102] E. Iturbe-Zabalo, J. M. Igartua, and M. Gateshki. *J. App. Crystallogr.* **46**: 1085–1093, 2013.

[103] A. Gómez-Pérez et al. *J. App. Crystallogr.* **47**: 745–754, 2014.

[6] B. Kocsis et al. *J. App. Crystallogr.* **47**: 1165–1179, 2014.

[104] R. Gaur, K. C. Singha, and R Laishram. *Ceram. Int.* **41**: 1413–1420, 2015.

[105] H. E. Mgbemere and G. A. Schneider. *Funct. Mater. Lett.* **3**: 25–28, 2010.

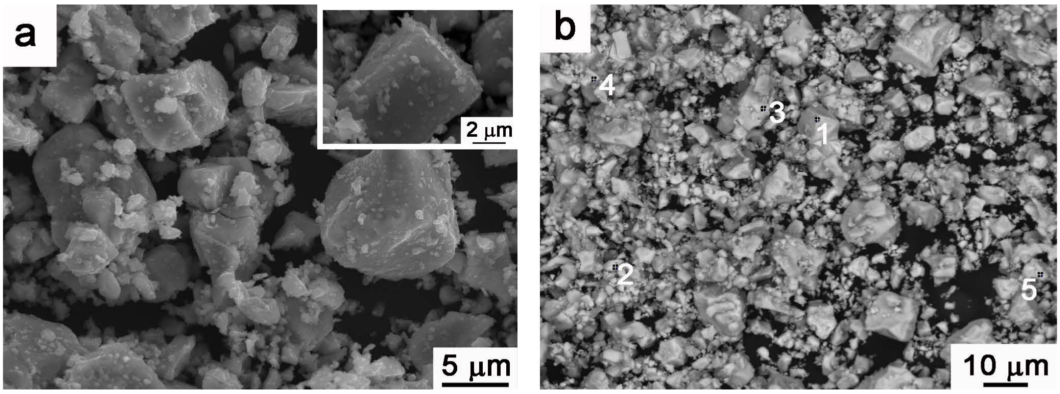

Figure 5.1: a) Secondary electron image showing the overall morphology of the powder sample. In the in-set a quite facetted particle is presented. b) Back-scattered electron image of the sample. Numbered points indicate the EDS analysis positions.

particle, what evidences the crystalline character of the sample. Figure 5.1b shows a back-scattered electron image that provides compositional information. Although no ultimate conclusion on the composition can be given from images acquired on such a powder sample, it can be said that the sample is fairly homogeneous and no significant impurities are present. Ever further, from the semi-quantitative EDS analyses obtained from the positions indicated in Figure 5.1b, the average composition in at.% was as follows: Na = 9.9±1.6, K = 8.9±0.1, Nb = 20.5±0.6 and O = 60.7±0.9. It is worth to note that the analyses were normalized, the oxygen content was determined by stoichiometry and a standardless quantification was applied. The average composition agrees reasonably well with the expected one. The largest scattering is observed for the Na content, what can be understood because the out-going Na low-energy photons can be significantly affected in such a powder sample.

5.2 Symmetry adapted mode-analysis for the room-temperature crystal structure

The diffraction patterns collected at RT from neutron powder diffraction (NPD) and X-ray powder diffraction (XRPD) measurements are shown in Figures (5.2a) and (5.2b), respectively. It can be seen that the $Na_{0.5}K_{0.5}NbO_3$ material is pure: no secondary phase has been detected. In the neutron pattern, an extra small reflection was detected around 72°, which corresponds to the Vanadium sample-container. In the figures, many diffraction lines are clearly split, as expected. The insets show in detail the presence of the 011 and 100 Bragg reflections corresponding to the known orthorhombic symmetry, with higher intensity for the 011 reflection. The data were refined in the $Amm2$ space group using the implementation of AMPLIMODES for FullProf.

The orthorhombic reported structure and the reference structure, the cubic parent phase, are listed in Table 5.1. The transformation between the conventional cell of the high- and that of the low-symmetry space groups is $(a+c, c, -a+c)(0,0,0)$: the former indicates the rotational part of the transformation relating the high and low symmetry lattices' cell

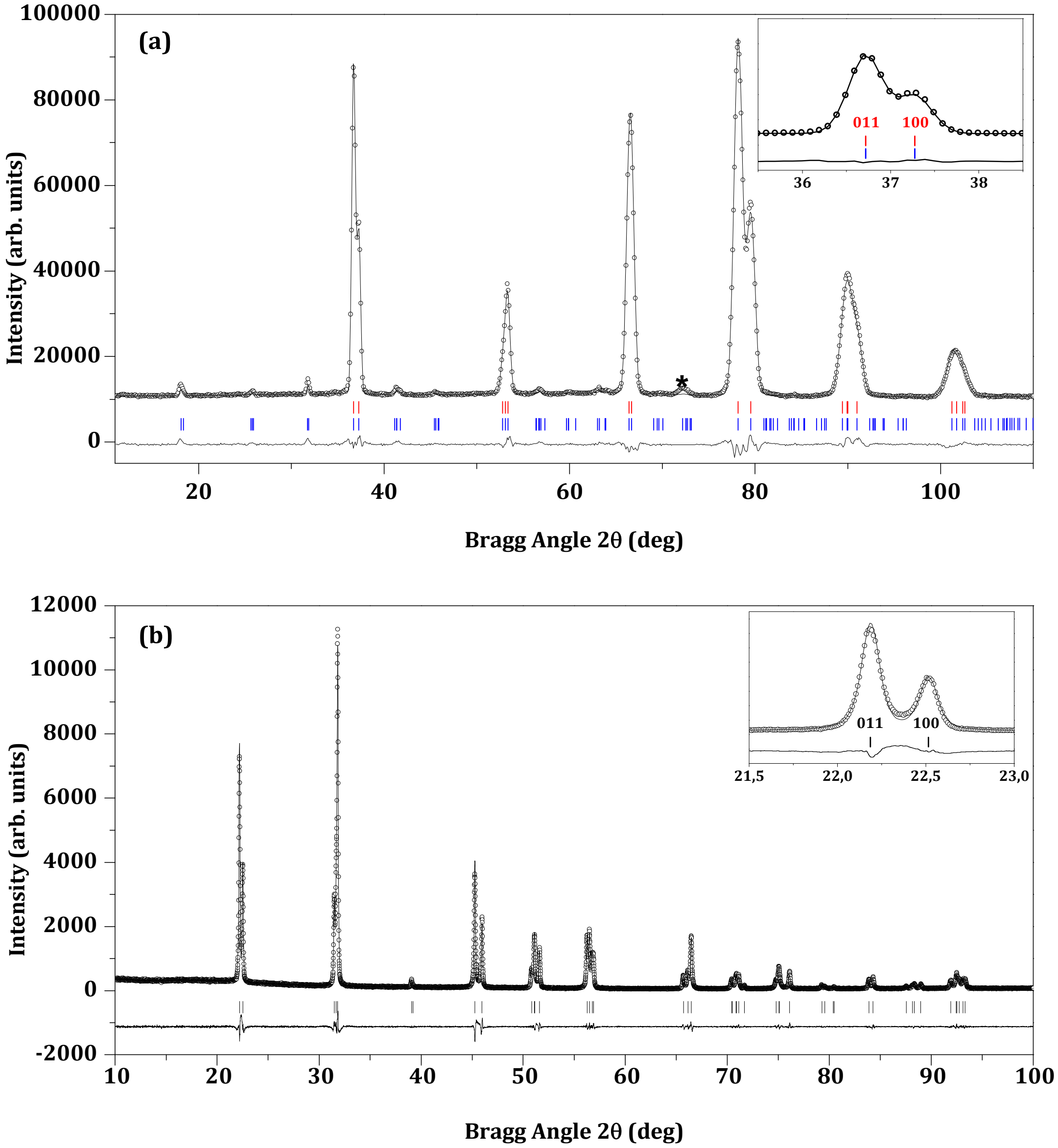

Figure 5.2: Experimental (symbols) and calculated (line) a) neutron and b) X-ray profiles for the Rietveld refinement of $Na_{0.5}K_{0.5}NbO_3$ at room-temperature using a structural model with *Amm*2 space group. Insets show in detail the presence of the 011 and 100 Bragg reflections corresponding to the orthorhombic symmetry. The (*)-symbol marked reflection corresponds to the signal of the Vanadium sample container used during the measurement. The bars in the lower part of the graphics represent the Bragg peak positions. In (a), the upper set of bars (in red) correspond to the first wavelength λ_1 = 2.52Å, and the lower set of bars (in blue) correspond to the second wavelength and λ_2 = 1.26Å.

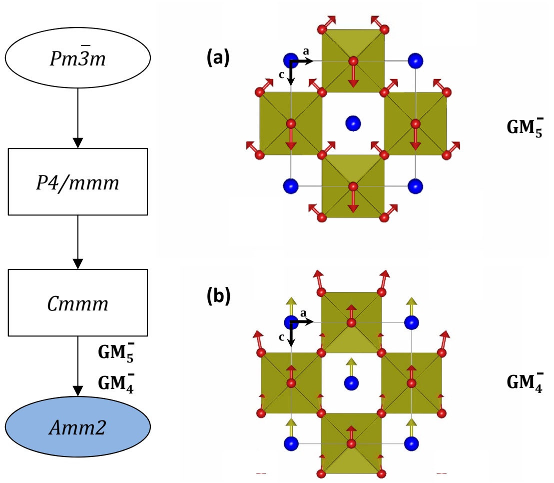

Figure 5.3: To the left, chain of maximal sub-groups of $Pm\bar{3}m$ space group down-to the experimentally observed room-temperature $Amm2$ space group. The calculations were completed in the standard setting of the room-temperature space group phase: $Amm2$. To the right, scheme of the structural polarization vectors, projected on the xz plane, of the distortion-modes transforming according to the GM_5^- and GM_4^- irreps, present in the $Amm2$ structure. The arrows represent the displacements of the atoms in the modes. The two distortion-modes are identified as necessary in the cubic-to-orthorhombic symmetry breaking.

parameters and the latter defines its origin shift between both.

The graph of maximal subgroups connecting the two space groups is displayed in Figure 5.3. In this case, the $Amm2$ distortion decomposes into two distortion modes of different symmetry, transforming according to the irreps GM_4^- and GM_5^-. Both irreps have $Amm2$ as isotropy subgroup [68] Thus, theory predicts that, in principle, no single irrep is sufficient to explain the full symmetry break for the transition from the cubic to the orthorhombic phase. That is, the $Amm2$ phase cannot be generated by a single mode distortion, but at least two distortion modes must be active.

In this case, there is a grand total of five modes, four corresponding to GM_4^- and one to, GM_5^-. The single mode GM_5^- involves only displacements of the high-symmetry orbit of oxygen atoms, O1. The total number of modes must be equal to the total number of free structural parameters necessary to describe the structure. Indeed, in the asymmetric unit of the $Amm2$ structure, there are five atomic components free by symmetry. Nevertheless, one of them has to be arbitrarily chosen to be null due to the polar character of the structure. As a first step, we have fixed the position of the Nb cation in the high symmetry location, that is, we have assigned a null displacement to it (see below, in the spontaneous polarization calculation section).

The Table 5.2 lists the two irreps present in the distortion and the absolute amplitudes of these two components of the global distortion. The table shows for each irrep its wave vector, the restricted direction within the irrep space that the modes fulfill, their isotropy subgroup, and the dimension of its subspace; that is, the number of basis symmetry-adapted modes of this symmetry. The GM_4^- subspace is four-dimensional. To describe such a kind

Table 5.1: Input information for AMPLIMODES for FullProf: high-symmetry phase information (virtual prototype structure), low-symmetry structure information and transformation matrix. *Amm*2 (ITA No.38), *R*3*c* (ITA No.161), *P*4*mm* (ITA No.99) and $Pm\bar{3}m$ (ITA No.221). Structures are given in the Server format, ready to be used.

High-symmetry structure
221
3.9551 3.9551 3.9551 90.00 90.00 90.00
3

Na/Ka	1	1*a*	0	0	0
Nb	1	1*b*	1/2	1/2	1/2
O	1	3*c*	1/2	0	1/2

Low-symmetry structure	**Low-symmetry structure**	**Low-symmetry structure**
161	038	099
5.6135 5.6135 13.7504 90.00 90.00 120.00	3.9551 5.6573 5.6717 90.00 90.00 90.00	3.9551 3.9551 4.0210 90.00 90.00 90.00

Transformation matrix	**Transformation matrix**	**Transformation matrix**
$\left(\begin{array}{ccc\|c} -1 & 0 & 2 & 0 \\ 1 & -1 & 2 & 0 \\ 0 & 1 & 2 & 0 \end{array}\right)$	$\left(\begin{array}{ccc\|c} 0 & 1 & 1 & 0 \\ 0 & -1 & 1 & 0 \\ 1 & 0 & 0 & 0 \end{array}\right)$	$\left(\begin{array}{ccc\|c} 1 & 0 & 0 & 0 \\ 0 & 1 & 0 & 0 \\ 0 & 0 & 1 & 0 \end{array}\right)$

of distortion four components must be given, corresponding to the four GM_4^- (orthonormal) basis modes, one for the A-site cations (Na and K), one for the Nb cations, and two for the oxygens. The subspace corresponding to the GM_5^- irrep is one dimensional, as only one basis mode of this symmetry exists. The four dimensional character of the GM_4^- mode-space is worth to note, as it includes the global translation of the structure. Fixing the origin, as in a standard crystallographic description, reduces the number of degrees of freedom to three, as mentioned, for this type of distortions.

The isotropy subgroup of the two irreps, GM_4^- and GM_5^- is *Amm*2, the low-temperature space group and, hence, any of the two irreps could the active one: the one actually breaking the symmetry from the cubic prototype to the orthorhombic. However, the amplitudes obtained for the two symmetry-adapted distortions are very different. The amplitude of GM_5^- distortion is negligible compared to that of GM_4^-, we are not showing it in the corresponding figure (see below). As mentioned in [6] this is an extreme case of what it is expected in distorted structures resulting (according to Landau theory, see below) from the instability of an order parameter with symmetry properties given, by a single active irrep. Its amplitude can be identified with the Landau order parameter connecting this phase with the cubic perovskite. The GM_4^- distortion is giving rise to the ferroelectric phase, while the GM_5^- distortion is a secondary effect allowed by symmetry, but it hardly influences the phase stabilization, because of its very low amplitude value.

The mode decomposition of the $Na_{0.5}K_{0.5}NbO_3$ experimental *Amm*2 structure with respect to its $Pm\bar{3}m$ parent structure is summarized in Table 5.2. The values for the refined amplitudes of the modes are displayed in the Table 5.3. The table shows also the values of

Table 5.2: Summary of the irreps taking part in the symmetry breaking from, space group ($Pm\bar{3}m$) to the orthorhombic $Amm2$, the rhombohedral $R3c$, the rhombohedral $R3m$ and the tetragonal $P4mm$. The list is part of the output of AMPLIMODES for FullProf. The number in parenthesis indicates the number of modes transforming according to the corresponding irrep. WP stands for Wyckoff positions.

Atoms	WP	Mode irreps
$Pm\bar{3}m \rightarrow R3c$		
O1	$3d$	$GM_4^-(2)$ $R_4^+(1)$
Na1/K1	$1b$	$GM_4^-(1)$
Nb1	$1a$	$GM_4^-(1)$
$Pm\bar{3}m \rightarrow R3m$		
O1	$3c$	$GM_4^-(2)$
Na1/K1	$1b$	$GM_4^-(1)$
Nb1	$1a$	$GM_4^-(1)$
$Pm\bar{3}m \rightarrow Amm2$		
O1	$3c$	$GM_4^-(2)$ $GM_5^-(1)$
Nb1	$1b$	$GM_4^-(1)$
Na1/K1	$1a$	$GM_4^-(1)$
$Pm\bar{3}m \rightarrow P4mm$		
O1	$3c$	$GM_4^-(2)$
Nb1	$1b$	$GM_4^-(1)$
Na1/K1	$1a$	$GM_4^-(1)$

the mode amplitudes calculated from the structure of $Na_{0.5}K_{0.5}NbO_3$ reported in [97] and the structure of $KNbO_3$,[106] which has an orthorhombic symmetry at RT. The calculated values are in agreement with the experimental results obtained from the structural refinements.

Table 5.3: Values after the refinement of the amplitudes (in Å) of the irreps modes, transforming according to the listed irreps, taking part in the symmetry breaking from $Pm\bar{3}m$ space group to the room-temperature $Amm2$ orthorhombic space group for the $Na_{0.5}K_{0.5}NbO_3$ in the present work (PW), compared to the one published in [97] and to $KNbO_3$ in [106].

Irrep	Amplitude		
	$Na_{0.5}K_{0.5}NbO_3$(PW)	$Na_{0.5}K_{0.5}NbO_3$	$KNbO_3$
GM_4^-	0.38(5)	0.34(6)	0.32(1)
GM_5^-	0.01(5)	0.03(4)	0.04(1)

5.3 TEM at room-temperature

Powders of the sample dispersed in Cu grids were investigated using TEM at room-temperature. Figure 5.4a shows a bright field image of a typical particle with electron transparent zones. As described in the SEM images, small fragments produced during the

---

[106] L. Katz and H. D. Megaw. *Acta Crystallogr.* **22**: 639–648, 1967.

crashing in the agate mortar can also be observed. Several selected area electron diffraction (SAD) micro-diffraction patterns were acquired on various particles for several different orientations (Figures 5.4b-f) to confirm the neutron and XRD information introduced in the previous section. Care has been taken to only gather the contribution outgoing from single crystalline zones. To make the indexation, the experimental electron diffraction patterns were compared with simulations calculated with the JEMS software and using the unit cell determined by the neutron data. Although in some cases the difference in the electron diffraction pattern geometries was relatively small (compare, for example ,Figures 5.4b and 5.4f or Figures 5.4c and 5.4e), taking into account carefully the angles between the reflexions it was possible to distinguish the different zones axes. It can be said that the TEM investigation at room-temperature was completely consistent with the neutron and XRD data.

5.4 Non-ambient crystal structures study

The objective of this non-ambient study is first to investigate the possible existence of low-temperature phase-transitions. We expect to find a more distorted structure as the temperature is decreased, as it is already known in related materials [6] and references therein. This is the case, for instance, of the $Na_{0.95}K_{0.05}NbO_3$ and $Na_{0.70}K_{0.30}NbO_3$ materials, for which a low-temperature phase with the $R3c$ space group was reported .[86] Secondly, we will re-investigate, and confirm, the observed high-temperature phase-transitions sequence: it is known to be $Amm2 \rightarrow P4mm \rightarrow Pm\overline{3}m$. As in the RT analysis, the temperature study will be performed using symmetry adapted modes. This kind of approach has shown to be very powerful and robust when dealing with phase-transition sequences. It has been successfully applied in the case of simple [68] and double perovskites .[40,99–101] Finally, to get profit from the refined polar structures using the symmetry-adapted-modes, we are calculating the spontaneous polarization. We will compare the obtained results to the ones reported, using an ad-hoc model .[97]

5.4.1 Low-temperature crystal-structure study

To study the low temperature possible phase-transitions of $Na_{0.5}K_{0.5}NbO_3$, *in situ* low-temperature neutron-diffraction experiments were performed between 2 and 300 K. Figure 5.5 (left) shows the projected scattered intensity 35°-39° 2θ interval. Black colour corresponds to high intensity and white, to low intensity. The selected 2θ regions have been identified as specially sensitive to the structural changes occurring in this kind of materials and represent reflections that distinguish among different symmetries.

From the phase transition diagram of $NaNbO_3$-$KNbO_3$, two space groups were proposed for the low-temperature structure in the material of the present study: the rhombohedral $R3c$ and the monoclinic Pm (ITA no.6) .[86,107–109] From the knowledge of the Miller indices of the superlattice reflections and lattice type of the structure, as revealed by the

---

[107] M. Ahtee and A. M. Glazer. *Acta Crystallogr. A* **32**: 434, 1976.

[108] M. Ahtee and A. W. Hewat. *Acta Crystallogr. A* **34**: 309–317, 1978.

[109] D. W. Baker, P. A. Thomas, N. Zhang, and A. M. Glazer. **95**: 091903, 2009.

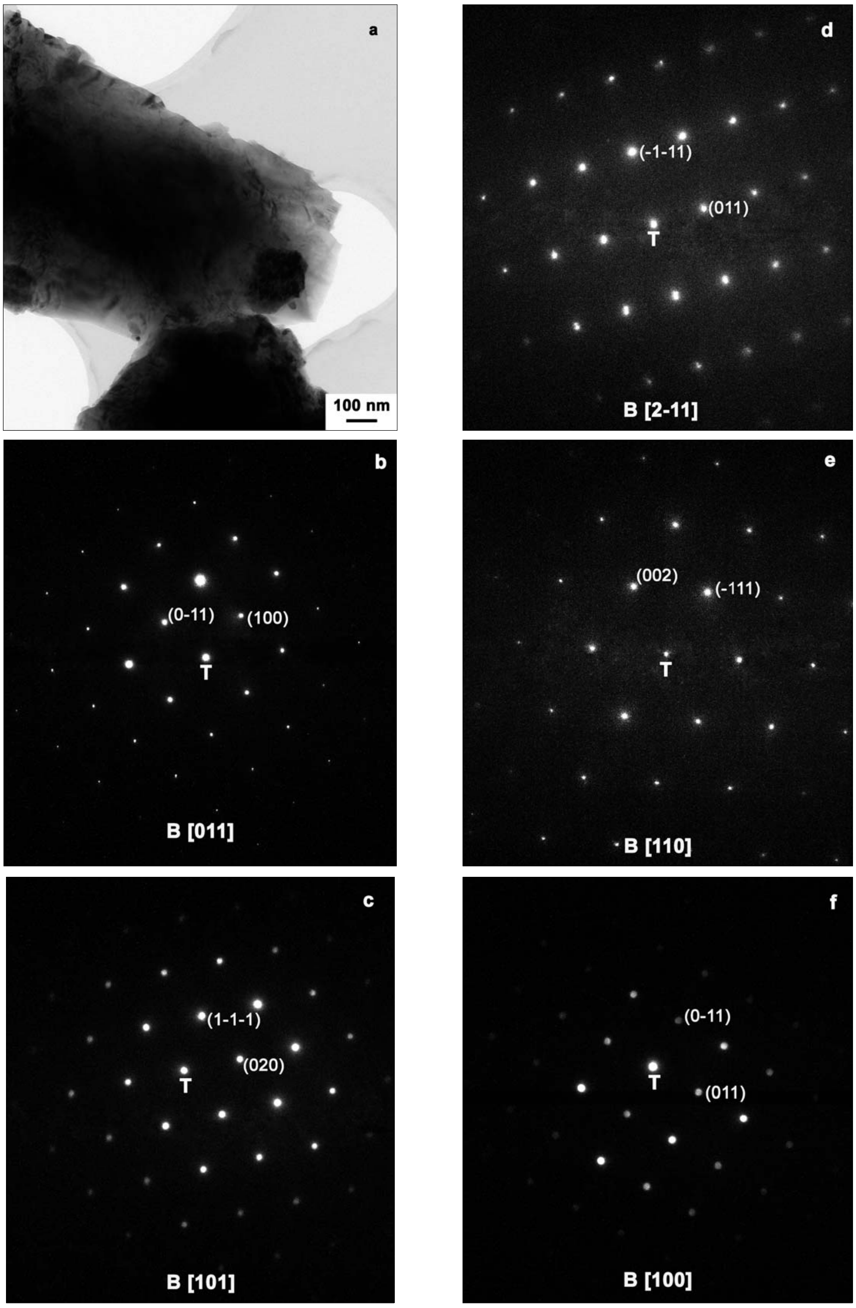

Figure 5.4: a) Bright field TEM micrograph of a typical particle in the sample. b), d) and e) SAD patterns acquired along the [011], [2-11] and [110] zone axes, respectively. c) and f) electron microdiffraction acquired along the [101] and [100] zone axes, respectively. The reflections indicated in the patterns were identified by simulations done with the JEMS software, using the neutron data presented in the previous sections.

splitting of main Bragg peaks, one can drastically restrict the number of the plausible space groups to be considered in the Rietveld analysis. Figure 5.6 shows two intervals of the experimental (symbols) and calculated (line) neutron-diffraction profiles for the Rietveld

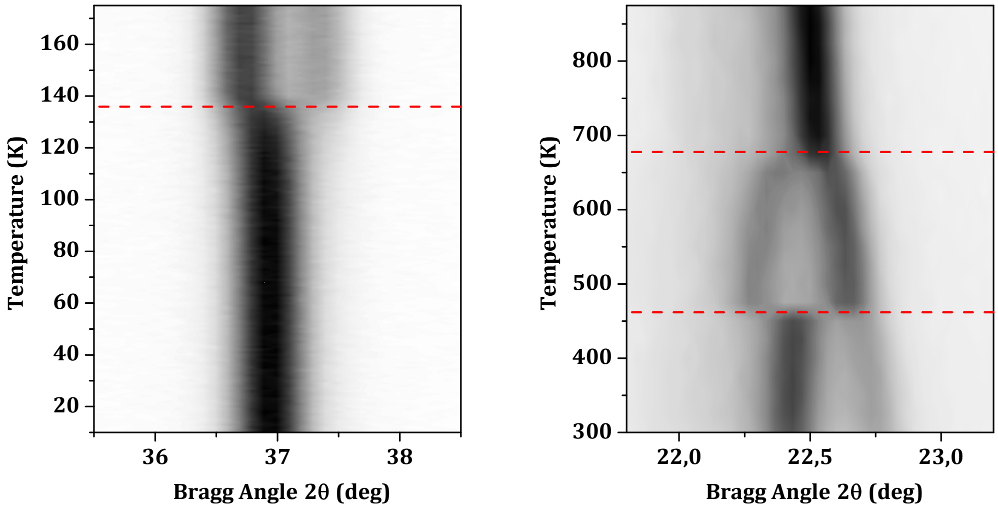

Figure 5.5: Thermal evolution at low-temperatures from NPD measurements (to the left) of the 101 rhombohedral reflection, and at high-temperatures from XRPD measurements (to the right) of the 011 and 100 orthorhombic reflections. The scattered intensity is represented with shades of grey: black corresponds to high intensity, and white, to low intensity. In the left graph, as temperature increases, the $R3c$ singlet splits into a doublet in the orthorhombic $Amm2$ space group: 011 and 100. In right graph, as temperature increases, the two orthorhombic reflections maintain in the tetragonal symmetry, but with their intensities interchanged. After further increasing of temperature, the tetragonal splitting disappears and the double reflection transforms to a single one in the cubic parent space group: 100.

refinements of $Na_{0.5}K_{0.5}NbO_3$, at 2 K, using a structural model with the two different space groups: Pm and $R3c$. The structural model of Pm proposed by ;[89] was used as a starting point. The important point is the splittings, which are evident, and from which the rhombohedral symmetry should be assigned. The rhombohedral distortion, leads to the splitting of the hhh type pseudo-cubic reflections into two, while the h00 type reflections would remain singlet. Thus, in Figure 5.7, the region shown from 34° to 40°, corresponding to the 100 cubic reflection, which is the unambiguous signature of the presence of the rhombohedral symmetry at low temperature. The attempts to refine the collected data at low temperature with the monoclinic Pm were unsatisfactory.

Figure 5.8 shows the graph of maximal subgroups connecting the space groups $Pm\bar{3}m$ (prototype virtual phase) and its subgroup $R3c$. It can be seen that a single irrep is not sufficient to explain the full symmetry break of the transition from the cubic to the rhombohedral phase, as for the RT structure. That is, the $R3c$ distorted structure cannot be generated by a single mode distortion, at least, two different distortion modes must be present: GM_4^- and R_4^+. The former is the polar distortion, giving rise to the $R3m$ symmetry, and the later doubles the unit cell, decreasing the symmetry from $R3m$ to $R3c$. This is a tilting mode of the oxygen octahedra with wave vector $(\frac{1}{2}, \frac{1}{2}, \frac{1}{2})$, at the point R of the Brillouin zone. For the origin choice used, its symmetry properties are given by the irrep $\mathrm{R4}^+$. It involves a single basis mode and this additional $\mathrm{R4}^+$ distortion mode is fully determined by a single mode amplitude.

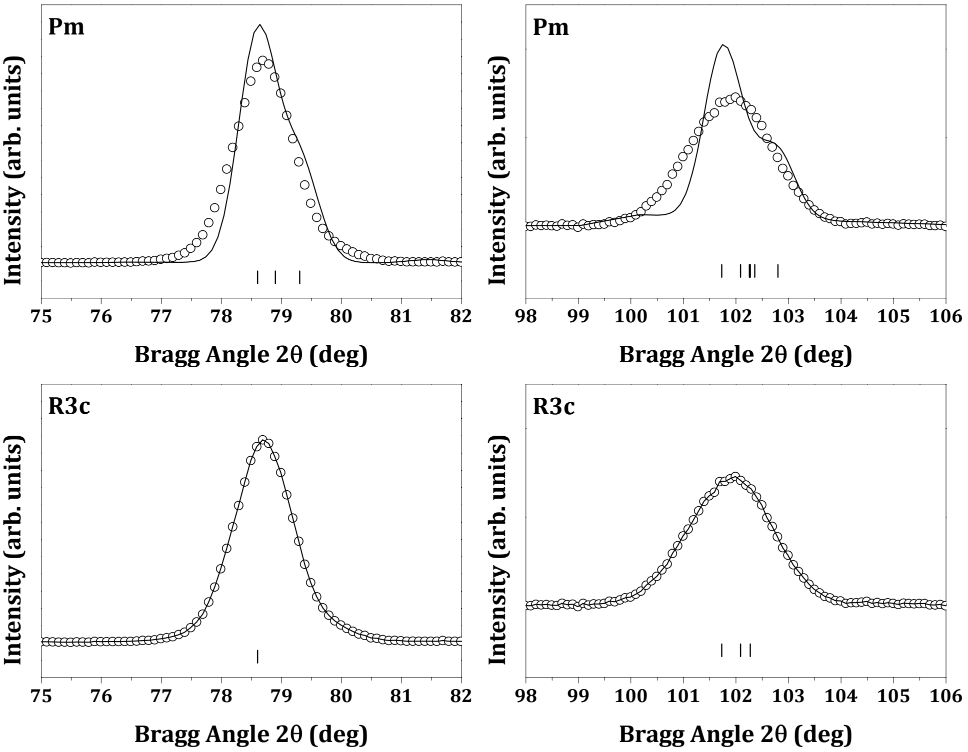

Figure 5.6: Results of the refinements, in the 75°-82° 2θ and 98°-106° 2θ intervals, in $Na_{0.5}K_{0.5}NbO_3$, at 2 K, using two different models with the monoclinic *Pm* and the rhombohedral *R*3*c* space groups. The rhombohedral space group takes into account perfectly the observed splitting, unlike the monoclinic *Pm*.

At the first stages of the analysis, all the attempts to refine the structure in the *R*3*c* space group, gave a zero amplitude value for the oxygen tilt-mode; which, as mentioned, corresponds to the *R*3*m* space group. In conclusion, although at the beginning our symmetry assignation for the low-temperature structure was *R*3*c*, following the reports on some related materials, our refinements, in principle, indicated that the proper space group was *R*3*m*. Table 5.2 shows of the irreps taking part in the symmetry breaking from the cubic space group to the rhombohedral *R*3*m* and *R*3*c*. The list is part of the output of AMPLIMODES for FullProf. The numbers in parenthesis indicate the number of modes transforming according to the irrep

In Figures 5.9a and 5.9b, we show the refinement results in the *R*3*m* and *R*3*c* space groups, respectively. In both figures there is a double set of vertical bars: the first one, up, indicates the Bragg reflections from the main wavelength (2.52Å) and the second one, from the leak (1.26Å= $\frac{1}{2}$2.52). With the colored boxes, blue and red, we have indicated the Bragg reflections assigned, incorrectly, to the wavelength leak, if the *R*3*m* space group model is used. It can be seen that the blue and the red marked reflections are more or less the same in intensity, so could be perfectly miss-assigned. But, using the *R*3*c* space group model, the one in the red box (continuous red line, the discontinuous one also indicates a tilt-related reflection, but not so clear) is caught by one of the reflections from the main

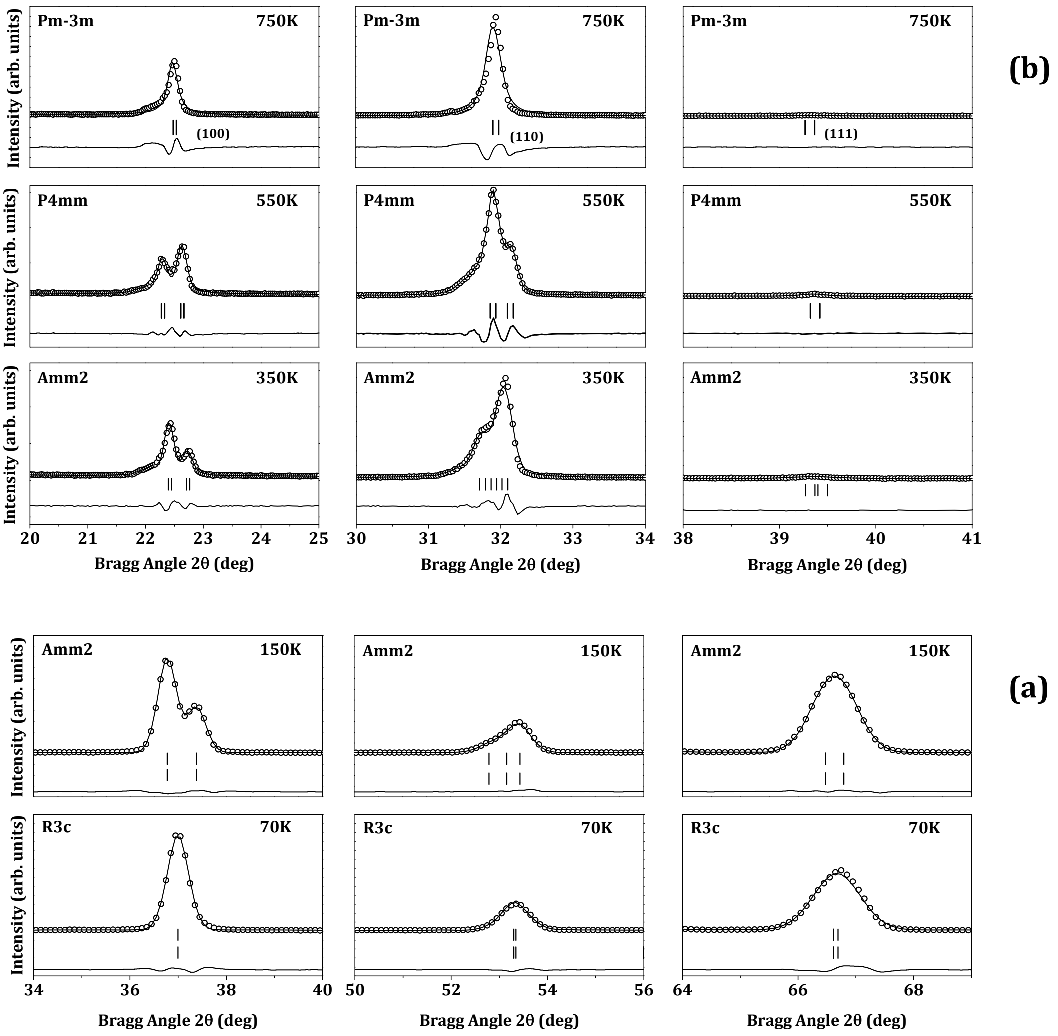

Figure 5.7: Portion of (a) NPD and (b) XRPD profiles for Na$_{0.5}$K$_{0.5}$NbO$_3$ showing, at selected temperatures 70, 150, 350, 550 and 750 K, the evolution with temperature of the cubic reflections: left panel 100, centre panel 110 and right panel 111.

wavelength with the *R*3*c* space group model. This subtle difference is the key fact to assign the low-temperature phase to the *R*3*c* space group. In Figure 5.9b, we have indicated in the low vertical bars, with a dot, the distinct Bragg reflections due to the wavelength leak in the *R*3*c* and *R*3*m* models. Hence, this discussion leads to the final assignation of the low-temperature phase to the *R*3*c* space group.

From the thermal evolution of the 100 cubic reflection, it can be seen that from 2 K up to 135 K the mentioned peak remains singlet, and the unit cell gets distorted, which is indicated by the appearance of a splitting at around 135 K. At that temperature a clear shadow is appearing (see Figure 5.5), confirming that the mentioned splitting corresponds to the orthorhombic reflections 011 and 100. In Figure 5.7a the same 2θ interval (corresponding

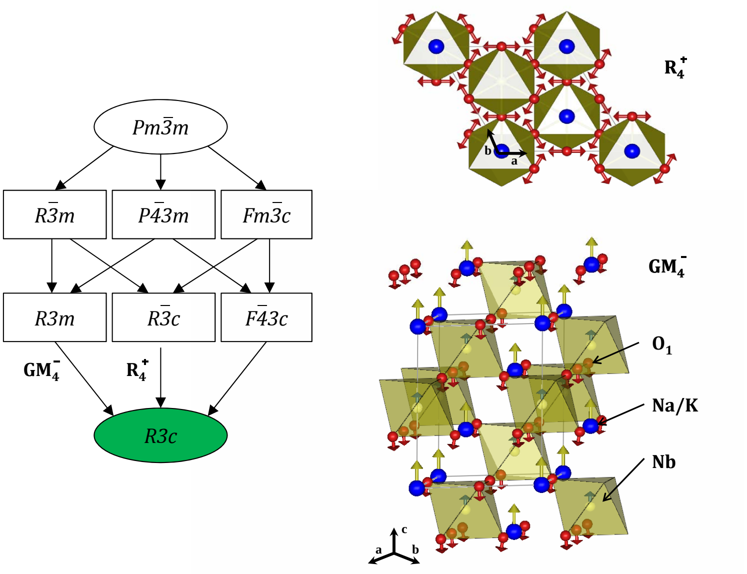

Figure 5.8: To the left, chain of maximal sub-groups of $Pm\bar{3}m$ parent phase space group down-to the experimentally observed low-temperature $R3c$ space group phase. To the right, scheme of the polarization vectors of the distortion-modes transforming according to the R_4^+ and GM_4^- irreps, present in the $R3c$ structure. The arrows represent the displacements of the atoms in the modes. The two distortion-modes are identified as necessary in the cubic-to-rhombohedral symmetry breaking.

to the 100 cubic reflection) as in Figure 5.5 is shown, but this time only portions of the profiles at a single temperature are plotted: at 70 K in the $R3c$ symmetry and at 150 K in the $Amm2$ one. Two additional 2θ intervals for the 110 and 111 cubic reflections are plotted for the same previous reported temperatures.

The data at 10 K were finally refined using the rhombohedral symmetry with $R3c$ space group. The Figure 5.9b shows the results of the refinement at 10 K. In Table 5.1, we show the input for AMPLIMODES. As an example, the crystal structure details and refinement results of $Na_{0.5}K_{0.5}NbO_3$ at 10 K are given in Table 5.4.

Table 5.4: Crystal structure data and refinement results for $Na_{0.5}K_{0.5}NbO_3$ determined using neutron diffraction data at 10 K using the $R3c$ space group. Cell parameters: a = 5.6188(6)Å, c = 13.7873(4)Å, V = 376.96(1)Å^3.

Atom	Site	x	y	z	B_{iso}(^{2})
Na/K	6a	0	0	0.2656(3)	0.94(5)
Nb	6a	0	0	0.0086(2)	0.55(1)
O1	18b	0.6630(4)	0.8178(4)	0.0752(1)	0.22(1)

Attempts to refine the data at 175 K using $R3c$ the space group were unsuccessful. The peak splitting appearing at around 135 K means that the material suffers a discontinuous phase transition from the rhombohedral symmetry to another one. From 135 K up to RT, no

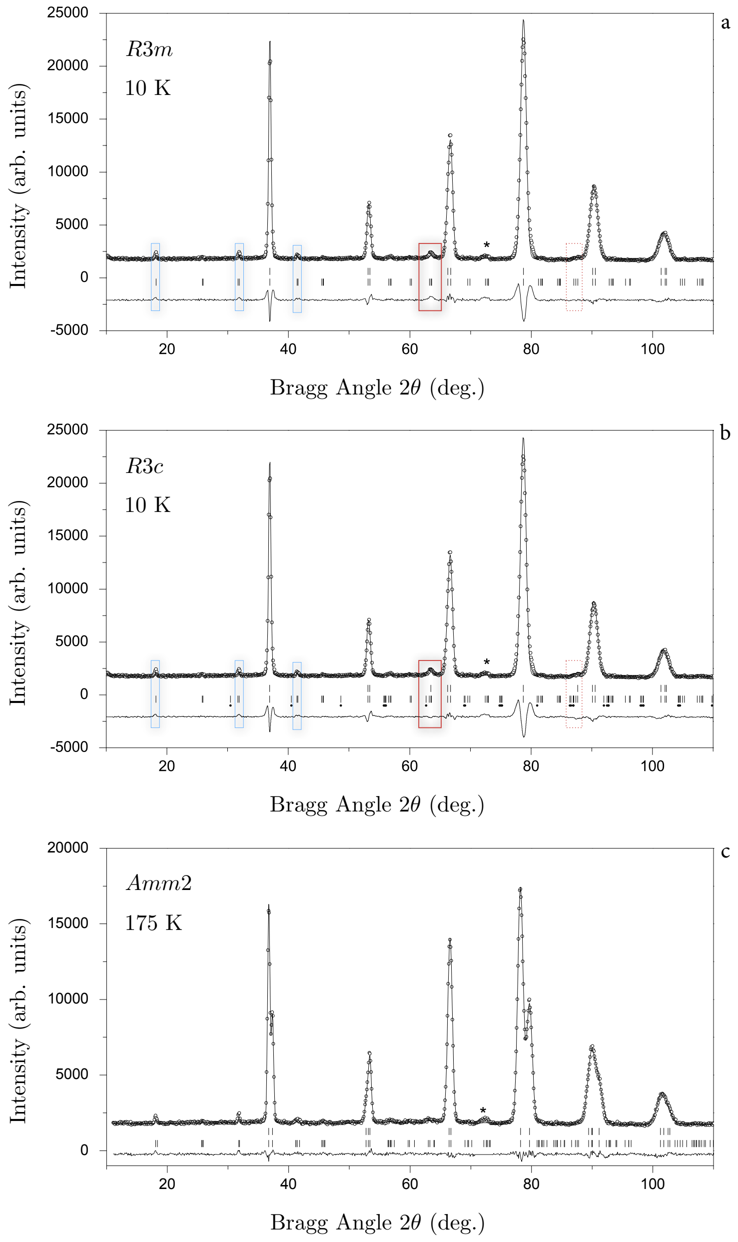

Figure 5.9: Experimental (symbols) and calculated (line) neutron profiles for the Rietveld refinement of $Na_{0.5}K_{0.5}NbO_3$ (a) and (b) at 10 K and (c) 175 K, using a structural model with (a) $R3m$, (b) $R3c$ and (c) $Amm2$ space groups. The double set of vertical bars in (a) and (b) indicates the Bragg reflections from the main wavelength (2.52Å) (upper) and from the leak (1.26Å$= \frac{1}{2}$2.52) (lower). The blue and red boxes show the Bragg reflections assigned, incorrectly, to the wavelength leak, if the $R3m$ space group model is used. The dots in the low vertical bars, (b), are the distinct Bragg reflections due to the wavelength leak in the $R3c$ and $R3m$ models.

more anomalies were observed, which confirms that the crystal structure of the material at

135 K is similar to the RT one. The refinement of the collected data at 175 K was successfully done using the orthorhombic symmetry *Amm*2 by using the structure obtained at 300 K as a starting model of our refinement (see Table 5.1). Figure 5.9c shows the results of the refinement.

5.4.2 High-temperature crystal-structure study

To re-investigate the phase-transitions in $Na_{0.5}K_{0.5}NbO_3$ at high temperatures, thermal evolution of the structure was studied by means of laboratory X-ray diffraction experiments, from 300 K to 870 K. Figure 5.5 (right) shows the scattered intensity in the 2θ interval 21.5° to 23.5°, projected and represented shades of grey. This region corresponds to the 011 and 100 peaks, which refer to the orthorhombic symmetry. It can be seen that as the temperature increases, the distortion of the unit cell gets smaller: the diffraction lines get closer to each other and the intensity of orthorhombic characteristic 011 and 100 reflections decrease. At about 465 K, a very clear discontinuous variation of the intensity is observed. These facts indicate that the structure transforms from the RT orthorhombic phase to intermediate tetragonal, as known. The tetragonal phase is characterized by the 001 and 100 peak splitting. At higher temperature, at around 700 K, as indicated, the splitting of the diffraction lines reduces appreciably and the mentioned two split peaks transform in a continuous way to a singlet, corresponding to the tetragonal-to-cubic phase-transition. This result is in agreement with the previously research reported by N. Ishizawa et al. ?[97] In Figure 5.7b, three 2θ intervals are shown, corresponding to the 100, 110 and 111 cubic reflections, at a single temperature: at 350 K in the *Amm*2 symmetry, at 550 K in the *P*4*mm* symmetry and at 750 K for the cubic $Pm\bar{3}m$. The first interval is the same as the one shown in Figure 5.5.

In the case of the tetragonal *P*4*mm* mode decomposition, the reported tetragonal structure in ?[97] was used as the low symmetry phase, and the reference structure, i.e., the cubic parent phase, was the same as the one used in the case of the *Amm*2 at RT and the low-temperature phase. The transformation between the conventional settings of the high and the low symmetry space groups is $(a, b, c)(0, 0, 0)$, all this information is displayed in Table 5.1. Input data for AMPLIMODES for the tetragonal *P4mm* symmetry are listed in Table 5.1. Table 5.2 shows the irreps taking part in the symmetry breaking from the cubic to the tetragonal symmetry.

Giving energy to the system, by increasing the temperature, the othorhombic distortion decreases. This fact is shown via the diminishing of the GM_4^- amplitude until the transformation to a more symmetric structure, the tetragonal one, takes place. At higher temperature, 450 K to 700 K, the structure behaves as previously, the GM_4^- amplitude diminishes with the temperature increase up to 700 K, where the system reaches the cubic symmetry.

Cyclic refinements have been done using the XRPD data collected from 300 to 875 K. The obtained variation of unit cell parameters and space group symmetries of $Na_{0.5}K_{0.5}NbO_3$ with temperature are shown in Figure 5.10. All the parameters have been scaled in order to be comparable with the edge of the parent cubic cell.

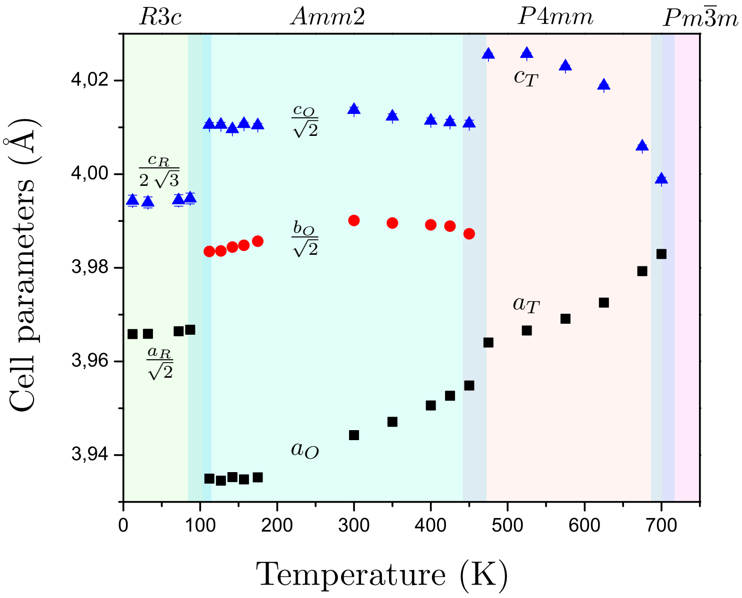

Figure 5.10: Thermal evolution of the lattice parameters of $Na_{0.5}K_{0.5}NbO_3$, as obtained from XRPD and NPD measurements. Solid circles up 300 K, were obtained in the low-temperature NPD measurement and solid circles, from 300 to 875 K in the high-temperature XRPD measurement. The solid red points correspond to the long acquisition data at 2, 10, 175 and 300 K temperatures. From 2 to 875 K the compound undergoes tree phase transitions with the following sequence: $R3c \rightarrow Amm2 \rightarrow P4mm \rightarrow Pm\bar{3}m$.

5.5 Polarization calculation

As mentioned, the temperature evolution of the structures using the symmetry-adapted-modes approach is very suitable for the calculation of the spontaneous polarization in the whole temperature range in which the material is polar, i.e., in all the distorted phases, in the present case. In the following lines, we present the ideas and concepts needed for the calculation of the spontaneous polarization, as an application of the novel way of refinement, by means of the values obtained for the amplitudes of the symmetry-adapted-modes. This analysis is based on the work reported in .[6]

The various phases of $Na_{0.5}K_{0.5}NbO_3$ are caused, following the Landau theory of phase transitions, from a common structural 3-fold degenerate instability of the high-symmetry parent phase, cubic $Pm\bar{3}m$:[110] this polar mode is the driving force of the distorted phases. The mode analysis relating the parent and the distorted phases, in turn, can be de-convoluted into changes of the atomic positions within the lattice unit cell, measured in relative units, plus a strain of this unit cell. Displacive modes refer to the first, and their translation in absolute length values is done using an unstrained lattice .[6,111]

In general, a distortion of this type can be described as a linear combination of a set

---

[110] E. Lines and A. Glass. *Principles and Applications of Ferroelectrics and Related Materials*. OUP, 1977.

[111] D. Orobengoa, C. Capillas, M. I. Aroyo, and J. M. Perez-Mato. *Acta Crystallogr* **42**: 820–833, 2010.

of normalized basis modes. The normalization of these basis modes is chosen such that the square root of the sum of the square of all atomic displacements within a unit cell is 1 Å, and this is done in the metric defined by the unit cell of the cubic structure used as reference. In this context, a structural distortion, with respect to the perovskite, in our case, can be described, no strain is taken into account, as:

$$\text{distortion} = Q \times \mathbf{e}^{\text{dir}} = Q \times \Big(\sum_{i=1}^{\text{dim irrep}} c_i \, \epsilon_i^{\text{dir}} \Big)$$

In that expression, the global amplitude Q is separated from the internal form of the distortion $\mathbf{e}^{\text{dir}}$, given by the normalized mode. This latter is what is called the *polarization vector of the distortion mode*.[68] It can be expressed as a linear combination of the normalized basis modes. Therefore, apart from the strain of the unit cell, not analysed here, the structure is completely described by an amplitude Q (in units of Å) and a n-dim normalized vector (c_i), the dimension of which depends on the irrep according to which it transforms. The components of the mode polarization vector may have opposite signs. This sign-change corresponds to an equivalent twin-related structure.

Summarizing: variations of the amplitudes of the distortion modes are separated from changes in its internal form, described by the polarization vector, a normalized mode that defines the specific linear combination of atomic displacements (basis symmetry modes) involved in the distortion. Thus, the relative contribution of different atomic displacements involved in a distortion mode is expected to be nearly independent on temperature. And thus, it is expected that the modes polarization vectors to be very similar, for the structures obtained under different conditions: the differences among them are expected to be shown, mainly, by the global amplitudes.

The space groups describing the distorted phases of $Na_{0.5}K_{0.5}NbO_3$ are polar and, hence, the structural model they describe will include, in general, an arbitrary global translation with respect to the cubic perovskite. As mentioned, we have chosen the origin such that the Nb cations are at the $(0.5, 0.5, 0.5)$ site, as mentioned. This implies an arbitrary choice done among possible different (but physically equivalent) relations between the cubic parent space group and the space group of the distorted phase. Nevertheless, with that choice, the refined structures, in general, are not comparable. To overcome this difficulty, we have assured that refined structures are comparable performing a parameterized refinement, see in what follows.

As all the phases are, in principle, caused by a similar polar instability (i.e. a three-fold degenerate unstable normal mode), the main difference between the phases being the change of direction of the order parameter, one expects that the distortion modes $\mathbf{e}^{\text{dir}}$ acting in any of the phases (previous equation) are similar to the ones observed in the other phases and, therefore, the components of the polarization vector should be directly comparable amongst them in all the phases. Furthermore, the global amplitude of the distortion should also be comparable, if the normalization condition is the same in both cases. The program AMPLIMODES gives, by default, the mode amplitudes using the primitive unit cell of the distorted phase for the mode normalization. This means that the default mode amplitudes given by this program for the three distorted structures, $R3c$, $Amm2$ and $P4mm$, are directly comparable, as the all the primitive unit cells are equal, for the irrep acting in the distortions.

The tetragonal $P4mm$ phase is the result of the condensation of a polar mode along z, for instance, this is the generic label used previously as "dir" (the irrep labels are those used by ISOTROPY,[112] it is represented schematically in Figure 5.11a. Each of these four basis modes along z, together with their analogous along x and y, form triplets $\{\epsilon_i^x, \epsilon_i^y, \epsilon_i^z\}$ which transform according to the 3-dim irrep GM_4^- of $Pm\bar{3}m$. A distortion of this type can be described as a linear combination of a set of four normalized basis modes $\{\epsilon_1^z, \epsilon_2^z, \epsilon_3^z, \epsilon_4^z\}$ with displacements directed along z (Figure 5.11b). Modes 1 and 2 correspond to the Na/K and Nb sites, respectively, while modes 3 and 4 correspond to the apical and the basal oxygen atoms respectively .[68,111] In this, the polarization vector is a four-dimensional (normalized) vector, whose components (c_1, c_2, c_3, c_4) in the selected basis $(\epsilon_i^z, i = 1, \ldots, 4)$. The tetragonal distortion can be described as:

$$P4mm \text{ distortion} = Q \times \mathbf{e}^z = Q \times (c_1\,\epsilon_1^z + c_2\,\epsilon_2^z + c_3\,\epsilon_3^z + c_4\,\epsilon_4^z)$$

In the orthorhombic phase the polar distortion corresponds to the [110] direction and transforms according to the GM_4^- irrep. The basis modes for this distortion mode are $\{\epsilon_i^o\}$, with $i = 1, \ldots, 4$, written in the form: $\{\epsilon_i^o\} = \frac{1}{\sqrt{2}}(\epsilon_i^x + \epsilon_i^y)$, for instance for the x and y couple. As in the previous case, there are another two analogous couples, i.e. x and z, and y and z. Those are the ones forming the triplet transforming according to the 3-dim irrep GM_4^- of $Pm\bar{3}m$. In terms of the orthorhombic basis modes the distortion is expressed in the form:

$$Amm2 \text{ distortion} = Q \times \mathbf{e}^o = Q \times (c_1\,\epsilon_1^o + c_2\,\epsilon_2^o + c_3\,\epsilon_3^o + c_4\,\epsilon_4^o)$$

The rhombohedral phase, with symmetry $R3c$, contains a polar distortion also corresponding to the irrep GM_4^-. While in the tetragonal phase the GM_4^- polar distortion takes the [001] direction in the 3-dim irrep space, and in the orthorhombic in the [110] direction of the 3-dim irrep space, in the rhombohedral phase it is along [111]. This means that the basis modes $\{\epsilon_i^r\}$, with $i = 1, \ldots, 4$ that describe the distortion mode, can be written in the form $\{\epsilon_i^r\} = \frac{1}{\sqrt{3}}(\epsilon_i^x + \epsilon_i^y + \epsilon_i^x)$, where the basis modes $\{\epsilon_i^x, \epsilon_i^y, \epsilon_i^x\}$ are those described previously and shown in Figure 5.11.

In terms of these rhombohedral basis modes, the structural distortion given by the atomic displacements with respect to the cubic structure, can be expressed in the form:

$$R3c \text{ distortion} = Q \times \mathbf{e}^r = Q \times (c_1\,\epsilon_1^r + c_2\,\epsilon_2^r + c_3\,\epsilon_3^r + c_4\,\epsilon_4^r)$$

Following the contents of the previous paragraphs, we have redone all the refinements in a parameterized way, in the following sense. We have taken refinement of the lowest temperature we had access to, 12 K, data from NPD. We have assumed that this is accurate enough, even if the experiment was done in a non-high-resolution diffractometer D1B for structural analysis, as the present case, to give us the fixed direction in the internal space of the GM_4^- irrep. It is interesting to note that this result obtained $(0.6845\ \ 0.3797\ \ -0.2734\ \ -0.5591)$, matches perfectly with the reference direction used in [6]: $(-0.703(3)\ \ -0.358(5)\ \ 0.320(5)\ \ 0.525(8))$. In fact, we have assumed this direction as our reference also. By the way, this has a very important implication: it is not only expected that the internal direction is going to be maintained from one phase to another in the same material (with the assumption that all the distorted phases are a result of the same instability, as in the present case), but it seems to be quite plausible that, going to different materials undergoing the same kind of phase transitions (with the same origin), the direction maintains.

---

[112] H. Stokes, D. Hatch, and B. Campbell. iso.byu.edu.

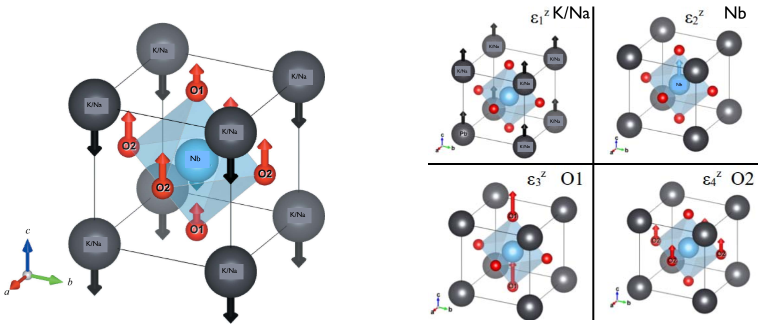

Figure 5.11: (a) Relative atomic displacements with respect to the cubic structure, in the P4mm phase: those define polar distortion mode. (b) The four basis symmetry-modes present in a polar distortion along z of the perovskite structure. The 12-dimensional subspace of all possible polar distortions is spanned by that set of basis modes and their analogous along x and y. it is worth noting that the first three modes involve one atom per unit cell, the mode ϵ_4^z involves two atoms per cell and, hence, the normalization condition implies that the atomic displacements in thi tetra-mode basis are smaller by a $\frac{1}{\sqrt{2}}$ factor.

Once that we have the direction, we have performed the refinements, at a selected set of temperatures, in all the phases, but "forcing" the individual amplitudes, i.e. ($A1\_GM_4^-$, $A2\_GM_4^-$, $A3\_GM_4^-$, $A4\_GM_4^-$) refined in FullProf, to follow the the relation: (1.000000 0.554710 $-$ 0.399418 $-$ 0.816799), which is simply a parameterization of the direction in the internal space. We have obtained two sets of results, without freeing the atomic displacement parameters and freeing them. In the latter case the results are nearly equal, except for a couple of temperatures.

All the mentioned results are shown in Figures 5.12, 5.13 and 5.14. In 5.12a and Figure 5.12b, we show the results obtained with the conventional symmetry adapted modes' amplitude refinements. In this case, we have started from the 12 K data and by fixing the position of the Nb. As mentioned above, this has been the convention for the rest of phases and temperatures as well. It can be seen that the Q_{Nb} is null at all the temperatures. For the rest of the amplitudes, we have freed them without imposing any restriction. It is clear from the results that there are changes in the amplitudes' signs and values. The sign change is related to energetically equal domains, which, in principle is possible, but has no sense when there is a non-coherent change in all the signs of the amplitudes, as we have found. The amplitude of the O1 apical goes from negative to positive when crossing from the trigonal to the orthorhombic, but the Na amplitude does not change sign and the O2 basal, goes to zero. The interpretation should be that the amplitude set does not describe a domain. It is worth noting that following to this refinement process, we have been forced to nullify the O2 basal amplitude: from the neutron data is goes to zero and from the x-ray data, being them not very good, we have set it to strictly zero. On the other hand, when the phase transitions take place, it is expected to find a jump in the amplitude values. Nevertheless, the big changes obtained indicate that there is something not physical underlying those refinement results. As mentioned before, the structures obtained in this way are not comparable, since due to the polar character of all of them, there is an arbitrariness in the origin choice. To make them comparable, we have passed to AMPLIMODES, as obtained, and we have applied the origin shift proposed by the program.

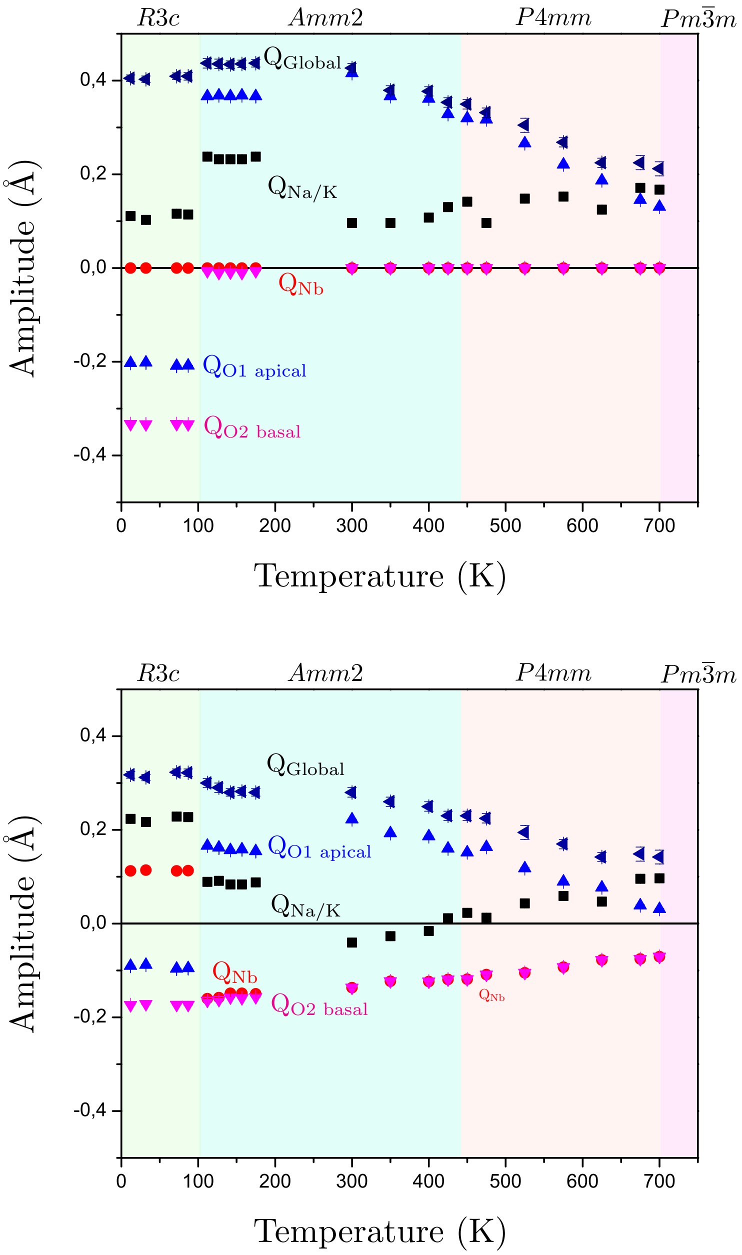

Figure 5.12: (a) Results from the conventional symmetry adapted modes' amplitude refinements. See the text for details. (b) The structures obtained after having passed to *AMPLIMODES*, after applying the origin shift proposed by the program. The anomalous evolution of the Na/K amplitude, in the whole temperature range, is even more evident.

The obtained results are shown in Figure 5.12b. Of course, the conclusions are the same as previously, but in this case, the anomalous evolution of the Na/K amplitude, in the whole temperature range, is even more evident.

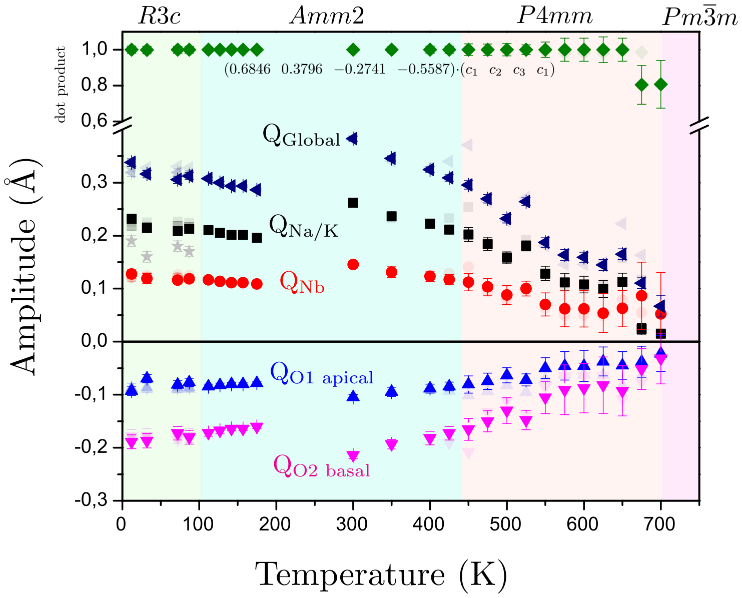

Figure 5.13: Results of the parameterized refinement. For further discussion, see the text. The dimmed symbols show the results obtained for the first parameterized refinement process without freeing the atomic displacements parameters. Also dimmed in the 0-100 K interval, the amplitude values in the *R*3*m* model are shown. With gray stars, we show the octahedral-tilt amplitude values ($R4^+$ irrep) from the *R*3*c* model.

On the contrary, in Figure 5.13, we show the results of the parameterized refinement: the direction in the internal irrep space is maintained in the refinement and the magnitude of the tetra-vector, the global amplitude, diminishes as the temperature increases. Of course, the components of the tetra-vector (the amplitudes refined in FullProf) diminish in a coherent way, going to zero as the distortion, seen from the cubic phase, disappears with temperature. There is no anomalous sign change. There are jumps at the phase transitions, as expected, but they have to be analysed. The jump at the trigonal-to-orthorhombic transition is typically the jump expected. The same is true for the one observed at the orthorhombic-to-tetragonal phase transitions. The anomaly shows in the orthorhombic phase: for instance, the value of the global amplitude, diminishes by a 30% relative value, which is not expected by two reasons. First, because it is very big, it should be something similar to the relative changes shown at the phase transitions. In fact, there should be no change at all, as the material is in the same phase. Second, because it is expected that as temperature diminishes the polar distortion increases and, hence, the global amplitude also, as they are proportional. This anomaly is due to the change of the experiment type, from XRPD to NPD. By the way, it is also worth noting that the same behaviour has been reported in [6]: from XRPD data bigger values than from NPD are obtained for the amplitudes. In the same figure we are showing, in dimmed, the results obtained for the first parameterized refinement process without freeing the atomic displacements parameters. As mentioned, there are a few temperatures at which they do not match.

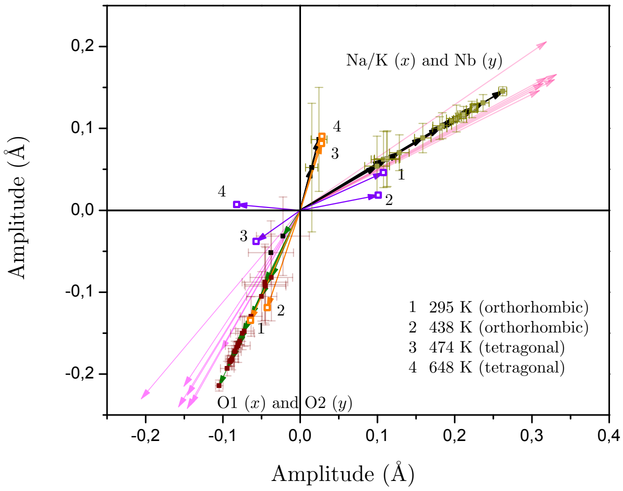

Figure 5.14: Evolution with temperature of the tetra-vector, but split in two parts: amplitudes of the modes Na/K (x) *versus* those of Nb (y); amplitude values of the modes acting on the O atoms, O1 (x) *versus* O2 (y). We are plotting two two-dimensional vectors in the xy plane: as black arrows, the evolution in all the distorted phases of the couple of amplitudes; at the vertices of the arrows, in green, the corresponding errors. The four points (1-4), represent values for the amplitudes obtained at the indicated temperatures, taken from ,[97] passed to AMPLIMODES. Data from single crystal XRD. We have also plot some results from ,[6] pertaining to structures of related compounds, all in the tetragonal phase. The matching of the internal direction is very good.

After the discussion on the low-temperature space group assignation, it is worth keeping the refinement results using both structural rhombohedral models: $R3m$ and $R3c$. As mentioned, the later incorporates another irrep (mono- dimensional), the octahedral tilting, but the polar distortion maintains. Indeed, this is what the results show: even if the tilt is included in the refinements, as needed, the direction in the tetra-space does not change, as expected, and the values of the amplitudes do not change. In Figure 5.13, in the low-temperature region (up to 100 K), also dimmed, we are showing the amplitude values in the $R3m$ model. As can be seen, both sets of amplitude values are almost equal. With gray stars, we show the octahedral-tilt amplitude values (R4$^+$ irrep) from the $R3c$ model. We have to mention that we attribute those oscillating values to the non high-resolution character of the used diffractometer. As mentioned in the discussion above, the existence of this tilt is deduced from Bragg reflection in which there is contribution also from the leak wavelength (very small in intensity). In our opinion, the data do not have resolution enough to obtain a proper temperature evolution of the tilt, which, in turn, is also reflected in the oscillation in the amplitude values in the tetra-space.

Also, in the same figure, in the top and in green, we show the results of the dot products of the reference tetra-vector, as indicated, and the one resulting from the refinement at each temperature. It is clear that the vector maintains its direction, of course we have fixed it approximately, except for the last two temperatures. In our interpretation, at those temperatures the material is already at the cubic phase, or at least the presence of the cubic phase is more evident.

Finally, in Figure 5.14, we show the evolution with temperature of the tetra-vector, but split in two parts: we are plotting the values of the amplitudes of the modes Na/K (x) vs those of Nb (y), in the one hand; and, in the other, the amplitude values of the modes affecting the oxygens, O1 (x) vs O2 (y). We are doing this, because, of course, we can not represent graphically a tetra-vector; but, also, because there is a fixed ratio (as the direction in the internal space is not changing) among amplitudes, components of the tetra-vector. In fact, we are plotting two 2-dimensional vectors in the $x - y$ plane. In black arrows we have the evolution in all the distorted phases of the couple of amplitudes. At the vertices of the arrows, in green, we are representing the corresponding errors, for each of the amplitude represented. It is clear that the arrows maintain the direction. It is also evident, that as the system approaches the cubic parent phase (as the vectors evolve to the lower magnitude part, to the centre of the cartesian plane), the errors increase, in both axis. We have also plot four points (indicated with figures from 1 to 4), which represent the values for the amplitudes obtained once the structures at the indicated temperatures, taken from ,[97] have been passed to AMPLIMODES. These data are coming from single crystal XRD. It is clear that those results do not match with ours: they are not following the expected trend, in relation to the maintenance of the direction in the internal space. In our opinion, those structures should be re-visited. And to finish, we have also plot some results from ,[6] pertaining to structures of related compounds, all in the tetragonal phase. As can be deduced and as it has been mentioned previously, the matching of the internal direction is incredible good. Again, this is an indication that the internal direction is maintain when going to some other families o sub-families of materials undergoing the same type of phase transitions sequence, with the same physical origin.

The calculation of the spontaneous polarization (SP) is done using the previously described distortions and it is shown in Figure 5.15. The model is crude, because we are constructing the SP vector using its definition: $P_s = e\frac{1}{V}\mathbf{c}\sum_{i}^{\text{cell}} q_i \delta z_i$. In that expression e is the electric charge of the electron, V is the volume of the unit cell, q_i are the nominal charges of the atoms (carried by the them as they are displaced by the calculated modes), and assuming the PS appears in the c axis direction, δz_i is the relative displacement of each atom in that axis. It means that we are replacing the actual charge distribution by the ionic charges: Na and K, $+1$; Nb, $+5$ and O, -2. This extremely simplified *toy model*, but physically meaningful, is enough to make the first approach to the order of magnitude of the spontaneous polarization, as has been previously reported in [4,113] for individual temperature values, and in our case, as we have the evolution in temperature of the distorted structures, it is also enough to obtain the first approach of the SP evolution in the whole temperature interval of distorted structures existence. In this sense, we think that we have improved the calculation of the SP reported in .[97] In that work, the authors construct the SP resolved in three components: P_s(total)= $P_s(KO_{0.5})$ + $P_s(NaO_{0.5})$ + $2P_s(NbO_{2.5})$. Then, in turn, each of those three components is further decomposed into more, depending on the coordination and the on the nominal charges. With the method reported in here, we have obtained a very close values to reported ones in [97] (but in our case using a physical meaningful approach). Finally, it is worth to mention that, of course, the same jumps

---

[4] T. Fukushima, A. Stroppa, S. Picozzi, and J. M. Perez-Mato. **13**: 12186–12190, 2011.

[113] D. Di Sante, A. Stroppaa, and S. Picozzi. 14673–14681, 2012.

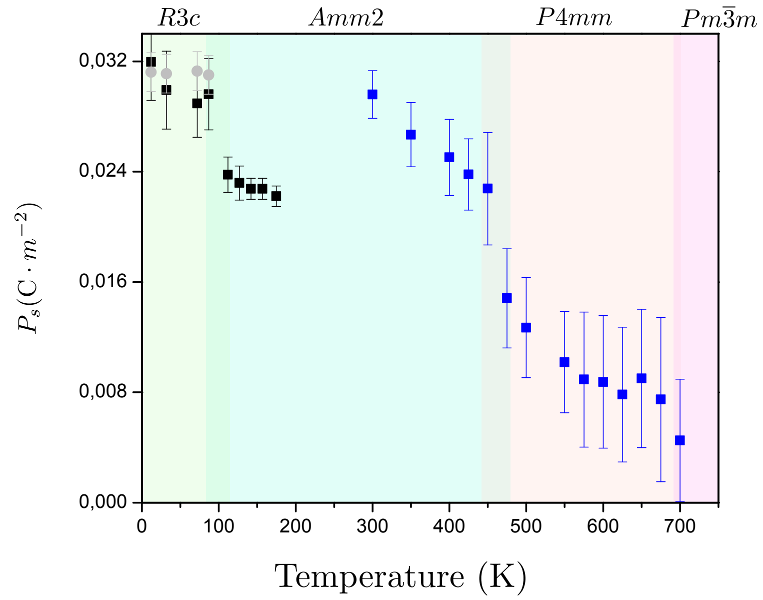

Figure 5.15: Calculated SP (see the text for further details). Different colours represent the points of the SP resulting from the data of different sources, *i.e.* NPD (black) and XRPD (blue). Dimmed symbols show the polarization values obtained in the $R3m$ model, without the octahedral tilt.

observed experimentally in the amplitude values are reflected as well in the polarization. One has to remember that the polarization is directly related to the displacements. To make it more evident, we have represented in different colours the points of the SP resulting from the data of different sources, i.e. NPD (black) and XRPD (blue). Again, the jump in the orthorhombic phase is fictitious: its origin is the change of the data source. Cooling down, the jump in the cubic-to-tetragonal phase transition shows as expected: the polarization increases. Cooling down further, in the phase transition from the orthorhombic-to-trigonal, the polarization increases, as well. The points in blue should be smaller. In our opinion, the discrepancy among the two sets of values does not diminish the value of the results, as a very good example of the new method of refining we have reported in the present work.

5.6 Conclusions

- It is been the first time that the low temperature structure of $Na_{0.5}K_{0.5}NbO_3$ was studied, it shows, as expected a more distorted structure: a rhombohedral symmetry with $R3c$ space group.
- For the $R3c$ distorted it must be present the polar irrep GM_4^- together with a small contribution of the R_4^+ irrep, which is a tilt, that decreases the symmetry from $R3m$ to $R3c$.
- The room-temperature analysis shows a negligible amplitude for the irrep GM_5^- compared to that of GM_4^- that gives rise to the ferroelectric phase.
- At high temperatures, the phase-transitions sequence $Amm2 \rightarrow P4mm \rightarrow Pm\bar{3}m$ was re-investigated and confirmed.
- The use of mode-crystallography has allowed us to calculate, without any ad-hoc assumption, the spontaneous polarization in the three distorted polar phases.
- The novel way of refinements was applied: parameterization of a direction in the internal space of the GM_4^- irrep responsible for the symmetry breaking from the parent cubic space group to the polar distorted low symmetry phases.
- The selected direction of the GM_4^- irrep is maintained when going to some other families of materials undergoing the same type of phase-transition sequence.

Chapter 6

Synthesis, Structural, Magnetic and phase-transition studies of the Ferromagnetic La_2CoMnO_6 double perovskite by symmetry-adapted modes

Perovskites containing rare earth and transition metal cations on A and B sites exhibit interesting and useful electronic and magnetic properties. The double-perovskites Ln_2MMnO_6 are characterized by subtle structural distortions, caused by concerted rotations of the BO6 octahedra and displacements of the A and B cations.

In the work of Dass *et al.* a series of $La_2CoMnO_{6-\delta}$ have been synthesized at different temperatures. All the samples treated at 1350°C under air or oxygen flux could indexed by the monoclinic $P2_1/n$ space group. While the sample prepared at 600°C, poorly crystalline with a big anionic deficient, was refined within a pseudo-tetragonal model. Later the same group has studied the La_2NiMnO_6 in different synthesis conditions. The structural analyses have shown : a random distribution of Ni and Mn over the octahedral sites occurred in the orthorhombic $Pbnm$ and $R\bar{3}c$, while an ordering of Ni and Mn into distinguishable sites can be accommodated in $P2_1/n$ and $R\bar{3}$ (or $R\bar{3}m$) .[114]

Bull *at al.* have proposed a monoclinic structure, with the space group $P2_1/n$, for La_2CoMnO_6 and La_2NiMnO_6 at room temperature. At high temperatures, a phase transition from the monoclinic $P2_1/n$ to the trigonal $R\bar{3}$ was for the first time observed in both

---

[114] R. I. Dass and J. B. Goodenough. *Phys. Rev. B* **67**: 014401, 2003.

compounds [115]The study of Troyanchuk *et al.* on the $La_2CoMnO_{6.1}$ has shown a coexistence of two symmetries at room temperature: 75% of the orthorhombic phase $Pbnm$ and 25% of the rhombohedral $R\bar{3}c$. While in the case of La_2CoMnO_6, a mixture of the $Pbnm$ and the $P2_1/n$ space groups was assigned. According to the authors, this coexistence is most likely associated with the inhomogeneous distribution of oxygen over a sample .[116] Some years later, the non-stoichiometric sample $Nd_2CoMnO_{6+\delta}$ was also investigated by Troyanchuk *et al.*, where an orthorhombic $Pbnm$ symmetry was assigned with a random distribution of Co^{2+} and Mn^{4+}. The reduction to a stoichiometric compound (δ=0) has led to a large ionic ordering and therefore to lowering the symmetry to a monoclinic structure $P2_1/n$.[117] Many works started to appear on this family of materials, with a more variety of cations-combinations. For instance, the series Ln_2NiMnO_6 (Pr, Nd, Sm, Gd, Tb, Dy, Ho and Y) has been studied by R.J. Booth *et al.*, where all the materials were indexed on monoclinic $P2_1/n$.[118]

Recently, two different samples of La_2CoMnO_6, have prepared by A. J. Barón-González *et al.*. The results have shown that the NPD data could be indexed in the monoclinic $P2_1/n$ with a 97% and 73% of ordering over the B-site.[119] The monoclinic $P2_1/n$ has been also assigned for Lu_2CoMnO_6 with a 97% of ordering[120] and for the crystals of Ln_2NiMnO_6 (Pr, Sm and Ho) .[121] Despite this variety, from the structural point of view, literature concerning detailed determination of the structural phase-transitions of the La_2CoMnO_6 double perovskite type is very scarce. Only in Bull *et al*. work a phase-transition analysis has been reported for the La_2CoMnO_6 and La_2NiMnO_6. Where a phase transition from the monoclinic $P2_1/n$ to the trigonal $R\bar{3}$ has been observed.

In the two chapters of this part we would like to show the power of the use of mode-crystallography, as we did in the previous chapter 5, for a simple perovskite case, but this time for a more complicated system; a double perovskite structure:

The first chapter is an experimental study in which we analyze the synthesized very pure and well crystallized sample of La_2CoMnO_6. The main goals of that chapter are four: After having observed the promising results of the first chapter and the power of the parametrization of the refinements, we would like to apply it in the La_2CoMnO_6 system. In particular, we focus our attention in the X_5^+ 3-dimensional irrep of the prototype $Fm\bar{3}m$ space group, and we explain how the parametrization is done: this is the second goal. The third target of the report is to explain how that the parametrization, deduced using reliable results from high-resolution neutron power diffraction data, can be securely used to refine data from other sources, like not high-resolution neutron diffraction data or x-ray powder diffraction. These last two targets are accomplished performing a comparative analysis at room-temperature of some members of two families related to the reported material: Ln_2CoMnO_6 and Ln_2NiMnO_6, a grand total of twelve structures taken from the literature

---

[115] C. L. Bull, D. Gleeson, and K. S. Knight. *J. Phys-Condens. Mat.* **15**: 4927, 2003.

[116] I. O. Troyanchuk et al. *J. Exper. Theor. Phys.* **99**: 363–369, 2004.

[117] A. P. Sazonov et al. *Phys. Status Solidi B.* **244**: 3367–3376, 2007.

[118] R. J. Booth et al. *Mater. Res. Bull.* **44**: 1559 –1564, 2009.

[119] A. J. Barán-González et al. *J. Phys-Condens. Mat.* **23**: 496003, 2011.

[120] S. Yañez Vilar et al. *Phys. Rev. B* **84**: 134427, 2011.

[121] Z. Ganghua et al. *J. Cryst. Growth* **327**: 262 –266, 2011.

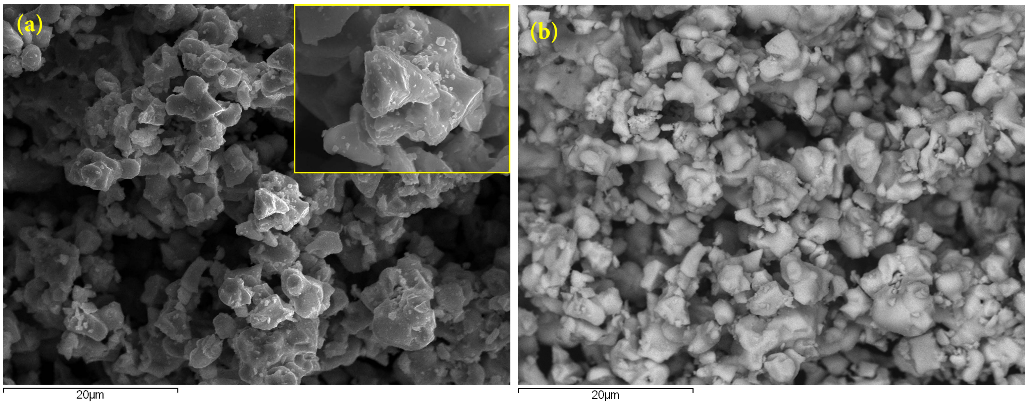

Figure 6.1: (a) Secondary electron image showing the overall appearance of the powder sample. The inset shows an enlargement of a particle. (b) Back-scattered electron image showing the homogeneous character of the powder sample.

having analyzed, corresponding to eight different materials. Finally, we also report the magnetic structure and we show its thermal evolution.

The second chapter, is an extending of the first one by applying the parameterization approach to other double perovskite materials, not only by changing the B cation as we did in the first chapter, but even by changing completely to another set of families (5 families) having different B′ cations, with different sizes and difference oxidation states (5+ and 6+). In this analysis we went deeply in the modes breaking the symmetry from the prototype phase to the distorted one. We have focused on the three-dimensional vector transforming according to the X_5^+.

6.1 Overall morphology and characteristics of the La_2CoMnO_6

The powder sample was investigated by SEM to analyze the overall appearance. Figure 6.1a shows a bimodal distribution of, on the one hand, equi-axed particles ranging from about 2 up to 20 μm and, on the other hand, particles with a size smaller than 1 μm (see the inset in Figure 6.1a. In addition, in the upper part of this inset, sharp edges of a sintered grain evidence the crystalline nature of the sample. Finally, the sample homogeneity can be observed in the back-scattered electron image shown in Figure 6.1b. The contrast in this type of images is mainly generated due to the differences in the average atomic number for flat samples. In our case, since it is a powder sample, the different contrasts come only from the heights, but no impurities were detected.

6.2 Transmission Electron Microscopy at Room Temperature

Different particles of the powder sample were also investigated by TEM. Figure 6.2a shows a bright field image of an electron transparent area of one particle; the contrast

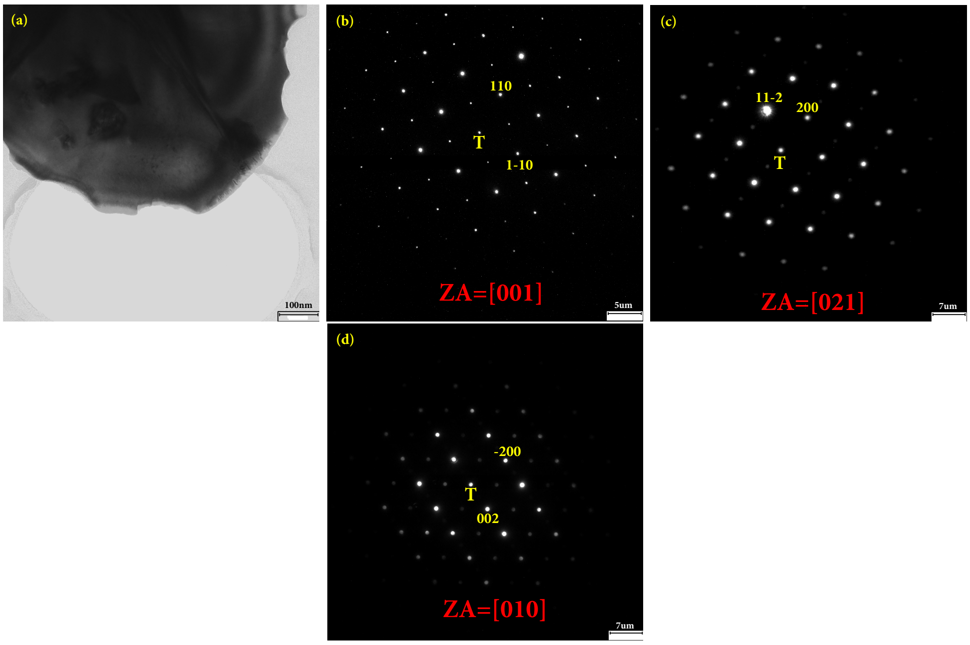

Figure 6.2: (a) Bright field image of electron transparent area of one particle. (b) Selected area electron diffraction pattern acquired along the [001] zone axis. (c) and (d) Electron micro-diffraction pattern acquired along the [021] and [010] zone axis, respectively. The reflections indicated in the patterns were identified by simulations done with the JEMS software, using the neutron data.

corresponding to small particles/fragments laying on the particle can be observed. Selected area and micro-diffraction electron diffraction patterns were acquired after orienting the particle along different high-symmetry zone axes (ZA). The patterns shown in Figure 6.2b, Figure 6.2c and Figure 6.2d correspond well with those obtained from the theoretical simulations for the [001], [021] and [010] zone axes, respectively, using the crystallographic data (lattice parameters, space group, atom positions and occupancy factors) determined from the XRD fitting described below. A full agreement between the electron diffraction investigation and the XRD data was observed.

6.3 Symmetry Adapted Mode-analysis of Phases and Phase-transition Sequence

The refinement-process has been done using the implementation of AMPLIMODES for FullProf, located in the Bilbao Crystallographic Server .[59] Our NPD data at room-temperature, taken at the D1B instrument, are not the best ones for a crystal-structure determination. On the one hand, the instrument is not a high-resolution one, and it is more suited for magnetic studies. On the other hand, it is also known that the material shows magnetic ordering ,[119] starting at around 235 K. This is another of the remarkable points:

---

[59] D. Orobengoa, C. Capillas, M. I. Aroyo, and J. M. Perez-Mato. *J. App. Crystallogr.* **42**: 820–833, 2009.

Table 6.1: Input information for AMPLIMODES for FullProf: high-symmetry phase (prototype structure), low-symmetry structure information and transformation matrix. $P2_1/n$, $R\bar{3}$ (ITA No.148), and $Fm\bar{3}m$ (ITA No.225). Second part of the table is a resume of the irreps taking part in the symmetry breaking from cubic $Fm\bar{3}m$ to the monoclinic $P2_1/n$ and $R\bar{3}$. The numbers in parenthesis indicate the number of modes transforming according to the irrep. The modes marked in bold character are the primaries ones.

High-symmetry structure: Fm$\bar{3}$m (a^{0}a^{0}a^0)[45,122]					
225					
7.9200 7.9200 7.9200 90.00 90.00 90.00					
4					
Mn	1	4*a*	0	0	0
Co	1	4*b*	1/2	1/2	1/2
La	1	8*c*	1/4	1/4	1/4
O	1	24*e*	0.2471	0	0

Low-symmetry cell: P2$_1$/n (a$^-$a$^-$b$^+$)[45,122]						**Low-symmetry cell: R$\bar{3}$ (a$^-$a$^-$a$^-$)**[45,122]					
014						148					
5.5251 5.4875 7.7786 90 89.94 90						5.61494 5.61494 13.7096 90.00 90.00 120.00					
6						4					
Mn	1	2*a*	0	0	0	Mn	1	3*a*	0	0	0
Co	1	2*b*	0	0	1/2	Co	1	3*b*	0	0	1/2
La	1	4*e*	-0.0066	0.4645	0.7499	La	1	6*c*	0	0	0.2467
O	1	4*e*	-0.2771	0.2168	-0.0362	O	1	18*f*	0.6645	0.8735	0.0781
O	2	4*e*	-0.7982	0.2942	0.0400						
O	3	4*e*	0.0753	0.0128	0.7580						

Transformation matrix	**Transformation matrix**
$\left(\begin{array}{ccc\|c} 1/2 & 1/2 & 0 & 0 \\ -1/2 & 1/2 & 0 & 0 \\ 0 & 0 & 1 & 0 \end{array}\right)$	$\left(\begin{array}{ccc\|c} -1/2 & 0 & 1 & 0 \\ 1/2 & -1/2 & 1 & 0 \\ 0 & 1/2 & 1 & 0 \end{array}\right)$

Fm$\bar{3}$m → P2$_1$/n		
O1	24*e*	GM$_1^+$(1) GM$_3^+$(1) **GM$_4^+$(1)** GM$_5^+$(2) X$_2^+$(1) **X$_3^+$(1)** X$_5^+$(2)
La1	8*e*	GM$_5^+$(2) X$_5^+$(1)
Fm$\bar{3}$m → R$\bar{3}$		
O1	24*e*	GM$_1^+$(1) **GM$_4^+$(1)** GM$_5^+$(1)
La1	8*e*	GM$_5^+$(1)

even in this case, with low-resolution (for crystal structure) data and with magnetic response at low temperatures, the XRPD refinements, at higher temperatures, will be improved, with the procedure we are proposing.

It is known, and the refinements also indicate it, the partial ordering of the cations Co^{2+} and Mn^{4+} over the two B- and B′-sites. It should be noted that it was not possible to fit the Co and Mn occupancies using the preliminary XRPD data (data we have at room temperature), due to the similarity in X-ray scattering factors between Mn^{4+} and Co^{2+} cations .[123,124] This is another reason for having collected NPD data.

Let us explain some aspects of the crystal structure procedure used for the refinements.

---

[123] K. Asai et al. *J. Phys. Soc. Jpn.* **67**: 4218–4228, 1998.

[124] T. I. Milenov et al. *Mater. Sci. Eng: B* **172**: 80 –84, 2010.

For that, we need to know which are the irreps taking part in the distorted symmetry we are describing and what the symmetry-modes transforming according to those irreps physically do. We start with the structural symmetry at room temperature: $P2_1/n$ (ITA No.14, non-standard setting).

The monoclinic reported structure and the reference one, the cubic parent phase (found using the program PSEUDO),[125,126] are listed in Table 6.1, which also shows the irreps taking part in the $Fm\bar{3}m \rightarrow P2_1/n$ symmetry breaking. There are seven irreps of the $Fm\bar{3}m$ space group taking part in the symmetry breaking: $GM_1^+(1)$, $GM_3^+(1)$, $GM_4^+(1)$, $GM_5^+(4)$, $X_2^+(1)$, $X_3^+(1)$, $X_5^+(3)$. There are 12 modes (one of them is the totally symmetric): 8 (+1) modes move only the oxygen atoms in (24*e*) Wyckoff position and the rest 3 modes move the A-site atoms in (8*c*).

The GM_3^+, expands the octahedra in the equatorial *ab* plane, while the apical oxygens (in the *c* axis) are moved along the *c* axis to the center of the octahedra. GM_4^+, is essentially a rotation around the *b* axis; although it deforms a bit the octahedra (the displacement of the oxygens in the *ab* plane and the ones in *c* axis are not the same). GM_5^+ is a four dimensional mode, actuating on A/A′-site cations and oxygens. Two of them displace the A/A′-site cations in *a* and *c* axes, respectively. The third one moves the equatorial oxygens in the *ab* plane, transforming in a rectangle the square formed by the equatorial oxygens; while the fourth, is a kind of rotation along *b* axis, with the apical oxygens displaced in the opposite direction of the rotation. The mode transforming according to X_3^+ is a pure rotation of the octahedra around the *c* axis; it acts only on the oxygen atoms of the *ab* plane. X_2^+ mode actuates on the equatorial oxygens, deforming into a rhombus the square formed by those. Finally, there is a three dimensional mode that transforms according to X_5^+. This mode actuates on the oxygens and on the A/A′-site cations. In the former case, it is a rotation around the *a* axis, although the amount of displacements in the *ac* plane and the ones in *b* are not the same. In the latter, displaces the A-site cations along the *b* axis.

From the Rietveld refinements results of La_2CoMnO_6, mode calculations of Ln_2MMnO_6 materials, shown in Table 6.2 and from previous experience in related materials ,[40,100–102] there are two active primary order parameters responsible for the cubic-to-monoclinic symmetry break, i.e. the monoclinic $P2_1/n$ is generated by two irreps of $Fm\bar{3}m$. The rest of the modes, appear allowed by symmetry. Depending on the material, they could show different combinations of non-null mode amplitudes. But, in the double perovskites families usually there is only another irrep, the mode transforming according to X_5^+, that shows a non-so-negligible value for the mode-amplitude.

In summary: there are two active irreps (GM_4^+ and X_3^+, both represent physically tilts of the octahedra, and together with these, there is another not negligible one, which is allowed by symmetry: X_5^+, in our experience, it is always there. It has been proven to be

---

[125] E. Kroumova et al. *J. App. Crystallogr.* **34**: 783–784, 2001.

[126] C. Capillas et al. *Z. Kristallogr.* **226(2)**: 477–485, 2011.

[40] A. Faik, D. Orobengoa, E. Iturbe-Zabalo, and J. M. Igartua. *J. Solid State Chem.* **192**: 273–283, 2012.

[100] E. Iturbe-Zabalo et al. *J. Solid State Chem.* **198**: 24–38, 2013.

[101] E. Iturbe-Zabalo et al. *J. Phys-Condens. Mat.* **25**: 205401, 2013.

[102] E. Iturbe-Zabalo, J. M. Igartua, and M. Gateshki. *J. App. Crystallogr.* **46**: 1085–1093, 2013.

tri-linearly coupled to the two main order parameters .[127] This is the physical origin to find non-converging refinements if one tries to nullify it in the refinements. Its values is always one order of magnitude smaller than the highest among the primary order parameters, i.e. GM_4^+, but being coupled, the refinements do not converge if it is excluded.

In relation to the refinement-process used, we have to mention also that, for the first temperature, at the beginning steps we have freed and refined all the mode-amplitudes, i.e. all the irreps, hence, all the degrees of freedom. Nevertheless, having seen the values for some of them and their corresponding associated errors, we have decided to nullified some. Hence, at the final step in the refinements, we have used only the following set of amplitudes, meaning that the final distorted structure is constructed using only those individual distortions: GM_4^+, X_3^+ and X_5^+.

We have refined the room-temperature NPD data. The idea is to find the best set, the best distribution, of the mode-amplitudes and use it for the subsequent refinements at high-temperature and with XRPD data. The idea, also, is not to have the magnetic response when finding the best distribution. The results of the refinements and the structural details at room temperature of the La_2CoMnO_6 are given in Table 6.2, Table 6.3 and Figures 6.4a and 6.4b.

---

[127] U. Petralanda and I. Etxebarria. *Phys. Rev. B* **89**: 064107, 2014.

Table 6.2: Refined values of the mode-amplitudes (in Å) taking part in the symmetry breaking from $Fm\bar{3}m$ to $P2_1/n$ (RT) for La_2CoMnO_6 in the present work [PW] with all modes freed and [PW*] with only the mode-amplitude (see text): GM_4^+, X_3^+ and X_5^+. The results are compared to mpde-amplitudes calculated for the materials in the Ln_2MMnO_6 family, which also show the same space group $P2_1/n$ at RT: La_2CoMnO_6 [115,119], Lu_2CoMnO_6[128], Nd_2CoMnO_6 [129,130], La_2NiMnO_6 [115], Sm_2NiMnO_6 [118], Tb_2NiMnO_6 [118], Ho_2NiMnO_6 [131], Y_2NiMnO_6 [132] and Bi_2NiMnO_6 [133].

Irrep	Isotropy subgroup	Amplitude												
		La_2CoMnO_6				Lu_2CoMnO_6	Nd_2CoMnO_6		Ln_2NiMnO_6				Y_2NiMnO_6	Bi_2NiMnO_6
		[PW]	[PW*]	115	119	128	129	130	Ni^{115}	Sm^{118}	Ho^{131}	Tb^{118}	132	133
$Fm\bar{3}m \rightarrow P2_1/n$														
GM_1^+	$Fm\bar{3}m$ (225)	0.004(11)	0.000	0.14(3)	0.17(2)	0.09(3)	0.11(2)	0.15(1)	0.05(4)	0.18(4)	0.09(2)	0.16(3)	0.15(3)	0.06(5)
GM_3^+	$I4/mmm$ (139)	0.01(3)	0.000	0.03(3)	0.02(2)	0.05(3)	0.07(3)	0.19(7)	0.04(6)	0.25(4)	0.01(3)	0.02(3)	0.07(3)	0.02(5)
GM_4^+	$C2/m$ (12)	1.087(6)	1.080(3)	1.12(3)	1.10(2)	1.84(4)	1.32(3)	1.29(8)	0.73(5)	1.46(5)	1.70(3)	1.51(3)	1.65(3)	1.35(7)
GM_5^+	$C2/m$ (12)	0.14(4)	0.000	0.15(2)	0.10(2)	0.26(1)	0.12(2)	0.42(7)	0.61(2)	0.25(5)	0.21(1)	0.22(8)	0.21(1)	0.15(7)
X_2^+	$P4_2/mnm$ (136)	0.042(15)	0.000	0.07(3)	0.01(2)	0.09(3)	0.01(2)	0.04(7)	0.09(2)	0.02(5)	0.04(2)	0.12(3)	0.03(2)	0.01(6)
X_3^+	$P4/mnc$ (128)	0.523(6)	0.532(5)	0.53(3)	0.58(2)	1.31(3)	1.02(2)	0.96(7)	0.40(2)	0.83(5)	1.27(2)	1.06(3)	1.27(2)	0.68(6)
X_5^+	$Pnnm$ (58)	0.336(4)	0.334(3)	0.27(6)	0.27(5)	0.99(1)	0.60(6)	0.56(2)	0.71(2)	0.74(3)	0.88(1)	0.82(1)	0.90(1)	0.67(5)
Tolerance factor (t_{obs})		0,9477	0,9477	0,9437	0,9436	0,8546	0,8926	0,8976	0,9795	0,8893	0,8578	0,8586	0,9020	0,8596
K-vector: GM_1^+ (0,0,0), GM_3^+ (0,0,0), GM_4^+ (0,0,0), GM_5^+ (0,0,0), X_2^+ (0,1,0), X_3^+ (0,1,0), X_5^+ (0,1,0)														
Direction: GM_1^+ (a), GM_3^+ (a,0), GM_4^+ (a,a,0), GM_5^+ (-b,a,-a), X_2^+ (0,a,0), X_3^+ (0,a,0), X_5^+ (a,a,0,0,a,-a)														

In Table 6.2 and in Figure 6.3, we are showing the set of amplitudes resulting from the refined structures, at room-temperature, obtained for the materials of two families, Ln_2CoMnO_6 and Ln_2NiMnO_6, after having used the published structures as input to AMPLIMODES. The published structures included in this report have been refined by the authors using the conventional method: refining freely the 12 degrees-of-freedom, in the form of atomic co-ordinates. This means that when inputed to AMPLIMODES, all the mode-amplitudes have been output. As mentioned before, the symmetry adapted mode-amplitude refinements naturally nullifies some distortions, although they are permitted by symmetry.

In the first two columns of the Table 6.2 with the resulting amplitude values, we show the results obtained for our material: firstly, having freed all the freedom, and then after seing the values for some amplitudes, having freed only the effectively acting mode-amplitudes. Regarding the mode-amplitudes included in our refinements, it can be said that there are some materials not following the general trends observed for the mode-amplitudes transforming according to the GM_4^+, X_3^+ and X_5^+ irreps, as it can be observed in Figure 6.3: Tb (in red, dimmed), Sm and Bi (in black, dimmed). The Tb shows smaller values for the GM_4^+ and X_3^+ irreps, than its counterparts for nearly the same tolerance factor. It also shows the same value for the global amplitude of the X_5^+ irrep, and nearly the same for the individual amplitudes in the internal sub-space. We have included two reports on the Sm material, and the results from both do not follow the trend. Although the values for GM_4^+ in both match the rest, and one of them reports a good value for X_3^+, the other values are systematically greater. This is also the case of the Bi material. On the other hand, in the same figure, we are showing some points in green. Among those, the case of La_2NiMnO_6, with the highest tolerance factor seems to be pathological, for the two reports shown. The values of all the amplitudes of all the irreps are completely different to the rest. In green we have also shown another two works on the same material we are reporting. See below to clarify the reason for showing them in green.

We note that except for our material, the rest of the materials in both families show an unusual big value of the X_5^+ mode-amplitude. This value increases as the global distortion of the material, that is the structural distance from the actual crystal structure to the reference structure, increases as the tolerance factor diminishes. The high-limit for the distortion in the Co-family is the Lu_2CoMnO_6. This facts plays in our favor, in the sense that being the distortion big it will be easier to be determined experimentally, as will be seen.

In subsequent paragraphs, we would like to focus our attention on the distortion transforming according to the X_5^+ irrep, because of the two reasons mentioned above: usually it shows a small value for the global amplitude of the mode and, on the other hand, it can not be excluded from the refinement. The target of this analysis is to clarify if there is a preferable direction in this internal space which gives rise to a common type of partial distortion associated to the X_5^+ irrep, irrespective of the material in both families selected to accompany this report on La_2CoMnO_6.

The X_5^+ irrep is three-dimensional: there are three modes transforming according to it (Figure 9 in ,[100]) two of which involve only oxygen atoms and the other one, only

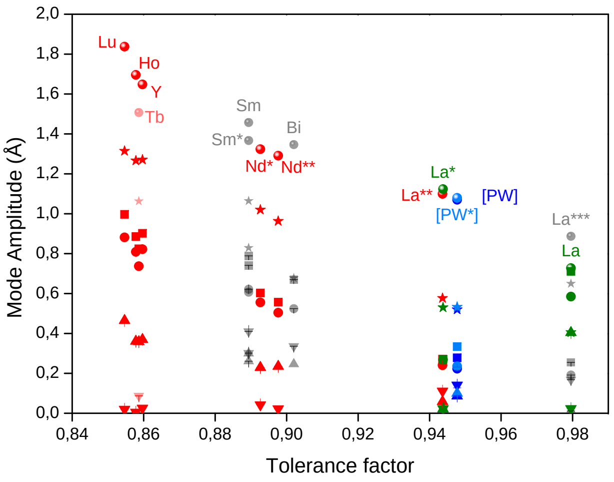

Figure 6.3: Amplitudes of GM_4^+ (spheres), X_3^+ (stars), the global amplitude-value for the tri-dimensional X_5^+ irreps (squares) and its components: A10 (circles), A11 (up triangle) and A12 (down triangle), in the room-temperature structures of the Ln_2CoMnO_6 (Ln= La[PW], La*[115], La**[119], Lu[128] Nd*[129], Nd**[130]), Ln_2NiMnO_6 (Ln=La[115], La***[134], Tb[118], Sm[118], Sm*[135],Ho[131]), Y_2NiMnO_6[132] and Bi_2NiMnO_6[133] compounds, versus the tolerance factor values, calculated using bond distances. PW stands for present work: [PW] with all modes freed and [PW*] only the effectively acting ones, see text.

the A-site cation (La, in this case). In a previous paper,[136] based on the work reported in ,[6] we have given enough experimental evidences of the fact that the polarization-vector, whose direction is equivalent to the direction of the generalized vector formed by the three amplitudes (the amplitudes taken as the components of the vector), maintains as the crystal structure evolves in the external field, temperature in this case, although its modulus decreases. The mentioned reports dealt with other materials, and other phases and irreps, but the concept is general. It is clear that the evolution should take place in the mentioned way, as the amplitudes represent the distortions of the reference structure: as temperature increases, approaching to the prototype cubic phase, the distortion tends to decrease, but the relative variation of the amplitudes of the modes transforming according to the same irrep maintains. We have used this fact to perform a parametrized refinement: the set of three amplitudes has been described by just one parameter, arbitrarily chosen among the three (X_5^+, A10 in the jargon of FullProf, the mode-amplitude corresponding to the A-site cation, a translation of the cation along the y-axis, (Figure 9 in [100]). The amplitudes of the other two have been fixed according to the following final direction: (0.95, -0.45, 0.00) (see below).

In our experience also, in some other related materials (ordered double perovskites) ,[100–102] this three-dimensional space reduces effectively to just a mono-dimensional one, since the relative importance of two of the three amplitudes is negligible: their values actually go to zero (taking into account the errors), and, hence, they are taken out from the refinements. In this material, though, we have observed that two of them show a not

---

[136] B. Orayech et al. *J. App. Crystallogr.* **48**: 318–333, 2015.

[6] B. Kocsis et al. *J. App. Crystallogr.* **47**: 1165–1179, 2014.

null value, according to the data we have: A10 and A11, see discussion below. We have included the third one for completeness and to observe if its values remain so small in all the materials we want to compare.

In Figure 6.5, we are showing the results only for the amplitudes of the 3-degenerate sub-space transforming according the X_5^+ irrep, at room-temperature. In panel (a), we are plotting in the xy plane the A11 amplitude, x-axis; and A12 amplitude y-axis. The third amplitude, A10, is plotted in the panel (b) of the same figure, at arbitrary fixed values in the x-axis, only for convenience, to separate in the same three sets and using the same color code, as in Figure 6.3. The actual value of the component is indicated in the y-axis.

In panels (a) and (b), we are plotting three sets of arrows, in black, red and green color. For each colored set, we have two sub-sets: full color and dimmed. The dimmed color set of arrows represent the direction in the X_5^+ transforming three-dimensional sub-space, that results for each of the materials; that is, the direction of the polarization vector of this irrep. The full-color set of arrows are the actual vector representing the partial distortion induced by X_5^+; that is, the dimmed vector's amplitudes are multiplied by their corresponding global amplitude value, the total result gives the resulting distortion. In the case of the A10 amplitude, we are representing the actual values, a little bit to the right of their dimmed version, just for visualizing reasons. There is a blue arrow (dimmed and full-colored), which represents our structural data. To reference to the materials, we have labelled the arrows. The color-code used distinguishes three behaviors, as in Figure 6.3: black arrows are defining a common direction, the red arrows another one, and the green arrows are the *outsiders*. We consider that these do not define a direction, with one exception, see below. We have discarded two of these three green results. Besides, we have grouped the heads of the black arrows, including the Tb red one, using an orange oval. All these materials have been studied using X-ray. The materials represented by red vectors, have been studied using high-resolution ND (Ho, single-crystal diffraction and the rest, powder diffraction). Hence, we are discarding the results represented by the black arrows and we are assuming the red arrows to give the good (A11, A12) sub-distortion transforming according to X_5^+.

Not taking into account the Tb red arrow, there are 6 arrows, two of which, as indicated, correspond to two reports on the same material, Nd_2CoMnO_6. All these materials show an A12-amplitude absolute value very small (only Tb_2NiMnO_6 shows a negative A12 value), negligible small: it vanishes if the error is taken into account. In view of this fact, we have assumed A12 to be actually zero. As a result, this gives an effective direction (c1, c2, 0.00) for the polarization vector, i.e. in the plane formed by the components (A10, A11), in the 3-dimensional sub-space transforming according to X_5^+. We show this effective direction in the (c) panel of the Figure 6.5, one arrow for each material. Finally, the blue arrow corresponds to our material. As mentioned, our data are non-high-resolution NPD data.

Table 6.3: Structural details of La_2CoMnO_6 obtained at different temperatures from NPD (D1B, ILL) data using the $P2_1/n$ structural model freeing only the mode-amplitude (see text): GM_4^+, X_3^+ and X_5^+. Mn/Co atoms occupy the site 2a (0, 0, 0), Co/Mn atoms occupy the site 2b (0, 0, 1/2), La atoms occupy the site 4e (x, y, z) and O atoms occupy the site 4e (x, y, z).

Temperatures		2 K	50 K	100 K	150 K	200 K	250 K	300 K
La	x	0.0000	0.0000	0.0000	0.0000	0.0000	0.0000	0.0000
	y	0.5213(3)	0.5218(3)	0.5229(2)	0.5222(2)	0.5215(2)	0.5206(3)	0.5211(3)
	z	0.2500	0.2500	0.25000	0.2500	0.2500	0.2500	0.2500
	B_{iso}(Å^2)	0.58(3)	0.58(3)	0.60(1)	0.71(1)	0.83(4)	0.88(1)	0.61(1)
O1	x	-0.7753(1)	-0.7748(7)	-0.7765(5)	-0.7740(5)	-0.7737(6)	-0.7739(6)	-0.7778(6)
	y	0.2757(1)	0.2752(7)	0.2735(5)	0.2733(5)	0.2736(6)	0.2726(6)	0.2697(6)
	z	0.0354(1)	0.0353(1)	0.0348(1)	0.0344(1)	0.0342(1)	0.0341(1)	0.0340(1)
	B_{iso}(Å^2)	0.61(1)	0.61(1)	0.68(3)	0.74(1)	0.78(2)	0.91(1)	0.82(2)
O2	x	-0.5709(2)	-0.5707(2)	-0.5696(16)	-0.5688(2)	-0.5684(2)	-0.5682(2)	-0.5681(2)
	y	0.5091(3)	0.5093(3)	0.5097(2)	0.5094(2)	0.5091(2)	0.5088(3)	0.5089(3)
	z	-0.2528	-0.2528	-0.2528	-0.2528	-0.2528	-0.2528	-0.2528
	B_{iso}(Å^2)	0.61(1)	0.61(1)	0.68(3)	0.74(1)	0.78(2)	0.91(1)	0.82(2)
O3	x	-0.2696(1)	-0.2691(7)	-0.2707(5)	-0.2683(5)	-0.2680(6)	-0.2682(6)	-0.2721(6)
	y	0.2186(1)	0.2191(7)	0.2208(5)	0.2210(5)	0.2207(6)	0.2217(6)	0.2246(6)
	z	-0.0354(1)	-0.0353(1)	-0.0348(1)	-0.0344(1)	-0.0342(1)	-0.0341(1)	-0.0340(1)
	B_{iso}(Å^2)	0.61(1)	0.61(1)	0.68(3)	0.74(1)	0.78(2)	0.91(1)	0.82(2)
Mn/Co	2a	0.28(1)/0.72(1)	0.28(1)/0.72(1)	0.28(1)/0.72(1)	0.28(1)/0.72(1)	0.28(1)/0.72(1)	0.28(1)/0.72(1)	0.28(1)/0.72(1)
Co/Mn	2b	0.72(1)/0.28(1)	0.72(1)/0.28(1)	0.72(1)/0.28(1)	0.72(1)/0.28(1)	0.72(1)/0.28(1)	0.72(1)/0.28(1)	0.72(1)/0.28(1)
Cell parameters	a (Å)	5.5029(1)	5.5034(1)	5.5048(2)	5.5065(1)	5.5084(1)	5.5112(1)	5.5128(1)
	b (Å)	5.4669(1)	5.4672(2)	5.4672(2)	5.4675(3)	5.4692(1)	5.4702(1)	5.4714(3)
	c (Å)	7.7435(1)	7.7438(1)	7.7431(8)	7.7456(1)	7.7473(5)	7.7493(1)	7.7526(1)
	β(°)	90.081(1)	90.053(1)	90.087(1)	90.081(1)	90.105(1)	90.135(1)	90.08(1)
	V (Å^3)	232.96(5)	233.00(1)	233.03(2)	233.19(1)	233.40(3)	233.62(1)	233.84(1)
Reliability factors	R_p(%)	2.75	2.63	2.25	2.14	2.18	2.33	1.57
	R_{wp}(%)	4.42	4.20	3.67	3.52	3.52	3.81	2.09
	R_{exp}(%)	0.85	1.13	0.85	1.13	1.13	1.13	0.90
	χ^2	5.2	5.8	5.2	5.71	5.67	4.2	5.32
	R_{Bragg}	4.5	5.1	4.01	4.67	5.10	3.5	4.89

There is an important remark on the green arrow represented materials: La_2NiMnO_6, which shows a positive A11 and a negative (negligible small) A12. In fact, the vector is on the same direction as the red vectors ones', but it is directed in the other sense. It is not difficult to show that both directions, considered the sense, represent equivalent structures, as they are associated, in the energy landscape, to two minima of the same depth. Hence, in fact, this green arrow actually is not an *outsider*, but, on the contrary, represents a refined structure as the red vectors do, hence, equivalent to them. We have mentioned that this mode transforming according to X_5^+ is tri-linearly coupled to the two order-parameters: GM_4^+ and X_3^+. Thus, in a classical description of the phase-transition by the Landau Theory of phase transitions, there will be a term in the expansion of the free energy of the from: $c\,A_{GM_4^+} \times A_{X_3^+} \times A_{X_5^+}$. Where c represents the intensity of the coupling and the A-factors the amplitude of mode transforming according the correspondig irrep. Being the order-parameters blocked, any global change of sign in the sub-space spanned by the $(-|c2|, |c3|)$ (corresponding to the red vectors), will not change the sign of the coupling energy, which will give rise to an equivalent minimum. With the experimentally observed direction, restricted to the mentioned 2-dimensional sub-space, the only additional global sign-change corresponds to $(|c2|, -|c3|)$: nothing else but La_2NiMnO_6 in green. As mentioned, the distortion represented by this vector should be considered equivalent to the ones represented by the red vectors. Note that $(-|c2|, |c3|)$ is effectively $\approx (-|c2|, 0)$.

Finally, in the same figure, panel (c), recovering the A10 component, we are plotting the effective direction (|c1|, -|c2|) (vectors formed by the A10 and A11 amplitudes, as we nulled the A12): the actual one used for the final parametrization of the refinements.

It is interesting to note that the inclusion of all the degrees of freedom of this irrep, does not change too much the final result, being careful in this statement. The X_5^+ (A10) values do not change to much in the mentioned three refinements, although the vector itself is completely different, of course. The statement means that although the vector changes completely, the projection of that vector in the axes representing the A-site cation distortion (X_5^+, A10), does not change too much. Interesting to note also is the fact that even the vector changes quite a lot, from one refinement to another (acquires components in the oxygen displacement sub-space, which physically represent a small tilt accompanied by a translation), the actual distortion is small.

The cell parameters of the corresponding materials at RT are shown in the Figure 6.7 versus the experimental tolerance factor. The materials are showing a similar behavior in a sense that size and volume of the cell get bigger as the tolerance factor increase, on the other hand, the three cell parameters $\sqrt{2}a$, $\sqrt{2}b$ and c get closer as the size of the Lanthanides placed on the A/A'-site gets bigger. In addition to that, even in the cell parameters evolution, the non-Lanthanides Y_2NiMnO_6 and Bi_2NiMnO_6, follow perfectly the behavior shown by the Lanthanides materials.

The refined structure at room-temperature was used as the starting point for the refinement at the lowest temperature without magnetic response: 250 K. Knowing that there is no structural phase transition down to 2 K, to solve the magnetic structure we have taken that structure and fixed it at 2 K, as there is no crystal-symmetry change from room-temperature to 2 K. In this case, we would like to have the highest possible magnetic

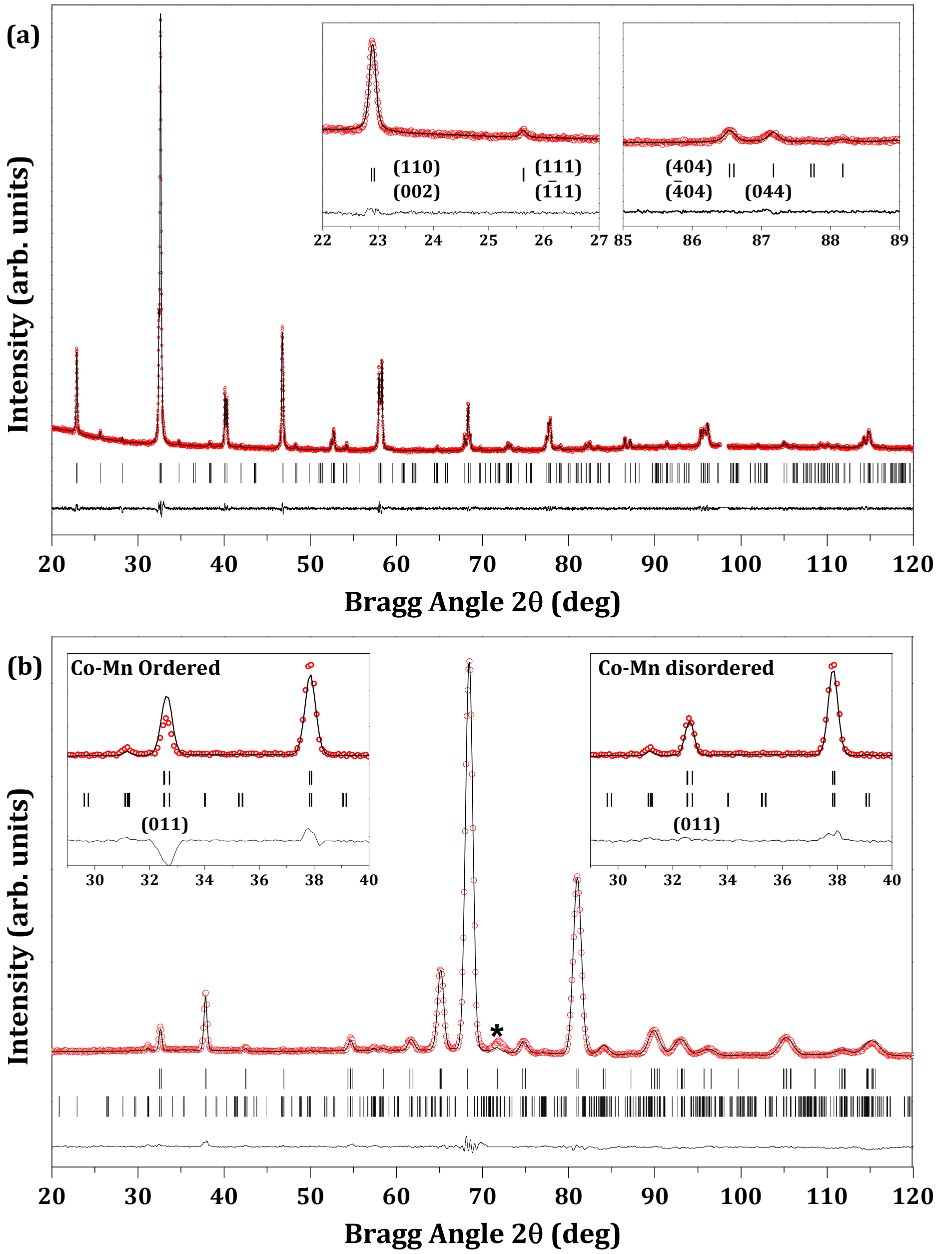

Figure 6.4: Experimental (symbols) and calculated (line) (a) X-ray profiles and (b) neutron profiles from the Rietveld refinements of La_2CoMnO_6, using a structural model with $P2_1/n$ space group, (a) and (b) at room temperature, from XRPD data and NPD, respectively. In (b), the (*)-symbol marked reflection corresponds to the signal of the Vanadium sample container used in the experiment. The bars in the lower part of the graphics represent the Bragg reflections' positions. In (b), the upper set of bars correspond to the first wavelength λ_1 = 2.52Å, and the lower set of bars correspond to the second wavelength λ_2 = 1.26Å. Insets show in detail (a): (22°-27°) the presence of the superlattice reflections of the form $h + k + l = 2n + 1$, corresponding to the $P2_1/n$ symmetry, (85°-89°) the cubic refections (444) clearly splitted in the monoclinic symmetry into (044) (-404) (404), (b): selected region, (011) reflection, of the fitted results using an ordered and a disordered structural models.

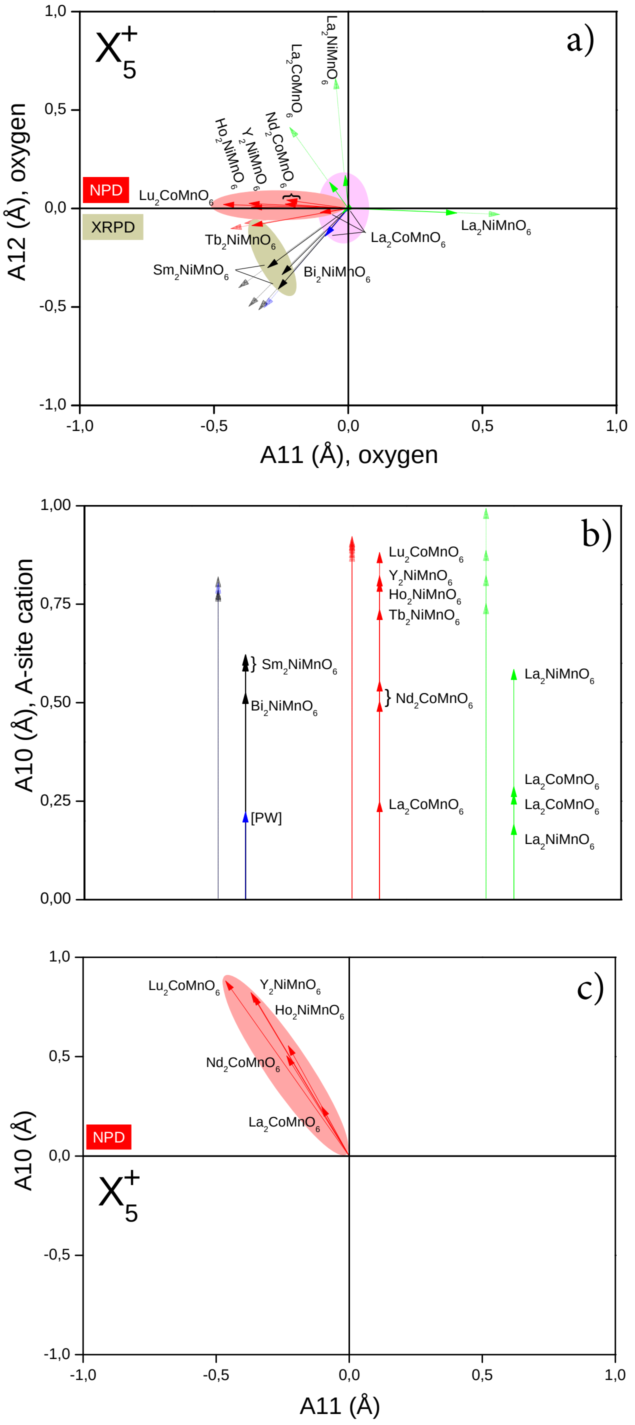

Figure 6.5: Two dimensional sections showing the mode-amplitudes of the three dimensional space transforming according to the X_5^+ irrep. The arrows represent a definite combination of those amplitudes deduced from the structures taken from the literature (as indicated), inputed in AMPLIMODES. Dimmed arrows represent the direction defined by the corresponding polarization vector. The full colored arrows indicate the actual distortion in this subspace (see text). (c) panel shows the final effective direction and the actual distortion in the reduced two-dimensional sub-space spanned by the modes A10 and A11. This is the direction used for the parametrization of the refinements.

Table 6.4: Main bond-distances (Å) for La_2CoMnO_6 obtained at different temperatures from NPD (D1B, ILL) data using the space group $P2_1/n$ (ITA No.14, non-standard setting)

Temperatures	300 K	250 K	200 K	150 K	100 K	50 K	2 K
Space group	$P2_1/n$	$P2_1/n$	$P2_1/n$	$P2_1/n$	$P2_1/n$	$P2_1/n$	$P2_1/n$
CoO_6 octahedra							
Co-O1×2	1.944(3)	1.943(6)	1.943(5)	1.943(1)	1.944(1)	1.944(1)	1.944(3)
Co-O2×2	1.952(1)	1.951(7)	1.951(1)	1.951(2)	1.951(1)	1.952(3)	1.952(1)
Co-O3×2	1.947(2)	1.946(1)	1.946(2)	1.946(2)	1.946(1)	.946(4)	1.946(2)
Average distance	1.947(4)	1.947(1)	1.946(1)	1.947(1)	1.947(1)	1.947(2)	1.947(1)
Predicted distance	1.95	1.95	1.95	1.95	1.95	1.95	1.95
MnO_6 octahedra							
Mn-O1×2	1.991(3)	1.990(6)	1.990(1)	1.990(2)	1.990(2)	1.991(1)	1.9917(5)
Mn-O2×2	1.994(1)	1.994(1)	1.993(5)	1.993(4)	1.993(1)	1.995(7)	1.995(4)
Mn-O3×2	1.988(3)	1.987(4)	1.987(1)	1.987(3)	1.988(1)	1.988(4)	1.989(1)
Average distance	1.991(1)	1.990(1)	1.990(1)	1.990(1)	1.990(1)	1.991(1)	1.991(1)
Predicted distance	2.07	2.07	2.07	2.07	2.07	2.07	2.07

response, to be more accurate in the magnetic structure refinement. The results of the refinements and the structural details at 2K of the La_2CoMnO_6 are given in Table 6.3 and Figure 6.4c.

The magnetic structure of La_2CoMnO_6 has been determined by means of neutron powder diffraction data collected in D1B at 2 K. The propagation vector is $\mathbf{k} = (000)$. The possible magnetic space groups are $P2_1/n$ and $P2_1'/n'$. As mentioned, from the crystal structure, it is known that the Co^{2+} and Mn^{4+} show disorder, in the two non-equivalent positions they occupy in the cell. It is also known that there is almost not magnetic contrast between Co^{2+} and Mn^{4+}. In this scenario, as the starting step for solving the magnetic structure, we have considered the amplitudes of the magnetic moments of the magnetic ions to be equal. Seeing the results from the refinements, we have constrained the sites to be equal, since the goodness of fit (gof) of the refinements do not vary.

Under all these considerations, there are three indistinguishable ferromagnetic models compatible with the data, with the magnetic moments along: y, $1.74(2)\mu_B$ ($P2_1/n$ and 8.64), z, $1.75(2)\mu_B$ ($P2_1'/n'$ and 8.67) and x, $1.74(2)\mu_B$ ($P2_1/n$ and 8.97), the gof R-factors are given with the corresponding magnetic space group.

After having obtained the magnetic structure at 2 K, with the crystal structure fixed; we freed the crystal structure, at the same temperature. Afterwards, we proceeded in the same way for the rest of the temperatures for which it is known the systems orders magnetically. In each case, we obtained the magnetic moment, for the three mentioned possible magnetic models. The final results for the magnetic moments, in the three equivalent models are plotted in the right inset, panel (c) in Figure 6.6. The results for the mode-amplitudes are shown in the Figure 6.9 (upper panel), with the rest of the values obtained for the amplitudes in the whole temperature range analyzed.

To investigate the phase transitions in the La_2CoMnO_6 compound at high temperatures, the structural thermal evolution was studied by laboratory X-ray diffraction mea-

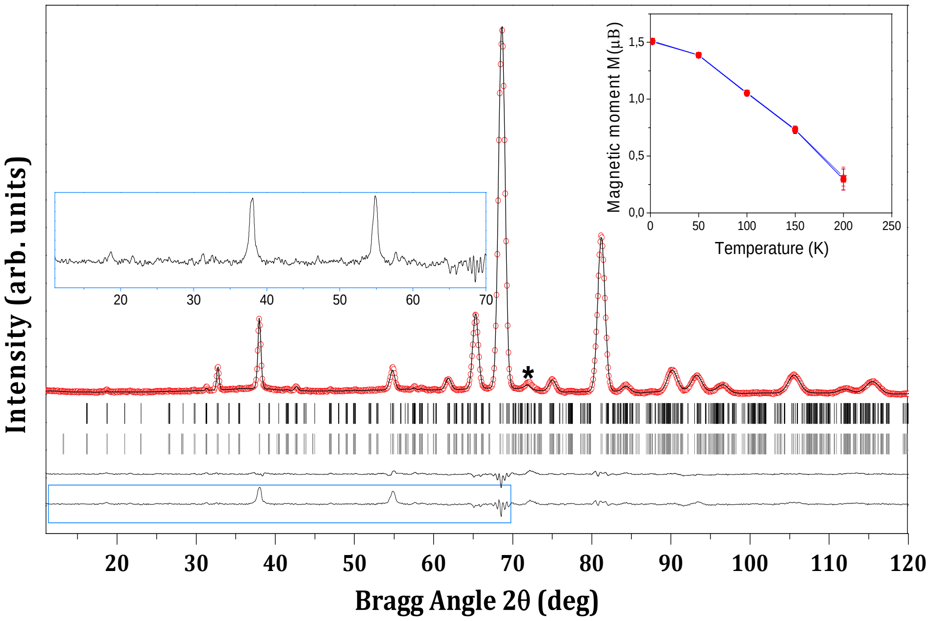

Figure 6.6: Experimental (symbols) and calculated (line) neutron profiles from the Rietveld refinements of La_2CoMnO_6, using a structural model with $P2_1/n$ space group at 2 K data from NPD. The (*)-symbol marked reflection corresponds to the signal of the Vanadium sample container used in the experiment. The bars in the lower part of the graphics represent the Bragg reflections' positions. The upper set of bars correspond to the nuclear structure reflections, and the lower set of corresponds to the magnetic structure reflections. Insets show in detail: the upper difference curve refers to the refinement with both, nuclear and magnetic structures, while the lower one was obtained from a refinement with only the nuclear structure (shown in details in the inset), to show isolated the magnetic reflections. We show in the right inset the evolution with temperature of the magnetic moments for the three proposed ferromagnetic models.

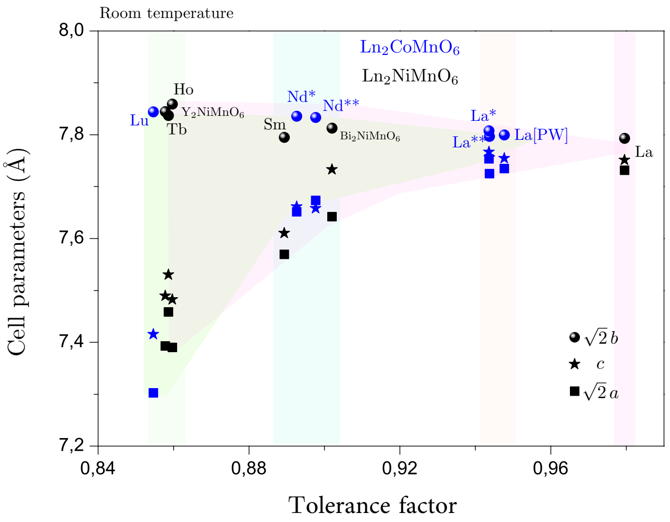

Figure 6.7: Evolution, at room temperature, of the cell parameters along the analyzed structures in the families: Ln_2CoMnO_6 (blue) (Ln= La[PW], La*[115], La**[119], Lu[128] Nd*[129], Nd**[130]); and, Ln_2NiMnO_6 (black) (Ln=La[115], Tb[118], Sm[118], Ho[131]), Y_2NiMnO_6[132] and Bi_2NiMnO_6[133]. As in figure6.3, we are using the experimental tolerance factor, calculated using the experimentally obtained bond-distances. PW stands for present work.

surements. Figures 6.8(a-c) shows the thermal evolution, of the scattering intensity for three 2θ intervals in the temperature range from 300 K to 1600 K. A close analysis of the projected scattering intensity shows that the diffraction lines get closer to each other and the splitting reduces as the temperature increases, which is related to the fact that the unit cell distortion gets smaller. Moreover, in Figure 6.8a, the scattered intensity shows an abrupt discontinuous evolution of the characteristic reflections for the primitive unit cell, *hkl* with $h+k+l=2n+1$, which vanishes at 450 K. Hence, the cell transforms from the primitive monoclinic RT cell to another structure with non-primitive cell, and higher symmetry. The observed phase transition has a discontinuous character, which can be clearly seen in Figure 6.8b. This is very similar to what was observed in our previous studies for the antimony family: Sr_2LnSbO_6 ,[137] where this change was interpreted as an evidence of the materials undergoing a discontinuous phase transition from the $P2_1/n$ space group to the trigonal phase $R\bar{3}$.

In addition to that, Bull et al. have reported that La_2CoMnO_6 shows a trigonal symmetry, $R\bar{3}$ space group, at 670 K .[115] Refinement attempts on the XRPD data above 450 K with the $R\bar{3}$ structure, were successfully carried out. These results confirm the structural phase-transition character observed at 450 K: a first-order phase-transition from a monoclinic to a trigonal symmetry: $P2_1/n \rightarrow R\bar{3}$. There is no group-subgroup relation between the monoclinic $P2_1/n$ and the trigonal $R\bar{3}$ and, thus, the experimentally observed phase transition should be of a first order, discontinuous, character which is the case. On the other hand, the intermediate trigonal phase $R\bar{3}$, will not be the reference structure of the RT phase. In the symmetry-mode analysis decomposition, the same virtual reference

---

[137] A. Faik, E. Iturbe-Zabalo, I. Urcelay, and J. M. Igartua. *J. Solid State Chem.* **182**: 2656–2663,

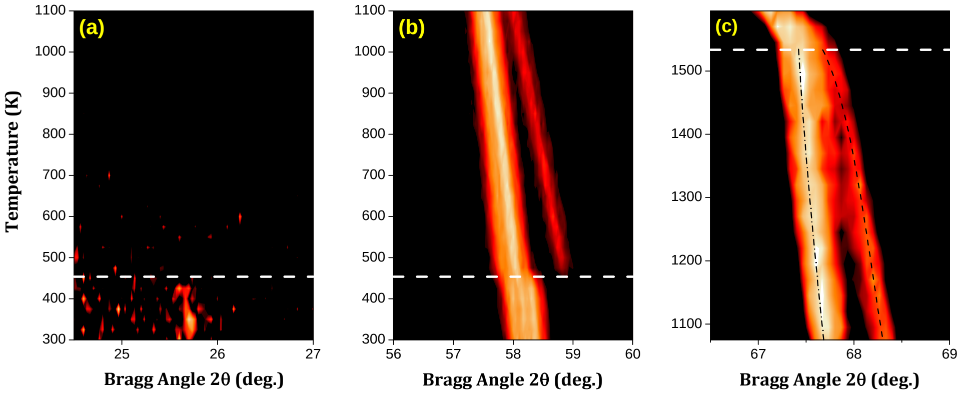

Figure 6.8: Thermal evolution of selected ranges in 2θ, obtained from the XRPD experiment: (a) 24.5-27°, corresponding to the (111) primitive peak and (b) 56.5-60° presenting a clear region to follow the evolving of the intensity. (c) Represents the 66.5-69° 2θ interval corresponding to the (440) cubic reflections. In all the figures, the horizontal lines in blue, a guide to the eye, show the transition temperatures. The other dashed lines, in black, are a guide to follow the disappearance of the splittings.

structure is used for the monoclinic and the trigonal (see Table 6.1).

At higher temperatures, the XRPD data show that all the reflections get closer. For instance, the splittings of the reference cubic reflections 440 and 642 disappears continuously, as seen in Figure 6.8c, and at about 1545 K the trigonal distortion of the unit cell disappears in a continuous way. This indicates the presence of a second phase transition from the intermediate trigonal symmetry to a higher symmetry one. The structural refinements of the patters have confirmed that above 1545 K the structure can be described with the $Fm\bar{3}m$ space group.

This is the first time where both, the trigonal-to-cubic phase-transition is reported and the complete phase-transition sequence $P2_1/n$ $(a^-a^-b^+) \rightarrow R\bar{3}$ $(a^-a^-a^-) \rightarrow Fm\bar{3}m$ $(a^0a^0a^0)$, is observed experimentally for the La_2CoMnO_6. The same phase-transition sequence was observed in the case of several materials of the antimony family having a large size-difference among the Ln^{3+} and Sb^{5+} cations .[12, 137–141] The temperature dependence of the amplitudes of the distortion-modes and the lattice parameters, from 2-1600 K, are shown in Figure 8.7 and Figure 6.10, respectively.

For the trigonal $R\bar{3}$ phase, as shown in Table 6.1, there are three irreps that can take part in the symmetry breaking from the cubic ($Fm\bar{3}m$) to the trigonal $R\bar{3}$; GM$_1^+$(1), GM$_4^+$(1) and GM$_5^+$(2), as usual, the number in parentheses indicates the number of modes transforming according to the corresponding irrep. The symmetry-mode decomposition performed by AMPLIMODES suggests that there is a single primary mode responsible for the symmetry breaking, the one marked in bold, which is the one transforming according

---

[138] A. Faik, J. M. Igartua, Gateshki M., and G. J. Cuello. *J. Solid State Chem.* **V182**: 1717–1725, 2009.

[139] A. Faik, J. M. Igartua, E. Iturbe-Zabalo, and G. J. Cuello. **963**: 145–152, 2010.

[140] A. Faik, I. Urcelay, E. Iturbe-Zabalo, and J.M. Igartua. *J. Mol. Struct.* **977**: 137–144, 2010.

[141] A. Faik, D. Orobengoa, E. Iturbe-Zabalo, and J.M. Igartua. *J. Solid State Chem.* **192**: 273–283, 2012.

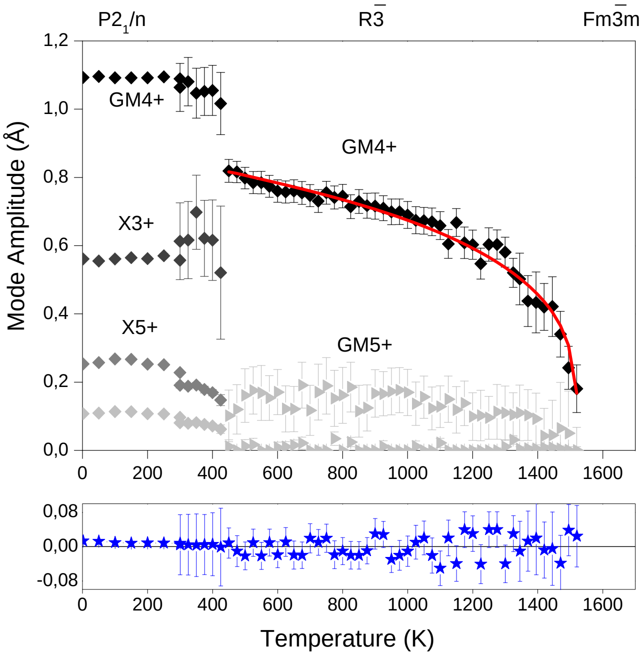

Figure 6.9: Temperature evolution of the amplitudes of the modes breaking the symmetry from the cubic to the $P2_1/n$ and $R\bar{3}$ symmetries, as obtained from the NPD (2-300 K)and XRPD (300-1600 K) data refinements. The GM$_4^+$, X$_3^+$, X$_5^+$ ($P2_1/n$) and GM$_4^+$ ($R\bar{3}$) are the irreps of the symmetry-modes whose presence sets the distortions in the mentioned distorted phases. In the case of the X$_5^+$ irrep, in the low-temperature range, we are showing separately the effectively freed two components of the 3 dimensional sub-space the irrep spans. In the case of the $R\bar{3}$ space group symmetry, we are also showing, dimmed, the two components of the GM$_5^+$ irrep: they do not contribute effectively, so the final values of GM$_4^+$ for this symmetry correspond to them having been freed alone. The lower part of the graph (blue symbols) shows the relative difference, in the whole temperature range, between the GM$_4^+$ values in two refinements: only the effectively acting modes and all the modes freed. The continuos line in red is the fitting of the trigonal GM$_4^+$ amplitude values to the equation: $A_{GM_4^+} = A(0)_{GM_4^+}[T_c - T]^{\alpha}$, with the refined values $A(0)_{GM_4^+}$ = 0.127(8), T_c = 1523(1) K and α = 0.26(1).

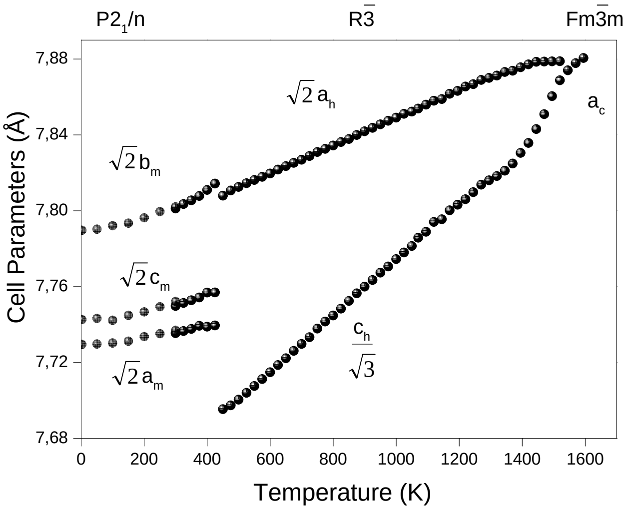

Figure 6.10: Variation with temperature of the lattice parameters for La_2CoMnO_6, as obtained from the NPD (2-300 K)(dimmed black symbols) and XRPD (300-1600 K) data refinements. In the studied temperature range (2-1600 K), the compound undergoes two phase transitions: first-order one, discontinuous, at ≃450 K transforming the cell from a monoclinic to a trigonal; and a second one of the second-order occurring at ≃1520 K from a trigonal to a non-distorted cell, cubic. The phase-transition sequence is the following: $P2_1/n \rightarrow R\bar{3} \rightarrow Fm\bar{3}m$.

to GM_4^+. The nullification of GM_1^+ and GM_5^+ did not affect the amplitudes of GM_4^+, the obtained results are plotted in the trigonal region, from 450 to 1600 K. It is worth noting the nearly continuous behavior, and decreases steadily of the GM_4^+ amplitudes value in $R\bar{3}$ symmetry. At the second phase-transition temperature, ≈1523 K, the GM_4^+ amplitudes value goes to zero. In Figure 6.9, and in the case of the $R\bar{3}$ space group symmetry, we are also showing, dimmed, the two components of the GM_5^+ irrep: they do not contribute effectively, as can be seen from their absolute values and/or their corresponding errors: they effectively nullify. Hence, the final values of GM_4^+ for this symmetry correspond to them having been freed alone. The lower part of the graph (blue symbols) shows the relative difference, in the whole temperature range, between the GM_4^+ values in two refinements: only the effectively acting modes and all the modes freed. As it can been seen, they are almost equal, except, perhaps, very near to the phase transition to the prototype cubic phase, where the underlying fluctuations give rise to higher errors in the determination of the structure.

Finally, the GM_4^+ amplitudes in this symmetry, were perfectly fitted to the equation $A_{GM_4^-} = A(0)_{GM_4^-}[T_c - T]^{\alpha}$ where T_c is the critical temperature: the phase transition temperature. The fitting results values are $A(0)_{GM_4^-}$ = 0.127(8), T_c = 1523(2) K and α=0.28(1). The exponent α value is very close to the Landau Theory prediction of 0.25 for a tri-critical transition. This behavior has also been observed and reported in some other cases, for instance in the $SrZrO_3$ simple perovskite .[142]This is an indication that the coefficient of the fourth power order parameter in the expression for the Gibbs free energy is negligibly small

---

[142] Brendan J. Kennedy, Christopher J. Howard, and Bryan C. Chakoumakos. *Phys. Rev. B* **59**: 4023–4027, 1999.

[143].

---

[143] E. K. H. Salje. *Phase Transitions in Ferroelastic and Co-elastic Crystals*. The Pitt Building, Trumpington Street, Cambridge CB2 1RP: Cambridge Topics in Mineral Physics and Chemistry Vol. 1, ed., Cambridge University Press, 1990.

6.4 Conclusions

- For the first time where both, the Trigonal-to-Cubic phase-transition is reported and the complete sequence: $P2_1/n \rightarrow R\bar{3} \rightarrow Fm\bar{3}m$ is observed for the La_2CoMnO_6.
- A disordered configuration of *Co*- and *Mn* cations over the *B*-site have been observed for the La_2CoMnO_6.
- The analysis carried in the tri-dimensional distortion subspace transforming according to the X_5^+ irrep has permitted us to consider some of the literature results as confident showing the same direction of the X_5^+ irrep, and some others not confident having completely another direction.
- This analysis has permitted also to define a direction, common to all the cases considered as good, as the direction in which the distortion associated to the irrep X_5^+ takes place: (c1, c2, 0.00)≈(0.920, -0.390, 0.00), are the components of the polarization vector.
- The X_5^+ direction parameterized, accordingly to (1.000, 0.424, 0.000), and used to perform all the subsequent refinements at low temperature has lead us to a very sensitive results.
- The assumption of the amplitudes of the magnetic moments of the magnetic ions to be equal has lead us to three indistinguishable ferromagnetic models compatible with the data, in the possible magnetic space groups: $P2_1/n$ and $P2_1'/n'$.

Chapter 7

Statistical analysis of $Sr_2MM'O_6$ (M'= W, Mo, Sb, Ru and Te)

In preparation

As a next step in paving the path to establish a more efficient workflow for the analysis of the kind of materials we are interested in, we have performed a statistical study of forty materials pertaining to five families. The main target of this study is to apply the workflow systematically to the selected materials and complement it with the aid of energy calculations. The energy calculations will give us more physical arguments that corroborate the main conclusions of the workflow we are developing. Those energy calculations have been started to be tested by Dr. Urko Petralanda, member of the Research sub-Group leaded by Professor Dr. I. Etxebarria.

First of all, we have made a classification of the all structures found in the database and the literature. In the one hand, we have a group of completely ordered (B and B′-sites occupied by different cations) and disordered structures. In the later group, we have included the found structures for which a disorder greater than a 15% has been found for one of the sites. Disorder less than 15% has been considered as complete order.

The reason for this first separation is that in the completely ordered cases there are two octahedra and in the completely disordered case, effectively, there is only one: some kind of mean octahedra. One of the parameters that governs the ordering is the size of the cations, or the size-difference between the cations occupying the B- and B′-site: the more close in size the more disordered, in principle. It has been observed experimentally that charge also plays a relevant role in the ordering-process. Big size differences tend to order the cations, and when the size difference is lower than a threshold [24] value, the big charge difference orders, usually, the sites. If the size difference and the charge difference are small, then disorder appears. Hence, in the two groups of materials, by construction, we have

---

[24] R. H. Mitchell. *Perovskites Modern and Ancient*. Almaz Press Inc., 2002.

two different (in size) octahedra, or just one mean one. Finally, as the degree of the tilting depends on the size of the octahedra, different tilting-degrees (hence, distortions) are going to be observed in the two groups.

We have prepared all the structures, as taken from the database and literature, in the same non-standard setting $P12_1/n1$ (cell choice 1) of the No. 14 (ITA [144]) space group, with the same origin choice: B′-site cation at the origin. Of course, we are using the same reference structure for all the cases. This assures that the basis vectors for the symmetry adapted modes used are the same. This is the information necessary to input for the energy calculations.

Let me explain, grossly, the procedure. The program receives the structure and relaxes it, to find where the minimum sits in the space spanned by the irreps we are freeing during the structural refinements.

One of the outstanding results for this systematic minimization is the fact that in all the materials analyzed the third component of the X_5^+ irrep transforming distortion is zero. That is, the theoretical prediction is the same as the experimental conclusion: the "good experimental structures" share the feature of having a zero c_3 component. Another interesting result is that the set of mode-amplitudes that "experimentally" nullify, and that we do not include in the final structural refinements, show zero values in the final minima. Thus, the experimental structure coincides with the relaxed one obtained theoretically. Therefore, as mentioned, according to the workflow, there are three irreps (four degrees of freedom) with not null values in the associated mode-amplitudes: GM4+, X_3^+ and X_5^+. The first two are one-dimensional and the third, three-dimensional, but only a two-dimensional projection is not null.

Usually, in these kind of energy analysis, if one the irreps taking part in the distortion has a dimension higher than one, its internal structure is not taken into account. That is, the minimization procedure is done using the global distortion associated to that multi-dimensional space. One of the novelties of the analysis we are developing is that we are seeking the minima taking into account explicitly the components of the X_5^+ irrep transforming distortion, and not only its global effect. Hence, we are spanning the free energy explicitly using the invariant terms related to the components c_1 and c_2. At the same time, we have developed the free energy of the system in the framework of the Landau Theory of Phase Transitions, that is the expansion in terms of the primary order-parameters and the secondary ones, together with the possible coupling terms, all of them invariant for the symmetry-breaking analyzed. The expansion has been carried out to the fourth terms. It contains quadratic and quartic terms of the four modes, and their couplings. The facts already mentioned, the tri-linear coupling between the GM_4^+ and X_3^+ with X_5^+, gives rise to 2 terms, as we are explicitly using the internal structure of X_5^+. Moreover, this fact also shows itself in another bilinear coupling term. The final polynomial use as the expansion of the free energy is the following:

---

[144] Th. Hahn. *International Tables for Crystallography Volume A: Space-group symmetry*. The International Union of Crystallography and Kluwer Academic Publishers: Dordrecht, Holland., 1992.

$$\begin{aligned}F(GM_4^+, X_3^+, c_1(X_5^+), c_2(X_5^+)) = p_0 + p_1 \cdot Q^2_{GM_4^+} \;+\; p_2 \cdot Q^4_{GM_4^+} \;+ \\ p_3 \cdot Q^2_{X_3^+} \;+\; p_4 \cdot Q^2_{X_3^+} \;+ \\ p_5 \cdot Q^2_{c_1(X_5^+)} \;+\; p_6 \cdot Q^4_{c_1(X_5^+)} \;+ \\ p_7 \cdot Q^2_{c_2(X_5^+)} \;+\; p_8 \cdot Q^4_{c_2(X_5^+)} \;+ \\ p_9 \cdot Q^2_{GM_4^+} \cdot Q^2_{X_3^+} + p_{10} \cdot Q^2_{GM_4^+} \cdot Q^2_{c_1(X_5^+)} + p_{11} \cdot Q^2_{GM_4^+} \cdot Q^2_{c_2(X_5^+)} \;+ \\ p_{12} \cdot Q^2_{X_3^+} \cdot Q^2_{c_1(X_5^+)} + p_{13} \cdot Q^2_{X_3^+} \cdot Q^2_{c_2(X_5^+)} \;+ \\ p_{14} \cdot Q^2_{c_1(X_5^+)} \cdot Q^2_{c_2(X_5^+)} \;+ \\ p_{15} \cdot Q_{GM_4^+} \cdot Q_{X_3^+} \cdot Q_{c_1(X_5^+)} + p_{16} \cdot Q_{GM_4^+} \cdot Q_{X_3^+} \cdot Q_{c_2(X_5^+)} \;+ \\ p_{17} \cdot Q_{c_1(X_5^+)} \cdot Q_{c_2(X_5^+)} \;+ \\ p_{18} \cdot Q^2_{GM_4^+} \cdot Q_{c_1(X_5^+)} \cdot Q_{c_2(X_5^+)} \;+ \\ p_{19} \cdot Q^2_{X_3^+} \cdot Q_{c_1(X_5^+)} \cdot Q_{c_2(X_5^+)} \;+\end{aligned}$$

The minimization is going to be performed for a set of forty points (one for each material, for the moment we have already done it in a couple of them) in the tetragonal space of the freed mode amplitudes. That is, for a tetra-value combination of amplitudes, the energy associated to the distorted structure (for each material) will be calculated. Thus, we will have a set of forty energy minima points. Once the set of minima has been found for the whole set of materials, we will fit the preceding polynomial. As the output of the fitting, we have the set of coefficients, which will be used to obtain the energy in a regularly spaced tetra-lattice in the freed mode-amplitudes space. In the next Figure 7.1 we show an example of an output for one material. We are showing a set of 16 two-dimensional projections, in the c_1 and c_2 space, corresponding to a fixed value of X_3^+ and one-each projection for the selected 16 lattice points in the GM_4^+ axis. We are analyzing these kind of energy diagrams. The preliminary conclusions are very promising. First, we are obtaining, as mention, the same distortion decomposition of the structures as we have deduced from the refinements. Second, the analysis of the energy is giving us an insight in the distorted structures which will be clearly clarify and simplify the refinement process. But, for the moment, we are working on it.

At the same time, we have applied AMPLIMODES[59] to all the structures. We have classified further the obtained results according to the following criteria. First, we fix our attention in the A-site, to make different groups of materials according to the A-site: one species and two (disordered) species. Second, each of those groups have been arranged in decreasing order of the global amplitude value for the X_5^+ amplitude. The third parameter taken into account to further classify the materials has been the experimental probe used to obtain the structure: x-rays (usually powder diffraction, but single crystal could also be present) and neutrons (again, mainly, neutron powder diffraction). For the latter criterium,

---

[59] D. Orobengoa, C. Capillas, M. I. Aroyo, and J. M. Perez-Mato. *J. App. Crystallogr.* **42**: 820–833, 2009.

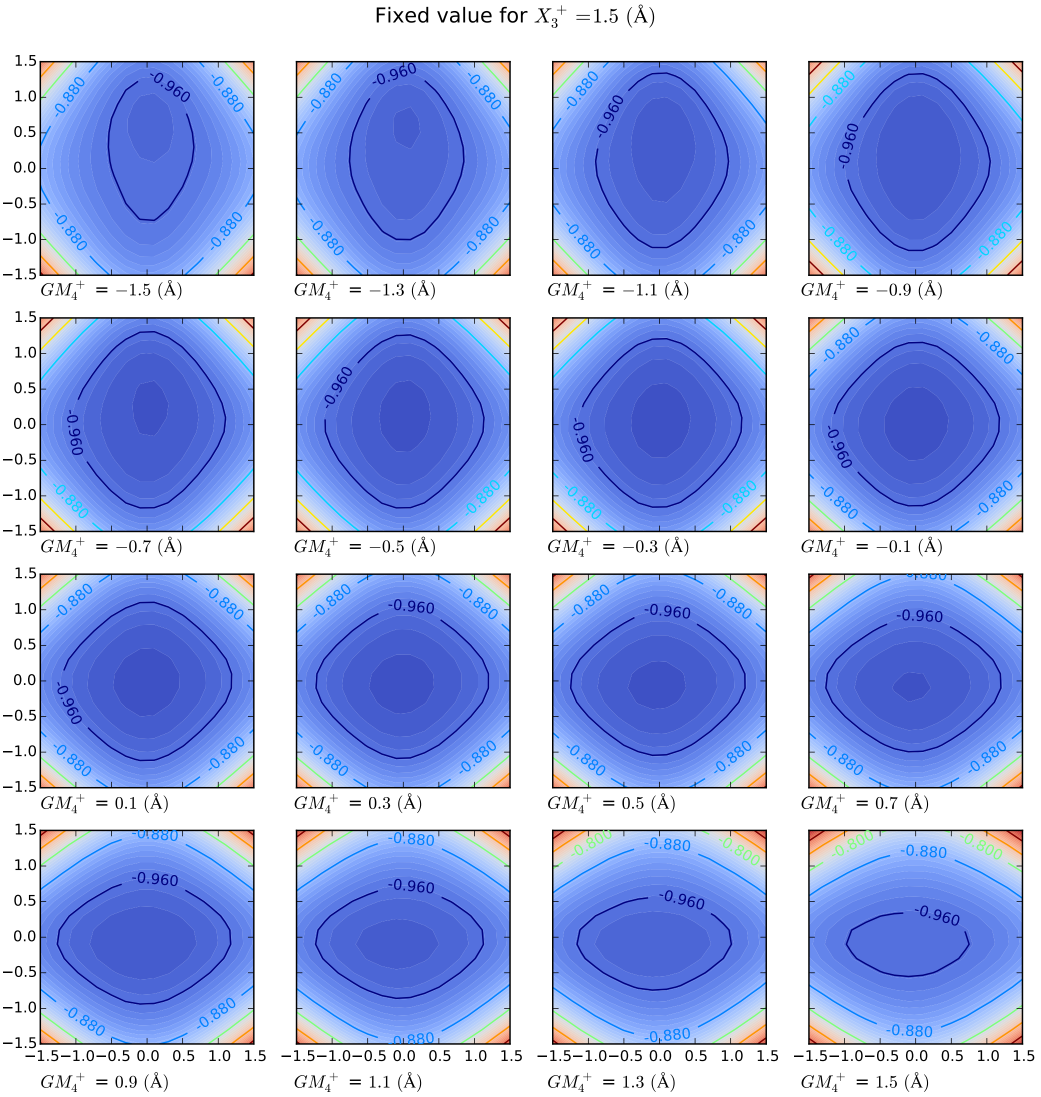

Figure 7.1: Energy projections, in the X5+ two-dimensional space (A10, A11), for a fixed value of X_3^+ as indicated and for the set of values of GM_4^+, as indicated. The values for the amplitudes, are taken from a regular grid (16 points in each dimension) created to construct the energy, one virtual distorted structure for the given set of amplitude-values in the grid. The energy tetra-surface is constructed after the relaxed structures' energies, obtained form the simulations, are fitted to the polynomial constructed with the invariant, up to the fourth-order, terms describing the symmetry breaking form the prototype $Fm\bar{3}m$ cubic to the $P2_1/n$ monoclinic.

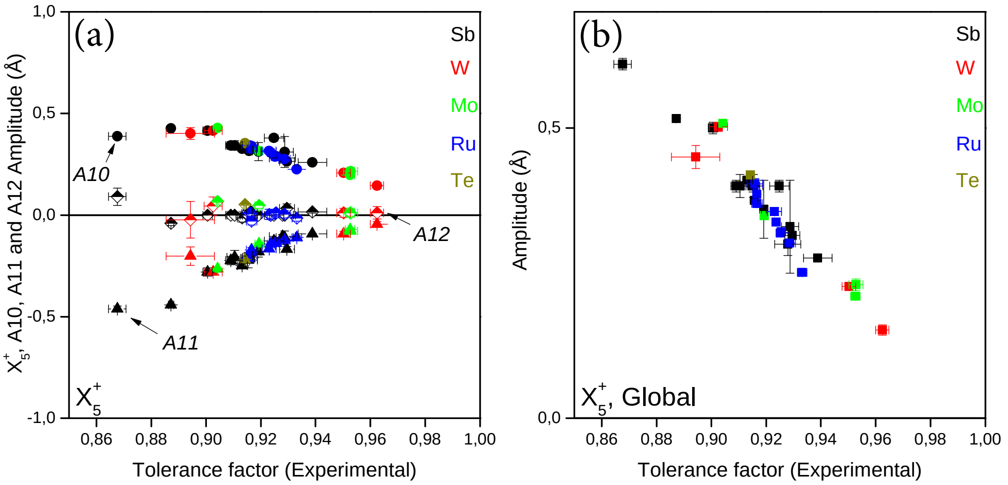

Figure 7.2: (a) Evolution with the tolerance factor of the partial distortion of the $Sr_2MM'O_6$ given by the three components of the X_5^+: A10,A11 and A12. The evolution of the global amplitudes of the tri-dimensional irrep X_5^+ with the tolerance factor, is shown in the panel (b)

we have also indicated if the experiment is high-resolution or not. This final aspect is relevant, as high-resolution for crystal structure refinement is considered as completely trustable. In fact, these structures have been considered as the "good ones". In the last step in the classification, we have made a separated sub-group with the materials, in each of the group, that show a nearly null value for the third component of the 3-dimensional vector transforming according to the X_5^+ irrep. The reason for this is that as can be seen in the table itself, and as will be analyzed below, the good structures, refined using high-resolution NPD, all show an effective only 2-dimensional, (c1, c2, 0) plane, X_5^+ irrep. transforming partial distortion. The result of this classification scheme is shown in the following Table 7.1.

In next figures we are showing the results from the refinements of the experimental data. In the (c_1, c_2,0) $\rightarrow$ (OX, OY, 0) plane, the vectors describing the 2-dimensional distortion, appear mostly with the c_1 component positive and in the 0.8-to-0.9 interval, and the c_2 component in the $(\approx -0.6, 0.0)$ interval. Hence, they show alternate signs. The values of the c_1 components could be considered as almost constant: the interval in which they appear distributed is a 10% of the possible whole interval. On the contrary, the values of the c_2 component appear spread over a 60% of the permitted values interval.

A remark on the remaining vectors plotted in the same figure: those, qualitatively, in the previous sector angle $+\pi$. That is, for those structures, again, the c_1 and c_2 signs are reversed, but in the other sense, in comparison to above mentioned gross vectors. In this sector also we observe the same behavior for the individual components of the distortion vector (c_1, c_2,0): the c_1 component mostly pertains to the $(-0.9, -0.8)$ interval, and the c_2 component higher dispersion extends the existence-interval from 0.0 to ≈ 0.6. In fact, the two sub-set of distortion vectors, in both sectors, are on the same direction: the sense of the vectors in both sectors are reversed, but they show a common direction. It is easily proven that the vectors on the same direction but with different sense, represent

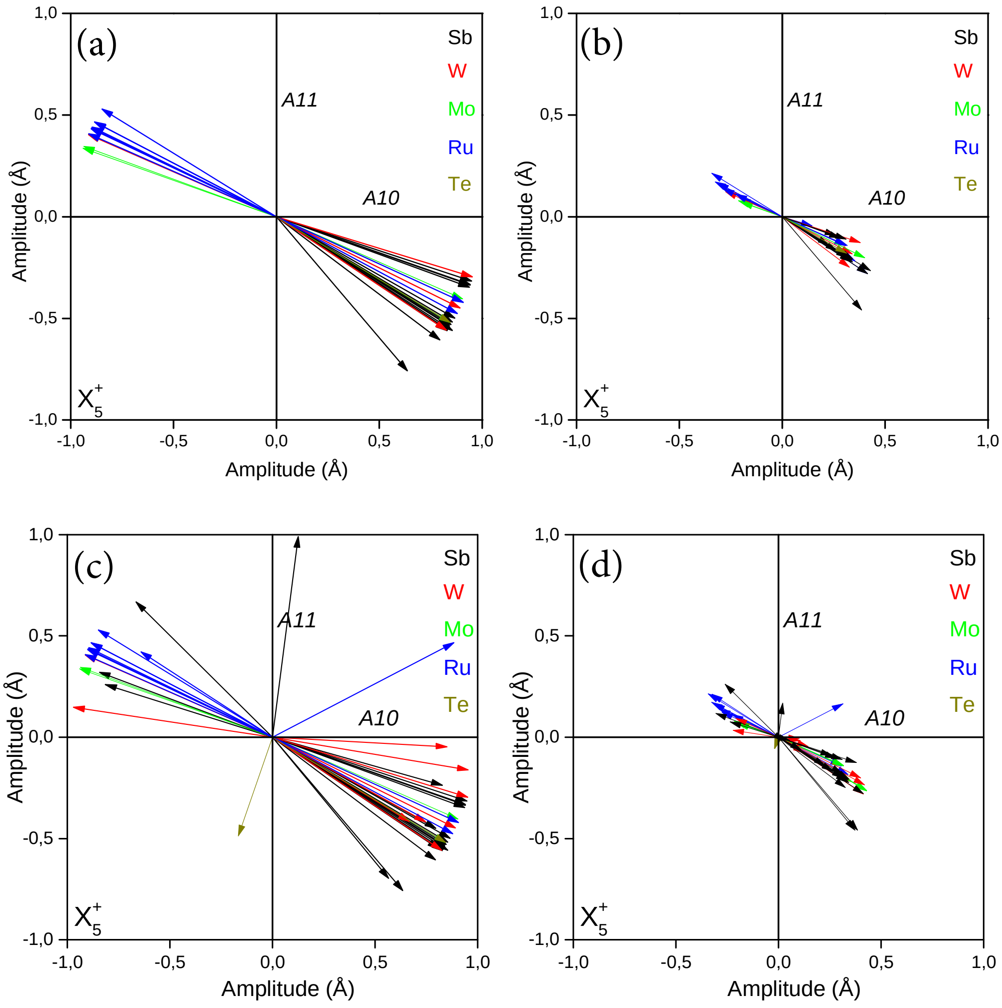

Figure 7.3: (a) Representation of the X_5^+ direction given by the components *c*1 et *c*2 for the $Sr_2MM'O_6$ and (b) their corresponding distortion given by the amplitudes of A10 and A11. (c) and (d) represent the X_5^+ direction and its corresponding distortion for the structures considered as outsiders.

equivalent structures. The point is that the authors analyzing those structures, in the course of the refinements have arrived to energetically equivalent minima, present in two different locations in the energy landscape. Hence, for the analysis we want to carry out, what actually matters is the direction in this 2-dimensional sub-space transforming according to X_5^+ , the relative values and the relative signs of c_1 and c_2: ($|c_1|$,-$|c_2|$,0) and (-$|c_1|$, $|c_2|$,0).

Care must be taken when analyzing some other few cases, the outsiders. In this case, the components of the 2-dimensional distortion vector show absolute values (and relative as well) similar to the previously analyzed ones. Nevertheless, the combination of signs gives rise to a non-equivalent structure. The direction grossly defined in the first sector $+\frac{\pi}{2}$ is actually a structure different to the previously mentioned ones. Of course, it will have its equivalent one, in that direction, but with the signs of the components changed.

Figure 7.3b is the same as Figure 7.3a, but we are plotting the amplitudes of the modes, instead of the vectors. Obviously, it is obtained multiplying the global amplitude value of X_5^+, A_G (X_5^+), times the (c_1, c_2, 0) vector, to obtain the vector whose components are the actual amplitudes of the distortion: (A10, A11, 0),in the FullProf jargon.

Table 7.1: Atomic displacement parameters of the forty materials of the $Sr_2MM'O_6$ (M'= W, Mo, Sb, Ru and Te) families.

Compound	t_{exp}	*Ord.Deg*	Data	Sr	B	B′	O1	O2	O3
Sr_2SmSbO_6	0,8616	100	XRD	0.61(4)	0.27(3)	0.29(3)	0.88(1)	0.88(1)	0.88(1)
Sr_2LaSbO_6	0,8676	100	XRD	0.85(3)	0.33(2)	0.35(2)	1.08(3)	1.08(3)	1.08(3)
$SrCaFeSbO_6$	0,8872	94	NDP	0.81(3)	0.56(6)	0.31(1)	0.88(9)	0.88(9)	0.88(9)
Sr_2DySbO_6	0,9132	100	NDP	0.78(2)	0.29(2)	0.34(4)	0.82(7)	0.83(7)	0.81(6)
Sr_2HoSbO_6	0,9157	100	NDP	0.83(2)	0.25(4)	0.39(5)	1.02(6)	0.83(5)	0.79(3)
Sr_2YSbO_6	0,9182	100	NDP	0.63(4)	0.06(3)	0.11(3)	1.10(2)	0.53(1)	0.56(1)
Sr_2InSbO_6	0,9264	100	NDP	0.36(4)	0.18(3)	0.10(3)	0.15(3)	0.51(4)	0.74(3)
Sr_2InSbO_6	0,9295	92	XRD	0.63(1)	0.09(7)	0.66(3	1.66(4)	1.63(6)	1.66(4)
$SrLaCuSbO_6$	0,9388	100	NDP	0.69(2)	0.61(2)	0.21(3)	1.01(3)	0.87(3)	0.96(2)
$SrLaNiSbO_6$	0,9430	90	NDP	0.71(2)	0.20(2)	0.20(2)	0.48(1)	0.84(1)	0.46(7)
Sr_2ScSbO_6	0,9627	100	NDP	0.50(3)	0.31(5)	0.28(3)	0.30(3)	0.60(4)	1.00(2)
Sr_2FeSbO_6	0,9871	90	NDP	0.66(2)	0.38(2)	0.38(2)	0.69(1)	0.69(1)	0.69(1)
Sr_2FeSbO_6	0,9872	90	NDP	0.62(2)	0.41(1)	0.41(1)	0.71(1)	0.71(1)	0.71(1)
Sr_2FeSbO_6	0,9884	80	NDP	0.72(2)	0.30(2)	0.30(2)	0.75(2)	0.75(2)	0.75(2)
Sr_2CaWO_6	0,8943	100	XRD	0.67(1)	0.41(1)	0.21(4)	3.00(4)	3.00(4)	3.00(4)
Sr_2CaWO_6	0,9026	100	XRD	0.46(3)	0.12(6)	0.10(2)	0.30(1)	0.30(1)	0.30(1)
Sr_2CdWO_6	0,9047	100	XRD	0.90(1)	0.70(1)	0.5(1)	2.70(1)	2.70(1)	2.70(1)
Sr_2MnWO_6	0,9502	100	NPD	0.76(5)	0.35(1)	0.20(1)	0.85(1)	0.96(12)	0.92(1)
Sr_2MnWO_6	0,9513	100	XRD	0.22(3)	0.27(4)	0.13(2)	0.82(1)	0.82(1)	0.82(1)
Sr_2FeWO_6	0,9609	100	NPD	0.63(4)	0.22(7)	0.34(9)	0.80(1)	0.69(1)	0.76(1)
Sr_2FeWO_6	0,9624	100	NPD	0.87(3)	0.36(8)	0.60(2)	0.97(1)	1.00(2)	1.10(1)
Sr_2ZnWO_6	0,9642	100	NPD	0.68(2)	0.46(4)	0.24(4)	0.63(1)	1.34(2)	0.71(1)
Sr_2CoWO_6	0,9769	100	HRNPD	0.55(5)	0.12(27)	0.67(1)	0.52(1)	0.95(2)	0.84(1)
Sr_2CaMoO_6	0,9042	100	D2b	0.96(3)	0.75(5)	0.42(3)	1.03(33)	0.95(3)	0.93(3)
Sr_2ErMoO_6	0,9193	100	D2b	0.86(3)	0.45(2)	0.45(2)	1.23(8)	0.79(6)	0.84(7)
Sr_2MnMoO_6	0,9525	100	D2b	0.94(4)	1.16(1)	0.51(5)	0.43(7)	0.97(8)	1.03(8)
Sr_2MnMoO_6	0,9527	100	D2b	1.10(1)	1.24(1)	0.51(1)	0.64(1)	1.08(1)	0.94(1)
Sr_2HoRuO_6	0,9158	100	NPD	0.30(3)	0.20(9)	0.38(1)	0.35(1)	0.42(1)	0.27(7)
Sr_2TbRuO_6	0,9166	100	NPD	0.41(3)	0.54(4)	0.10(3)	0.68(3)	0.66(4)	0.76(5)
Sr_2TbRuO_6	0,9166	100	NPD	0.80(1)	0.30(1)	0.30(1)	0.50(1)	0.80(1)	0.90(1)
Sr_2ErRuO_6	0,9212	100	NPD	0.10(3)	0.10(3)	0.10(3)	0.10(3)	0.10(3)	0.10(3)
Sr_2HoRuO_6	0,9229	100	NPD	0.79(4)	0.13(5)	0.48(6)	0.92(9)	0.74(8)	0.83(7)
Sr_2HoRuO_6	0,9229	100	NPD	0.79(4)	0.13(5)	0.48(6)	0.92(9)	0.74(8)	0.83(7)
Sr_2YRuO_6	0,9236	100	NPD	0.52(2)	0.34(3)	0.44(4)	0.65(2)	0.65(2)	0.65(2)
Sr_2ErRuO_6	0,9252	100	NPD	0.73(3)	0.50(4)	0.48(5)	0.84(8)	0.84(8)	0.84(8)
Sr_2YbRuO_6	0,9255	100	NPD	0.33(2)	0.11(3)	0.10(4)	0.43(6)	0.37(5)	0.31(5)
Sr_2TmRuO_6	0,9286	100	NPD	0.74(3)	0.47(4)	0.20(4)	0.78(7)	0.96(8)	0.64(4)
Sr_2LuRuO_6	0,9330	100	NPD	0.36(3)	0.21(8)	0.27(8)	0.93(9)	0.25(8)	0.29(8)
Sr_2CaTeO_6	0,9142	100	NPD	0.94(2)	0.63(5)	0.39(4)	0.94(4)	0.94(3)	0.86(3)
Sr_2CoTeO_6	0,9758	100	NPD	1.01(4)	0.20(2)	0.80(1)	1.03(6)	1.10(1)	0.90(1)

Introduction to Sr_2MSbO_6 (Ca_2MSbO_6) Antimony Family

After having analyzed a simple perovskite system, we move to more complicated systems with a double perovskite structure. The fist type of double perovskite to be analyzed in the present thesis is the antimony family with the general formula: $Sr_2M^{3+}Sb^{5+}O_6$. The works we are reporting in the present report, are results of a systematic work done in our group on this type of materials, and from which many publications are derived from it. The emphasis in those works was mainly sitting on the structural characterization at different temperatures and on the analysis of the structural phase-transition sequences. Indeed, on of the main targets of the present work, was as continuation of the conclusions derived from previous works.

One of the results shown in the work of our group on this antimony family, is that due to the charge difference between the two cations placed on the B-site (M^{3+} and Sb^{5+}), the ordering of the obtained structure could change. In fact, this charge difference is smaller that the one observed in other families as in the case of the tungsten $Sr_2M^{2+}W^{6+}O_6$, where the difference is of the order of 4, that big difference gives rise to structures with a complete ordering of the M^{2+} and W^{6+} cations over the B-site. The other factor that could act on the ordering degree of the materials, is the synthesis process itself. The other factor could be the size of the cation placed together with the Sb^{5+} at the B-site.

From reported works done on this antimony family have shown a complete ordered structures in the case of Sr_2MSbO_6 (Sc, Sm and La), while a partial ordering was found in Sr_2MSbO_6 (Fe, Mn, Co, Cr, Ga and Al). Also it was reported that the synthesis temperature could affect the structure ordering: The highest is the synthesis temperature (reasonable high), the more ordered is the material.

The previously analyzed antimony materials, present a large variety of space groups at room temperature, depending of the cations M^{3+}. The results of the phase transitions analysis at high and low temperatures have shown the existence of two possible phase-transitions sequences, depending on the size difference between the B-site cations, the sequence could be one or the other: $P2_1/n - R\overline{3} - Fm\overline{3}m$, with a trigonal intermediate phase or $P2_1/n - I2/m - I4/m - Fm\overline{3}m$ with two intermediate phase, tetragonal and monoclinic.

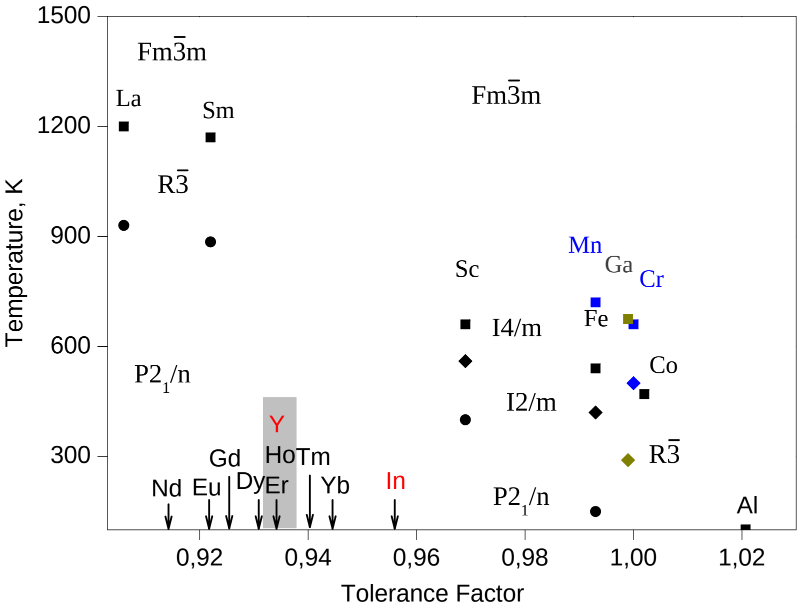

The phase-diagram of this antimony family, which is a representation of the transition-temperatures versus the tolerance factor of each of the members of that family, shows a general decreasing tendency of the transition temperatures as the tolerance factor values increase. With some exceptions in the case of the materials presenting *Jahn-Teller* effect Sr_2MnSbO_6 and Sr_2CrSbO_6, which do not follow the shown trend.

In order to compete the study carried out on the antimony family, a series of materials pertaining to this family has been synthesized and characterized experimentally with the following formula: Sr_2MSbO_6 (M= Nd, Eu , Gd, Dy, Ho, Y, Er, Tm, Yb and In) and $Sr_2Sc_{1-x}In_xSbO_6$. The objectives from this analysis is to clarify the following points:

1. What is the real form of the phase-diagram in the region of small tolerance factor values, between the Sm and Sc?
2. The intermediate phase $R\bar{3}$ is maintained in range between Sm and Sc? Or $I2/m$ and $I4/m$?
3. What happens to the existence region of the $R\bar{3}$ as the tolerance factor increases?
4. What is the "origin" of the observed phase-transition sequence?
5. The cations Ho, Er and Y have close size and, hence, close tolerance factor values. Should they show the same behavior?
6. In and Y are not Lanthanides. Do they behave as Lanthanides?
7. What is the evolution of symmetry-mode amplitudes with tolerance factor at RT?

Chapter 8

Sr_2MSbO_6 (M = *Ln*, Y): Mode-Crystallography approach of the structural and high temperature phase transition studies

The perovskite structure type is one of the most regularly observed structure types in condensed matter sciences and in advanced materials research and applications, as well.[145,146] This is due to the wide array of proprieties it shows like superconducting and magnetoresistance .[19,147,148] The structure of double perovskite is very simple, the B and B′ cations form octahedra and are connected alternary each to other via vertices. The A-atoms occupy the interstitial spaces between the octahedra. The rotations and/or deformation of the BO_6 and $B'O_6$ octahedra with respect to the crystallographic axes of the material cause a distortion of the structure from the ideal cubic symmetry ($Fm\bar{3}m$, No. 225) .[45,53,65,122,149,150]

In the last five years, the symmetry-adapted modes analysis has been started to be used

---

[145] Sebastián A. Larrégola et al. *Inorganic Chemistry* **53**: 5609–5618, 2014.

[146] Javier Sánchez-Benítez et al. *Phys. Chem. C* **118**: 9652–9658, 2014.

[19] K-I. Kobayashi et al. *Nature* **395**: 677–680, 1998.

[147] M. DeMarco et al. *Phys. Rev. B* ,.

[148] E. J. Cussen, J. F. Vente, P. D. Battle, and T. C. Gibbb. *J. Mater. Chem.* **7**: 459–463, 1997.

[45] A. M. Glazer. *Acta Crystallogr. B* **28**: 3384–3392, 1972.

[53] C. J. Howard and H. T. Stokes. *Acta Crystallogr. B* **54**: 782–789, 1998.

[65] C. J. Howard and H. T. Stokes. *Acta Crystallogr. B* **60**: 674–684, 2004.

[122] Christopher J. Howard and Harold T. Stokes. *Acta Crystallogr. A* **61**: 93–111, 2005.

[149] H. T. Stokes, E. H. Kisi, D. M. Hatch, and C. J. Howard. *Acta Crystallogr. B* **58**: 934–938, 2002.

[150] M. A Cheah, P.J. Saines, and B.J. Kennedy. *J. Solid State Chem.* ,

in the structural phase-transition studies. It is based on the works by Howard *et al*. [53,65,122,149] and Aroyo *et al*. [57–59,62,63] and Perez-Mato et *et al*. [6,68]. In many cases, the distorted crystalline structures can be considered pseudo-symmetric with respect to a higher symmetry, real or a virtual parent phase. By definition, a group-subgroup relation necessarily exists between the space groups of the parent structure and the experimentally observed one. This latter can then be qualified as a distorted structure and can be described as the parent crystalline structure plus a static symmetry-breaking structural distortion. If the distortion is sufficiently small, a thermally driven structural transition to the configuration of higher symmetry may take place at higher temperatures.

The distortion present in a distorted structure (pseudo-symmetric) contains a primary component, corresponding to a mode or modes which are unstable in the parent high-symmetry configuration, and are fundamental for explaining the stability of the distorted structure. In addition, the distortion contains other secondary contributions of less importance, associated with modes which are allowed by symmetry and become frozen through coupling with the primary ones. Those distortion modes are associated with different irreducible representations (irreps) of the parent space group. The separation of the contributions of the different modes in a structural distortion is done using the symmetry-mode analysis. [57,58]

Two concepts have to be properly defined: the structural distortion itself (relating the parent and the distorted phases; which can be decomposed into two contributions: a homogeneous strain and an atomic displacement field given by the displacements of each atom in the low-symmetry structure with respect to its position in the parent structure. And the basis with respect to which that atom displacements field can be decomposed and formed by the symmetry modes compatible with the symmetry break between the space groups of the parent phase and the analyzed phase .[68] The general method for the symmetry mode decomposition is well documented in .[56,64–66,151] Recently the strontium antimony oxide compounds with double perovskite structure have attracted considerable attention.

---

[57] M. I. Aroyo and J. M. Perez-Mato. *Phase Transit.* **63**: 235–255, 1997.

[58] M. I. Aroyo and J. M. Perez-Mato. *Acta Crystallogr. A* **54**: 19–30, 1998.

[59] D. Orobengoa, C. Capillas, M. I. Aroyo, and J. M. Perez-Mato. *J. App. Crystallogr.* **42**: 820–833, 2009.

[62] M. I. Aroyo et al. *Z. Kristallogr.* **221**: 15–27, 2006.

[63] M. I. Aroyo et al. *Acta Crystallogr. A* **62**: 115–128, 2006.

[6] B. Kocsis et al. *J. App. Crystallogr.* **47**: 1165–1179, 2014.

[68] J. M. Perez-Mato, D. Orobengoa, and M. I. Aroyo. *Acta Crystallogr. A* **66**: 558–590, 2010.

[56] H. T. Stokes, D. M. Hatch, and J. D. Wells. *Phys. Rev. B* **43**: 11010–11018, 1991.

[64] C. J. Howard, B. J. Kennedy, and P. M. Woodward. *Acta Crystallogr. B* **59**: 463–471, 2003.

[66] C. J. Howard and H. T. Stokes. *Acta Crystallogr. A* **61**: 93–111, 2005.

[151] C. J. Howard and H. T. Stokes. *Acta Crystallogr. B* **54**: 782–789, 1998.

[148,152–159] In our previous works, [31,137–141] the room temperature structures and the possible phase transitions at low and high temperature for several compounds of this family have been studied. In order to complete this study, eighteen members of this family, thirteen of them are synthesized for the first time, will be studied in this work.

Three compounds from those nine, have been synthesized and studied at room temperature. To the best of our knowledge the other five have not been previously reported. From those three: The room-temperature space group of Sr_2DySbO_6 and Sr_2HoSbO_6 was reported to be $P2_1/n$.[160] The third one is the Sr_2YSbO_6, which has been reported in several times and different space groups were reported .[161,162] Fu *et al*. [161] have proposed the monoclinic $P2_1/n$ space group. However, Ortiz-Diaz *et al*. [162] did not agree with the previous results and they have proposed the cubic $Fm\overline{3}m$ space group to the Sr_2YSbO_6. In Table 8.1, the available results in the literature done on Sr_2MSbO_6 (Dy, Ho, Y) compounds, are summarized and compared to the obtained results in the present work. However, to the best of our knowledge, no previous studies have been carried out neither on room-temperature crystal structure determination, nor on the temperature-dependent structural modifications of the other members of the studied family Sr_2MSbO_6.

The present work is a part of a systematic study that we have undertaken on the antimony family A_2MSbO_6 (A= Sr and Ca), in this paper we are focusing on the Strontium antimony one. In order to compete the study carried out on the antimony family, a series of materials pertaining to this family has been synthesized and characterized experimentally with the following formula: Sr_2MSbO_6.

The main goals of the present study are: Fist, this contradiction point on the space group of the Sr_2YSbO_6 was the motivation to re-examine the room temperature structure of this material. Secondly; we have selected two materials having the same tolerance factor value, Sr_2HoSbO_6 and Sr_2YSbO_6, but not pertaining to the same series of chemical elements (Yttrium being not a Lanthanide): Should they show the same behavior, the same phase-transition sequence.

---

[152] N. Kashima, K. Inoue, T. Wada, and Y. Yamaguchi. *Appl. Phys. A* ,.

[153] H. Karunadasa et al. **V100**: 8097–8102, 2003.

[154] V. Primo-Martín and M. Jansen. *J. Solid State Chem.* **157**: 76–85, 2001.

[155] A. Tauber, S.C. Tidow, R. D. Finnegan, and W. D. Wilber. *Physica C* ,.

[156] W. T. Fu and D. J. W. Ijdo. *Solid State Comm. doi = (10.1016/j.ssc.2005.01.018) pages = 177-181 , volume = 134, year = 2005,* ,

[157] M.W. Lufaso et al. *J. Phys-Condens. Mat.* ,

[158] S. A. Ivanov, P. Nordblad, R. Tellgren, and A. Hewat. *Mater. Res. Bull.* ,

[159] C. Bharti and T. P. Sinha. *Solid State Sci.* ,

[31] A. Faik et al. *J. Solid State Chem.* **181**: 1759–1766, 2008.

[137] A. Faik, E. Iturbe-Zabalo, I. Urcelay, and J. M. Igartua. *J. Solid State Chem.* **182**: 2656–2663,

[138] A. Faik, J. M. Igartua, Gateshki M., and G. J. Cuello. *J. Solid State Chem.* **V182**: 1717–1725, 2009.

[139] A. Faik, J. M. Igartua, E. Iturbe-Zabalo, and G. J. Cuello. **963**: 145–152, 2010.

[140] A. Faik, I. Urcelay, E. Iturbe-Zabalo, and J.M. Igartua. *J. Mol. Struct.* **977**: 137–144, 2010.

[141] A. Faik, D. Orobengoa, E. Iturbe-Zabalo, and J.M. Igartua. *J. Solid State Chem.* **192**: 273–283, 2012.

[160] H. Karunadasa et al. *P. Natl. Acad. Sci. USA* **V100**: 8097–8102, 2003.

[161] W. T. Fu and D. J. W. Ijdo. *Solid State Commun.* **134**: 177–181, 2005.

[162] O. Ortiz-Diaz et al. *Physica B* ,.

Table 8.1: Preparation conditions of A_2MSbO_6 compounds. The data shown are as follows: Ionic radii in [3]; $\Delta r=|r_{M^{3+}} - r_{Sb^{5+}}|$; tolerance factor; highest temperature of treatment; the detected impurities; symmetry of the crystal structure at room temperature and literature reference. PW stands for present work.

Compound	I.R(Å)	Δr(Å)	*t*	S.T.(K)	Impurities	SG. at 300K	Ref.
Sr_2NdSbO_6	0.983	0.383	0.914	1570		$P2_1/n$	PW
Sr_2EuSbO_6	0.947	0.347	0.921	1570		$P2_1/n$	PW
Sr_2GdSbO_6	0.938	0.338	0.923	1770	≤1% Gd_2O_3	$P2_1/n$	PW
Sr_2DySbO_6	0.912	0.312	0.929	1770		$P2_1/n$	PW
				1670		$P2_1/n$	[160]
Sr_2HoSbO_6	0.901	0.301	0.931	1770	≤1% Ho_2O_3	$P2_1/n$	PW
				1670		$P2_1/n$	[160]
Sr_2YSbO_6	0.900	0.300	0.931	1770		$P2_1/n$	PW
				1545		$P2_1/n$	[161]
				1370		$Fm\bar{3}m$	[162]
Sr_2ErSbO_6	0.890	0.290	0.934	1770		$P2_1/n$	PW
Sr_2TmSbO_6	0.880	0.280	0.936	1770	≤1% Tm_2O_3	$P2_1/n$	PW
Sr_2YbSbO_6	0.868	0.268	0.938	1770	≤1% Yb_2O_3	$P2_1/n$	PW

The phase diagram constructed based on our previous works (to be published), shows the existence of a gap at high tolerance factor values. In order to fill that gap, it has been taught to synthesize and analyze the following series of nine materials: Sr_2MSbO_6 M = Ln (Nd, Eu, Gd, Dy, Ho, Er, Tm, Yb) and Y: What is the origin of the phase-transition sequences observed in the antimony materials studied previous by our group.

8.1 Mode-crystallography analysis of Sr_2MSbO_6 (M = *Ln*, Y): room temperature

All the structural analysis done in the present are made using the symmetry mode approach with AMPLIMODES, [59] which is a perfect tool to analyze and study the phase transitions. But discussing the obtained refinements results, let's explain some aspects of the crystal structure procedure used for the refinements. For that, there is a need to know which are the main irreducible representations (irreps), of taking part in the symmetry break to bring the structure from the prototype $Fm\bar{3}m$ to the distorted monoclinic $P2_1/n$ (Figure 8.2).

For that, the information listed in Table 1 in [100,101] is necessary, which are the monoclinic structure, the reference one (prototype reached by PSEUDO[67]) and the transformation matrix relating both cells. AMPLIMODES calculates the atomic displacements relating both structures (by a the transformation matrix between both cells), if their magnitudes lay within some tolerance range. A complete basis of symmetry-adapted distortion modes is then determined and defined. Then, the program decomposes the distortion in terms of this

---

[100] E. Iturbe-Zabalo et al. *J. Solid State Chem.* **198**: 24–38, 2013.

[101] E. Iturbe-Zabalo et al. *J. Phys-Condens. Mat.* **25**: 205401, 2013.

[67] C. Capillas et al. *Z. Kristallogr.* **226(2)**: 186–196, 2011.

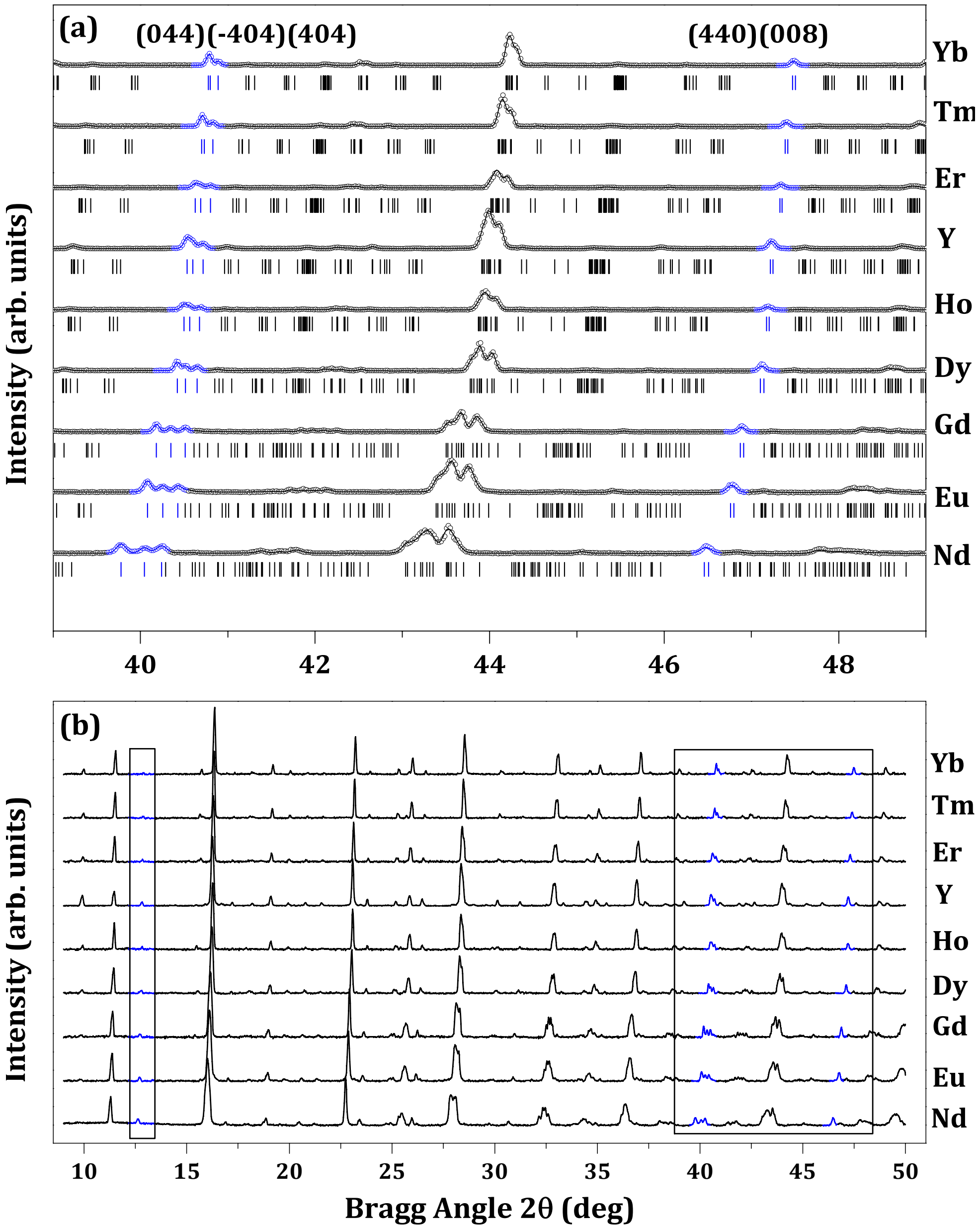

Figure 8.1: (a) Evolution of the synchrotron X-ray powder diffraction patterns at room temperature of the Sr_2MSbO_6 (M = Ln, Y) materials. The first black rectangle section is showing the presence of the primitive Bragg peak reflections with $h + k + l = 2n + 1$, for all the materials. The second black rectangle section, shown bigger the lower graph (b), presents selected regions of diffraction pattern. The regions selected are those that correspond to the cubic reflections (444) and (800), which split in the monoclinic symmetry into a triplet and doublet, respectively.

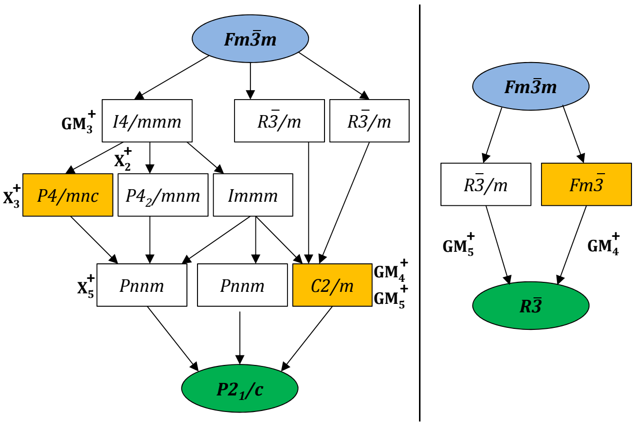

Figure 8.2: Graph of maximal subgroups relating the space groups of the parent phase (highlighted in blue) and distorted phase (highlighted in green) of Sr_2MSbO_6 compounds in the $P2_1/n$ and $R\bar{3}$. For each subgroup any irrep yielding this symmetry is indicated and the primary active irreps evidenced by the Rietveld refinement are highlighted in orange. In the scheme we are using the standard settings of the space groups as the Bilbao Crystallographic Server does for generating these graphs. The $P2_1/c$ is the standard setting of $P2_1/n$

basis of symmetry modes, and calculates the amplitudes for each of the symmetry-adapted distortions. Modes are given in terms of atomic displacements in relative units for the atoms of the asymmetric unit of the distorted phase.

It is known from the previous works for materials having the monoclinic space group $P2_1/n$ that there seven irreps that take par in the symmetry breaking from the cubic $Fm\bar{3}m$. A full description of those irreps are presented in details in .[100,101] It has been proven, that the monoclinic $P2_1/n$ cannot be generated by a single irrep, the most important ones are the two primary: GM_4^+, X_3^+ and the tri-dimensional X_5^+. The three components of X_5^+ are (for FullProf): A10, A11 and A12. These notations will be used in the next section.

The tolerance factors, t, at room temperature of the titled series, have been calculated using the ionic radius suggested in Shannon database [163] and the obtained values are listed in Table 8.1. The excepted room temperature symmetry of the nine materials Sr_2MSbO_6 (M = Ln and Y) is the $P2_1/n$. This fact was confirmed based on the collected synchrotron X-ray diffraction patterns. As it can be seen in Figure 8.3, all the nine patterns show the presence of the primitive reflections the monoclinic primitive peaks ($\bar{1}11$) and (111), (violate the I-centering condition on the hkl reflections with $h + k + l = 2n$). In the same figure, it can been observed the distorted character of all the materials based on the cubic splitted reflections (444) and (800). All these facts can only confirm that $P2_1/n$ symmetry for all the materials. It is worth noting that a continuous change in the position of the peaks and their form is observed. The peaks shift to higher 2θ angle as M^{3+} cation radius decreases, which could be explained by the shrinking of the unit cell as the B-site cations get smaller.

The high contrast between the M^{3+} and Sb^{5+} cations allowed us to free their fractions:

---

[163] R. D. Shannon. *Acta Crystallogr. A* **32**: 751–767, 1976.

a complete ordering of the B-type cations over the two sites was found, this was expected due to the large size difference between the cation M^{3+} (the lanthanides and Y) and the Sb^{5+} cation. As well, the oxygen fractions were also freed, but the obtained values were so close to unity that they were fixed to 1.

In order to show the quality of the refinements carried out, we have selected to show, in Figure 8.3, the patterns of Sr_2NdSbO_6 and Sr_2YbSbO_6. In the insets, two 2θ intervals are plotted: the first one corresponds to the monoclinic primitive peaks (-111) and (111). The second set, corresponds to the monoclinic splitting of the (444) cubic reflection into the (440) and (008) reflections. The refinements results and the mode amplitudes are shown in the lower block of Table 8.2 and their variation according to the tolerance factor is plotted in Figure 8.4.

In addition those two irreps, a contribution is needed from the another not negligible one, which is allowed by symmetry: the tri-dimensional X_5^+, which when included in the refinements makes them stable and converged. In some recent analysis done on Ln_2CoMnO_6 Ln_2NiMnO_6, it has been shown that the X_5^+ has a preferable direction in this internal space which gives rise to a common type of partial distortion associated to the X_5^+ irrep, irrespective of the material. That direction was fixed during the refinements from one material to the other.

The X_5^+ irrep is three-dimensional: it has three modes transforming according to it (A10, A11 and A12), two of which involve only oxygen atoms and the other one, only the Sr cation. In principal, the direction of the generalized vector formed by those components, maintains as the crystal structure evolves in temperature, but its modulus decreases .[136]

The direction of that vector transforming according to the X_5^+ , which represents the partial distortion, has been parameterized in the refinements. This has been used in the analysis of the whole series. This parameterized refinements have been done by setting the $A12$ component to zero and by linking the other two, $A10$ and $A11$ by the same code and freeing them in dependent way.

It is clear from Figure 8.4 that the evolution is taking place in the mentioned way, i.e: as the tolerance factor increases there is notable decreasing of the mode amplitudes, in another words, as we get the ideal tolerance factor value 1 (for the prototype phase): the distortion decreases. In the same graph, the amplitudes of the mono-dimensional GM_4^+ and X_3^+ are plotted. As a conclusion from the irreps, there is a clear tendency of decreasing of the modulus as the distortion decreases: as the size of the B-site cation decreases, the rotation of the octahedra and displacement of the cations get smaller, which apply the diminishing of the mode amplitudes, getting more symmetric structure.

The variation at room temperature of the a, b and c lattice parameters, the monoclinic angle β and the unit cell volume as a function of the tolerance factor, of the Sr_2MSbO_6 series is shown in Figure 8.5. It can be seen that the lattice parameters and the volume decrease linearly with the increase of the tolerance factor, on the other hand, the monoclinic angle β showed a large deviation from 90° and decreases with the increasing of the tolerance factor,

---

[136] B. Orayech et al. *J. App. Crystallogr.* **48**: 318–333, 2015.

which is due to the substitution of the M^{3+} cation in the B site with smaller ones.

The scaled cell parameters have a big difference value between each other in the case of Sr_2NdSbO_6, which has the biggest M^{3+} cation size, this difference decreases with the M^{3+} cation size decrease, as a consequence the volume of the MO_6 octahedra space decreases which reflects in the decreasing of the lattice parameters.

This observation is in agreement with the fact that Nd is bigger than Yb, for instance, making a bigger octahedra space and generating the big titl of the octahedra, unlike the Yb having a smaller size, produce not a such big octahedra titl as the Nd. The decreasing of the volume of the MO_6 octahedra B-site leads to the decrease in the tilt systems which is observed by decreasing of the monoclinic angle β and the modes amplitudes values (see Figure 8.4). Hence, the smaller M^{3+} cation size, the smaller the titling of the octahedra and the more symmetry the structure.

In all the previous Figures, the Yttrium Y was presented with a different color, since it is not a Lanthanide element. Our aim by encompassing this element was to study it's behaviour at RT and HT in comparison to the rest of the Lanthanides studied in the present series and specially to compare it to the Sr_2HoSbO_6, since they have the same ionic radii: same tolerance factor.

In all the sections of the present work, the Sr_2YSbO_6 material, has shown an identical behaviour to what Sr_2HoSbO_6 did, and follows the trend that Lanthanides elements show in the cell parameters and the modes amplitudes. All these points, prove that the origin of the observed phase transitions can only be the steric factor.

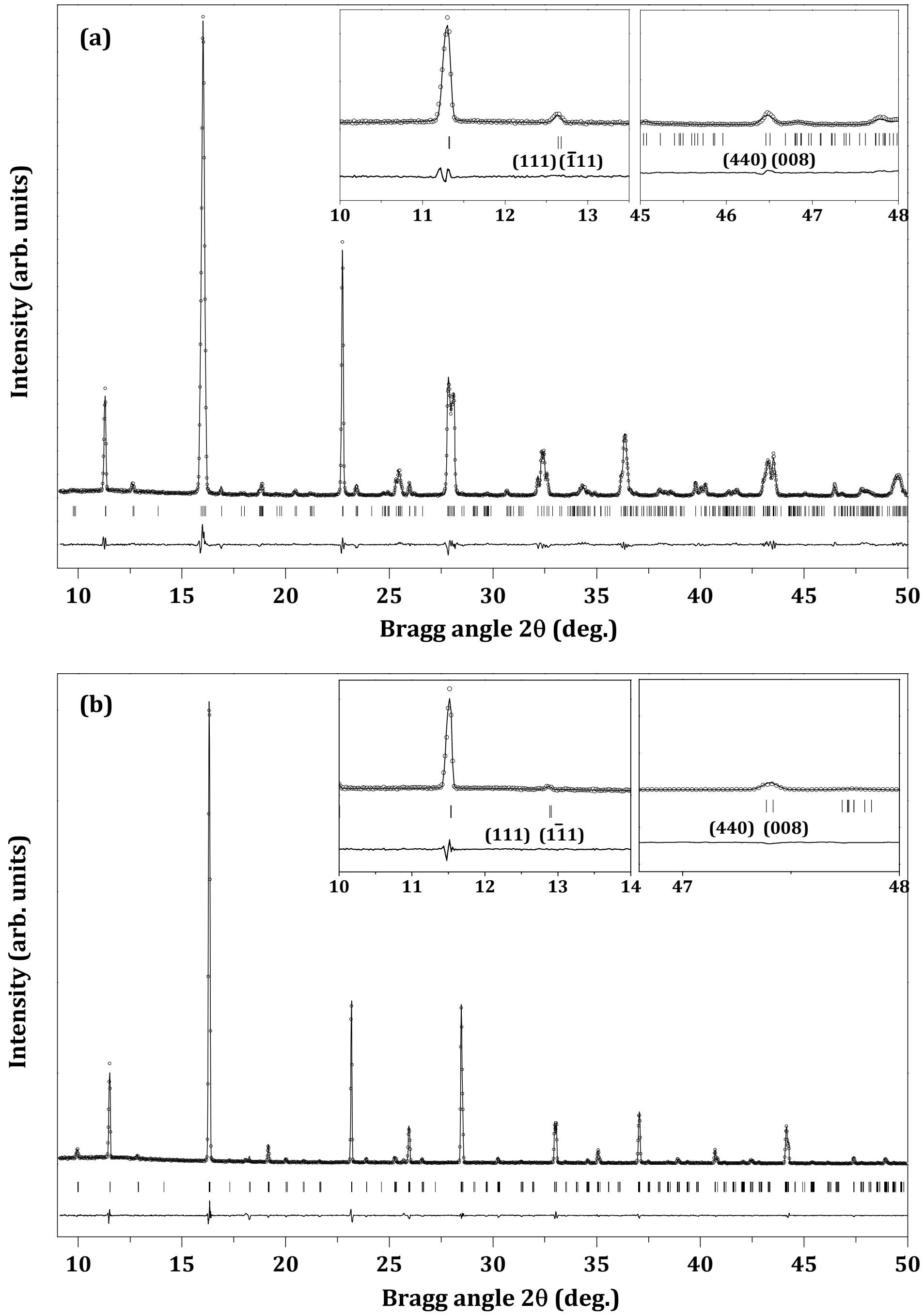

Figure 8.3: Experimental and calculated powder diffraction profiles for the Rietveld refinement of Sr_2NdSbO_6 (a) and Sr_2YbSbO_6 (b) at room temperature, using a structural model with $P2_1/n$ space group. The bars in the lower part of the graphics represent the Bragg peak positions.

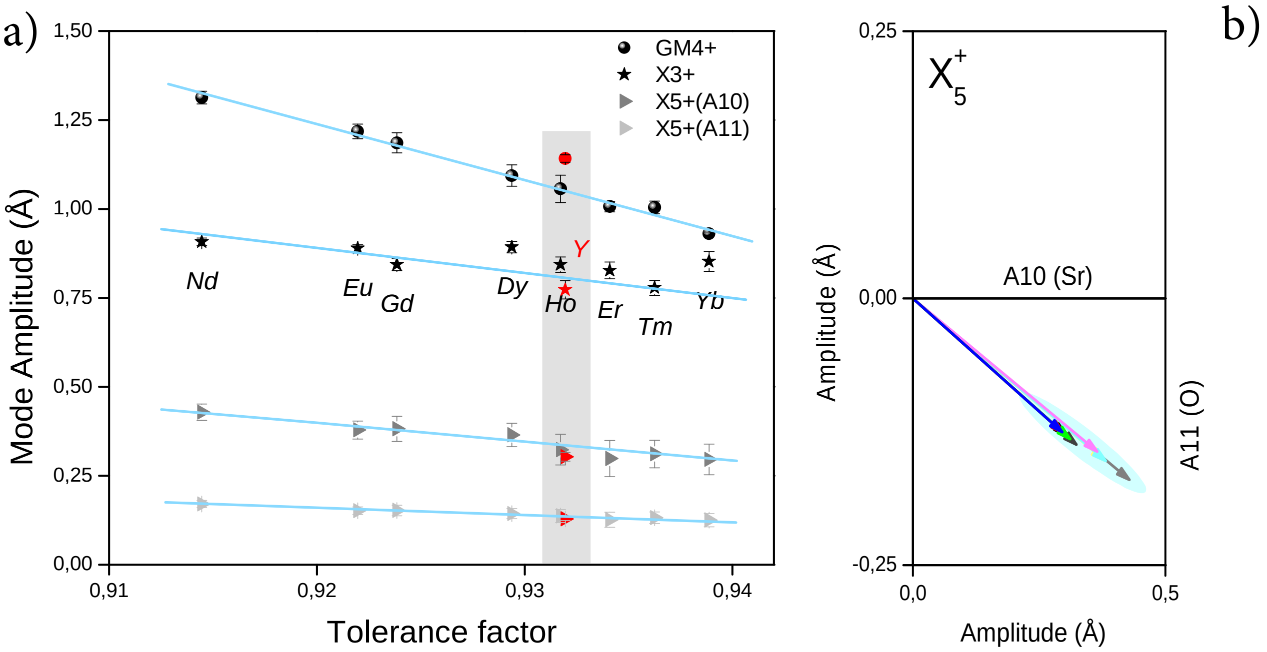

Figure 8.4: a): Amplitudes of GM_4^+, X_3^+ and X_5^+ irreps consolidating the RT phases of Sr_2MSbO_6 M = Ln (Nd, Eu, Gd, Dy, Ho, Er, Tm, Yb and Y materials in the monoclinic symmetry $P2_1/n$, as function of the tolerance factor. The red balls stand for the Sr_2YSbO_6 amplitudes, since the Yttrium, Y, does not belong to the Lanthanides. b): Two dimensional section showing the obtained amplitudes of the irreps (Blue) GM_4^+, (Red) X_3^+ and the two components of the tri-dimensional X_5^+: A10 in x-axis and A11 in y.

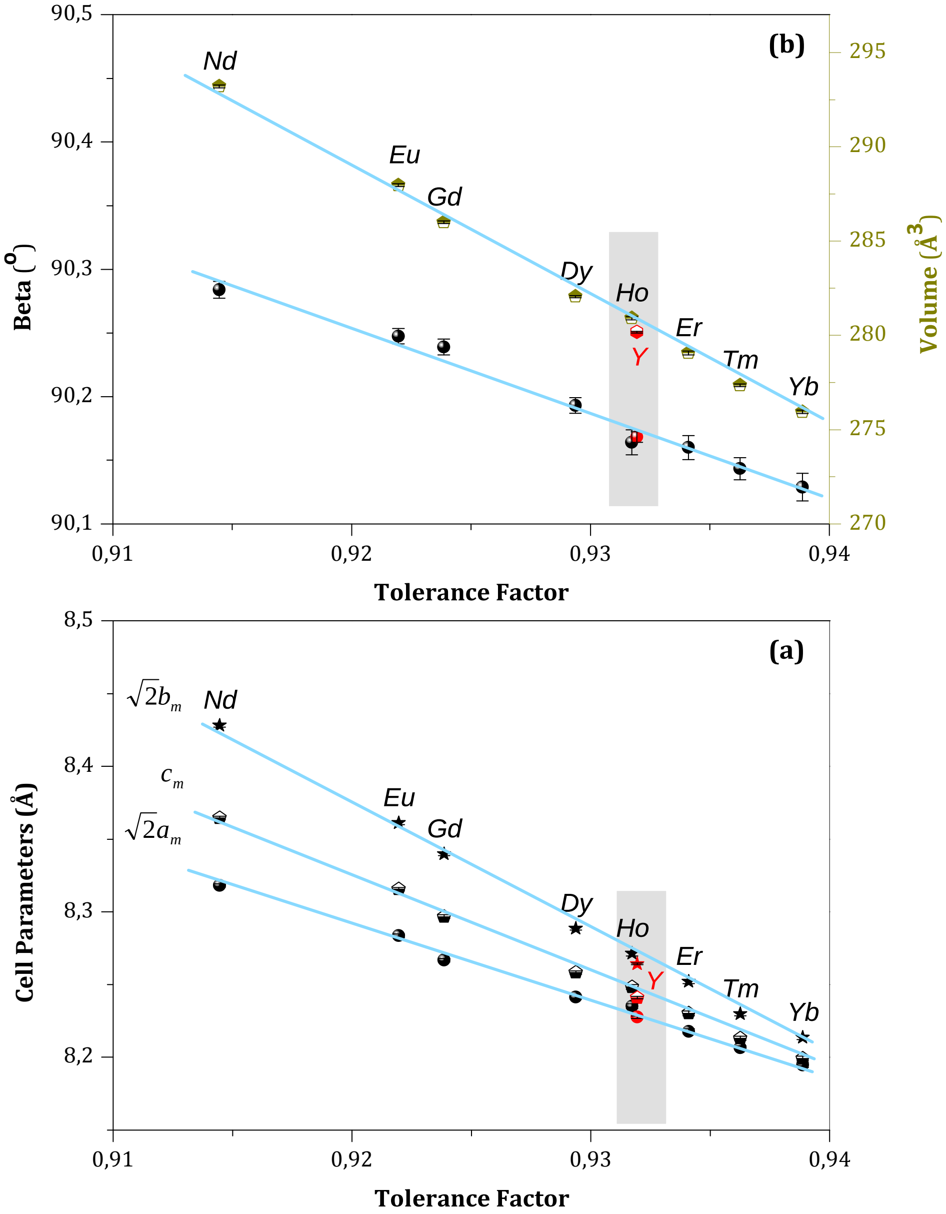

Figure 8.5: Evolution, as a function of the tolerance factor increasing of the unit-cell parameters (a), the unit-cell volume (b) and the monoclinic angle (β) (b) at room temperature of the synthesized materials Sr_2MSbO_6 (M = Nd, Eu, Gd, Dy, Ho, Er, Tm, Yb and Y).

Table 8.2: Crystal structure data and refinement results, at room temperature for Sr_2MSbO_6; M = Ln (Nd, Eu, Gd, Dy, Ho, Er, Tm, Yb) and Y), from Synchrotron powder diffraction. The atomic positions and isotropic atomic displacement parameters were refined in the space group $P2_1/n$. Sb atoms occupy the site 2a (0, 0, 0); M atoms occupy the site 2b (0, 0, 1/2); Sr and O atoms occupy the site 4e (x, y, z).

Compound		Sr_2NdSbO_6	Sr_2EuSbO_6	Sr_2GdSbO_6	Sr_2DySbO_6	Sr_2HoSbO_6	Sr_2YSbO_6	Sr_2ErSbO_6	Sr_2TmSbO_6	Sr_2YbSbO_6
Sr (4*e*)	x	0.0000	0.0000	0.0000	0.0000	0.0000	0.0000	0.0000	0.0000	0.0000
	y	0.5382(2)	0.5338(2)	0.5340(3)	0.5325(3)	0.5288(4)	0.5270(1)	0.5266(5)	0.5277(4)	0.5263(4)
	z	0.2500	0.2500	0.2500	0.2500	0.2500	0.2500	0.2500	0.2500	0.2500
O1 (4*e*)	x	-0.7123(3)	-0.7131(3)	-0.7152(4)	-0.7130(4)	-0.7152(5)	-0.7183(5)	-0.7159(7)	-0.7181(3)	-0.7148(5)
	y	0.2066(1)	0.2074(3)	0.2095(4)	0.2073(4)	0.2095(5)	0.2126(5)	0.2102(7)	0.2123(3)	0.2091(5)
	z	-0.0414(1)	-0.0384(2)	-0.0374(3)	-0.0345(3)	-0.0333(5)	-0.0360(1)	-0.0317(7)	-0.0316(3)	-0.0293(5)
O2 (4*e*)	x	-0.4171(2)	-0.4231(3)	-0.4251(3)	-0.4309(4)	-0.4332(6)	-0.4279(2)	-0.4364(8)	-0.4366(4)	-0.4412(6)
	y	0.5152(2)	0.5135(8)	0.5135(3)	0.5128(2)	0.5122(3)	0.5114(8)	0.5112(5)	0.5117(2)	0.5111(3)
	z	-0.2528	-0.2528	-0.2528	-0.2528	-0.2528	-0.2528	-0.2528	-0.2528	-0.2528
O3 (4*e*)	x	-0.2066(3)	-0.2074(2)	-0.2095(4)	-0.2073(3)	-0.2095(5)	-0.2126(5)	-0.2102(7)	-0.2123(3)	-0.2091(5)
	y	0.2876(3)	0.2868(1)	0.2847(4)	0.2869(4)	0.2847(5)	0.2816(5)	0.2840(7)	0.2818(3)	0.2851(5)
	z	0.0414(2)	0.0384(4)	0.0374(3)	0.0345(3)	0.0333(5)	0.0360(4)	0.0317(7)	0.0316(3)	0.0293(5)
$B_{iso}(^2)$	M	0.26(1)	0.68(1)	0.28(5)	0.79(3)	0.43(7)	0.42(1)	0.38(8)	0.64(1)	0.43(3)
	Sb	0.30(2)	0.28(2)	0.20(4)	0.47(1)	0.49(1)	0.40(5)	0.30(1)	0.28(5)	0.26(1)
	Sr	0.79(3)	0.86(1)	0.80(2)	1.04(7)	0.65(8)	0.63(1)	0.87(2)	0.72(3)	1.04(8)
	O1, O2, O3	1.10(2)	1.06(3)	0.88(6)	1.23(2)	0.91(2)	0.97(8)	1.10(1)	1.08(1)	1.08(1)
Cell parameters	*a*(Å)	5.8818(1)	5.8573(8)	5.8455(1)	5.8455(8)	5.8231(1)	5.8178(5)	5.8108(1)	5.8029(1)	5.7945(1)
	b(Å)	5.9595(1)	5.9121(8)	5.8971(8)	5.8608(7)	5.8486(1)	5.8436(4)	5.8350(1)	5.8192(8)	5.8074(1)
	c(Å)	8.3645(1)	8.3155(1)	8.2967(1)	8.2583(1)	8.2483(1)	8.2410(8)	8.2303(1)	8.2130(1)	8.1992(1)
	$\beta(^\circ)$	90.28(1)	90.24(1)	90.23(1)	90.19(1)	90.16(1)	90.17(1)	90.16(1)	90.14(1)	90.12(1)
	V($Å^3$)	293.19(1)	287.96(1)	286.00(1)	282.05(1)	280.91(1)	280.17(1)	279.06(1)	277.34(1)	275.94(1)
Modes amplitudes	GM^{4+}	1.42(2)	1.31(5)	1.29(2)	1.20(1)	1.21(8)	1.21(7)	1.15(6)	1.10(1)	1.02(4)
	X^{3+}	1.02(1)	0.97(2)	0.96(1)	0.90(7)	0.87(5)	0.82(4)	0.81(2)	0.80(1)	0.71(2)
	X^{5+}	0.56(4)	0.48(1)	0.45(1)	0.45(4)	0.41(2)	0.38(3)	0.35(1)	0.35(1)	0.29(6)

8.2 High-temperature phase transitions in Sr_2MSbO_6

Hence, to investigate the phase transitions in the Sr_2MSbO_6 compounds at high temperatures, thermal evolution of the structures was studied by laboratory X-ray diffraction measurements at high temperatures. Figure 8.6 shows the thermal evolution, of the scattering intensity for two 2θ intervals in the temperature range from 300 K to 1475 K. The first one from 22° to 26°, corresponding to the monoclinic primitive Bragg peaks (111,-111) and the second one from 84° to 90°, corresponding to the (642) cubic reflection that has been identified as specially sensitive to the structural changes occurring in this kind of materials.

In all these compounds, it can be observed that the diffraction lines get closer to each other and the splitting of the diffraction lines reduces clearly, which means, the distortion of the unit cells gets smaller at about 925 K, 825 K, 800 K, 750 K, 725 K, 675 K, 675 K, 625 K and 500 K in Sr_2MSbO_6, M = Nd, Eu, Gd, Dy, Ho, Y, Er, Tm and Yb, respectively. Moreover, at these temperatures also, the characteristic reflections for the primitive unit cell, hkl with $h+k+l=2n+1$, disappear in the patterns of all compounds. Which means that from room temperature to high temperature, the structures transform from low distorted symmetry, which is in this case the monoclinic symmetry $P2_1/n$, to another structure with higher symmetry and non-primitive cell.

At higher temperatures, at about 1200 K, 1150 K, 1100 K, 975 K, 925 K, 875 K, 875 K, 850 K, and 750 K for Sr_2MSbO_6, M = Nd, Eu, Gd, Dy, Ho, Y, Er, Tm and Yb respectively, the XRPD data show that the splitting of the diffraction lines disappears continuously, this indicates the presence of a second phase transition from the intermediate symmetry to higher one, which is the cubic ($Fm\bar{3}m$).

In the antimony double perovskite family, different symmetries have been reported at room temperature: $P2_1/n$ [137,141,164,165], $I2/m$ [138,139,166,167], $R\bar{3}$ [31], $I4/m$ [44,168–171] and $Fm\bar{3}m$ [31]. The intermediate phase from the lowest observed symmetry $P2_1/n$ to the higher one, cubic $Fm\bar{3}m$, depends on the size difference between the M^{3+} and Sb^{5+} cations. Two sequences for the antimony family were reported: a rhombohedral phase was observed as an intermediate phase with the transition sequence: $P2_1/n$ $(a^-a^-b^+) \rightarrow R\bar{3}$ $(a^-a^-a^-) \rightarrow Fm\bar{3}m$ $(a^0a^0a^0)$ in the case of big sizes differences, and a tetragonal intermediate one was observed as an intermediate phase with the transition sequence: $P2_1/n \rightarrow I2/m \rightarrow I4/m \rightarrow Fm\bar{3}m$ in the case of small sizes differences. As it has been reported in the case of Sr_2ScSbO_6, the transition from $P2_1/n$ to $I2/m$ is a continuous one. We attempted to refine the patterns in the temperature where the second phase transition was observed, in the $I4/m$ space group, trying to get the observed splitting, but the results were not satisfactory. That means the

---

[164] R. Shaheen and J. Bashir. *Solid State Sci.* ,

[165] M. Retuerto et al. *J. Mater. Chem.* ,

[166] E.J. Cussen, J.F. Vente, P.D. Battle, and T.C. Gibb. *J. Mater. Chem.* **7**: 459–463, 1997.

[167] N. Kashima, K. Inoue, T. Wada, and Y. Yamaguchi. *Appl. Phys. A* ,.

[44] T. K. Mandal, V. V. Poltavets, M. Croft, and M. Greenblatt. *J. Solid State Chem.* **181**: 2325–2331, 2008.

[168] M.W. Lufaso et al. *J. Phys-Condens. Mat.* ,

[169] A. Tauber, S.C. Tidow, R.D. Finnegan, and W.D. Wilber. *Physica C* ,.

[170] B. Orayech, A. Faik, and J. M. Igartua. *Paper in process, Sr_2GaSbO_6, Sr_2MnSbO_6* , 2015.

[171] M. Cheah, P. J. Saines, and B. J. Kennedy. *J. Solid State Chem.* ,

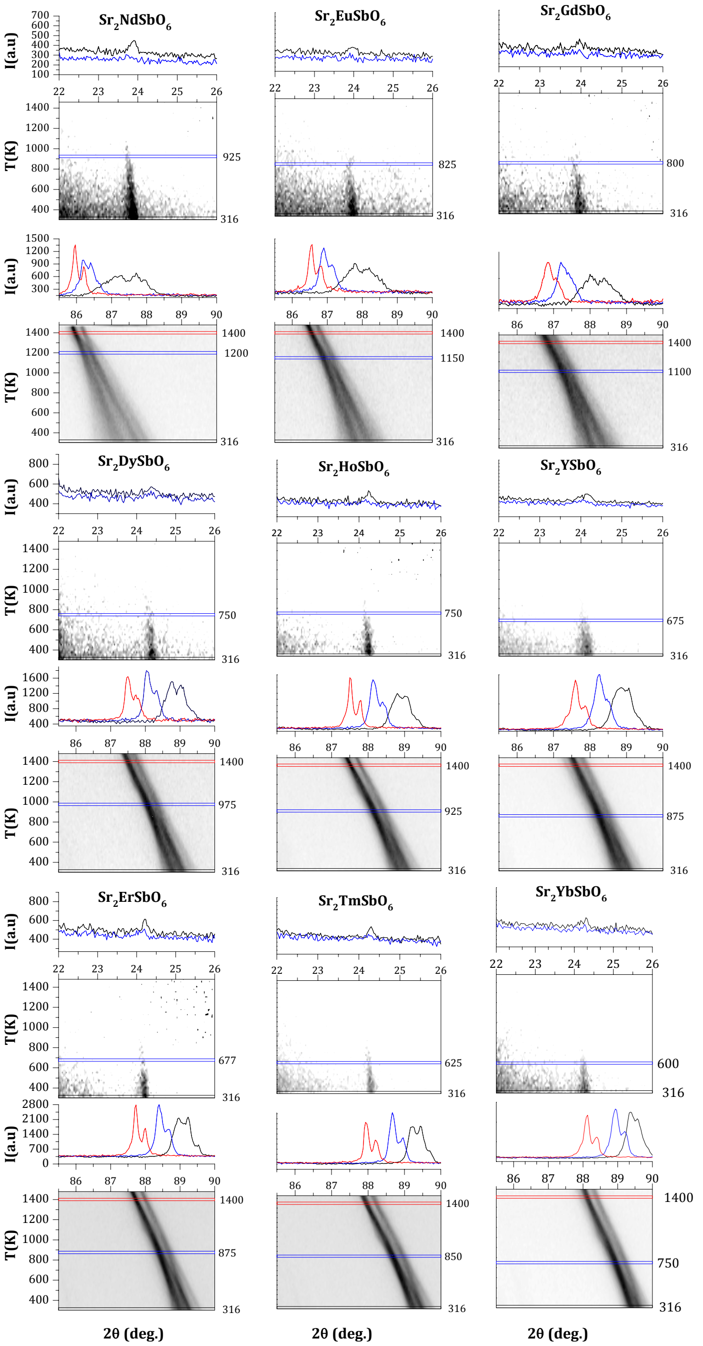

Figure 8.6: Thermal evolution of the 22-26° 2θ interval, corresponding to the monoclinic primitive reflections (-111) and (111) (top) which disappears as temperature increases and the second 2θ interval 85.5-90° (bottom) corresponding to the (642) cubic reflection splits clearly in the trigonal phase obtained from XRPD experiment. The scattered intensity is projected and represented with shades of gray. Black corresponds to high intensity, and white to low intensity. The horizontal lines are a guide to the eye, and mark the temperatures at which the phase transitions in the Sr_2MSbO_6 compounds were observed.

materials did not undergo the phase transition sequence $P2_1/n \rightarrow I2/m \rightarrow I4/m \rightarrow Fm\bar{3}m$, proposed for the Sr_2ScSbO_6.

In our case, the first observed phase transition is a discontinuous one. This is very similar to that observed in Sr_2LaSbO_6 and Sr_2SmSbO_6,[137] where this change was interpreted as an evidence of the materials undergoing a discontinuous phase transition from the room-temperature monoclinic phase ($P2_1/n$ space group), to the trigonal phase $R\bar{3}$. As the attempt to refine the structure after the first phase transition using $I4/m$ failed, we tried to refine the patterns in the $R\bar{3}$. The satisfactory results obtained confirm that the observed discontinues phase transition is $P2_1/n \rightarrow R\bar{3}$.

Since there is no group-subgroup relation between the monoclinic $P2_1/n$ and the trigonal $R\bar{3}$ (see Figure 8.2), this implies two things: First, (a) experimentally the phase transition observed should be of a first order, discontinuous, which is the case. On the other hand, (b) the intermediate trigonal phase $R\bar{3}$, will not be the reference structure of the RT phase. In the symmetry-mode analysis decomposition, the same virtual reference structure is used for the monoclinic and the trigonal (see Table 6.1).

From Table 6.1 and Figure 8.2, the trigonal $R\bar{3}$ phase could be generated from the cubic ($Fm\bar{3}m$) by three irreps which responsible to break the symmetry, those irreps listed in the table are the following: a totally symmetric one $GM_1^+(1)$, the primary one $GM_4^+(1)$ and $GM_5^+(2)$. In the trigonal cell, the GM^{4+} is the unique irrep that involves the movements of all the oxygen atom in the octahedra by displacing the atoms of the *ab* plane. The GM^{5+} has two modes acting on the Sr cations and the oxygens. The first modes of GM^{5+} displaces the Sr cations of the A-site along the *c* axis, while the second one deforms the octahedra along the three axis. AMPLIMODES suggests only one single mode which could break the symmetry (marked in bold): the mono-dimensional GM_4^+. By freeing the amplitudes of the others irreps, very small values of the GM_5^+ were obtained, which forces us to nullify them, which does not affect the amplitudes of the primary irrep GM_4^+.

From the mode analysis point of view, following the theory prediction, the three order parameters GM^{4+}, X^{3+} and X^{5+} irreps actuating in the monoclinic $P2_1/n$ phase, are expected to become zero at higher temperature; from that point of view, as the GM^{4+} mode is larger than X^{3+} and X^{5+}, the last two irreps would arrive closer to zero to the intermediate phase and the GM^{4+} would be the only active in the new phase $R\bar{3}$.

The trigonal distortion of the unit cell disappears in a continuous way and at about 1200 K, 1150 K, 1100 K, 975 K, 925 K, 875 K, 875 K, 850 K and 750 K for Sr_2MSbO_6, M = Nd, Eu, Gd, Dy, Ho, Y, Er, Tm and Yb, respectively. The structural refinements of the patters has confirmed that, at those temperatures, the structures can be described with the $Fm\bar{3}m$ space group. The cells transform from trigonal to cubic. The same transformation was observed in the case of Sr_2LaSbO_6 and Sr_2SmSbO_6,which confirm the same transition sequence $R\bar{3} \rightarrow Fm\bar{3}m$.

The thermal evolution of the mode amplitudes for all the Sr_2MSbO_6 compounds is shown in Figure 8.7. It exhibits the temperature evolution of the amplitudes of GM^{4+}, X^{3+} and X^{5+} (A10 and A11) modes in $P2_1/n$ and GM^{4+} in $R\bar{3}$. The GM_4^+ is present in both space groups; $P2_1/n$ and $R\bar{3}$. Notable is the nearly continuous behavior and the decreases steadily of the GM^{4+} amplitudes value in both, $P2_1/n$ and $R\bar{3}$ symmetries. However, a subtle, but very important, jump was noticed in the GM^{4+} irrep's distortion amplitude through the phase transition. That jump in the amplitude values is due to the change of the direction of the tilt in which it is acting in both space groups, which generate the discontinuous behaviour in the mode amplitudes evolution. The diminishing of the mode amplitudes with temperature, involves the reducing of the rotation of the octahedra and displacement of the cations (Sr), getting more symmetric and close to the prototype.

The variation of the GM^{4+}, in the trigonal symmetry, being well described by the equation $A_{GM_4^-} = A(0)_{GM_4^-}[T_c - T]^\alpha$ where T_c is the transition temperature. The exponent α values are very close to the Landau theory prediction of 0.25 for a tricritical transition .[142,143] This is an indication that the coefficient of the fourth power order parameter in the expression for the Gibbs free energy is negligibly small.

In order to determine the variation of the lattice constants with the temperature in Sr_2MSbO_6 family, cyclic refinements were done using the 48 X-ray powder diffraction profiles obtained at different temperatures between 300K and 1475K, in 2θ range from 15° to 110°. The variation of unit cell parameters and space group symmetries of Sr_2MSbO_6 with temperatures are shown in Figure 8.8. The monoclinic and trigonal parameters have been scaled in order to be comparable with the edge of the centered cubic. In all compounds, the transitions are clearly seen: a discontinuous variation of the parameters indicative of the first order nature of the corresponding transition from monoclinic symmetry $P2_1/n$ to trigonal symmetry $R\bar{3}$, and at higher temperatures, a continuous variation of parameters is clearly observed which indicates the second order nature of the corresponding transition form $R\bar{3}$ to $Fm\bar{3}m$.

Thus, the structural analysis of Sr_2MSbO_6 family has shown two phase transitions at high temperatures, the first one being discontinuous and the second one continuous as the following phase transition sequence: $P2_1/n \rightarrow R\bar{3} \rightarrow Fm\bar{3}m$. This double phase transition sequence, from primitive monoclinic $P2_1/n$ at room temperature to cubic symmetry $Fm\bar{3}m$ at high temperature with a trigonal intermediate phase has been reported only for Sr_2LaSbO_6 and Sr_2SmSbO_6 [137] and La_2CoMnO_6.

---

[142] Brendan J. Kennedy, Christopher J. Howard, and Bryan C. Chakoumakos. *Phys. Rev. B* **59**: 4023–4027, 1999.

[143] E. K. H. Salje. *Phase Transitions in Ferroelastic and Co-elastic Crystals*. The Pitt Building, Trumpington Street, Cambridge CB2 1RP: Cambridge Topics in Mineral Physics and Chemistry Vol. 1, ed., Cambridge University Press, 1990.

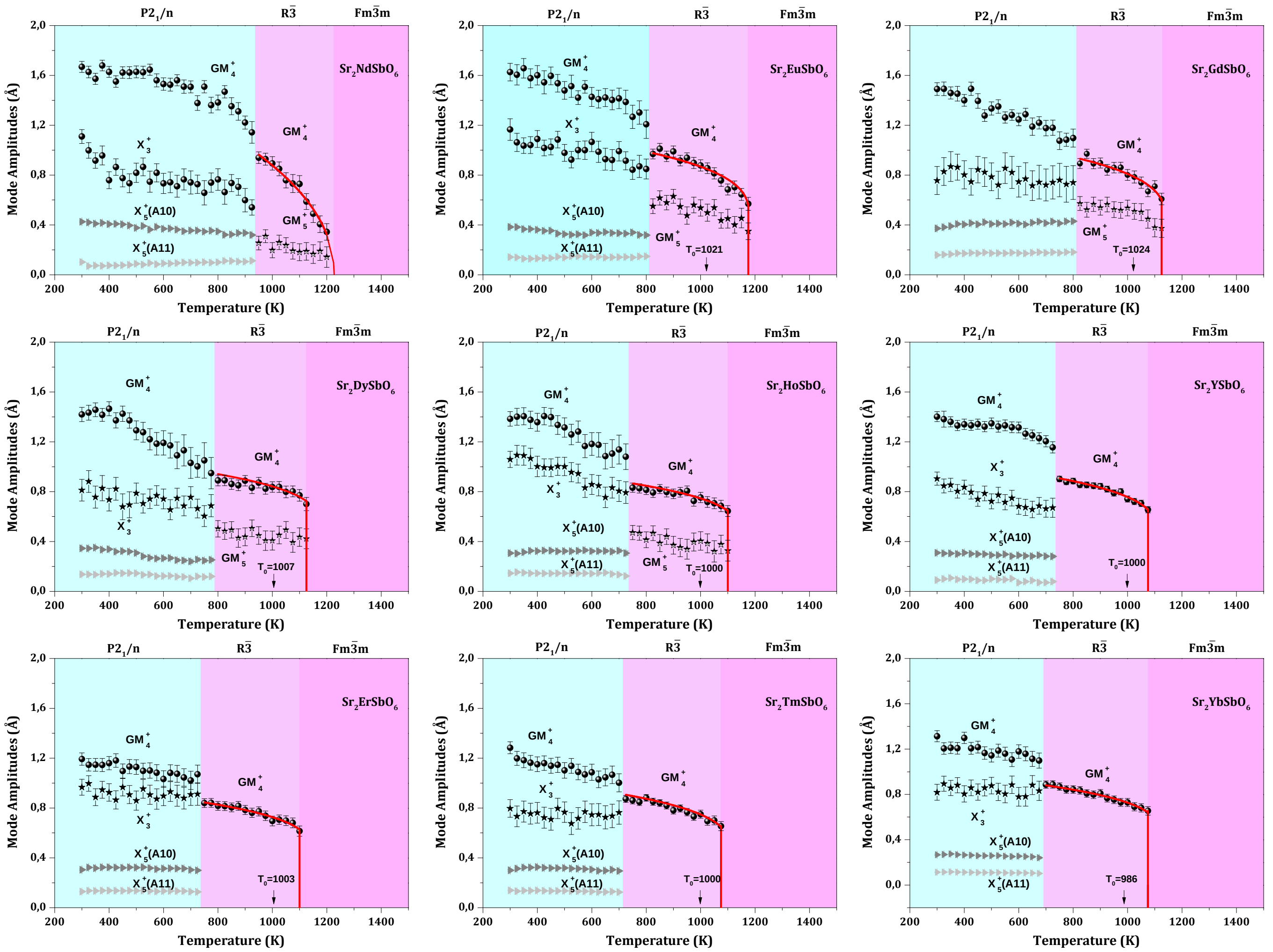

Figure 8.7: Temperature evolution of the amplitudes of some of the symmetry adapted modes in $P2_1/n$ and $R\bar{3}$, as obtained from the XRPD data refinements for (top) Sr$_2$NdSbO$_6$ and Sr$_2$YSbO$_6$ (bottom) . GM$_4^+$, X$_3^+$, X$_5^+$ and GM$_4^+$, GM$_5^+$ are the freed modes in the refinements for the $P2_1/n$ and $R\bar{3}$ respectively. The amplitudes of the irreps in the high symmetry phase, $R\bar{3}$, have been scaled (multiplied by 3/2) to see the evolution, since the program AMPLIMODES uses mode normalization within the corresponding primitive unit cell and the obtained values were fitted with the equation $A_{GM_4^-} = A(0)_{GM_4^-}[T_c - T]^{\alpha}$ with $A(0)_{GM_4^-}$ = 0.62(5), T_c = 1225 K and α=0.20(8) for Sr$_2$NdSbO$_6$ and $A(0)_{GM_4^-}$ = 0.46(1), T_c = 875 K and α=0.22(4) for Sr$_2$YSbO$_6$.

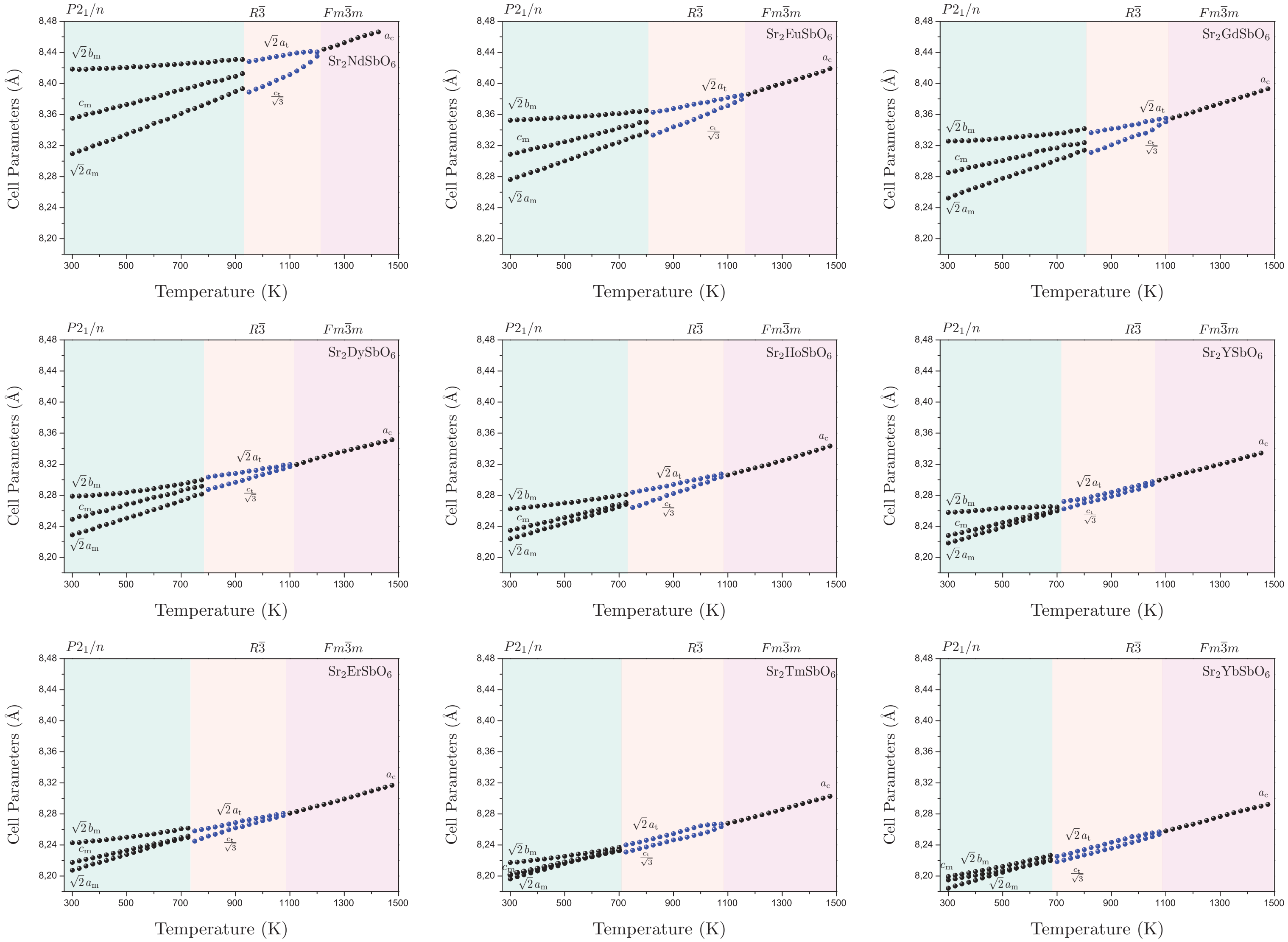

Figure 8.8: Temperature evolution of the lattice parameters of Sr$_2$MSbO$_6$. The cell parameters of the trigonal phase are shown in the hexagonal notation. The monoclinic and hexagonal parameters have been scaled to be comparable with the edge of the centered cubic. The Sr$_2$MSbO$_6$ materials undergo two phase transitions: a first-order one, discontinuous, transforming the cell from a monoclinic to a trigonal and a second one of the second-order from a triginal to a cubic cell. The phase-transition sequence is the following: $P2_1/n \rightarrow\ R\bar{3} \rightarrow\ Fm\bar{3}m$.

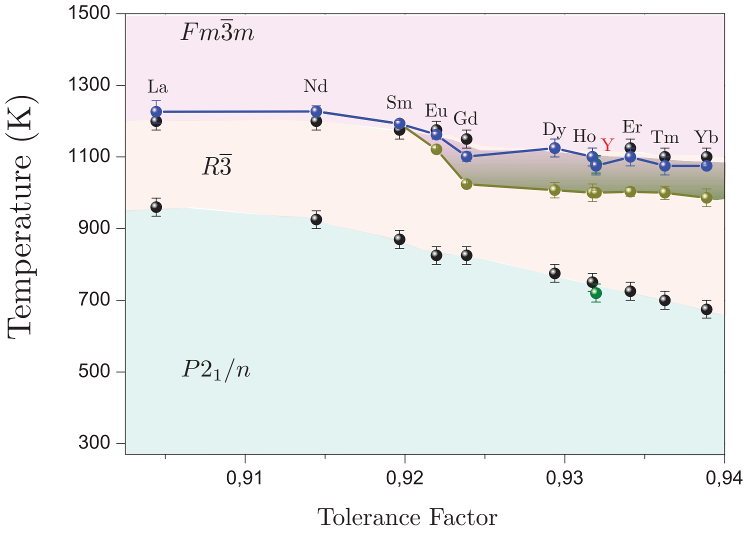

Figure 8.9: Phase diagram (phase transition temperatures versus tolerance factors) for the Sr_2MSbO_6 (M=Ln, Y) compounds

The phase diagram (phase transition temperatures versus tolerance factors) for several Sr_2MSbO_6 compounds is presented in Figure 8.9. From this figure it can be seen that there is a sole phase transition sequence possible for all the series of the lanthanide cations: $P2_1/n \rightarrow R\bar{3} \rightarrow Fm\bar{3}m$. In the same phase-diagram, the materials Sr_2LaSbO_6 (which has the biggest ionic radii) and Sr_2SmSbO_6 reported by Faik *et al.* to undergo the same phase-transition sequence with a trigonal intermediate phase. On the other hand, the non-lanthanide Y^{3+} cation, which has a close tolerance factor to the Ho^{3+}, shows the same phase-transition sequence among the lanthanides.

Figure 8.9 also shows a common trend among all the included compounds. The materials with more distorted structures at RT (larger amplitudes of the distortion modes, La in this case) show higher transition temperatures.

Three sets of points are shown in the case of the second phase-transition (Trigonal to Cubic): The black circles correspond to the experimentally observed transition temperature, based on the refinements and on the data projections. The blue and the olive points are the theoretically calculated values based on the equations used for the high mode amplitudes fitting (Figure 8.7).

8.3 Conclusions

- The crystal structures at room temperature of Sr_2MSbO_6 (M= Ln, Y and In) compounds are described in the $P2_1/n$ space group (No. 14, non-standard setting).

- The Sr_2MSbO_6 compounds show a complete B- and B'-site cation ordering.

- A general trend is observed for all compounds in the transition temperatures: smaller the distortion mode amplitudes (more symmetric the structure), smaller is the transition temperature.

- The phase-diagram shows the existence of two phase-transition sequences, $P2_1/n \rightarrow R\bar{3} \rightarrow Fm\bar{3}m$ and $P2_1/n \rightarrow I2/m \rightarrow I4/m \rightarrow Fm\bar{3}m$.

- The materials Sr_2HoSbO_6 and Sr_2ErSbO_6, which have the same tolerance factor, show the same behaviour at RT and HT, in terms of the mode amplitudes and the transition temperatures.

- The non-lanthanide Sr_2YSbO_6 follow also the trend shown by Ho and Er, which confirm that the origin of the phase-transitions is purely steric.

Introduction to $Sr_2M_{1-x}M'_xTeO_6$ Tellurium Family

The study of cobalt containing double perovskites with the formula $A_2CoB'O_6$ has gained interest in recent years. $Ba_2CoMo_{0.5}Nb_{0.5}O_{6-\delta}$, with mixed Co^{2+}/Co^{3+} oxidation state, for example, was proposed as a potential Solid Oxide Fuel Cells (SOFC) cathode ,[172] whereas $La_{2-x}Sr_xCoTiO_6$ oxides, have shown promising results both as cathode and anode electrodes for SOFCs .[173] The oxides with the formula A_2CoTeO_6 (A = Sr, Pb, Ca, Ba and Cd) have shown, on the other hand, that their magnetic behavior do not follow the one observed in similar compounds with B′ cations different than Te^{6+} .[174,175] The later compounds show interesting structural changes when A-site cation is changed (from conventional perovskite phases if A is small to hexagonal modifications when it is very large as in the case of Ba^{2+} ions [176]) and also when temperature is changed (if A = Sr[175,177] or Pb,[178] so far). The latter compounds, despite the differences in their structure, always show antiferromagnetic behavior due to the super-exchange interactions between Co^{2+} ions.

The Sr_2NiTeO_6 oxide has been of great interest in the scientific community since the 40′s. The first studies focused on its properties, such as ceramic pigment [179] or dielectric material for capacitors .[180] The first structural study was done by P. Köhl and co-workers .[181] According to them, the symmetry of the crystal is $C2/m$ and its cell parameters are: a=7.91 Å, b=7.91 Å, c=7.87 Å and β= 90.2°. More precise parameters were provide by D. Iwanaga *et al.* in a more recent work: a=7.9174(4) Å, b=7.8765(4) Å, c=7.916(1) Å and β = 90.378(1)°. The later work suggested that the NiO_6 and TeO_6 octahedra are rotated, out of phase, around one of the three axes of the primitive perovskite. However, all theoretical and experimental studies done up to now show that symmetry of the crystal structure

---

[172] Z.Q. Deng et al. *Chem. Mater.* **21**: 5154–5162, 2009.

[173] A. Gómez-Pérez et al. *J. Power Sources* **227**: 309 –317, 2013.

[174] R. Mathieu, S. A. Ivanov, R. Tellgren, and P. Nordblad. *Phys. Rev. B* **83**: 174420, 2011.

[175] M. S. Augsburger et al. *J. Mater. Chem.* **15**: 993–1001, 2005.

[176] S. A. Ivanov et al. *Dalton T.* **39**: 5490–5499, 2010.

[177] L. Ortega-San Martín et al. *J. Mater. Chem.* **15**: 183–193, 2005.

[178] S. A. Ivanov et al. *Dalton T.* **39**: 11136–11148, 2010.

[179] W. D. J. Evans. *Brit. Ceram. Trans. J.* **67**: 397–419, 1968.

[180] Yu. N. Venevtsev, E. D. Politova, and G. S. Zhdanov. *Ferroelectrics* **8**: 489–490, 1974.

[181] P. Köhl, E. Schultze-Rhonhof, and D. Reinen. *Z. Anorg. Allg. Chem.* **378**: 129–143, 1970.

resulting from this rotation system corresponds to the tetragonal space group $I4/m$, with cell parameters $a = b \approx \sqrt{2}a_p$, and $c \approx 2a_p$. The structural analysis of this compositions has been done carefully and paying special attention to previous inconsistencies as for example the rotations of the octahedra and the space group. Based on electron diffraction measurements, another structural model of the Sr_2NiTeO_6, where the monoclinic space group, with non-standard setting, $I12/m1$ was reported .[182]

On the other hand the Sr_2MgTeO_6 has been reported to have tetragonal structure with the space group $I4/m$. These findings were confirmed with X-ray diffraction, Raman and Infrared spectroscopic investigations .[183] In a more recent work the structure of the later material has been re-examined by means of X-ray diffraction, it has been shown that the structure appears like a pseudo-tetragonal phase, but the structure which describes it best is monoclinic with the space group $I2/m$.[184]

The previous part was devoted to the antimony family A_2MSbO_6 (A= Sr and Ca). After having studied that family, we move to the tellurium one, with the formula Sr_2MSbO_6, this family shows a large difference between the B-site cations in terms of size and oxidation state (+2, +6). As has been shown previous studies reported on the tungsten family, this difference has a crucial role on the ordering of the cations over the B-site; now of our objectives is to analysis that point for the studied materials of this tellurium family. Others reasons to study this system, is that there are few materials pertaining to this family that has been synthesized and analyzed structurally, both at room temperature and low- and high-temperatures. It is worth noting that the tellurium family is a good candidate to elucidate how the change of the system,from (3+, 5+) to (2+, 6+), could changes to characteristics of the phase-diagram, which are mainly three: the phase transition sequence existing for the whole family, the change of the RT symmetry as the tolerance factor increases and the stability of the intermediate phases itself with the tolerance factor increasing.

The aim of the chapter dedicated to $Sr_2Co_{1-x}Mg_xTeO_6$ is twofold: first, a complete structural study and of the phase transitions in some compositions using mode-crystallography ,[99,136,139,140] is reported with a revisiting of the previously reported pure Co-material. the second target consist of determining the magnetic structure of $Sr_2Co_{0.9}Mg_{0.1}TeO_6$, and a full revision of the that of the parent phase Sr_2CoTeO_6, which has been made by the use of the full symmetry of the materials, as deduced from the diffraction experiments and from the magnetic properties.

The chapter presents a complete analysis on the $Sr_2Ni_{1-x}Mg_xTeO_6$ perovskite oxides, where magnetic and structural data are presented. Data on the room-temperature structure published before for the parent compound ($x = 0$) [182] are reviewed using mode-crystallography .[99,136,139,140] The change in the perovskite structure with x and with temperature in all cases is proposed for the first time. Magnetic data are evaluated in accordance with the structural results.

---

[182] L. Ortega-San Martín et al. *Z. Anorg. Allg. Chem.* **631**: 2127–2130, 2005.

[183] Rick Ubic et al. *Chem. Mater.* **22**: 4572–4578, 2010.

[184] R. Ubic, S. Letourneau, and S. Thomas. *J. Aus. Ceram. Soc* **47**: 49, 2011.

[99] A. Faik, J. M. Igartua, M. Gateshki, and G. J. Cuello. *J. Solid State Chem.* **182**: 1717–1725, 2009.

Chapter 9

Structural phase transitions, Magnetic and Spectroscopic properties of the double perovskites $Sr_2Co_{1-x}Mg_xTeO_6$ (x=0.1, 0.2 and 0.5)

9.1 Room-temperature crystal-structures

The room-temperature crystal structures of the polycrystalline samples of $Sr_2Co_{1-x}Mg_xTeO_6$ have been analyzed by the use of X-ray powder diffraction (XRPD), for all the compositions, and by the use of high resolution neutron powder diffraction (NPD) for one of them: $x = 0.1$.

Due to the high degree of pseudo-symmetry observed in double perovskites, the symmetry assignment was done observing the small reflections and the split ones ,[151] that result from the distortion of the ideal prototype of cubic symmetry: $Fm\overline{3}m$ (No. 225, ITA) .[144] $Sr_2Co_{0.9}Mg_{0.1}TeO_6$ was analyzed following the same protocol as with the parent phase ($x = 1$). All the observed reflections in the pattern of $Sr_2Co_{0.9}Mg_{0.1}TeO_6$ could be indexed in a cell with parameters $a \approx \sqrt{2}\,a_p$, $b \approx \sqrt{2}\,a_p$ and $c \approx 2\,a_p$.

The splitting of the cubic reflection $(444)_c$, Figure 9.1, is very important to assign the symmetry, it was analyzed considering it as being the triplet (404), (-404) and (044), which indicates that $a \neq b$ and $\beta \neq 90°$. This fact, together with the presence of the mentioned reflections, can be explained by a primitive cell and a monoclinic distortion, so the usual

---

[151] C. J. Howard and H. T. Stokes. *Acta Crystallogr. B* **54**: 782–789, 1998.

[144] Th. Hahn. *International Tables for Crystallography Volume A: Space-group symmetry*. The International Union of Crystallography and Kluwer Academic Publishers: Dordrecht, Holland., 1992.

monoclinic space group was assigned to the RT crystal structure: $P2_1/n$ ($P1\,2_1/n\,1$, non-standard setting of the $P2_1/c$, No.14 space group) .[144]

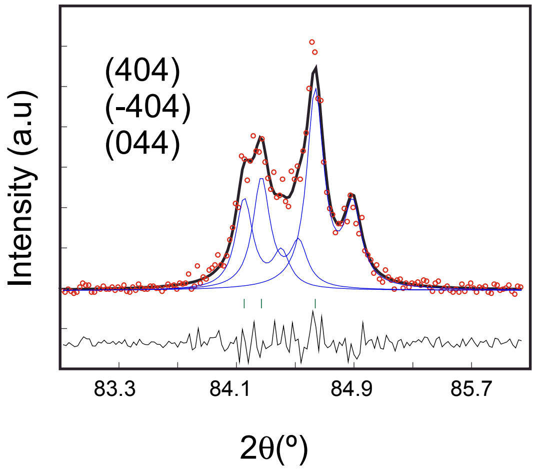

Figure 9.1: Splitting of the singlet cubic reflection $(444)_c$ into a triplet: (404), (-404) and (044) reflections. The plot shows a fit with three reflections.

Figure 9.2a shows that the [(311)(-311),(131)(-131)] primitive doublet reflection, disappears for $x = 0.2$. (For completeness, we are also showing the $x = 0, 0.1, 0.2, 0.5$ and 1 compositions in this figure.) The two compositions $Sr_2Co_{1-x}Mg_xTeO_6$ with $x \geq 0.2$ analyzed in the present work, could be indexed in an I centered cell, with the same metrics, and with a splitting scheme compatible with a monoclinic symmetry, so we assigned the monoclinic $I2/m$ ($I1\,2/m\,1$ non-standard setting of $I2/c$, No.12 ITA) to the RT structures of those compositions. However, a new transformation can be suspected with the increase of x, as observed by the decrease of the splitting in some reflections (Figure 9.2b and 9.2c).

In a recent report ,[183] the authors show evidences proving that the RT space group of Sr_2MgTeO_6 is $I4/m$. We have also measured that composition and, in our case also, the high degree of pseudo-symmetry and the fact that we only have laboratory XRPD data, have forced us to assign the tetragonal space group. In conclusion, in the progressive diminution of the monoclinic distortion, as the Mg doping increases, there should be an intermediate composition, $x > 0.5$, for which the monoclinic distortion disappears.

Rietveld refinement [54] of the crystal structures was performed using the program AMPLIMODES for FullProf ,[59] part of the Bilbao Crystallographic Server ,[62,63] and the WinPlotr/FullProf package .[55] The peak shape was described by a pseudo-Voigt function, and the background level was modeled using a polynomial function. The refined parameters were: scale factor, zero shift, lattice constants, peak profile, asymmetry parameters, ampli-

---

[183] Rick Ubic et al. *Chem. Mater.* **22**: 4572–4578, 2010.

[54] H. M. Rietveld. *J. App. Crystallogr.* **2**: 65–71, 1969.

[59] D. Orobengoa, C. Capillas, M. I. Aroyo, and J. M. Perez-Mato. *J. App. Crystallogr.* **42**: 820–833, 2009.

[62] M. I. Aroyo et al. *Z. Kristallogr.* **221**: 15–27, 2006.

[63] M. I. Aroyo et al. *Acta Crystallogr. A* **62**: 115–128, 2006.

[55] J. Rodríguez-Carvajal. *Physica B* **192**: 55–69, 1993.

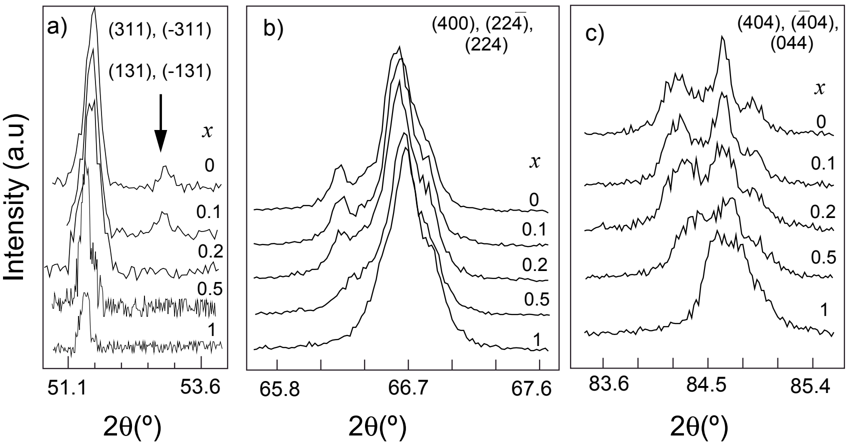

Figure 9.2: Selected 2θ intervals for the four compositions of the $Sr_2Co_{1-x}Mg_xTeO_6$ series. a) Vanishment of the reflection that violates the I-centering condition on the *hkl*. b-c) Change of the cubic reflection splitting with the increase of the magnesium content.

tudes of the modes transforming according to the irreducible representations (irreps) and independent isotropic atomic displacement parameters. The high contrast between the Co and Te cations in the simultaneous refinements of the X-ray and neutron data, allowed us to free their fractions: no disorder was found. Oxygen fractions were also freed, but the obtained values were so close to unity that they were fixed to 1.

The initial structural information needed for the symmetry-adapted mode analysis with AMPLIMODES [40,59,99,185–187] is: the reference structure, high symmetry phase (the prototype cubic phase for the ordered double perovskites, space group $Fm\bar{3}m$: atomic positions and cell-parameters); the RT phase's cell-parameters and space group ($P2_1/n$, for ($x = 0.0, 0.1$) compositions, and $I2/m$, for ($x = 0.2, 0.5$)); finally, the transformation matrix between both cells: the reference and the RT cell .[185,186] A complete description of the procedure is given in .[186] For completeness of the refinements, we are including the $x = 0.0$ composition in all the calculations.

For the symmetry-mode analysis AMPLIMODES performs, it is not necessary to know a real prototype structure. The contributions of the much more important symmetry-breaking distortion-modes present in the distorted phase do not depend on any choice of the atomic coordinates of the prototype structure. To our knowledge, by the time of writing this report, there is no experimentally known cubic symmetry structure for these compounds. Hence, and for the sake of simplicity on the comparisons, we have adopted the same virtual high temperature high symmetry structure for all the compositions in this report, and in future reports related to the same families. We expect to find that parent structure at high-temperatures, if no decomposition of the material takes place. AMPLIMODES obtains

---

[40] A. Faik, D. Orobengoa, E. Iturbe-Zabalo, and J. M. Igartua. *J. Solid State Chem.* **192**: 273–283, 2012.

[99] A. Faik, J. M. Igartua, M. Gateshki, and G. J. Cuello. *J. Solid State Chem.* **182**: 1717–1725, 2009.

[185] E. Iturbe-Zabalo et al. *J. Phys-Condens. Mat.* **25**: 205401, 2013.

[186] E. Iturbe-Zabalo et al. *J. Solid State Chem.* **198**: 24–38, 2013.

[187] R. B. Macquart, B. J. Kennedy, and M. Avdeev. *J. Solid State Chem.* **183**: 2400–2405, 2010.

a complete basis of symmetry-adapted distortion modes and decomposes the distortion in terms of this basis of symmetry modes, and calculates the amplitudes for each of the symmetry adapted distortions. Modes are given in terms of atomic displacements in relative units for the atoms of the asymmetric unit of the distorted phase. The results of AMPLIMODES are show in Table 9.1.

In the case of the RT monoclinic space group $P2_1/n$, there are seven irreducible representations (irreps) of the $Fm\bar{3}m$ space group, that can take part in the symmetry breaking, and these are, as shown in Table 9.1: $GM_1^+(1)$ (totally symmetric), $GM_3^+(1)$, $GM_4^+(1)$, $GM_5^+(4)$, $X_2^+(1)$, $X_3^+(1)$ and $X_5^+(3)$. The theoretical predictions (and the Rietveld refinement of the mode amplitudes, see below) suggest that there is more than one active mode responsible for the $Fm\bar{3}m \rightarrow P2_1/n$ symmetry break: $P2_1/n$ phase cannot be generated by a single mechanism, or a single unstable mode of the cubic configuration. At least two modes must be present. These two active modes responsible for the stabilization of the $P2_1/n$ phase in double perovskites are known to be transforming according to the GM_4^+ and X_3^+ irreps .[40,186] On the other hand, there are five irreps of the $Fm\bar{3}m$ space group that can take part in the symmetry breaking from that space group to the room-temperature $I2/m$ monoclinic space group: GM_1^+, $GM_3^+(1)$, $GM_4^+(1)$ and $GM_5^+(2)$, twice.

It is worth noting that the output for the $Fm\bar{3}m \rightarrow I2/m$ symmetry braking is contained in the $Fm\bar{3}m \rightarrow P2_1/n$ symmetry breaking. Nevertheless, for the former, as there are two irreps, i.e. GM_4^+ and GM_5^+, that break the symmetry down to $I2/m$, there are two possible primary order parameters. The final refinement results for the amplitude values of the modes involved in this symmetry break, (see Figure 5 in .[40]), indicate that, from the possible two primary order parameters, there is only one, GM_4^+, whose amplitude is at least one order of magnitude greater than the rest of the amplitudes. The polarization vector associated with GM_4^+, going down to $P2_1/n$ or going down just to $I2/m$ is the same, and it involves all the oxygen atoms in the monoclinic phases (three distinct in $P2_1/n$, and two distinct in $I2/m$). GM_4^+ is essentially a rotation of the octahedra around the *b* axis in the monoclinic cell; although it also slightly distorts the octahedra: the amount of rotation of the oxygens in the *ab* plane, (≈0.25, ≈0.25, ≈0) set of coordinates, and the one above and perpendicular to that plane, (≈0, ≈0, ≈0.25) set of coordinates, are not the same.

Theory also states that those modes that experimentally should break the symmetry down to the RT observed phase, should be the ones with the highest amplitudes. This is also observed experimentally as shown in Table 9.2: there are three global mode-amplitudes (GM_4^+, X_3^+ and X_5^+ irreps) that are higher than the rest. The necessary ones to break the symmetry are GM_4^+ and X_3^+, as those are the ones that have the RT monoclinic space group as the maximum subgroup.

Indeed, in the case of the primitive monoclinic RT space group symmetry $P2_1/n$, all modes, except GM_4^+ and X_3^+, do appear as degrees of freedom due to the symmetry break. In the case of $I2/m$ RT space group, the modes allowed by symmetry (but not breaking) are all except GM_4^+. For symmetry considerations, and referring to displacive phase-transitions, they represent allowed atomic displacements giving rise to configurations of higher symmetry than that of the low-symmetry space group and compatible with the parent space group of higher symmetry. The space groups of these (*intermediate*)

Table 9.1: Input information for AMPLIMODES for FullProf: high-symmetry phase information (prototype structure), low-symmetry structure information and transformation matrix for $Sr_2Co_{1-x}Mg_xTeO_6$. $P2_1/n$ (ITA No.14, non-standard setting), $I2/m$ (ITA No.12, non-standard setting), $I4/m$ (ITA No.87, standard setting) and $Fm\bar{3}m$ (ITA No.225, standard setting). The second part shows a list of the irreps taking part in the symmetry breaking from the cubic space group ($Fm\bar{3}m$) to the monoclinic $P2_1/n$ and $I2/m$ space groups observed experimentally at RT, and to the tetragonal space group $I4/m$, observed as intermediate high-temperature space group. The list is part of the output of AMPLIMODES for FullProf. The number in parenthesis indicate the number of modes transforming according to the irrep. The irreps in bold are the ones representing the order parameters: 2 in the $P2_1/n$ and one in the $I2/m$ space groups, respectively (see text)

High-symmetry structure
225
7.9209 7.9209 7.9209 90.00 90.00 90.00
4

Te	1	4a	0.00000	0.00000	0.00000
M	1	4b	0.50000	0.50000	0.50000
Sr	1	8c	0.25000	0.25000	0.25000
O	1	24e	0.24714	0.00000	0.00000

Low-symmetry cell	**Low-symmetry cell**	**Low-symmetry cell**
014	012	087
5.5569 5.5932 7.8647 90.00 90.013 90.00	5.5574 5.5782 7.8506 90.00 90.06 90.00	5.6009 5.6009 7.9209 90.00 90.01 90.00
Transformation matrix	**Transformation matrix**	**Transformation matrix**

$$\left(\begin{array}{ccc|c} 1/2 & 1/2 & 0 & 0 \\ -1/2 & 1/2 & 0 & 0 \\ 0 & 0 & 1 & 0 \end{array}\right) \qquad \left(\begin{array}{ccc|c} 1/2 & 1/2 & 0 & 0 \\ -1/2 & 1/2 & 0 & 0 \\ 0 & 0 & 1 & 0 \end{array}\right) \qquad \left(\begin{array}{ccc|c} 1/2 & 1/2 & 0 & 0 \\ -1/2 & 1/2 & 0 & 0 \\ 0 & 0 & 1 & 0 \end{array}\right)$$

Atoms	**WP**	**Modes**
$Fm\bar{3}m \rightarrow P2_1/n$		
O1	24e	GM_1^+(1) GM_3^+(1) **GM_4^+(1)** GM_5^+(2) X_2^+(1) **X_3^+(1)** X^{5+}(2)
Sr1	8c	GM_5^+(2) X_5^+(1)
$Fm\bar{3}m \rightarrow I2/m$		
O1	24e	GM_1^+(1) GM_3^+(1) **GM_4^+(1)** GM_5^+(2)
Sr1	8c	GM^{5+}(2)
$Fm\bar{3}m \rightarrow I4/m$		
O1	24e	GM_1^+(1) GM_3^+(1) **GM_4^+(1)**

Table 9.2: Amplitudes of the modes (in Å) of the irreps taking part in the symmetry breaking from $Fm\bar{3}m$ space group to the monoclinic space groups $P2_1/n$ and $I2/m$ for $Sr_2Co_{1-x}Mg_xTeO_6$ ($x = 0.0, 0.1, 0.2, 0.5$) compounds at room-temperature after the refinement of (a) all modes and (b) only the effectively acting mode-amplitudes.

Irrep	Amplitude							
	Sr_2CoTeO_6		$Sr_2Co_{0.9}Mg_{0.1}TeO_6$		$Sr_2Co_{0.8}Mg_{0.2}TeO_6$		$Sr_2Co_{0.5}Mg_{0.5}TeO_6$	
	$P2_1/n$-NPD		$P2_1/n$-NPD		$I2/m$-XRPD		$I2/m$-XRPD	
	(a)	(b)	(a)	(b)	(a)	(b)	(a)	(b)
GM_1^+	0.1825(4)	0.1840(1)	0.1833(4)	0.1881(4)	0.0622(3)	0.0000	0.1102(3)	0.0000
GM_3^+	0.0173(2)	0.0000	0.0007(1)	0.0000	0.0943(1)	0.0000	0.0075(6)	0.0000
GM_4^+	0.7941(1)	0.7964(5)	0.7770(1)	0.7814(2)	0.5741(3)	0.6742(3)	0.6174(6)	0.6680(6)
GM_5^+	0.0230(1)	0.0000	0.0630(1)	0.0000	0.0765(5)	0.0000	0.0866(5)	0.0000
X_2^+	0.0074(5)	0.0000	0.0165(5)	0.0000				
X_3^+	0.2680(1)	0.2648(6)	0.1737(5)	0.1863(2)				
X_5^+	0.0032(2)	0.0037(1)	0.0469(5)	0.0263(4)				

configurations are the isotropy space groups. These compatible displacements are described by the amplitudes of the modes associated to the rest of the irreps: GM_3^+, GM_5^+ and X_2^+, in the primitive space group; and GM_3^+ and GM_5^+, in the centered space group. Those amplitudes can have big (always smaller than the symmetry breaking ones) or small values. Indeed, if they have small values they can be fixed to zero without affecting the results and improve the efficiency of the refinement due to the use of less degrees of freedom.

Table 9.2 shows the final amplitude values, at RT, of the two different refinements performed on all the compositions, included the pure Co. In the first refinement we freed all the mode amplitudes and in the second one, only those fulfilling the above criteria: GM_4^+, X_3^+ and X_5^+ in $P2_1/n$ and GM_4^+, for $I2/m$. The resulting neutron powder diffraction (NPD) and X-ray diffraction (XRPD) patterns from the refinements of the four compounds at RT are shown in Figure 9.3. Tables 9.3 and 9.4 show, respectively, the structures and the distances, resulting form the mentioned two different refinements. The general conclusion regarding the set of amplitudes and the set of structures is the same: there is no appreciable difference between the model with all the freedom or with a (symmetry-guided-) restricted freedom. The fixed amplitudes left the atomic displacements related to the corresponding modes without effect, which indicates that the distortion with respect to the cubic prototype phase they represent is not effectively present. Hence, some atomic coordinates in the RT distorted structure do not differ from those in the prototype cubic. This is the case, for instance, of the Sr cation, located in the 8c Wyckoff position (0.25 0.25 0.25) in the cubic prototype, which is (0.0 0.50 0.25) described in the $P2_1/n$ cell: it moves to (0.0 0.4976 0.25). Only its y-coordinate has changed in the refinement.

Figure 9.4a shows the mode-amplitudes versus the tolerance factor value (t). It is worth noting that the interval for the calculated (t) values is actually very small, 2.5×10^{-3}. Nevertheless, as expected from the previous analysis, there are two regions for the values of the GM_4^+ amplitude, corresponding to the two monoclinic space groups: the primitive and the centered. The $x = 0.0, 0.1$ compositions show the same value, and the $x = 0.2, 0.5$ compositions occur the same: both materials show the same distortion and both values

Table 9.3: Crystal structure data and refinement results for $Sr_2Co_{1-x}Mg_xTeO_6$ (x=0.0, 0.1, 0.2 and 0.5) from NPD at room-temperature after the refinement of (a) all modes and (b) only the effectively acting mode. Co/Mg (2b (0,0,1/2)), Te (2a (0,0,0))

		Sr_2CoTeO_6		$Sr_2Co_{0.9}Mg_{0.1}TeO_6$		$Sr_2Co_{0.8}Mg_{0.2}TeO_6$		$Sr_2Co_{0.5}Mg_{0.5}TeO_6$	
		$P2_1/n$-NPD		$P2_1/n$-NPD		$I2/m$-XRPD		$I2/m$-XRPD	
		(a)	(b)	(a)	(b)	(a)	(b)	(a)	(b)
t		0.9758		0.9763		0.9769		0.9787	
Sr	x	-0.0003(4)	0.0000	-0.0015(4)	0.0000	0.001(3)	0.0000	0.006(5)	0.00000
	y	0.5003(1)	0.5003(1)	0.4970(1)	0.4976(1)	1/2	1/2	1/2	1/2
	z	0.2492(7)	0.2500	0.2521(1)	0.2500	-0.7533(7)	-0.75000	-0.7553(12)	-0.75000
	B_{iso}(Å^2)	1.02(3)	1.03(3)	1.03(2)	1.07(2)	0.94(2)	0.94(2)	0.97(3)	0.97(3)
O1	x	-0.7460(7)	-0.7477(3)	-0.7721(1)	-0.7680(3)	0.223(4)	0.24714	0.235(6)	0.24714
	y	0.2285(7)	0.2286(3)	0.2536(1)	0.2486(3)	0.271(4)	0.24714	0.271(6)	0.24714
	z	-0.0238(1)	-0.0251(1)	-0.0271(1)	-0.0247(1)	-0.023(4)	-0.0301(1)	-0.017(7)	-0.0300(2)
	B_{iso}(Å^2)	1.06(1)	1.06(3)	1.32(1)	1.32(1)	1.06	1.06	1.06	1.06
O2	x	-0.4503(3)	-0.4497(2)	-0.4533(4)	-0.4533(2)	0.057(7)	0.060(2)	0.075(1)	0.060(4)
	y	0.5008(1)	0.5008(1)	0.4973(1)	0.4984(2)	0	0.00000	0	0
	z	-0.2604(5)	-0.2595(2)	-0.2596(5)	-0.2597(1)	-0.743(4)	-0.7528	-0.748(6)	-0.75286
	B_{iso}(Å^2)	1.06(1)	1.06(3)	1.32(1)	1.32(1)	1.06	1.06	1.06	1.06
O3	x	-0.2294(7)	-0.2286(3)	-0.2437(1)	-0.2486(3)				
	y	0.2518(7)	0.2523(3)	0.2359(1)	0.2320(3)				
	z	0.0267(1)	0.0251(8)	0.0242(1)	0.0246(1)				
	B_{iso}(Å^2)	1.06(1)	1.06(3)	1.32(2)	1.32(2)				
Te	B_{iso}(Å^2)	0.76(2)	0.77(3)	0.74(3)	0.79(3)	1.62(2)	1.62(2)	1.56(1)	1.56(1)
Co/Mg	B_{iso}(Å^2)	0.76(2)	0.77(3)	0.74(3)	0.79(3)	1.62(2)	1.62(2)	1.56(1)	1.56(1)
a (Å)		5.6434(1)	5.6434(1)	5.6417(1)	5.6417(1)	5.6302(4)	5.6304(3)	5.6230(1)	5.6230(1)
b (Å)		5.6091(1)	5.6091(1)	5.6074(1)	5.6074(1)	5.5986(4)	5.5988(4)	5.5968(1)	5.5968(1)
c (Å)		7.9271(2)	7.9270(2)	7.9213(1)	7.9213(1)	7.9078(5)	7.9078(5)	7.9060(1)	7.9060(1)
β (°)		89.950(4)	89.950(1)	89.952(4)	89.950(4)	89.985(6)	89.985(6)	89.985(1)	89.985(1)
V (Å^3)		250.92(1)	250.92(1)	250.93(1)	250.93(1)	249.28(3)	249.28(2)	248.83(1)	248.83(1)
R_p(%)		4.07	4.08	4.11	4.48	8.5	8.9	7.6	8.02
R_{wp}(%)		5.23	5.25	5.31	5.80	7.5	7.9	6.2	7.1
R_{exp}(%)		1.72	1.72	2.17	1.66	5.66	5.68	4.82	4.83
χ^2		6.25	6.31	5.98	6.06	6.57	6.93	11.3	11.2
R_{Bragg}		4.31	4.97	7.31	4.48	8.90	8.97	4.97	4.54

are almost equal. Hence, we distinguish both distortions, in the symmetry change. Of course, the octahedra tilt-angles in the centered phase are a little bit smaller than those in the primitive.

Regarding the evolution of the cell parameters and volume of the unit cell (Figure 9.4b), it can be said that the relative variation of the cell parameters (%5, for $a - b$, which is the

Table 9.4: Main bond distances (Å) and selected angles (°) for $Sr_2Co_{1-x}Mg_xTeO_6$ (x=0.0, 0.1, 0.2 and 0.5) at room temperature. The values were obtained refining (a) all modes and (b) only the effectively acting mode.

	Sr_2CoTeO_6		$Sr_2Co_{0.9}Mg_{0.1}TeO_6$		$Sr_2Co_{0.8}Mg_{0.2}TeO_6$		$Sr_2Co_{0.5}Mg_{0.5}TeO_6$	
	$P2_1/n$-NPD		$P2_1/n$-NPD		$I2/m$-XRPD		$I2/m$-XRPD	
	(a)	(b)	(a)	(b)	(a)	(b)	(a)	(b)
Co/MgO_6 octahedra								
Co/Mg-O1	2.069(3)×2	2.076(3)×2	2.067(3)×2	2.076(3)×2	2.027(1)×4	2.021(1)×4	2.020(1)×4	2.018(1)×4
Co/Mg-O2	2.083(1)×2	2.077(1)×2	2.073(4)×2	2.075(4)×2	2.030(2)×2	2.027(2)×2	2.029(2)×2	2.029(2)×2
Co/Mg-O3	2.077(3)×2	2.078(3)×2	2.081(3)×2	2.074(3)×2				
Average distance	2.076(1)	2.077(1)	2.074(1)	2.075(1)	2.026(3)	2.023(3)	2.023(6)	2.022(6)
Predicted distance	2.0985	2.0985	2.0985	2.0985	2.0985	2.0985	2.0985	2.0985
TeO_6 octahedra								
Te-O1	1.932(3)×2	1.926(3)×2	1.927(3)×2	1.921(3)×2	1.977(1)×4	1.976(1)×4	1.975(1)×4	1.973(1)×4
Te-O2	1.920(1)×2	1.927(1)×2	1.922(3)×2	1.923(3)×2	1.986(2)×2	1.983(2)×2	1.985(2)×2	1.985(2)×2
Te-O3	1.927(3)×2	1.925(3)×2	1.919(4)×2	1.922(4)×2				
Average distance	1.926(1)	1.926(1)	1.923(1)	1.922(1)	1.981(6)	1.979(6)	1.978(6)	1.977(6)
Predicted distance	1.9170	1.9170	1.9170	1.9170	1.9170	1.9170	1.9170	1.9170
∠O1-Co/Mg-O2	89.9(4)	89.8(2)	89.8(4)	90.0(2)	89.9(1)	89.9(2)	89.9(2)	89.9(2)
∠O1-Co/Mg-O3	89.5(3)	89.1(1)	88.1(3)	89.1(1)	90.1(1)×2	90.1(2)×2	90.0(7)×2	90.0(7)×2
∠O2-Co/Mg-O3	89.8(3)	89.7(2)	89.2(4)	90.0(2)				
∠O1-Te-O2	89.4(4)	89.6(2)	89.8(4)	89.9(2)	89.9(3)	89.9(1)	89.9(4)	89.9(4)
∠O1-Te-O3	88.7(3)	89.1(1)	89.9(4)	89.1(1)	90.2(1)×2	90.2(1)×2	90.1(4)×2	90.1(4)×2
∠O2-Te-O3	89.5(4)	89.9(2)	89.0(4)	89.9(2)				
∠Co/Mg-O1-Te	166.8(2)	167.3(7)	168.6(2)	168.2(1)	165.6(5)	165.4(2)	165.7(5)	165.7(5)
∠Co/Mg-O2-Te	163.8(2)	163.7(5)	164.6(2)	164.1(1)	159.6(2)×2	159.4(2)×2	159.6(8)×2	159.6(8)×2
∠Co/Mg-O3-Te	167.7(2)	167.3(7)	167.0(2)	167.1(1)				

biggest one) is three times smaller than the relative variation of the amplitudes: $\approx 15\%$.

9.2 High-temperature crystal-structures

Since $Sr_2Co_{0.9}Mg_{0.1}TeO_6$ is the only material with $P2_1/n$ symmetry at RT, the thermal study was focused, initially, on the reflections which do not satisfy the condition $h+k+l=2n$ such as the [(311)(-311),(131)(-131)] group, (Figure 9.5), which disappear between 300 and 400 K. The non-primitive reflections underwent no change at that temperature so the patterns were fitted in the $I2/m$ space group.

Diffraction patterns in Figure 9.6 shows the thermal evolution of the splitting of the cubic reflection (444) for all the materials of the $Sr_2Co_{1-x}Mg_xTeO_6$ series. The group of reflections around 84° in 2θ lose completely their splitting at about 620 K, 620 K and 570 K, for $Sr_2Co_{0.9}Mg_{0.1}TeO_6$, $Sr_2Co_{0.8}Mg_{0.2}TeO_6$ and $Sr_2Co_{0.5}Mg_{0.5}TeO_6$, respectively, and, consequently, all the reflections of the patterns can be fitted by a model based on the tetragonal space group $I4/m$ above the cited temperatures. At even higher temperatures, all the peaks become unique, as seen in Figure 9.6. This indicates that the materials undergo a final structural transition from the tetragonal structure to the parent phase, cubic. This transition occurs at lower temperatures with the increase of x.

In the tetragonal-($I4/m$)-to-cubic ($Fm\bar{3}m$) phase-transition there are two mono-dimensional modes (the third irrep, GM_1^+ is the totally symmetric), $GM_3^+(1)$ and $GM_4^+(1)$, all of them involving oxygen atoms located at the *24e* Wyckoff positions of the prototype cubic phase. The GM_3^+ mode is responsible for the breaking of the symmetry to the $I4/mmm$ tetragonal space group. This mode involves the movements of all the oxygen atoms in the octahedra, in a way that the oxygens located in the $(00z)$ positions move to the center of the octahedra; the oxygen atoms located in the xy plane move outwards along the diagonals of the basal plane of the octahedra. On the other hand, the mode GM_4^+ is responsible for the breaking of the symmetry down to the $I4/m$ space group, and involves movements only of the oxygens located in the xy plane.

It is worth noting that despite the fact that the irreps of the primary modes lowering successively the symmetry from the cubic to the monoclinic ($I2/m$) are the same, in both cases involve only oxygen atoms, and can be interpreted as tilts of the octahedra, the cubic-to-tetragonal phase transition is continuous, as predicted by theory, and the tetragonal-to-monoclinic is discontinuous. The discontinuous character of the last transition is related to the change of the direction of the GM_4^+ irrep on the three-dimensional representation space .[40] The direction of the GM_4^+ irrep in the $I4/m$ phase is $(0, 0, a)$, while it changes to $(a, a, 0)$ in the monoclinic phases. From a structural point of view, this change of the direction is reflected on the relative orientation of both space groups: $I2/m$ is a subgroup of $I4/m$, but when the two-fold axis is located in the same direction as the four-fold one, which is not the case. There is no way to go in a continuous manner from the tetragonal to the monoclinic symmetry when the two-fold axis is perpendicular to the four-fold axis, as it is the case in the tetragonal-to-monoclinic phase transition.

Figure 9.7 shows the temperature evolution of the mode-amplitudes set free in the final restricted refinement and the cell parameters. First of all we would like to stress that we have found experimentally the cubic prototype phase. As mentioned, the transition from the cubic to the intermediate distorted tetragonal phase is continuous, as observed in Figure 9.7. On the other hand, the finite jump at the same transition, in the amplitude values could attributed to the non complete second order character of the transition. This is often observed experimentally in these kind of systems. In the framework of the Landau Theory of Phase transitions, the jump can be explained by including in the expansion of the free energy a sixth-order term in the order parameter, in the case that the fourth order term is not enough to stabilize the symmetry break caused by the sign change of the second-order term, or in the case that the fourth order term is negative. In those conditions, the sixth term forces the character of the phase transition to be of the first order. Apart for this, the evolution of the amplitudes as the external field is released (temperature is decreased) is the expected one: a continuous increase of the distortion. There are no appreciable jumps in the amplitude values evolution of GM_4^+ when the systems cross the phase transitions, down to the lowest temperatures measured, as expected. Finally, one remark on the relative values of the mode-amplitudes in the $P2_1/n$. X_5^+ is almost 20 times smaller than the biggest one, in the three cases. It could be thought that only this fact would force us to take out from the symmetry-directed refinement: this is the main argument on which our refinement process is based. Nevertheless, this mode has to be included in the refinement even if its values is so small. The reason is that it is trillinearly coupled **Urko** to the two order parameters and the not inclusion in the refinement makes it not converging. This is the behavior observed experimentally in these kind of materials.

9.3 Magnetic structure

The magnetic structures of Sr_2CoTeO_6 and $Sr_2Co_{0.9}Mg_{0.1}TeO_6$ have been determined by means of neutron powder diffraction data collected in D1B. In order to solve the spin arrangement, first the crystal structure has been refined from data collected in the high-resolution diffractometer D2B at 4 K. The diffraction patterns of both compounds show several new reflections which arise due to the long-range magnetic order of the Co^{2+} cations. These additional peaks were added to the refinements as a second phase. The collected data show no evidence of any structural phase transition at low temperatures and Rietveld refinements were carried out using the model previously deduced at RT ($P2_1/n$). Refined structural parameters are shown in Table 10.3. The only particularity is the diminution of the angles M-O-Te (M=Co,Mg), attributed to the slight monoclinic distortion, a consequence of the cell contraction caused by temperature.

Additional diffraction patterns (Figure 9.8) have been collected as the temperature decreased in D1B. The magnetic reflections have been indexed with $\mathbf{k} = (0,0,0)$ propagation vector. In other words, the magnetic cell is equivalent to the crystalline cell. The temperature at which magnetic peaks appear (16K) reasonably coincides with the expected from magnetic susceptibility measurements in both cases.

The full symmetry of a paramagnetic state has an additional symmetry operation that has not been considered up to now: the time reversal $\{1'|000\}$. This operation leaves invariant all the atomic parameters of the atoms and reverses their magnetic moment. In these materials, the full symmetry of the crystal in the paramagnetic state is described by the Shubnikov group $P2_1/n1'$.[188] The magnetic ordering is a symmetry breaking process from a paramagnetic phase to a magnetically ordered one where the time-reversal symmetry is lost and therefore, the symmetry of the emerging magnetic structure is described by a subgroup of $P2_1/n1'$ where the operation $\{1'|000\}$ is not present .[188,189]

There are four maximal subgroups of $P2_1/n1'$ compatible with $\mathbf{k} = (0,0,0)$: $P2_1/n$, $P2_1'/n'$, $P2_1/n'$ and $P2_1'/n$. These subgroups have a one-to-one correspondence to the four magnetic *irreps* $mG1+$, $mG2+$, $mG1-$ and $mG2-$, since the latter four are one-dimensional .[190] Being M_x, M_y and M_z the magnetic-moment components of an atom, each symmetry operation transforms them according to an axial vector and, if the symmetry operation includes the time reversal, an additional change of sign must be done to the moments. The $P2_1/n'$ and $P2_1'/n$ magnetic space groups forbid any magnetic ordering when the magnetic atom is located at (0, 0, $\frac{1}{2}$) position: these groups contain the $\{\bar{1}'|000\}$ operation

---

[188] V. A. Koptsik. *Shubnikov Groups. Handbook on the Symmetry and Physical Properties of Crystal Structures*. translated by Kopecky, J. and Loopstra, B. O. Fysica Memo 175, Stichting, Reactor Centrum Nederlands, 1971.

[189] C. J. Bradley and A. P. Cracknell. *The mathematical theory of symmetry in solids : representation theory for point groups and space groups*. Oxford : Clarendon Press, 1972.

[190] J.M. Perez-Mato et al. *Ann. Rev. Mater. Res.* **45**: 1–30, 2015.

that prohibits any magnetic ordering at that position and, therefore, these groups are discarded. In the case of $P2_1/n$ and $P2_1'/n'$, the three magnetic components of the Co atoms at (0, 0, $\frac{1}{2}$) position are independent (M_x, M_y, M_z). Once these components are determined, the orientation of the magnetic moments of the symmetry-related Co atom at the ($\frac{1}{2}$, $\frac{1}{2}$, 0) position is fully determined: (-M_x, M_y, -M_z) in $P2_1/n$, i.e. antiferromagnetic coupling for x- and z-spin components and ferromagnetic for the y-spin component; and (M_x, -M_y, M_z) in $P2_1'/n'$, antiferromagnetic coupling for the y-spin components and ferromagnetic x- and z-spin components.

Neutron diffraction data in the magnetically ordered phase of the pure Sr_2CoTeO_6 and the $Sr_2Co_{0.9}Mg_{0.1}TeO_6$ samples have been analyzed using both $P2_1/n$ and $P2_1'/n'$ magnetic space groups. It has been observed that in both compositions the data is best fitted using the group $P2_1/n$, see Figure 10.7. The refined components of the magnetic structures are given in Table 10.4. According to the refinements, the y-spin component, that would give rise to macroscopic ferromagnetic ordering, is zero. Consequently, the structures consist of antiferromagnetically coupled layers along the c axis. In each layer the spins are ferromagnetically ordered with the atoms located within the ac plane making an angle $\delta = 26(3)^\circ$ with the c axis. The direction of the atoms is not unambiguously solved: the refinements are equivalent for δ and δ values, see Figure 10.8.

Table 9.5: Refined parameters of the magnetic structures of Sr_2CoTeO_6 and $Sr_2Co_{0.9}Mg_{0.1}TeO_6$ at 4 K. Only the spin components of Co atoms in (0,0,$\frac{1}{2}$) are given. The data can not distinguish Model 1 from Model 2.

Co at (0,0,$\frac{1}{2}$)	Sr_2CoTeO_6	$Sr_2Co_{0.9}Mg_{0.1}TeO_6$
Model 1		
M_x	0.93(7)μ_B	0.84(8)μ_B
M_y	0	0
M_z	1.88(5)μ_B	1.77(5)μ_B
M	2.10(9)μ_B	1.96(9)μ_B
δ	26(3)°	26(3)°
Model 2		
M_x	-0.93(7)μ_B	-0.84(8)μ_B
M_y	0	0
M_z	1.88(5)μ_B	1.77(5)μ_B
M	2.10(9)μ_B	1.96(9)μ_B
δ	-26(3)°	-26(3)°
R_p/%	2.13	2.13
R_{wp}	3.06	3.12

Note that, if any canting is present in the structure, as predicted by magnetic measurements, this must occur along the y axis, since it is along this direction that a ferromagnetic coupling is allowed. At zero magnetic field this canting is not observed, probably because it is too small to be detected by powder neutron diffraction.

The expected value at low temperatures for the moments, calculated from the $\mu_{\mathrm{eff}} = g\,S$ equation, should be $\mu_{\mathrm{eff}} \approx 3\,\mu_{\mathrm{B}}$, with $S = \frac{3}{2}$ and $g \approx g_{\mathrm{e}}$. The obtained values are considerably deviated from the expected value. But, taking into account that the Co^{2+} ion, at low temperatures, changes to an effective spin value of $S' = \frac{1}{2}$, and that $g \approx 4.3$, the theoretical value is $\mu_{\mathrm{eff}} \approx 2.17\,\mu_{\mathrm{B}}$. The experimental value $\mu_{\mathrm{eff}} \approx 2.10(9)\,\mu_{\mathrm{B}}$, and the ones from EPR, are in a very good agreement with that theoretical value.

The analysis we have done and in the way we are proposing the magnetic structure, we are making use of the total symmetry of the system, which takes into account the crystal and magnetic degrees of freedom. This results in some restrictions on the magnetic structure, imposed by the total symmetry of the system, and reveals some ambiguities, in the form of spurious degrees of freedom introduced *ad-hoc* in the course of the data treatment without taking into account the symmetry of the crystal. The only resulting arbitrariness in the present analysis comes from the fact that the data can not distinguish among the model 1 and model 2 proposed.

Table 9.6: Crystal structural data for $Sr_2Co_{1-x}Mg_xTeO_6$ (x = 0.0, and 0.1), at 4K. The refinements have been done freeing only there mode-amplitude (see text): GM_4^+, X_3^+ and X_5^+. The Co, Mg and Te cations are located in: Co/Mg [2b (0, 0, $\frac{1}{2}$)], Te [2a (0,0,0)].

		Sr_2CoTeO_6	$Sr_2Co_{0.9}Mg_{0.1}TeO_6$
Sr	x	0.0000	0.0000
	y	0.4911(4)	0.4922(5)
	z	0.2500	0.2500
	B_{iso}(Å^2)	0.76(2)	0.86(2)
O1	x	-0.7798(2)	-0.7771(3)
	y	0.2592(2)	0.2579(3)
	z	-0.0267(1)	-0.0261(1)
	B_{iso}(Å^2)	0.95(2)	1.08(14)
O2	x	-0.44656(2)	-0.4477(2)
	y	0.5000	0.5000
	z	-0.26031(6)	-0.2595(2)
	B_{iso}(Å^2)	0.95(1)	1.08(2)
O3	x	-0.2592(1)	-0.2579(3)
	y	0.2201(1)	0.2229(3)
	z	0.0267(1)	0.0261(1)
	B_{iso}(Å^2)	0.95(1)	1.08(2)
Te	B_{iso}(Å^2)	0.81(3)	0.95(2)
Co/Mg	B_{iso}(Å^2)	0.81(3)	0.95(2)
a (Å)		5.6314(2)	5.6278(1)
b (Å)		5.5969(3)	5.5935(1)
c (Å)		7.9196(4)	7.9144(1)
β (°)		245.48(2)	249.14(1)
V (Å^3)		89.954(4)	89.952(4)
R_p(%)		4.46	5.20
R_{wp}(%)		5.81	6.81
R_{exp}(%)		2.74	2.80
χ^2		6.2	7.3
R_{Bragg}		4.44	5.59

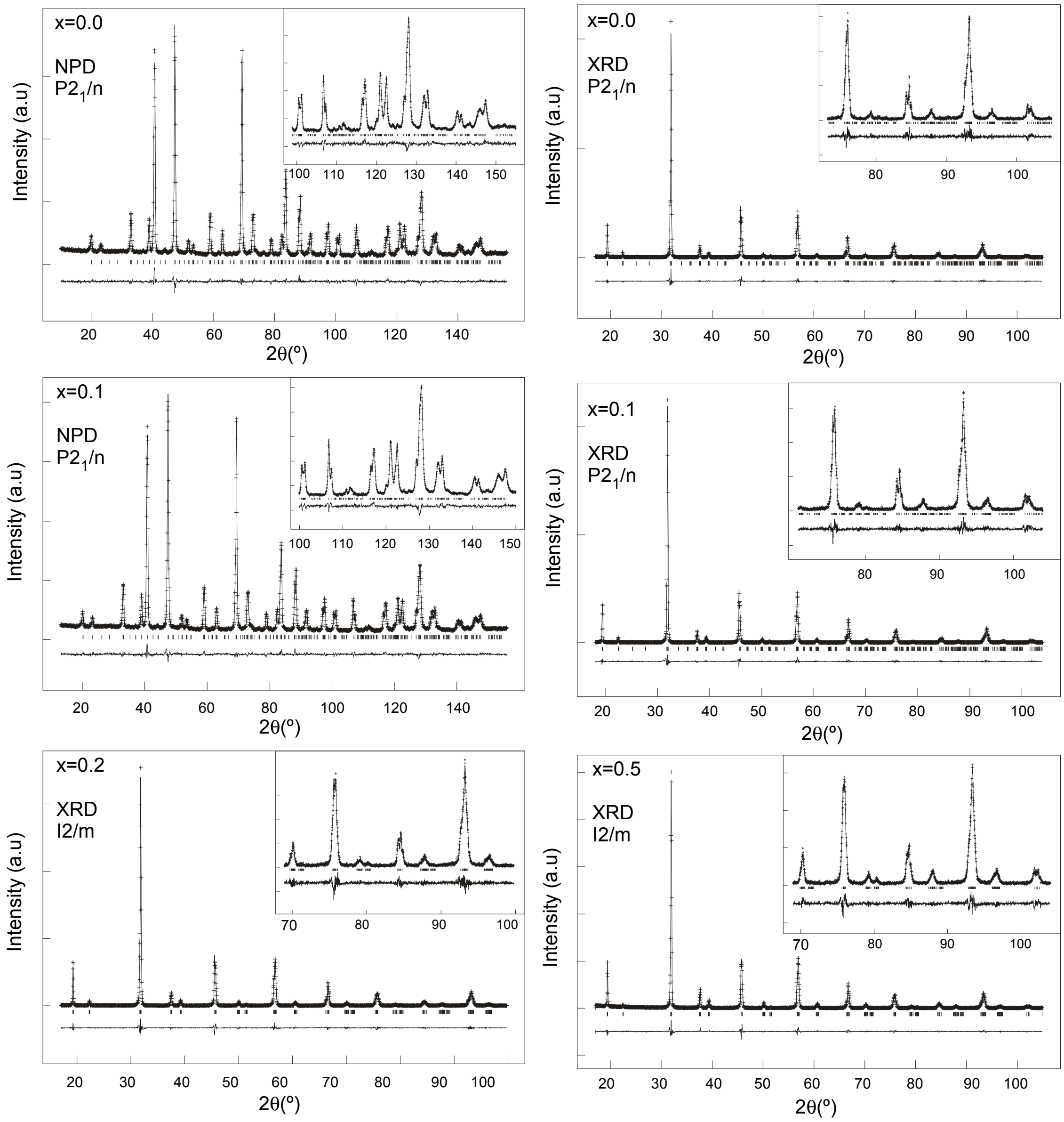

Figure 9.3: Experimental (symbols) and calculated (line) X-ray profiles and neutron profiles for the Rietveld refinement of the $Sr_2Co_{1-x}Mg_xTeO_6$ series at room temperature using a structural model with $P2_1/n$ space group for (x= 0.0 and 0.1) and $I2/m$ for (x=0.2 and 0.5). The bars in the lower part of the graphics represent the Bragg peak positions.

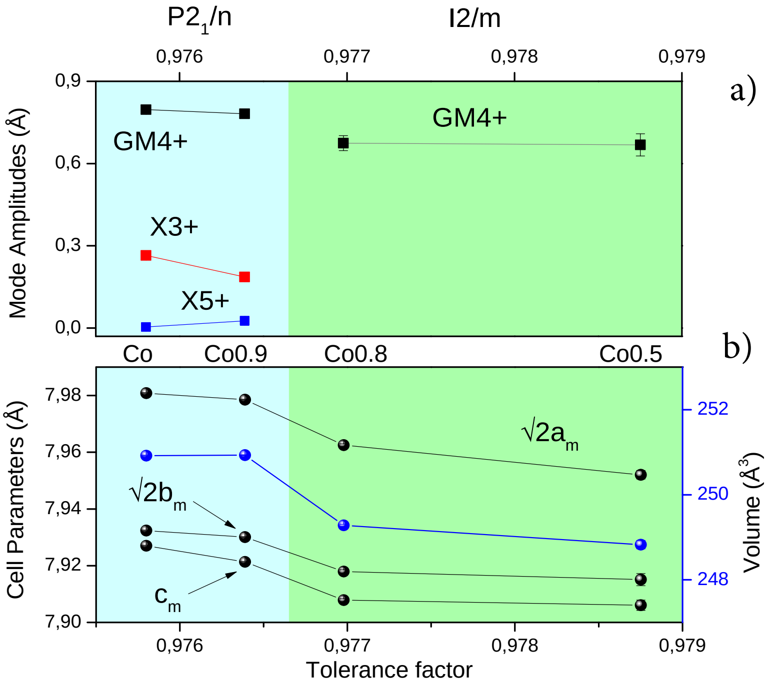

Figure 9.4: Variation, as function of the tolerance factor, of the three distortion irrep amplitudes GM_4^+ (black), X_3^+ (red) and X_5^+ (blue), and the cell parameters (black) and the unit cell volume (blue) for the $Sr_2Co_{1-x}Mg_xTeO_6$ series at room-temperature. The colored backgrounds indicate the regions of the two space groups, $P2_1/n$ and $I2/m$, observed for the four compositions.

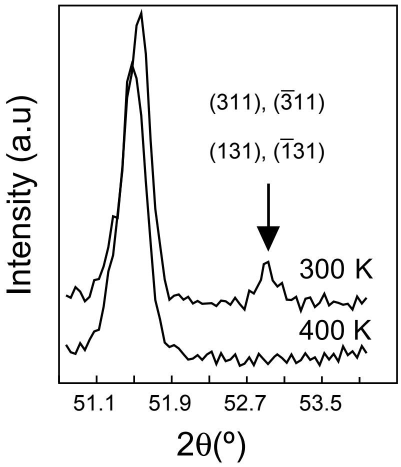

Figure 9.5: Disappearance, as temperature increases, of the primitive reflections (311), (-311), (131) and (-131) of the $Sr_2Co_{0.9}Mg_{0.1}TeO_6$ compound.

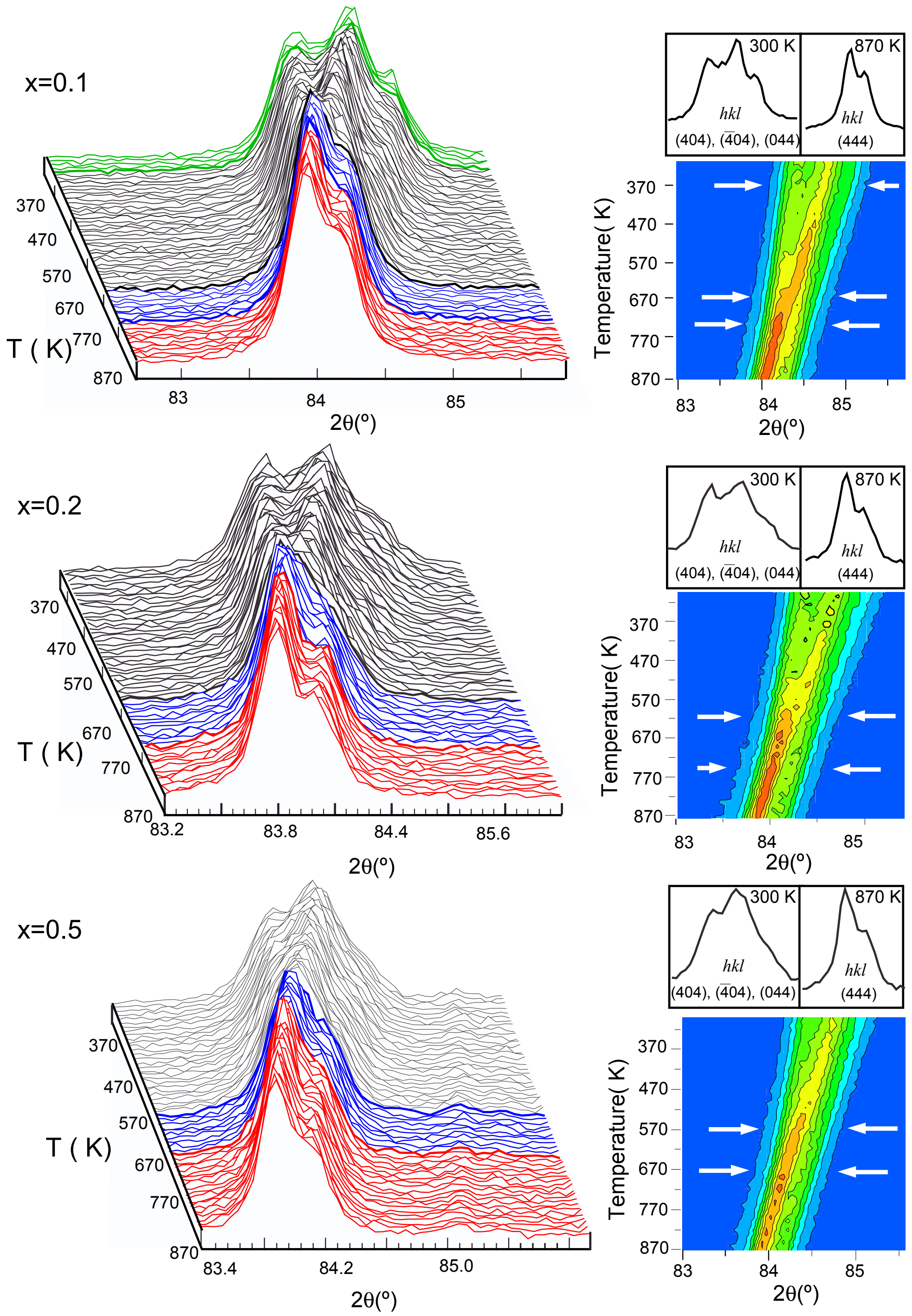

Figure 9.6: Thermal evolution of the (444) cubic reflection splitting located in the interval (82° $< 2\theta <$°86) for the $Sr_2Co_{1-x}Mg_xTeO_6$ compounds with ($x = 0.1, 0.2, 0.5$). The splitting of the triplet (404), (-404) and (044) is clearly seen at 300 K and as temperature increases, the reflections get closer, up to 870 K where they remain as a single peak.

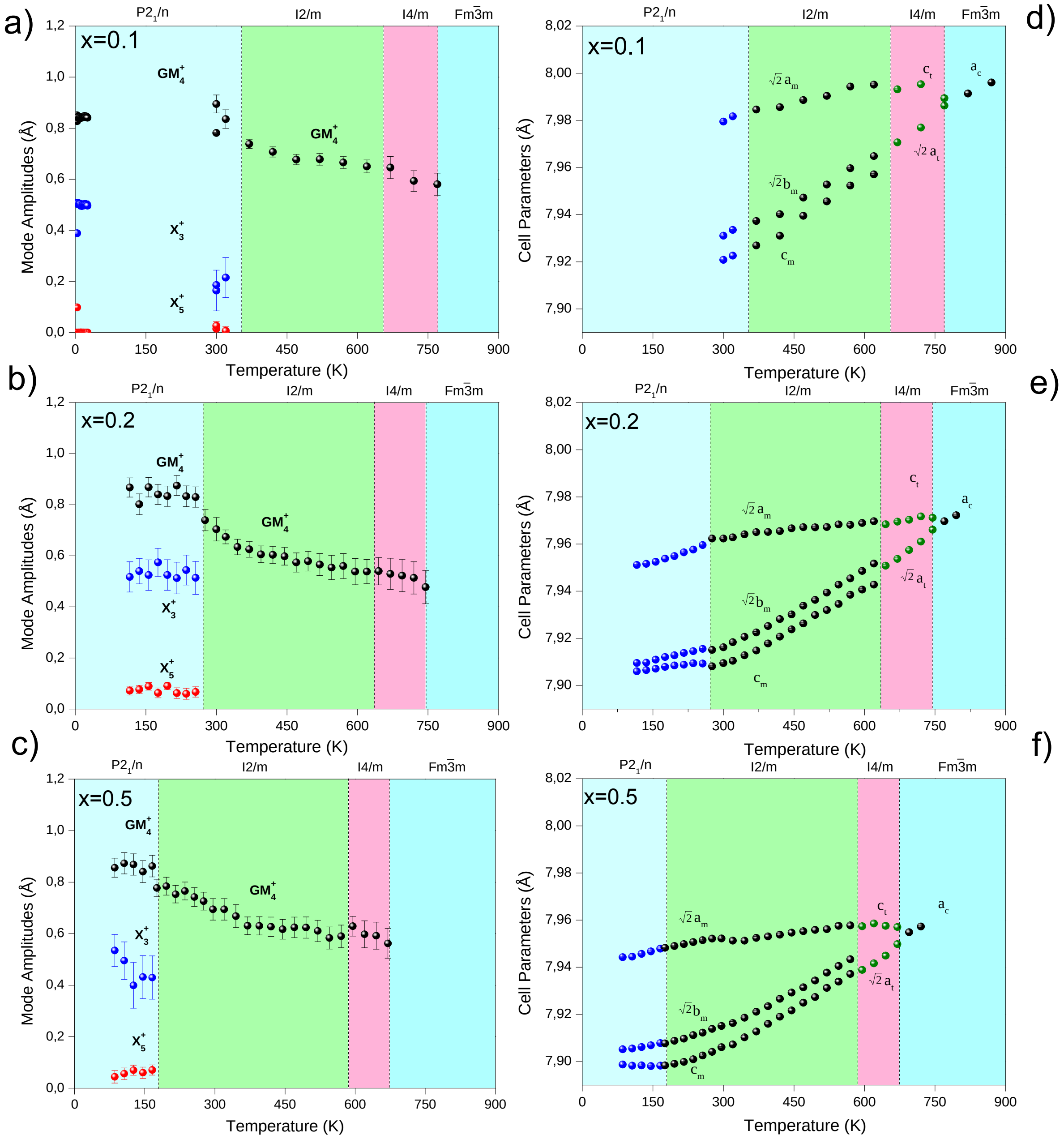

Figure 9.7: Temperature dependence of (a-c) the amplitudes of the modes related to the $P2_1/n$, $I2/m$ and $I4/m$ symmetries and (d-f) their corresponding cell parameters, as obtained from NPD and XRD data refinements, for the $Sr_2Co_{1-x}Mg_xTeO_6$ compounds with ($x = 0.0, 0.1, 0.2, 0.5$)

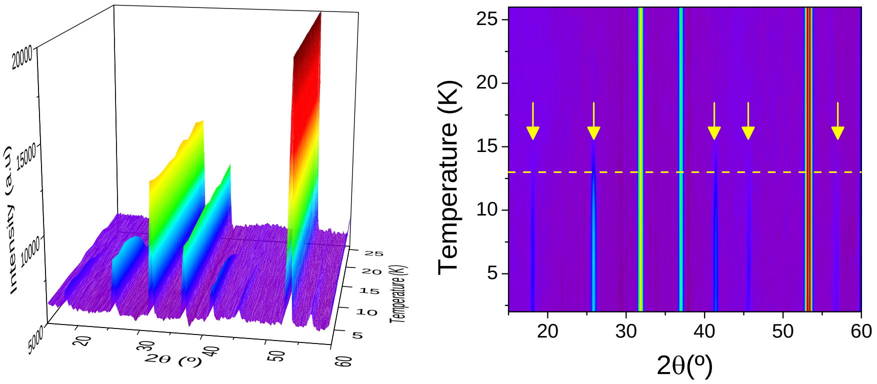

Figure 9.8: Diffraction patterns collected in D1B as temperature decreased for $Sr_2Co_{0.9}Mg_{0.1}TeO_6$. Emergence of magnetic reflections is marked by an arrow at T_N. Zoom of the low 2θ.

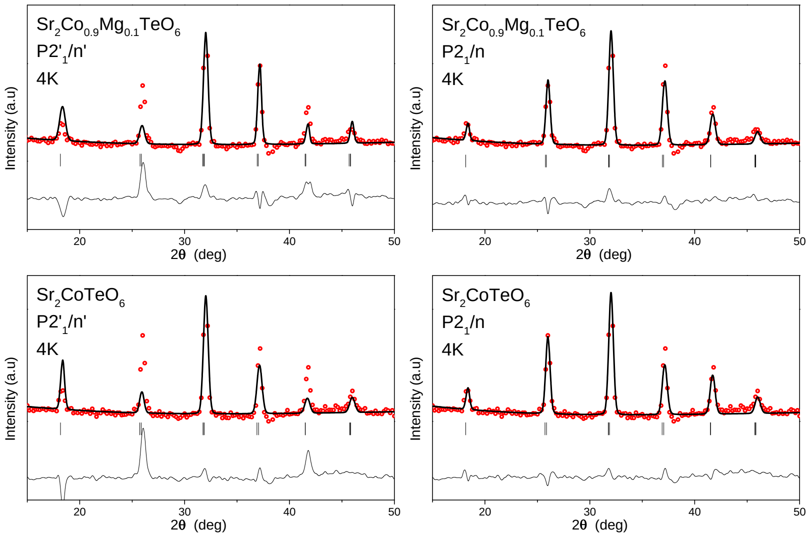

Figure 9.9: Refinements results from the neutron diffraction data of the magnetically ordered Sr_2CoTeO_6 and $Sr_2Co_{0.9}Mg_{0.1}TeO_6$ using both $P2_1/n$ and $P2_1'/n'$ symmetries.

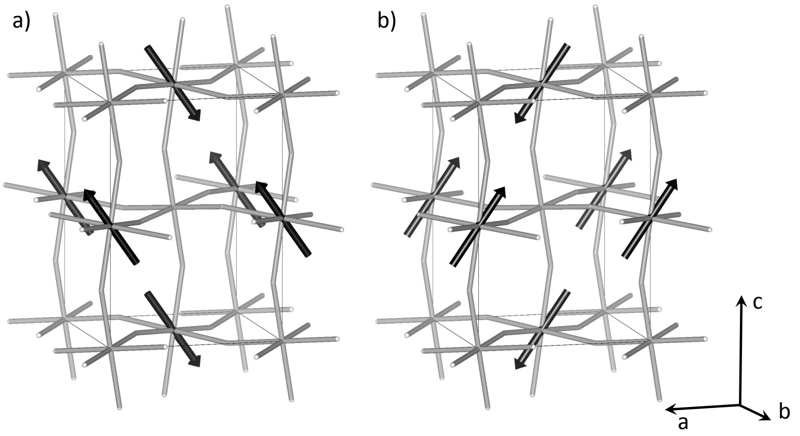

Figure 9.10: Sketch of a) Model 1 and b) Model 2 for the magnetic structure of Sr_2CoTeO_6 and $Sr_2Co_{0.9}Mg_{0.1}TeO_6$ at 4 K.

9.4 Conclusions

- The system $Sr_2Co_xMg_{1-x}TeO_6$ experiments structural changes at room temperature from $P2_1/n$ if $x \leq 0.1$ to $I2/m$ if $x \leq 0.5$ to $I4/m$ if $x \geq 0.5$).
- The materials of the $Sr_2Co_{1-x}Mg_xTeO_6$ (x=0.1, 0.2 and 0.5) present two different space groups at room temperature: $P2_1/n$ for (x=0.0 and 0.1) for and $I2/m$ for (x=0.2 and 0.5).
- Only three relevant modes GM_4^+, X_3^+ and X_5^+ in $P2_1/n$ and only one, GM_4^+, in $I2/m$ and $I4/m$ contribute to the distorted structures observed experimentally.
- All the materials of the tellurium family $Sr_2Co_{1-x}Mg_xTeO_6$ show the sole phase-transition sequence: $P2_1/n \rightarrow I2/m \rightarrow I4/m \rightarrow Fm\bar{3}m$.
- The expected correlation between the distortion degree at room-temperature and the temperature at which distortion disappears, was confirmed: the bigger the distortion, the higher is the interval in which the system is distorted.
- The $P2_1/n$ describes both the low temperature crystal and magnetic structures leading to an antiferromagnetic coupling for x- and z-spin components and a ferromagnetic coupling for the y-spin component between the cobalt atoms (Appendix **??**).

Chapter 10

Structural phase transitions, Magnetic and Spectroscopic properties of the double perovskites $Sr_2Ni_{1-x}Mg_xTeO_6$ (x=0.1, 0.2, 0.3, 0.5)

10.1 Crystal Structures: High Temperatures and Room Temperature

The phase-transition sequence observed experimentally in this solid solution is: $Fm\bar{3}m \rightarrow I4/m \rightarrow I2/m \rightarrow P2_1/n$ (decreasing the temperature) (Figures 10.4 and 10.5), the same encountered in the previously reported one from Co to Mg: Chapter 9.**Orayech2015b**

We have not done different refinements freeing all the degrees of freedom allowed by symmetry (all the mode-amplitudes) in the first refinement, and, setting in turn some amplitudes to zero, until we have found the set of mode-amplitudes that actually describe the symmetry. As mentioned in some previous reports ,[100,136] in many cases, the system does not use all the symmetry it can, and although some displacements with respect to the prototype phase are permitted, they are not found experimentally. In the present case, there is a reduced set of mode-amplitudes describing the distorted phases, and this is the one we have used. In the low-symmetry primitive monoclinic phase $P2_1/$: GM_4^+, X_3^+ (the primary order parameters) and X_5^+, tri-linearly coupled to the formers, and always necessary for the convergence of the refinement, even if its value is always many times smaller than the highest amplitude-value. In the other two intermediate phases $I2/m$ and

---

[100] E. Iturbe-Zabalo et al. *J. Solid State Chem.* **198**: 24–38, 2013.

[136] B. Orayech et al. *J. App. Crystallogr.* **48**: 318–333, 2015.

$I4/m$ only GM_4^+. The values for all those amplitudes (obtained from the NPD data and assumed to be the best possible), have been used for the refinements of the XRPD data. We have performed experiments with neutrons only for two compositions, $x = 0.0, 0.1$, in the solid solution. And those have been the first data refined. In that way, we are using as the starting points for the analysis of the XRPD data the more accurate results for the mode-amplitudes affecting the oxygens. The resulting neutron powder diffraction (NPD) and X-ray diffraction (XRPD) patterns from the refinements of the four compounds at RT are shown in Figure 10.1. Tables 10.1 and 10.2 show, respectively, the resulting structures and the distances.

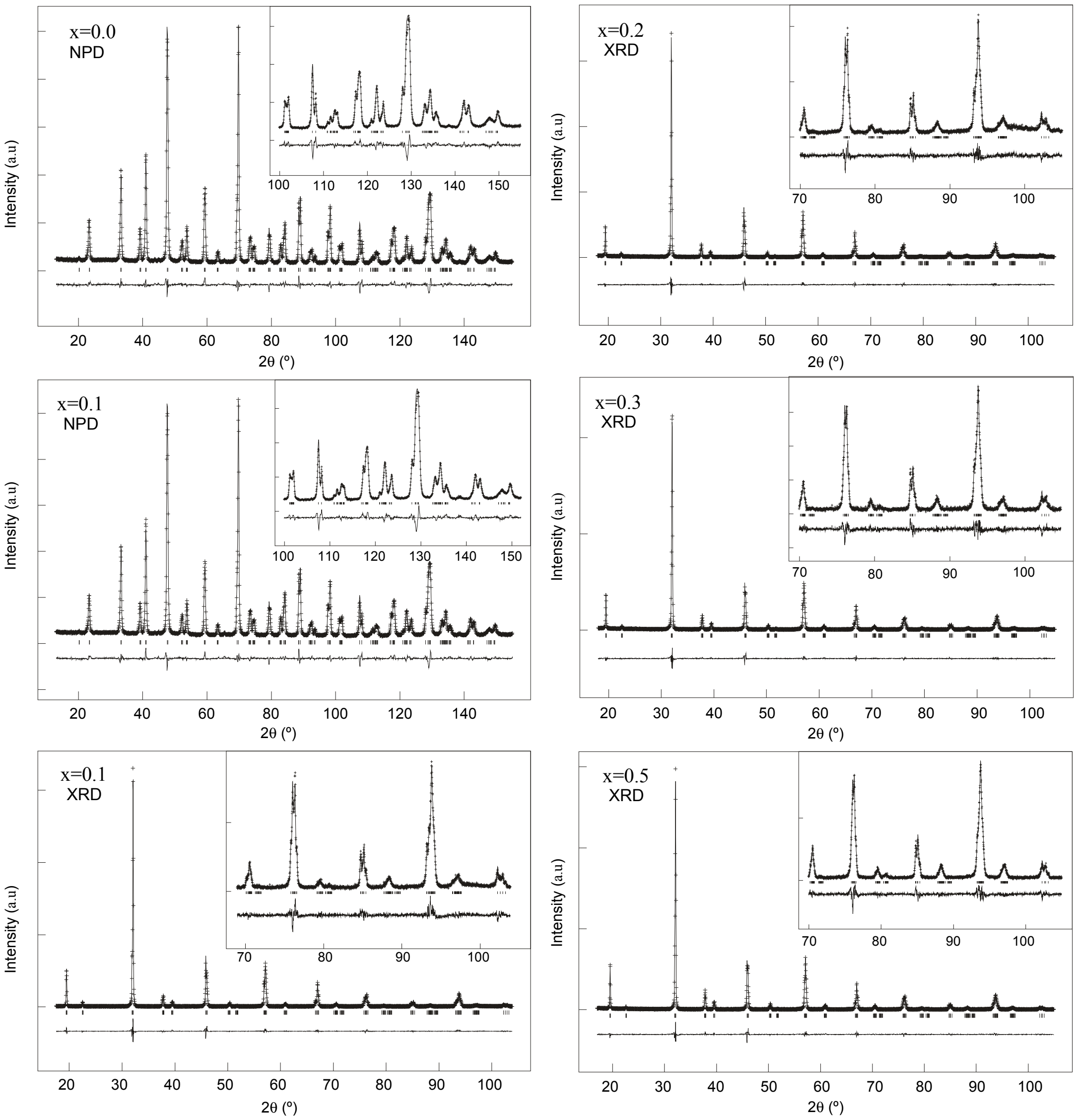

Figure 10.1: Experimental (symbols) and calculated (line) X-ray profiles and neutron profiles for the Rietveld refinement of the $Sr_2Ni_{1-x}Mg_xTeO_6$ series at room temperature using a structural model with $I2/m$ space group for (x= 0.0, 0.1, 0.2 and 0.5). The bars in the lower part of the graphics represent the Bragg peak positions.

Table 10.1: Crystal structural data and refinement results for $Sr_2Ni_{1-x}Mg_xTeO_6$ (x = 0.0, 0.1, 0.2 and 0.5), at room-temperature. The refinements have been done freeing only one mode-amplitude (see text): GM_4^+, the primary mode for the transition from the cubic $Fm\bar{3}m$ to the monoclinic $I2/m$. The Ni, Mg and Te cations are located in: Ni/Mg [2*b* (0, 0, $\frac{1}{2}$)], Te [2*a* (0,0,0)].

		Sr_2NiTeO_6	$Sr_2Ni_{0.9}Mg_{0.1}TeO_6$	$Sr_2Ni_{0.8}Mg_{0.2}TeO_6$	$Sr_2Ni_{0.7}Mg_{0.3}TeO_6$	$Sr_2Ni_{0.5}Mg_{0.5}TeO_6$
GM_4^+		0.6473(4)	0.6043(1)	0.5902(2)	0.5940(6)	0.5078(1)
Sr	x	0.00000	0.00000	0.00000	0.00000	0.00000
	y	1/2	1/2	1/2	1/2	1/2
	z	-0.75000	-0.75000	-0.75000	-0.75000	-0.75000
	$B_{iso}(^2)$	0.58(3)	0.50(3)	0.94(2)	0.57(3)	0.51(3)
O1	x	0.24714	0.24714	0.24714	0.24714	0.24714
	y	0.24714	0.24714	0.24714	0.24714	0.24714
	z	-0.0272(1)	-0.0239(1)	-0.023(2)	-0.023(1)	-0.0227(18)
	$B_{iso}(^2)$	0.95(1)	1.06(1)	1.27(1)	1.00(1)	1.28(4)
O2	x	0.054(3)	0.048(3)	0.046(4)	0.046(4)	0.045(4)
	y	0	0	0.00000	0	0
	z	-0.75286	-0.75286	-0.7528	-0.75286	-0.75286
	$B_{iso}(^2)$	0.95(1)	1.06(1)	1.27(1)	1.00(1)	1.28(4)
Te	$B_{iso}(^2)$	0.61(1)	0.51(1)	0.49(1)	0.56(1)	0.62(1)
Ni/Mg	$B_{iso}(^2)$	0.61(1)	0.51(1)	0.49(1)	0.56(1)	0.62(1)
a (Å)		5.6123(2)	5.6113(1)	5.6108(3)	5.6087(3)	5.6062(3)
b (Å)		5.5740(3)	5.5754(1)	5.5766(4)	5.5772(4)	5.5790(3)
c (Å)		7.8722(4)	7.8744(1)	7.8762(4)	7.8768(4)	7.8812(4)
β (°)		246.27(2)	246.35(1)	246.44(2)	246.41(6)	246.50(2)
V (Å^3)		89.965(4)	89.967(4)	89.967(1)	89.966(5)	89.965(5)
R_p(%)		8.02	8.74	9.2	9.12	9.01
R_{wp}(%)		6.2	7.5	8.1	8.41	8.37
R_{exp}(%)		5.61	6.03	5.88	5.81	5.71
χ^2		10.7	10.8	11.13	11.48	11.05
R_{Bragg}		5.61	5.54	7.07	6.84	6.77

Table 10.2: Main bond distances (Å), selected angles (°), and $\Phi(\Phi')$ and $\Psi(\Psi')$ tilt angles, for $Sr_2Ni_{1-x}Mg_xTeO_6$ (x=0.0, 0.1, 0.2, 0.3 and 0.5) at room temperature. The values were obtained refining the mode breaking the symmetry from the cubic $Fm\bar{3}m$ to the monoclinic $I2/m$.

	Sr_2NiTeO_6	$Sr_2Ni_{0.9}Mg_{0.1}TeO_6$	$Sr_2Ni_{0.8}Mg_{0.2}TeO_6$	$Sr_2Ni_{0.7}Mg_{0.3}TeO_6$	$Sr_2Ni_{0.5}Mg_{0.5}TeO_6$
Ni/MgO_6 octahedra					
Ni/Mg-O1	2.011(1)×4	2.010(1)×4	2.009(1)×4	2.008(1)×4	2.007(1)×4
Ni/Mg-O2	2.012(2)×2	2.009(1)×2	2.008(2)×2	2.009(2)×2	2.008(2)×2
Average distance	2.011(6)	2.010(6)	2.009(6)	2.008(6)	2.007(1)
Predicted distance	2.0605	2.0605	2.0605	2.0605	2.0605
TeO_6 octahedra					
Te-O1	1.966(1)×4	1.964(1)×4	1.964(1)×4	1.963(1)×4	1.962(1)×4
Te-O2	1.968(2)×2	1.965(1)×2	1.965(2)×2	1.964(2)×2	1.963(2)×2
Average distance	1.967(6)	1.964(6)	1.964(1)	1.964(6)	1.962(6)
Predicted distance	1.9170	1.9170	1.9170	1.9170	1.9170
∠O1-Ni/Mg-O2	89.9(2)	89.8(2)	89.9(2)	90.1(1)	90.1(2)
∠O2-Ni/Mg-O2	89.1(1)	89.0(7)	90.0(7)	90.1(7)	90.2(7)
∠O1-Te-O2	89.8(4)	89.9(4)	89.9(4)	89.9(4)	89.9(4)
∠O2-Te-O2	89.1(4)	90.1(4)	90.1(4)	90.1(4)	90.1(4)
∠Ni/Mg-O1-Te	164.5(1)	164.7(5)	164.5(1)	163.7(2)	163.5(2)
∠Ni/Mg-O2-Te	169.1(1)	169.0(8)	169.1(2)	168.6(3)	168.2(4)
$\Phi(TeO_6)/\Phi'(Ni/MgO_6)$	8.852(2)	7.879(1)	7.551(2)	7.547(2)	7.345(2)
$\Psi(TeO_6)/\Psi'(Ni/MgO_6)$	8.656(2)	7.704(1)	7.385(2)	7.379(2)	7.181(2)

The GM_4^+ irrep is the same in both intermediate phases. Physically it represents a tilting of the octahedra: in the monoclinic phase around the monoclinic axis and, in the tetragonal, around the tetragonal. Hence, the tilt is not oriented in the same way. This has been already mentioned in the work .[40,101] On the other hand, that tilt continues to be the same in the primitive monoclinic phase.

Those mode-amplitudes freed give rise to the symmetry-mode driven distortions present in the distorted phases. Nevertheless, there is another distortion taking place as well and simultaneously: the deformation. In a first approximation, the effects of both distortions can be analyzed independently. In fact, this is what actually AMPLIMODES does .[59]

Let's describe the phase-transition sequence, in terms of the symmetry-mode driven and deformation driven distortions. There are two mechanisms to release the energy, as thermal energy, in the process of temperature decrease: the contraction of the cell and the displacements of the atoms in the unit cell (oxygens mainly, tilting of the octahedra) with respect to the positions they have in the prototype reference phase. We are assuming that the experimentally observed phase transitions are of the displacive type and imply distortions of the reference structure. Those two mechanisms act in conjunction alongside the existence of all the distorted phases.

---

[40] A. Faik, D. Orobengoa, E. Iturbe-Zabalo, and J. M. Igartua. *J. Solid State Chem.* **192**: 273–283, 2012.

[101] E. Iturbe-Zabalo et al. *J. Phys-Condens. Mat.* **25**: 205401, 2013.

[59] D. Orobengoa, C. Capillas, M. I. Aroyo, and J. M. Perez-Mato. *J. App. Crystallogr.* **42**: 820–833, 2009.

Starting from the cubic and decreasing the temperature, the point at which the tilt starts to appear (in principle, in a continuous way, see below), the cell transforms, and one of the three cell parameters becomes different, the other two maintain equal to each other. The phase transition induces the tetragonal cell metrics and the tilt of the octahedra, compatible with the tetragonal symmetry. The breaking of the equality of the cell parameters, accompanied with a further decrease of symmetry elements (the third-order symmetry-axes are lost, for instance), give the content of the unit cell more freedom, in principle: this freedom gain (symmetry lose) is what the mode-driven distortions describe. This happens at every phase transition of this type, in particular in all the ones present in the observed phase-transition sequence.

During the subsequent temperature diminution, both distortions continue, until the cell is not able to maintain the two cell parameters equal in the course of the contraction, and transforms, abruptly, to the monoclinic phase. At the same time, the tilt of the octahedra appears oriented in another direction. This phase transition is discontinuous: there is no way to transform continuously the orientation of the tilt axis. This time, the freedom gain inside the cell comes from the lose, among other symmetry elements, of the tetragonal axis. The process continues until, at some temperature, the cell loses the centering (though the metrics is maintained) and transforms to a primitive cell. This phase transitions is continuous: the cell parameters and GM_4^+ irrep induced distortion show no jump. The point is that the tilting conserves the direction and the metrics is not changed. In the further decrease of the temperature, the tilt of the octahedra continues increasing. Although now, the new symmetry needs to be accompanied by another symmetry-mode, transforming according to the X_3^+ irrep, to break the cubic symmetry down to the monoclinic. As pointed out, another mode-amplitude allowed by symmetry also appears, as it is coupled to the order parameters.

Taking into account the preceding descriptions regarding the phase-transition sequence, let's analyze the results obtained for the solid solution, in the whole temperature range studied. The results are shown in Figure10.3 and Figures10.2 for the mentioned distortions, respectively: the deformation distortion, described by the cell parameters' evolution and the mode-symmetry driven distortions, described by the evolution of the refined mode-amplitudes.

The cell parameters and the cell volume across the compositions, at room-temperature (Figure10.2a, lower panel), show a clear linear behavior in the tolerance factor (t) axis. Nevertheless, it is worth noting that the relative change in t across the solid solution is of the order of $\Delta t \approx 0.5\%$. The same is true for the cell parameters and the volume, their relative changes are less than 0.1%, in both cases. This means that, actually, even if we can distinguish the these physical properties, they can be considered to be the same; similarly, for the mode-driven distortion at room-temperature. Remember that at room-temperature all compositions show the same space-group ($I2/m$), for which we have only freed the amplitude transforming according to the GM_4^+ irrep: the tilt of the octahedra around the monoclinic axis. Indeed, in the panel of the amplitudes at room-temperature (Figure 10.2a), we have colored, in blue, a band centered at the mean value of the amplitude-values opened, up and down, with the standard deviation of the mean value. Just as a guide for the eye, to observe that they are almost the same. The conclusion is, for the deformation distortion,

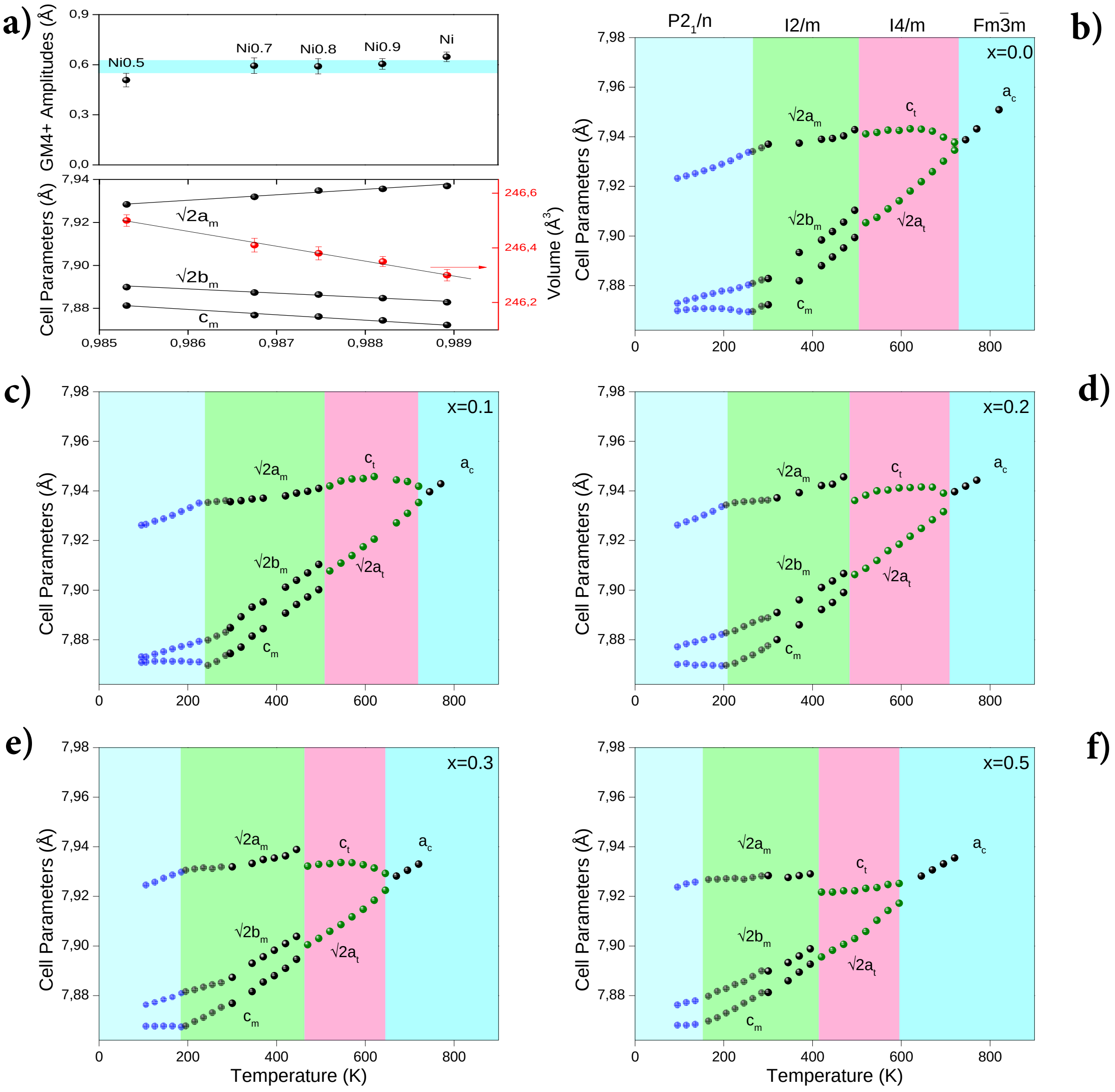

Figure 10.2: (a): Variation, as function of the tolerance factor, of the distortion-amplitude transforming according to the GM_4^+ irrep and the cell parameters (black) and the unit-cell volume (blue) at room temperature. (b-e): Thermal evolution of the cell parameters refined in the $P2_1/n$, $I2/m$ and $I4/m$ space groups for the $Sr_2Ni_{1-x}Mg_xTeO_6$ series (x = 0.0, 0.1, and 0.2)

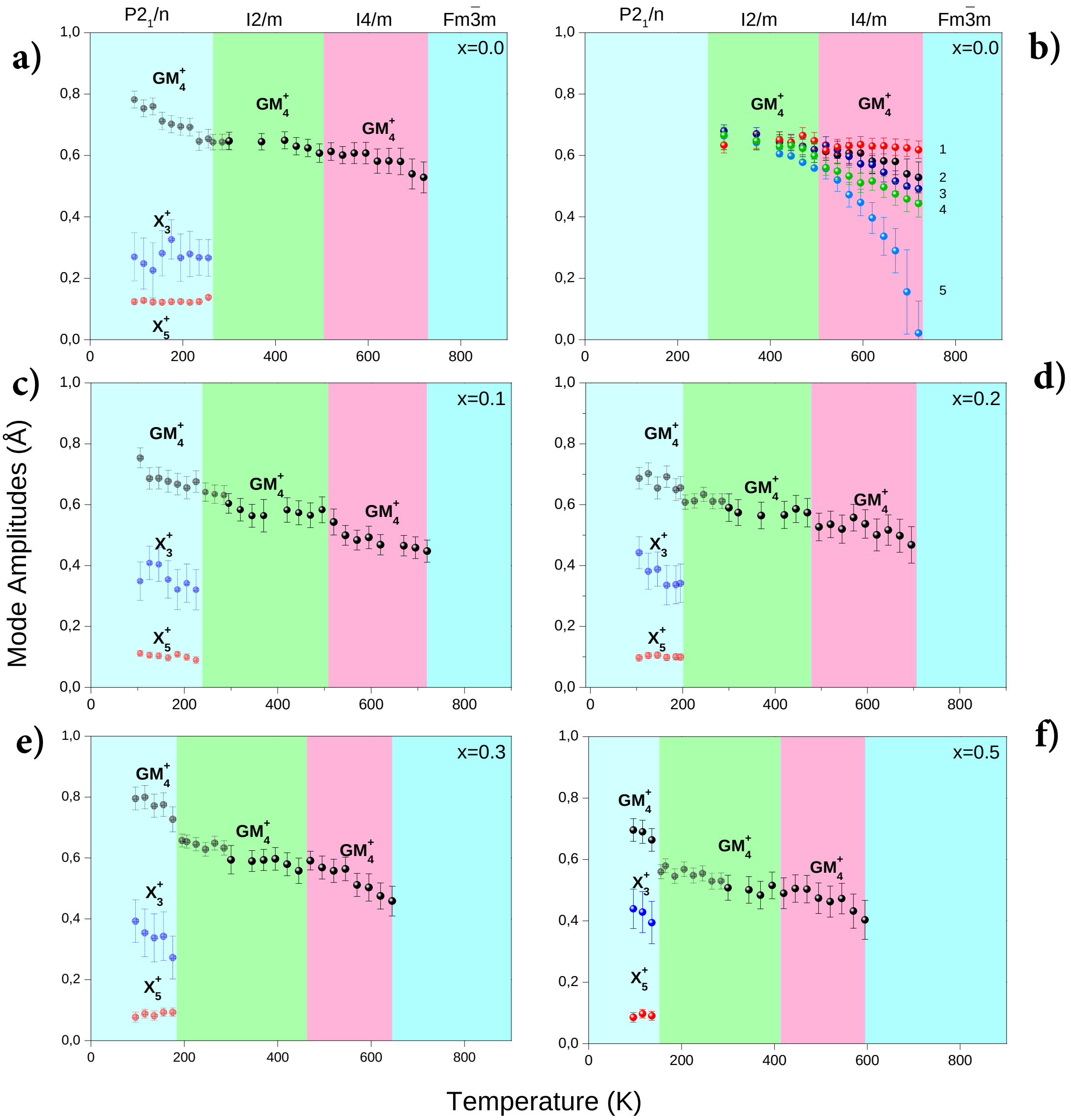

Figure 10.3: Temperature dependence of the mode-amplitudes refined in the $P2_1/n$, $I2/m$ and $I4/m$ space groups for the $Sr_2Ni_{1-x}Mg_xTeO_6$ series (x = 0.3 and 0.5)

that although we can distinguish among the compositions, it could be said that the solid solution as a whole, at least for the analyzed compositions, accommodates the same tilt at room-temperature.

Focusing on the cell parameters' evolution with temperature, this solid solution shares with the previously published one ,[177] not only the phase-transition sequence but, also the global features of the sequence.

---

[177] L. Ortega-San Martín et al. *J. Mater. Chem.* **15**: 183–193, 2005.

Usually, we do free the atomic displacements parameters in the final stages of the refinements and, usually, coupled to each other. In these kind of materials, we have observed that freeing the atomic displacement parameters (adp) without any coupling turns out the refinements unstable. One way to maintain them stable, but giving enough structural freedom to the system, is to free the 'adp' coupled to each other. In our experience, the best results are usually found when the cations in the B and B′ sites in the double perovskite structure are given the same values; the A-site cations another value, and all the oxygens, another one. Focusing our attention on the 'adp' of the oxygens and depending on the symmetry of the (intermediate) phases present in the material, there are different types of oxygens, which could, in principle, have different adp, if considered anisotropic. For instance, in the two intermediate phases in which we are concern now, there are two types of oxygens: four basal (O1 in the asymmetric unit), surrounding in a square the central cation, Ni and Te; and two apical, up and down in the octahedra (O2 in the asymmetric unit). In either case, we have considered to be isotropic, and we have assigned to all them the same value: one value for the oxygens (curve 1) Figure10.3b.

Turning to the rest of the atoms, in the first approach, we have assigned to all them the same value to the adp, taken to be isotropic. We wanted to analyze the effect on the mode-amplitudes, as the adp couple to the actual displacements taking part in the distortions. For instance, in the case of the oxygens, whose positions are changed by the only symmetry-mode freed in the intermediate phases, clearly, it is expected that an increase in the Biso will reduce the values of the mode-amplitude, and vice versa. As a first approach to measure that effect, in the second set of refinements performed, we consider adequate to separate the adp into two blocks, the oxygens and the rest of the atoms, and free them in the whole temperature range. The results of this approach show a decrease in the values of the amplitudes, mainly in the tetragonal phase, curve 2 in the Figure10.3b. From the results in curve 1, we should say that the phase transition from the cubic to the tetragonal is not continuous, as expected, or at least shows a high first order character. On the other hand, clearly, as the amplitude does not change (almost) in none of the intermediate phases, the conclusion is that the distortion (tilt) anchors in a value. Hence, in response to the change in the external field, temperature decreasing, the system fixes a tilt (abruptly) and allows the cell to deform (continuously).

The deformation is mainly assumed by the *a* and *b* axis; the *c* axis maintains its value of the prototype phase, nearly in the existence-range of both intermediate phases. The octahedral tilt around the tetragonal axis (in *c*), and the main contraction appears in the plane perpendicular to it. In principle, those two distortions could be treated independently, but it is obvious that the deformation in the cell parameters is facilitated (if not triggered) by the tilting of the octahedra (around the tetragonal axis), or vice-versa. Of course, as mentioned, in the tetragonal to the centered monoclinic phase-transition, there is a change in the metrics.

The direction of the *c* parameter in the tetragonal is the *a* direction in the monoclinic. In this phase, this is the parameter that hardly changes as temperature is decreasing. The main contraction also flips from the *ab* plane in the tetragonal phase to the *ac* plane in the monoclinic, which is also the *ac* in the tetragonal: the (approximate) transformation matrix between both cells is the identity, there is no metrics change, although β angle separates (slightly) from 90°. Again, in the monoclinic phase, the contraction effect of the tilt is observed in the plane perpendicular to the axis of the tilting: the monoclinic axis, *b*.

As a third approach to obtain the Biso values in the whole range of temperature, we have taken their refined values (from the previously described process) at selected temperatures, to avoid the fluctuations observed in the final values of the mode-amplitudes. The selected temperatures were taken from the lowest measured one in the $P2_1/n$ space group, but without magnetic response (remember taken by NPD), the highest one (by XRPD) in the cubic phase and at another three temperatures, in the middle of each phase: 96 K and 256 in $P2_1/n$, 266 and 495 K in $I2/m$, 520 K in $I4/m$ and 720 K in the prototype cubic. A nearly pseudo-linear behavior has been observed. The slope for the oxygen Biso is approximately twice that obtained for the rest of the atoms, which is quite reasonable. With this two slopes, we have calculated the fitted values for the Biso at each experimental temperature. We have refined again all the data freeing everything, as previously described, except the Biso: fixed by the fitted values. Again, as expected the amplitude values are the same, except that some of the fluctuations of the previous approach have disappeared. Based in our experience and, in our opinion, the main conclusion from these two refinement-sets is that we do not have a good quality data to infer the positions of the atoms and the adp. The data we are treating are XRPD data, and we have a high attenuation of the intensity in the high 2θ angle range and, hence, not a high resolution for deducing the adp.

In the works by Kennedy *et al.* ,[142] devoted to a couple of simple perovskites materials, $SrZrO_3$ and $CaTiO_3$, they report their success in obtaining the adp evolution with temperature at very high temperatures, using neutrons. As they note, they were forced to describe the adp as highly anisotropic. They report the evolution of the adp for two atoms that we have in our structure: Sr and O. The knowledge of the adp's, in principle from whatever source, could be used (and, perhaps, should be used), if they are not only precise, but accurate. Our idea was to use those reported values in our materials. The actual adp values in our materials should differ from those, because many physical parameters in the structures are different. There are some structural features affecting the adp values shared in the simple and double perovskites, the structural framework, for instance. In the simple ones there is only one octahedra and in the double (ordered) ones, two. The predicted octahedra in our structure do not differ to much, a 6% in the mean distances, from those in the mentioned works, for example. Another source for the actual differences is the symmetry: this restricts the adp values, if analyzed as anisotropic, as mentioned. But, we want to make a more simple description, so we are going to use isotropic adp, in which case, we do not need to care about the symmetry. Nevertheless, we need to adapt the reported anisotropic values.

Regarding the two main approaches used: 1) the Biso fitted to our experimental data (curve 3 in Figure10.3b), 2) the Biso extrapolated from the literature and adapted to our data (curve 4 in Figure10.3b), there is no a big difference among them, implying that the data we are working with do not have resolution enough, they are not accurate enough, to give rise to a good behavior of the amplitude values, because the phase-transition character of the tetragonal-to-cubic phase transition deduced is first order. Or, in the other hand, they

---

[142] Brendan J. Kennedy, Christopher J. Howard, and Bryan C. Chakoumakos. *Phys. Rev. B* **59**: 4023–4027, 1999.

predict the correct behavior of the amplitude values at the mentioned phase-transition, but this is continuous with a strong first order character, as the amplitude does not nullify at the phase transition.

Finally, focused in the tetragonal phase, if we tune the Biso values we can make the mode-amplitudes show the diminishing trend expected in the case of a second order phase transition. We can force them go to zero with a nearly square root dependence on the temperature. This is the fitting result to a Landau Theory second order phase transition continuous behavior of the primary order parameter. And with increasing errors, which also agrees with the expected behavior for those kind of phase transitions, as the fluctuations, in a mean field theory, increase as the distance to the phase transitions diminishes.

On the other hand, in the case of the monoclinic intermediate phase, the distortion does not show so a big diminishing trend: it maintains almost constant. The errors corresponding to this mode-amplitude values are smaller and more homogeneous than in the tetragonal. Finally, there is a jump between the values of the distortion mode-amplitude for both intermediate phases. Even if both modes represent the same collective displacement pattern, they are oriented in different directions, as mentioned (referred to the prototype cubic), so the phase transition has a strong first order character, as it is clearly seen in the obtained results.

At room temperature, all the materials show up with the same space group: $I2/m$. In Figure10.2a, we show the results of the mode amplitude and cell parameters at room temperature. The values for the amplitudes are almost the equal, we have plotted the mean value of all, to visualize the very small differences. It means, following the preceding argument, that the monoclinic distortion at room temperature stabilizes nearly at the same value: the doping hardly changes the distortion. With respect to the cell parameters, a similar discussion is in turn. All the compositions end up nearly at the same unit cell: the cell parameters show a slightly changing trend. But the changes are lower than a 0.1%, in the case of the cell parameters, and even less in volume.

Decreasing further the temperature, in the case of the primitive monoclinic phase, again, the system does not use all the allowed freedom. This time, there are three mode-amplitudes present in the refinements: two primary order parameters, GM_4^+ and X_3^+, with a relative value ratio of 2:1, and the X_5^+ ten times smaller that the highest one, but necessary because it couples tri-linearly to the primary ones, and without it the refinements are not stable. Nevertheless, the value of X_5^+ remains constant in the whole temperature range of each of the compositions measured and this values maintains across the points in the solid solution (Figure10.3a,c-f). It means that the coupling takes place exactly in the same way, irrespective of the combination of the cations. In this case, the doping of the Sr_2NiTeO_6 with Mg, does not influence the coupling of the primary order parameters in the $P2_1/n$ space group symmetry phase. The values of those amplitudes do change as the pure Ni material is doped with Mg: the values fluctuate across the solid solution. The fluctuation is more clear in the X_3^+ irrep transforming mode, for which also the errors are bigger than in the case of the GM_4^+ irrep, being in both cases homogeneously distributed.

In the very recently published paper devoted to the analysis of a similar solid solution from Co to Mg ,$^{\textbf{Orayech2015b}}$ we have found the same overall picture of the solid solution: the same phase-transition sequence, the main difference among the materials reflecting itself in the cell parameters evolution with temperature (the deformation of the cell is the more effective thermal energy releasing mechanism), only one distortion present in the intermediate phases (even that in that case we did not study the alterations in the mode-amplitude values by means of the disjoint freeing of the adp) which hardly changes across the interval of existence of those phases; and, finally, the same pattern for the three mode-amplitudes only present in the low temperature phase. The only difference between both solid solutions is the mean values of the cell parameters and the mode-amplitudes: in the case of the Co solid solution, everything is displaced to lower values. This behavior should be expected if we observe the tolerance factor values: $t_{\mathrm{Co}} < t_{\mathrm{Ni}}$, which means that it is more distorted, as a whole.

A final remark concerning the evolution with temperature. The study of these two solid solutions implies, so to say, a big zoom in the tolerance factor axis: the calculated t values for this solid solution are different, but very close to each other, see Figure 9.4 and Figure10.2a. The differences have been found because we have made a big effort in the analysis, trying to make use of all the power the mode-crystallography offers together with some good experimental data sets. Nevertheless, we are conscious that zooming-out in the t axis will bring all these values to just one big point. The tolerance-factor interval for which we have already studied similar materials, is fifty times bigger. Hence, these two solid solutions are just a point, all together, in that axis (see Figure 10.9).

It is also interesting to note, as we did for the Co-Mg solid solution, Chapter 9, that there is a general trend, with two characteristic features, in the evolution with temperature: as the tolerance factor decreases across the solid solution (even if the diminution is very small, as mentioned), the distortion is bigger, the temperature of the phase transition to the cubic prototype phase is bigger and the interval of existence of the intermediate phases, in conjunction, and of each separately increases.

10.2 LT-crystal and magnetic structures

At 4 K, extra reflections appear in the neutron powder diffraction patterns, as can be seen in Figure 10.6. Those new reflections correspond to the magnetic ordering and can be indexed by $\mathbf{k} = (0, 0, 0)$ propagation vector. The crystal structure does not undergo any additional distortion induced by the magnetic transition.

The symmetry analysis done to figure out the possible magnetic symmetries compatible with the data is explained in detailed in Section **??**. Just a note to recall that the full symmetry of the parent group is in this case $P2_1/n1'$ and the magnetic ordering should be described by a subgroup of the parent group (paramagnetic), where the time-reversal operation is not present. The maximal subgroups of the parent group compatible with $\mathbf{k} = (0, 0, 0)$ and which allow magnetic ordering for Ni atoms located in $(0\ 0\ \frac{1}{2})$ position are $P2_1/n$ and $P2_1'/n'$. These magnetic groups are the outcome of the activation of the magnetic irreps $mG1+$ and $mG2+$ of $P2_1/n1'$, respectively.

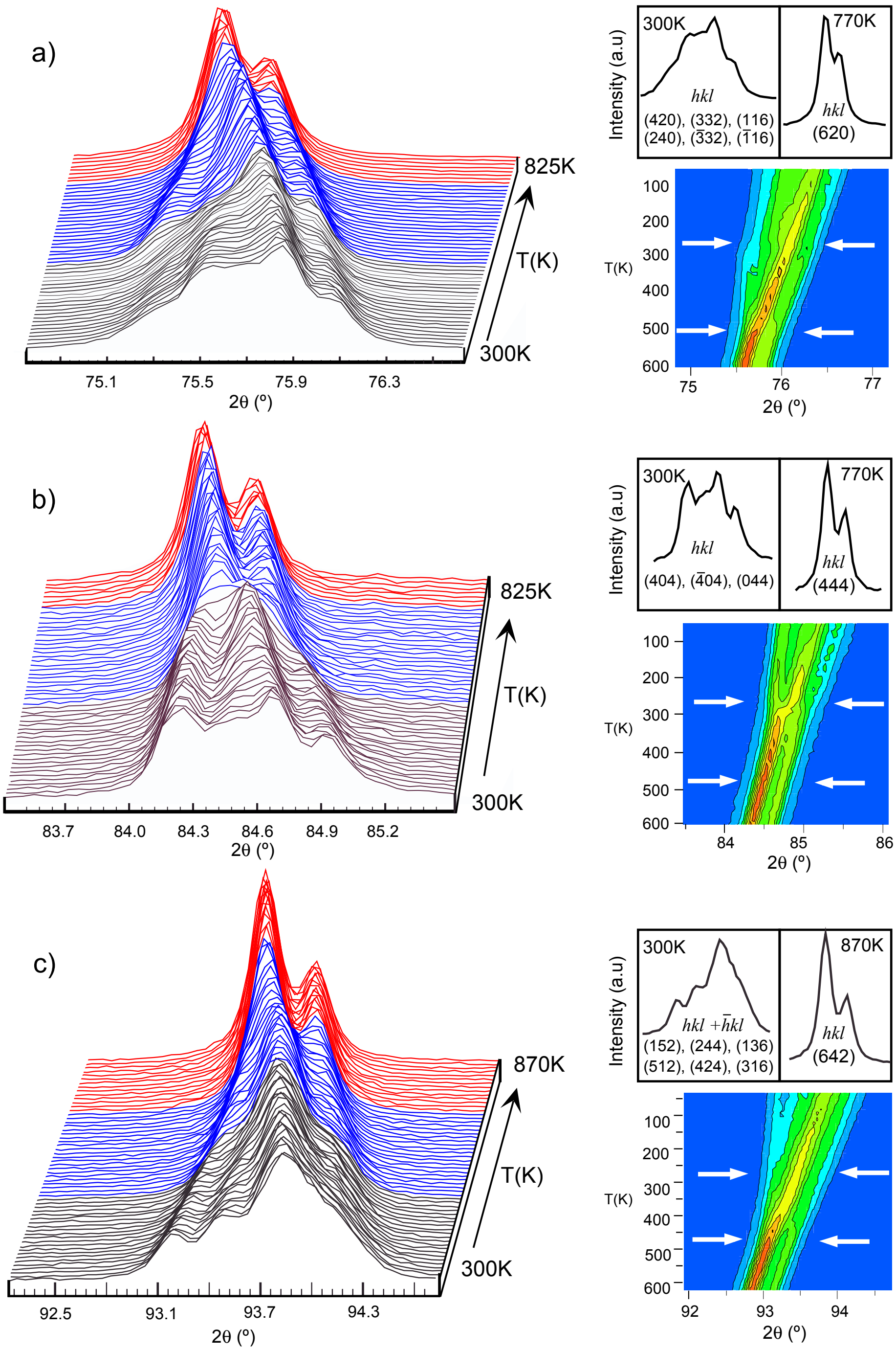

Figure 10.4: Thermal evolution of different splitted reflections for the Sr_2NiTeO_6 compound.

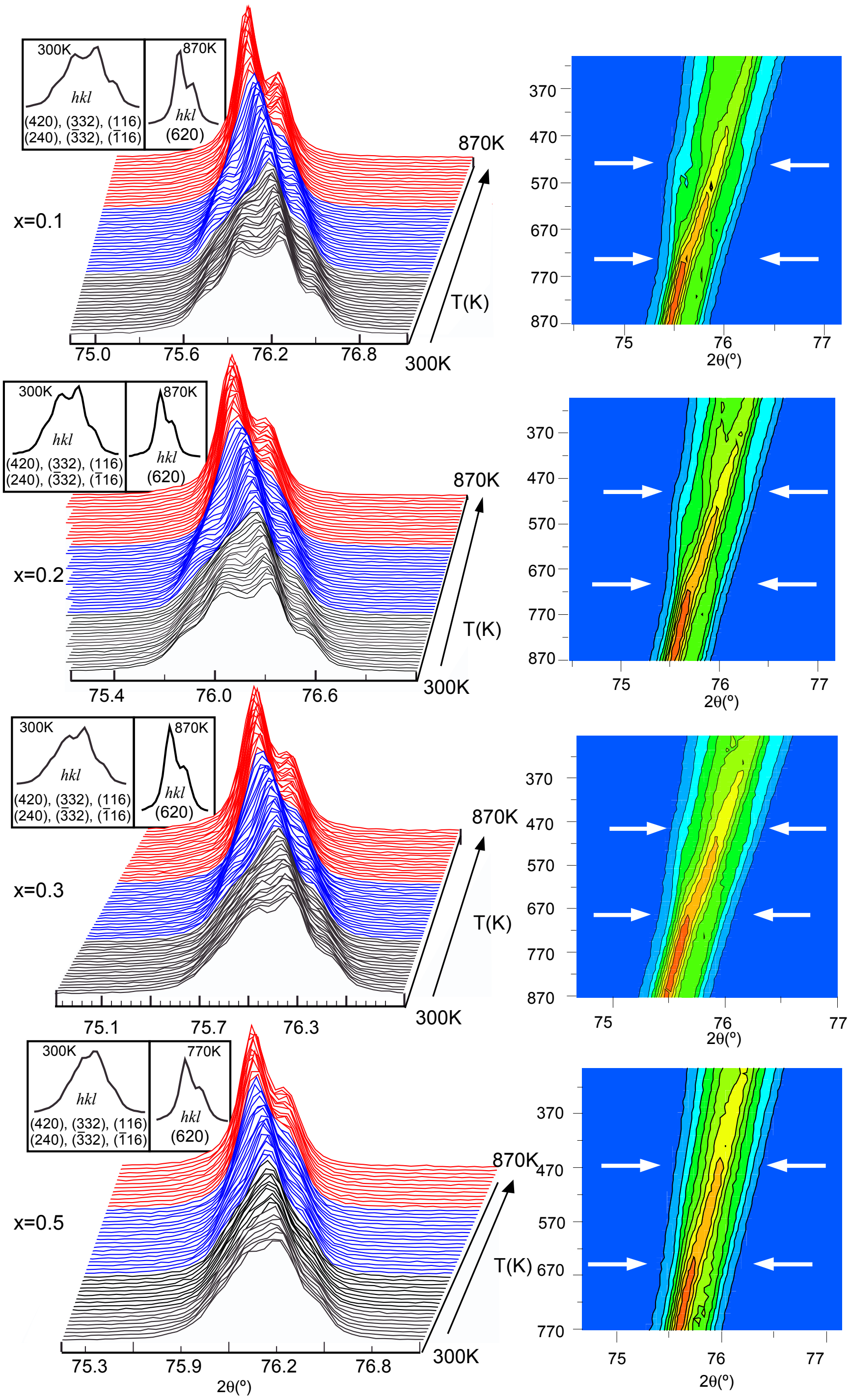

Figure 10.5: Thermal evolution of different splitted reflections located in the interval ($75^\circ < 2\theta < ^\circ 77$) for the $Sr_2Co_{1-x}Mg_xTeO_6$ compounds with ($x = 0.1, 0.2, 0.3 and 0.5$).

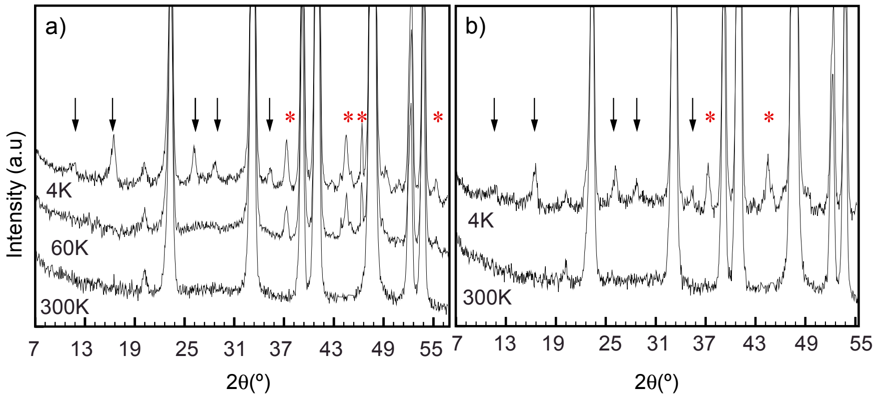

Figure 10.6: Diffraction patterns collected on D2B for a) Sr_2NiTeO_6 and b) $Sr_2Ni_{0.9}Mg_{0.1}TeO_6$. The arrows point magnetic reflections whereas the stars mark the reflections associated with the $P2_1/n1'$ monoclinic distortion.

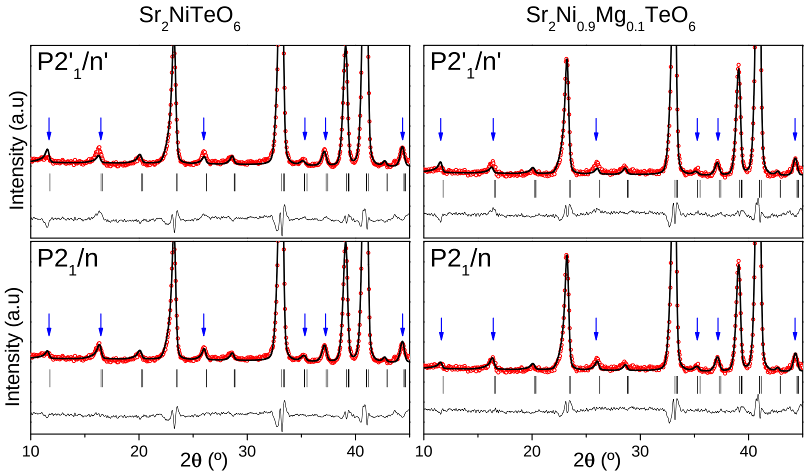

Figure 10.7: Refinement results from the neutron diffraction data of the magnetically ordered Sr_2NiTeO_6 and $Sr_2Ni_{0.9}Mg_{0.1}TeO_6$, using both $P2_1/n$ and $P2_1'/n'$ space group models.

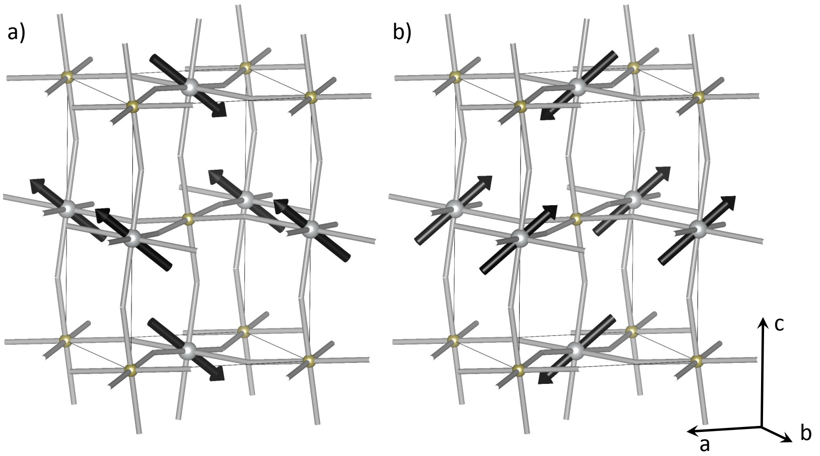

Figure 10.8: Sketch of a) Model 1 and b) Model 2 for the magnetic structure of Sr_2NiTeO_6 and $Sr_2Ni_{0.9}Mg_{0.1}TeO_6$ at 4 K.

Neutron diffraction data at 4 K of both compositions have been analyzed using $P2_1/n$ and $P2_1'/n'$ magnetic space groups. Both magnetic structures have $P2_1/n$. The fittings are shown in Figure 10.7. It is clearly observed that the refinement with the $P2_1'/n'$ space group does not fit well the magnetic reflections, whereas $P2_1/n$ symmetry does. The magnetic components obtained from the refinements are given in Table 10.4. Within experimental error, there is no difference between the magnetic structure of the pure Sr_2NiTeO_6 and that of $Sr_2Ni_{0.9}Mg_{0.1}TeO_6$. The spin arrangement consists of ferromagnetic layer antiferromagnetically coupled along the c axis. In each layer the spins are parallel within the ac plane, making an angle δ with the c axis: $\delta = 42(3)^\circ$ and $\delta = 43(3)^\circ$ for the $x = 0.0$ and $x = 0.1$ compositions, respectively. However, the refinements are not conclusive in the sense that they are indistinguishable for δ and $-\delta$ values, see Figure 10.8, and consequently none of these results can be disregarded.

Table 10.3: Crystal structural data for $Sr_2Ni_{1-x}Mg_xTeO_6$ (x = 0.0, and 0.1), at 4K. The refinements have been done freeing only there mode-amplitude (see text): GM_4^+, X_3^+ and X_5^+ the primary modes for the transition from the cubic $Fm\bar{3}m$ to the monoclinic $P2_1/n$. The Ni, Mg and Te cations are located in: Ni/Mg [2*b* (0, 0, $\frac{1}{2}$)], Te [2*a* (0,0,0)].

		Sr_2NiTeO_6	$Sr_2Ni_{0.9}Mg_{0.1}TeO_6$
Sr	x	0.0000	0.0000
	y	0.4959(11)	0.4930(8)
	z	0.2500	0.2500
	$B_{iso}(^2)$	0.78(2)	0.77(2)
O1	x	-0.7718(3)	-0.7656(3)
	y	0.2560(3)	0.2599(3)
	z	-0.0249(1)	-0.0254(1)
	$B_{iso}(^2)$	1.08(2)	1.23(2)
O2	x	-0.4501(2)	-0.4492(2)
	y	0.5000	0.50000
	z	-0.2579(2)	-0.2528(1)
	$B_{iso}(^2)$	1.08(2)	1.23(2)
O3	x	-0.2560(3)	-0.2599(3)
	y	0.2282(3)	0.2344(3)
	z	0.0249(1)	0.0254(1)
	$B_{iso}(^2)$	1.08(2)	1.23(2)
Te	$B_{iso}(^2)$	0.83(2)	0.89(2)
Ni/Mg	$B_{iso}(^2)$	0.83(2)	0.89(2)
a (Å)		5.6046(2)	5.6052(1)
b (Å)		5.5649(3)	5.5667(1)
c (Å)		7.8707(4)	7.8718(1)
β (°)		245.48(2)	245.62(1)
V (Å^3)		89.958(4)	89.955(4)
R_p(%)		4.90	5.54
R_{wp}(%)		6.48	7.12
R_{exp}(%)		4.46	4.01
χ^2		3.7	3.15
R_{Bragg}		4.85	4.44

Table 10.4: Refined parameters of the magnetic structures of Sr_2NiTeO_6 and $Sr_2Ni_{0.9}Mg_{0.1}TeO_6$ at 4 K. Only the spin components of Ni atoms in (0,0,$\frac{1}{2}$) are given. The data can not distinguish Model 1 from Model 2.

Ni at (0,0,$\frac{1}{2}$)	Sr_2NiTeO_6	$Sr_2Ni_{0.9}Mg_{0.1}TeO_6$
Model 1		
M_x	1.18(7)μ_B	1.23(8)μ_B
M_y	0	0
M_z	1.34(6)μ_B	1.34(7)μ_B
$\mathbf{M}$	1.78(9)μ_B	1.8(1)μ_B
δ	42(3)°	43(3)°
Model 2		
M_x	$-1.18(7)\mu_B$	$-1.23(8)\mu_B$
M_y	0	0
M_z	1.34(6)μ_B	1.34(7)μ_B
$\mathbf{M}$	1.78(9)μ_B	1.8(1)μ_B
δ	$-42(3)$°	$-43(3)$°

10.3 Conclusions

- The room temperature crystal structures of all the compositions of $Sr_2Ni_{1-x}Mg_xTeO_6$ (x = 0.0, 0.1, 0.2, 0.3 and 0.5) are monoclinic with space group symmetry $I2/m$.
- All the compositions undergo three structural phase transitions in temperature, with the sequence: $P2_1/n \rightarrow\ I2/m \rightarrow I4/m \rightarrow Fm\bar{3}m$.
- Only three relevant modes GM_4^+, X_3^+ and X_5^+ in $P2_1/n$, and only one, GM_4^+, in $I2/m$ and $I4/m$ have been shown to contribute to the distorted structures observed experimentally, as in the $Sr_2Co_{1-x}Mg_xTeO_6$ series.
- A parameterized combinations of B_{iso} have been set to reproduce a diminishing trend of the amplitudes with the temperature increase.
- Replacing the ion Ni^{2+} by Mg^{2+}, hardly changes the distortion. All the compositions end-up nearly at the same unit cell, a slightly changing trend has been shown.
- Both, the crystal structure and magnetic structure were described by $P2_1/n$, which imposes an antiferromagnetic coupling for x- and z-spin components and a ferromagnetic coupling for the y-spin component between the Nickel atoms (Appendix ??).

Part III

Conclusions and Future work

Conclusions

Final Remarks and Conclusions

In this memory we have presented the Synthesis, the Analyzed by Conventional X-ray, Synchrotron, and/or neutron data, the Refinements using, the *Symmetry-Adapted Modes* approach, of the Structural and Phase Transitions of 46 Materials, 23 for the first time, Perovskites with the general formula:

- $Na_{0.5}K_{0.5}NbO_3$
- La_2MMnO_6
- Sr_2MSbO_6 (Ln=Nd, Eu, Gd, Dy, Ho, Er, Tm and Yb)
- $Sr_2\mathit{M}SbO_6$ (M=In, Y and Sc)
- Ca_2MSbO_6 (Ln=Nd, Eu, Gd, Dy, Ho, Er, Tm and Yb)
- $Ca_2\mathit{M}SbO_6$ (M=In, Y and Sc)
- $Sr_2M_{1-x}M'_xTeO_6$ (M, M'= Co, Mn, Ni, Fe and Mg)
- $Na\mathit{LnMM'}O_6$ (Ln=La, Nd, Pr; M=Co, Mn, Mg; M'= W and Te)

1. Three different phase-transitions sequences were observed:
    - $R3c \rightarrow Amm2 \rightarrow P4mm \rightarrow Pm\bar{3}m$
    - $P2_1/n \rightarrow R\bar{3} \rightarrow Fm\bar{3}m$
    - $P2_1/n \rightarrow I2/m \rightarrow I4/m \rightarrow Fm\bar{3}m$
2. A general phase-diagram has been constructed for the antimony family Sr_2MSbO_6 series (Figure 10.9):
    - A general trend is observed for all compounds in the transition temperatures: smaller the distortion mode amplitudes (more symmetric the structure), smaller is the transition temperature.
    - The phase-diagram shows the existence of two phase-transition sequences, $P2_1/n \rightarrow R\bar{3} \rightarrow Fm\bar{3}m$ and $P2_1/n \rightarrow I2/m \rightarrow I4/m \rightarrow Fm\bar{3}m$.

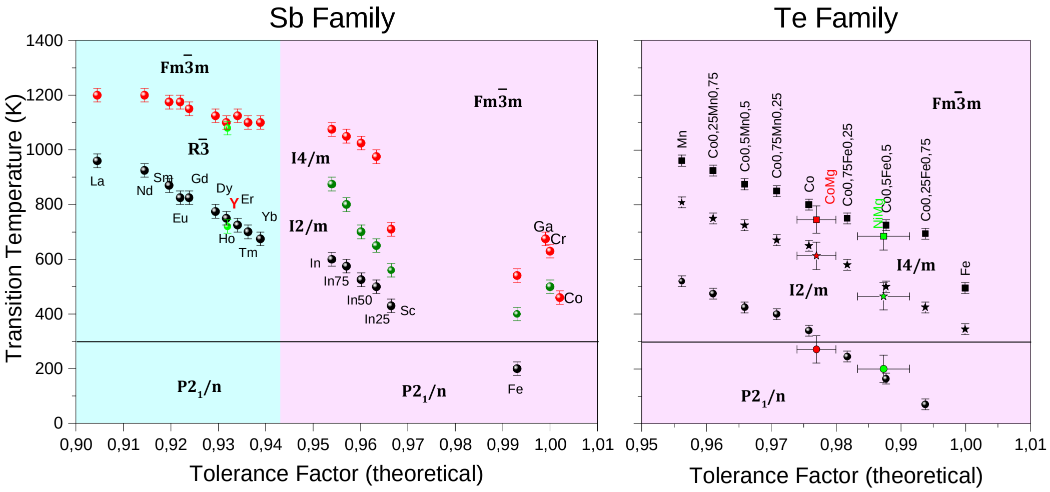

Figure 10.9: Tolerance factor and temperature dependence phase diagram of Sr_2MSbO_6 and Sr_2MTeO_6. The backgroupd color are indicating the phase-transition sequence's domain. An horizontal line is set at 300 K as guide to figure-out the RT space group for each material.

3. The phase-diagram of the tellurium family shows the existence of the sole phase-transition sequence $P2_1/n \rightarrow I2/m \rightarrow I4/m \rightarrow Fm\bar{3}m$ (Figure 10.9)

    - There is a correlation between the distortion degree at room-temperature and the temperature at which distortion disappears: the bigger the distortion (i.e., the less symmetric it is) the bigger is the interval in which the system is distorted, irrespective of the intermediate distorted phase; indeed, considering both.
    - There is also a correlation between the interval in which the second distorted structure is present: the transition temperature between both intermediate phases also increases with the distortion.

4. From the analysis of the $Na_{0.5}K_{0.5}NbO_6$ system:

    (a) Data from medium- and low-resolution experiments can be very *efficiently used* for structural refinements of data taken at normal conditions of temperature and pressure or at extreme conditions of temperature, at least.

    (b) Efficiently means that the mode-crystallography based refinement of a single set of data (at a fixed structural phase) from a high-resolution experiment fixes not only the starting point for the refinements but the direction to be parametrized in the space transforming according to a multidimensional irrep. Direction which maintains fixed as the structure evolves in an external field, i.e. temperature.

    (c) The final results from this parametrized refinements is *accurate*. The ambiguities arising from a non-parametrized symmetry-adapted mode-amplitude refinements disappear. In the analyzed case, the amplitudes of the modes present in the distorted phases do not change their relative signs, which would imply that the refinement results will be alternatively describing different domains in the sample.

(d) The final results from this parametrized refinements are *coherent*. The mentioned direction in the internal space of a multidimensional irrep transforming set of degrees of freedom is maintained from one material to another, of the same kind, if the phase is the same, if the phase transition is the same and if the phase-transition sequence is the same. The dot product of the parametrized direction in the analyzed material and in the materials analyzed in the work on which we are basing our study is 1: the directions match perfectly.

(e) The refinements themselves can be done more efficiently. The parametrization describes a structure, and its evolution in temperature, for instance, more close to the actual physical structure and this, in turn, reduces the refinement time and outputs lower R-value results.

(f) The medium- and low-resolution data, x-ray powder diffraction data, refined using this workflow can be used to obtain a trustable indirect calculation of a physical property of the studied system: the spontaneous polarization, in our case. The result obtained in this way and compared to the result obtained using a reported "toy-model" is better, more physical and without ad-hoc assumptions, but shows its limitations, as well.

5. From the analysis of the La_2CoMnO_6 and Ln_2MMnO_6 systems:

   (a) The application of the newly adopted, and adapted, refinement-process workflow extended to another material and to a family related to that, all of them double perovskites, has proven to be:

   - extendable and coherent:
     - the direction in the internal space transforming according to a multidimensional irrep maintains in the analysis of one phase, previous to the parametrization. This fact allows us to fix the parametrization: it is used in the analysis of the structure in the whole phase
     - the same direction is found, previous to the parametrization, in the analyzed structures (from literature) in the same phase, deduced from high-resolution data This fact allows us to extend the parametrization to another materials
   - predicting:
     The extendability and coherence of the parametrization through the structure of a material in the same phase and through the structures of the same phase of related materials fixes the direction in the analyzed internal space, which in turn means that for any material observed in the same phase but whose distorted partial structure is not obtained in the same direction, is not correctly described and should be re-visited.
   - efficient:
     The refinement of data from high-resolution experiments, own or taken from the literature, fixes the parametrized direction inside the present multidimensional internal spaces, which can be used with confidence as the

good parametrized direction in the analysis of structures of different but related materials in the same phase. Thus, for instance, laboratory experiments, more accessible, less expensive, less time-consuming, acquire more importance.

   (b) The comparisons amongst the structures of related materials resulting from this workflow, in which the degrees of freedom are refined in the same way in the same phases, is more accurate and more confident, i.e. the tilts of the octahedra.

6. From the Statistical Analysis

   (a) The statistical analysis performed on the structures and the phase-transitions of whole set materials, included in the five families studied regarding the proposed refinement workflow, has been is in the way to be confirmed by the novel energy-analysis of the ground states of the relaxed structures, in the following aspects:
      i. Distorted phases, particularly the phase with the $P2_1/n$ space group, do not use all the possible freedom allowed by symmetry. That is, a reduced set of modes describes properly that symmetry.
      ii. The novelty of the energy analysis has proven that:
         - There is a fixed direction in the internal space transforming according to the X_5^+ irrep.
           The fixed direction is defined by the vectors of components: $(\pm|c_1|, \mp|c_2|, 0)$, with $\pm|c_1| \approx 0.90$ and $\pm|c_2| \approx 0.40$.
         - Experimental structures described by both vectors are equivalent.
         - Experimental structures described by a different vector, that is, with a different sign-combination of the components and/or with a relative-value big difference between the components, is not a correct structure. The relaxation process brings those experimental structures to the structure described by the fixed direction. Hence, these not correct structures should be re-visited.
      iii. The trilinear coupling between GM_4^+, X_3^+ and X_5^+ apart from being allowed by symmetry is necessary for the refinements and it is responsible for the encountered fixed direction

   (b) The proposed workflow which encompasses two levels of parametrization a) not all the freedom allowed by symmetry is used, *preferable directions* in the degrees of freedom space, equivalently in the irreps spanned space are present and 2) *preferable directions* in the possibly present multidimensional spaces associated with some irreps are present, thus, sits on stable physical grounds.

7. From the Sr_2LnSbO_6 family

   (a) The low tolerance-factor portion of the phase diagram constructed from the analyzed lanthanides matches perfectly in the phase diagram shown by the transition metals cations. That portion fills the gap shown in the phase diagram. That portion of the phase diagram divides it into two zones:

- $t <\approx 0.97$: with the $P2_1/n \rightarrow R\overline{3} \rightarrow Fm\overline{3}m$ phase-transition sequence item $1 > t >\approx 0.97$: with the $P2_1/n \rightarrow I2/m \rightarrow I4/m \rightarrow Fm\overline{3}m$ phase-transition sequence

It has been corroborated that the phase transitions are purely steric, in a gross way of saying.

- The materials containing Ho and Er, which are almost equal in size, show approximately (the same within the errors in the amplitude values) the same structures and phase-transition temperatures in the phase-transition sequence.
- Y not being a lanthanide but having approximately the same size as Ho and Er, shows the same structure and the same phase-transition temperatures in the phase-transition sequence.

(b) Systematically the system does not use all the freedom it gains when the symmetry breaks from the prototype phase to the distorted ones. In this context, the system is understood to be the set of degrees of freedom present in all the distorted phases appearing experimentally. That is, it is *systematically*, in all the materials showing the same phase-transition sequence, found that some mode-amplitudes are identically null (the experimental errors taken into account) and *coherently*, the same degrees of freedom are used or not used across materials and families of materials.

(c) A parametrization, at a higher level (transcending the multidimensional internal spaces transforming according to some irreps) is proposed. In these kind of materials (double perovskites) the experimental structures are described, in the phases showing the listed space groups, by the following irreps:

   i. $P2_1/n$: $\mathrm{GM}_4^+, \mathrm{X}_3^+$ and X_5^+ $(c_1 \approx, c_2 \approx, 0)$
   ii. $I2/m$: GM_4^+
   iii. $I4/m$: GM_4^+
   iv. $R\overline{3}m$: GM_4^+

8. From the $Sr_2Co_{1-x}Mg_xTeO_6$ and $Sr_2Ni_{1-x}Mg_xTeO_6$ systems

   (a) The proposed workflow is not infallible: wrong results could be inferred if it is applied blindly, taking for grant that its solid grounds are sufficient for obtaining good results.

   (b) Low-resolution or very low-resolution data and/or medium-resolution data but with a high pseudo-symmetry present in the system can lead to a large set of plausible final different results, i.e. crystal structures and their temperature evolution. This fact has shows the weakness of the workflow, if applied blindly.

   (c) A good parametrization of the atomic displacements parameters is needed to use the workflow properly. As for the rest of the parametrizations they should be deduced from high-resolution data.

Future work

M^{3+} Size effect in the Ca_2MSbO_6 (M = *Ln*, Y) and their Mode-amplitudes changing

In preparation

For many double perovskite oxides the size of the A cation is too small, thereby, the cavity formed by the twelve O atoms are stabilized, and octahedral tilting and shifts of cations occur, lowering the symmetry of the structure from that of the ideal cubic double perovskite. The effect of the cation size on the structure can be quantified by using the tolerance factor. Table 10.5 presents the calculated tolerance factors for Ca_2MSbO_6 materials, using Shannon ionic radii .[163] As can be observed, the values are smaller than the unit and also smaller than those for Sr_2MSbO_6 materials, which means that the fact of substituting the Strontium by the Calcium in the A-site leads to a more distorted structure: the Ca_2MSbO_6 materials are more distorted than the Sr_2MSbO_6 ones. Given that the $P2_1/n$ is the RT symmetry of Sr_2MSbO_6, the latter space group should be used as a starting model in the Rietveld analysis of the Ca_2MSbO_6 materials.

The monoclinic structure ($P2_1/n$ space group) is characterized by rock-salt like ordering, in this case, of the M^{3+} and Sb^{5+} cations, over alternative layers. The degree of cation ordering depends mostly on the charge difference, size, and polarization of B and B′ site cations of the double perovskite oxide with the general formula $A_2BB'O_6$. The M and Sb atoms are totally ordered in the two distinct B sites in Ca_2MSbO_6 compounds due to the significantly larger difference in the effective ionic radii of the $M^{3+} - Sb^{5+}$. According to our previous works on the calcium antimony family, the degree of ordering between the Ca^{2+} and M^{3+} cations depends of their sizes difference. It was found totally ordered in the case of Ca_2FeSbO_6 and partially ordered in the case of Ca_2SmSbO_6 and Ca_2LaSbO_6 .[139,140]

Room temperature X-ray powder diffraction data was recorded for the Ca_2MSbO_6 (M = Ln and Y) compounds. Figure 10.10a show the obtained patterns for the whole Antimony

---

[163] R. D. Shannon. *Acta Crystallogr. A* **32**: 751–767, 1976.

[139] A. Faik, J. M. Igartua, E. Iturbe-Zabalo, and G. J. Cuello. **963**: 145–152, 2010.

[140] A. Faik, I. Urcelay, E. Iturbe-Zabalo, and J.M. Igartua. *J. Mol. Struct.* **977**: 137–144, 2010.

Table 10.5: Preparation conditions of Ca_2MSbO_6 compounds. The data shown are as follows: Ionic radii in [3]; $\Delta r=|r_{M^{3+}} - r_{Sb^{5+}}|$; tolerance factor; highest temperature of treatment; the detected impurities; symmetry of the crystal structure at room temperature and literature reference. PW stands for present work.

Compound	I.R(Å)	Δr(Å)	t	S.T.(K)	Impurities	SG. at 300K	Ref.
Ca_2NdSbO_6	0.983	0.383	0.8825	1770		$P2_1/n$	PW
Ca_2EuSbO_6	0.947	0.347	0.8900	1770	≤3% Eu_2O_3	$P2_1/n$	PW
Ca_2GdSbO_6	0.938	0.338	0.8916	1820		$P2_1/n$	PW
Ca_2DySbO_6	0.912	0.312	0.8970	1770	≤3% Dy_2O_3	$P2_1/n$	PW
Ca_2HoSbO_6	0.901	0.301	0.8991	1820	≤3% Ho_2O_3	$P2_1/n$	PW
Ca_2YSbO_6	0.900	0.300	0.8994	1820	≤3% Y_2O_3	$P2_1/n$	PW
Ca_2ErSbO_6	0.890	0.290	0.9014	1870		$P2_1/n$	PW
Ca_2TmSbO_6	0.880	0.280	0.9035	1870		$P2_1/n$	PW
Ca_2YbSbO_6	0.868	0.268	0.9060	1820	≤3% Yb_2O_3	$P2_1/n$	PW

Calcium family Ca_2MSbO_6. A close analysis of the collected data shows that many splitted peaks can be observed, as presented in Figure 10.10b. The refinements results using models of ordered structures show that the superlattice peaks did not fit well.

In order to clarify the exact cation distribution in this Ca_2MSbO_6 materials, the structure proposed in [32] was used as starting model, in which the Ca^{2+} and M^{3+} cations are partially disordered over the A and B sites. The results show a successful fitting of all the Ca_2MSbO_6 patterns in the monoclinic symmetry $P2_1/n$, using symmetry-mode analysis, and with a disordered distribution of the Ca^{2+} and M^{3+} over the A and B sites. As example, the Rietveld refinement results of Ca_2EuSbO_6 is shown in Figure 10.11. All diffraction lines are indexed based on a monoclinic symmetry with the $P2_1/n$ space group. It is worth noting that in this case we have used the same virtual structure listed in Table 6.1 to perform the symmetry-mode decomposition analysis.

The results of this analysis show that Ca^{2+} ions partially occupy the B site. The Ca_2MSbO_6 is represented as $[Ca_{1+x}M_{1-x}][M_xCa_{1-x}]SbO_6$. In addition, they show that the B and B′ ions are regularly ordered. The B′ site is occupied by only Sb^{5+} ion and B site is randomly occupied by Ca^{2+} and M^{3+} ions. The final atomic parameters, cell parameters and occupations for Ca_2MSbO_6 are listed in Table 10.6.

As expected, the Ca_2MSbO_6 structures show higher values of the primaries modes amplitudes, GM^{4+}, X^{3+} and X^{5+}, than the ones observed at room temperature for the Sr_2MSbO_6 materials, this may be argued by the fact that the magnitudes of the octahedral rotations and tilts increase by the A-site cation size decrease (Sr_2MSbO_6 to Ca_2MSbO_6). Such a scenario, is happening inside the Ca_2MSbO_6 family itself: since the A-site is randomly occupied by Ca^{2+} and M^{3+}, the M cation size decrease reduces the octahedral tilts. The distortion-mode amplitudes in the title family, are plotted in Figure 10.12.

The variation of lattice parameters for Ca_2MSbO_6 materials with the tolerance factor is plotted in Figure 10.14. The lattice parameters a, b and c trend to reduce with increasing the tolerance factor (decreasing the M^{3+} ion size). However, a subtle, but very important, change in the cell parameters evolution slope was noticed between Ca_2GdSbO_6 and

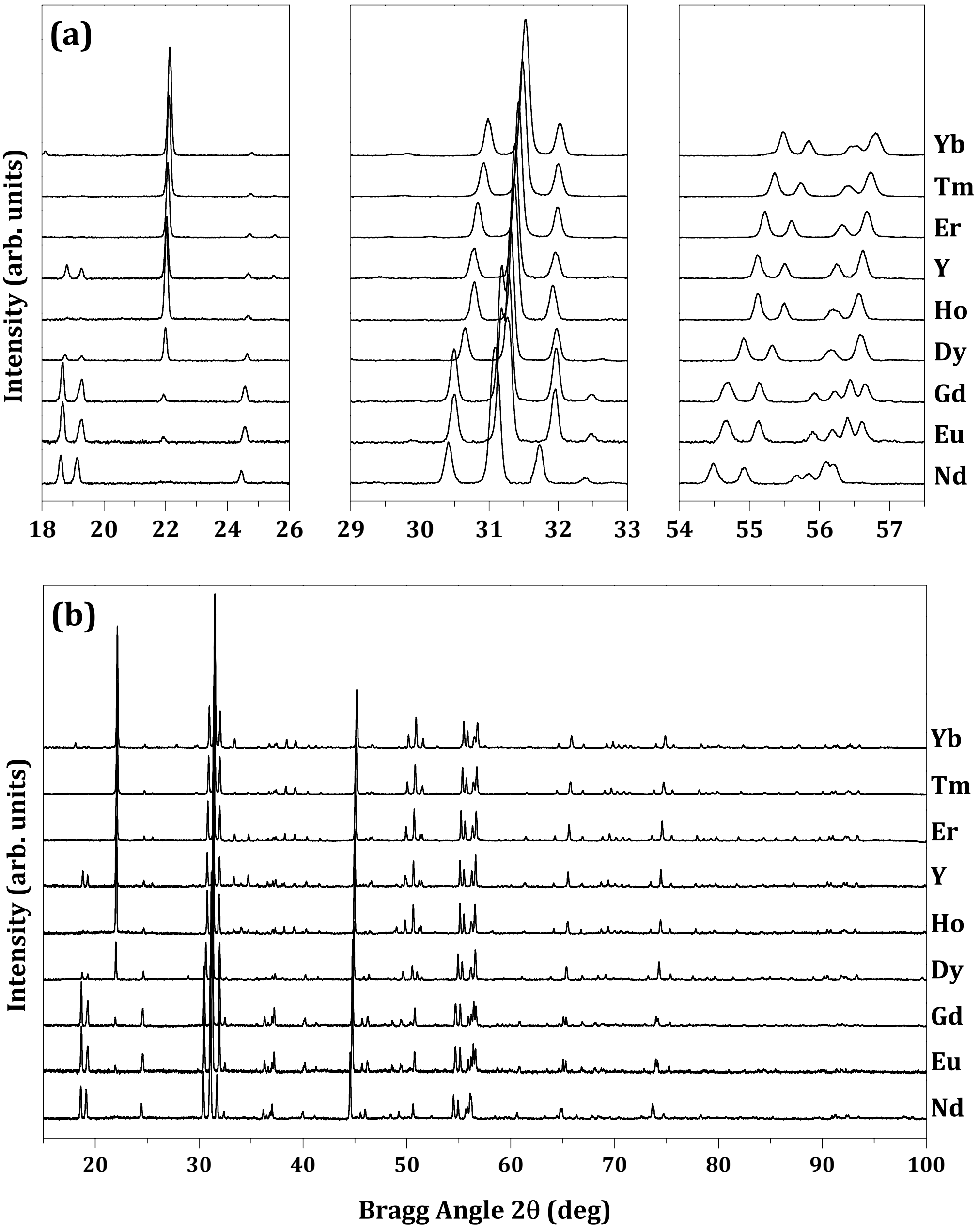

Figure 10.10: (a) Evolution of the laboratory X-ray powder diffraction patterns of Ca_2MSbO_6 (M = Nd, Eu, Gd, Dy, Ho, Er, Tm, Yb and Y) at RT. (b) Details from the X-ray powder diffraction patterns of the latter compounds in the selected 2θ intervals; 18°-26°, 29°-33° and 54°-57°, to show the continuous evolution of the patterns with the ionic radius of the M^{3+} cation.

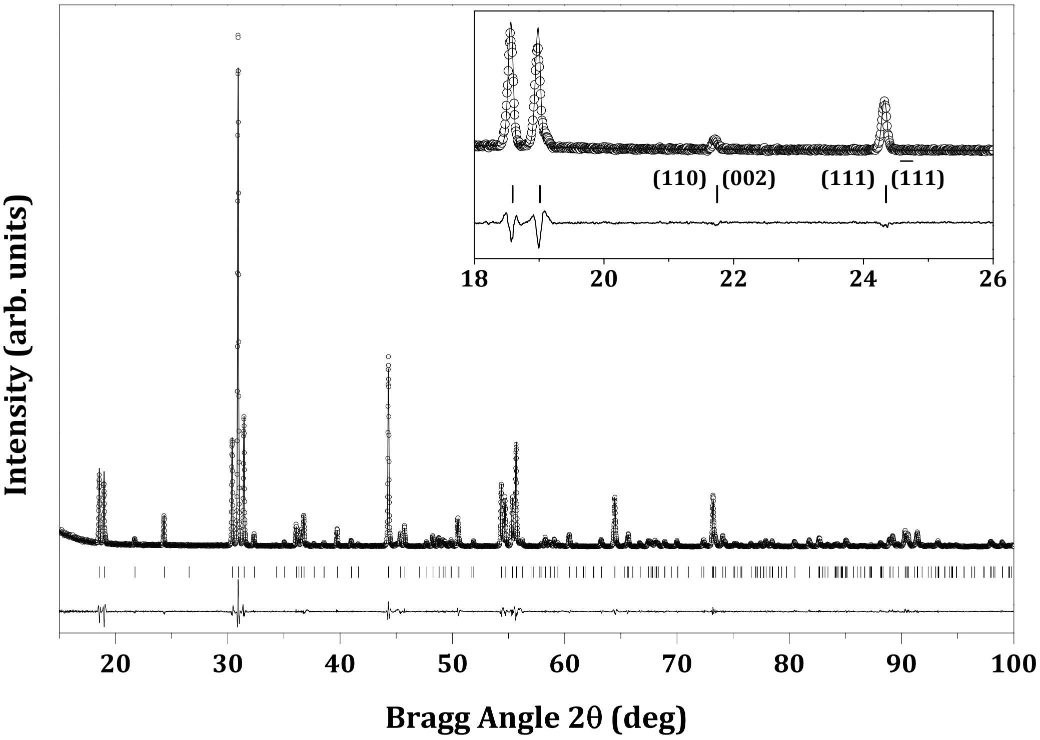

Figure 10.11: Experimental (symbols) and calculated (line) X-ray powder diffraction profiles for the Rietveld refinement of Ca_2EuSbO_6 at room temperature using a structural model with $P2_1/n$ space group. Insets shows in detail the presence of the primitive Bragg peaks corresponding to the $P2_1/n$ symmetry.

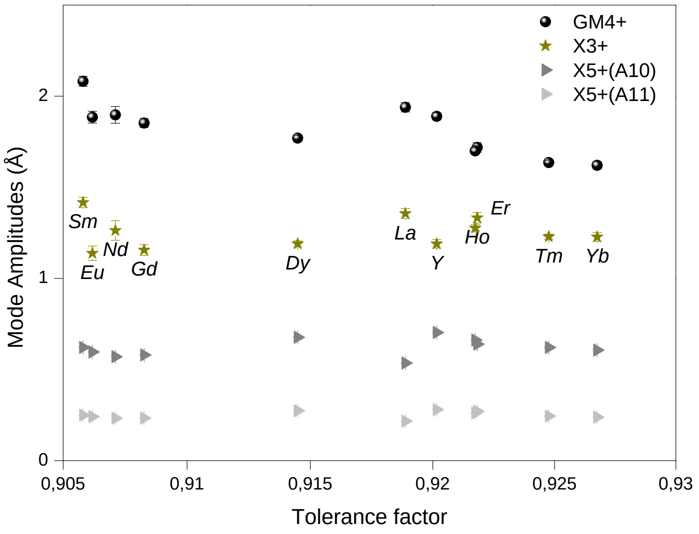

Figure 10.12: Variation of the GM_4^+, X_3^+ and X_5^+ distortion irreps in the monoclinic symmetry $P2_1/n$ consolidating the RT phases of Ca_2MSbO_6 M = Ln (Nd, Eu, Gd, Dy, Ho, Er, Tm, Yb and Y materials, as function of the tolerance factor. The red balls stand for the Ca_2YSbO_6 amplitudes, since the Yttrium, Y, does not belong to the Lanthanides. The dashed lines are guide of the eye to follow the evolution of each irrep.

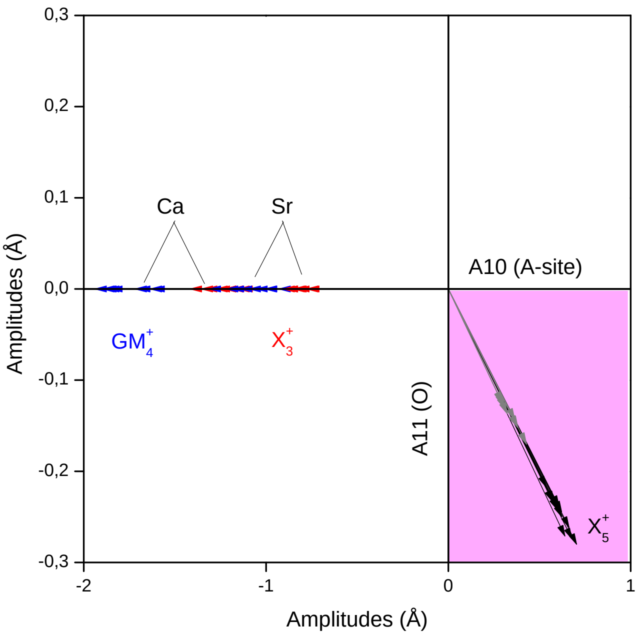

Figure 10.13: Two dimensional section showing the obtained amplitudes of the irreps (Blue) GM_4^+, (Red) X_3^+ and the two components of the tri-dimensional X_5^+: A10 in x-axis and A11 in y, for Ca_2MSbO_6. The results from Sr_2MSbO_6 family, studied in Chapter 8, are shown as well, for comparison.

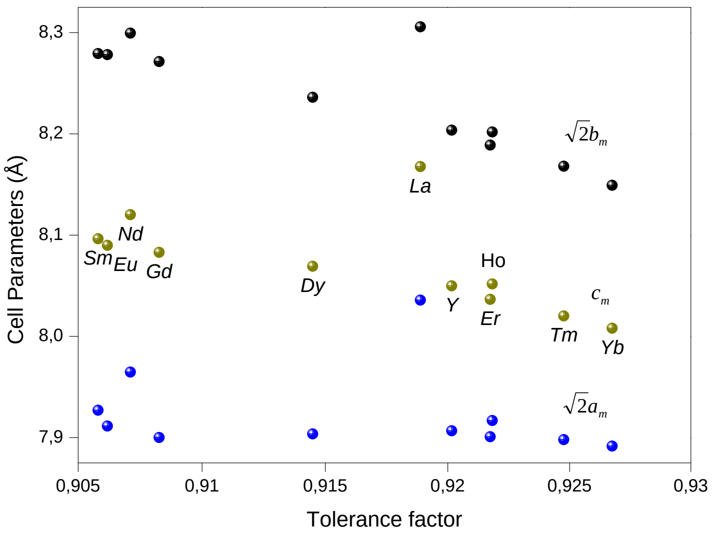

Figure 10.14: Evolution, as a function of the tolerance factor increasing of the unit-cell parameters (a), the unit-cell volume (b) and the monoclinic angle (β) (b) at room temperature of the synthesized materials Ca_2MSbO_6 (M = Nd, Eu, Gd, Dy, Ho, Er, Tm, Yb and Y

Ca_2DySbO_6.

The results obtained for the nine members of the calcium antimony family are in agreement with the previous works obtained in the antimony family [139,140] and also in the ruthenium family .[191] The lanthanide cation enters in the A-site position, displacing the Ca^{2+} cation to the B-site, but depending on the size of the lanthanide, the displacing effect is different. The figure 11 shows the evolution of the occupancy with the ionic radii of the M^{3+} in the antimony and the ruthenium families. It is revealed that the x value depends on the M^{3+} radius. For the compounds Ca_2MSbO_6 (M = Nd, Eu and Gd), the Ca^{2+} ion mainly occupies the A-site. For Ca_2MSbO_6 (M = Dy, Ho, Er, Tm, Yb and Y), the Ca^{2+} ion is gradually replaced by the M^{3+} ion at the A-site. This drastic change is in agreement with the one of the lattice parameters.

---

[191] C. Sakai, Y. Doi, and Y. Hinatsu. *J. Alloy. Compd.* ,

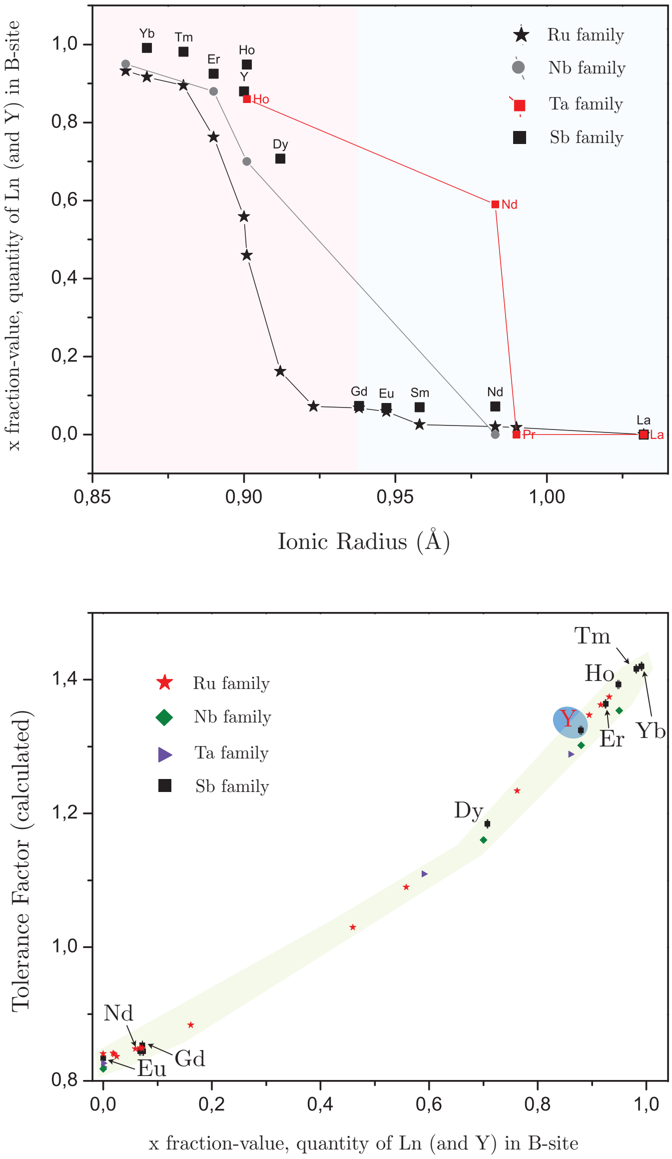

Figure 10.15: Evolution of the occupancy x (which is the fraction of the Calcium in the B-site occupying by the M^{3+} element in the formula $[Ca_{1+x}M_{1-x}][M_xCa_{1-x}]SbO_6$) with the ionic radii of the M^{3+} in the antimony and the ruthenium families .[191]

Table 10.6: Crystal structure data and refinement results, at room temperature for Ca_2MSbO_6; M = Ln (Nd, Eu, Gd, Dy, Ho, Er, Tm, Yb) and Y), from X-ray powder diffraction. Sb atoms occupy the site 2c (0, 1/2, 0); M2/Ca2 atoms occupy the site 2d (1/2, 0, 0); Sr atoms occupy the site 4e (x, y, z) and O atoms occupy the site 4e (x,y, z). The B_{iso} values for M and Ca cations were fixed in 0.5 ^{2} in order to guarantee the refinement convergence.

Compound		Ca_2NdSbO_6	Ca_2EuSbO_6	Ca_2GdSbO_6	Ca_2DySbO_6	Ca_2HoSbO_6	Ca_2YSbO_6	Ca_2ErSbO_6	Ca_2TmSbO_6	Ca_2YbSbO_6
M1/Ca2 (4*e*)	x	0.0095(5)	0.0090(2)	0.0080(5)	0.0012(2)	0.0012(2)	0.0011(1)	0.0010(8)	0.0010(3)	0.0120(1)
	y	0.0470(2)	0.0460(2)	0.0450(2)	0.0490(1)	0.0510(2)	0.0520(2)	0.0500(1)	0.0510(1)	0.0551(4)
	z	0.2520(1)	0.2515(1)	0.2510(5)	0.2520(1)	0.2520(1)	0.2530(3)	0.2520(1)	0.2520(6)	0.2551(1)
O1 (4*e*)	x	0.268(1)	0.263(1)	0.262(2)	0.271(1)	0.273(1)	0.274(2)	0.272(2)	0.270(7)	0.284(2)
	y	0.289(5)	0.285(8)	0.284(5)	0.292(1)	0.294(3)	0.295(1)	0.294(2)	0.298(6)	0.302(8)
	z	0.041(6)	0.037(5)	0.039(1)	0.044(3)	0.046(1)	0.047(3)	0.049(1)	0.049(2)	0.059(1)
O2 (4*e*)	x	0.305(6)	0.300(5)	0.299(3)	0.307(4)	0.309(2)	0.310(2)	0.309(2)	0.312(5)	0.319(2)
	y	0.278(3)	0.272(1)	0.271(2)	0.282(2)	0.284(7)	0.283(2)	0.281(7)	0.285(2)	0.291(3)
	z	0.475(6)	0.470(3)	0.471(1)	0.461(1)	0.459(1)	0.457(3)	0.461(1)	0.456(1)	0.443(1)
O3 (4*e*)	x	0.870(1)	0.867(5)	0.866(1)	0.876(3)	0.878(8)	0.880(9)	0.876(2)	0.879(8)	0.896(1)
	y	0.484(6)	0.464(1)	0.504(1)	0.494(6)	0.496(2)	0.498(5)	0.484(2)	0.497(2)	0.454(4)
	z	0.238(2)	0.235(4)	0.244(1)	0.239(1)	0.241(7)	0.241(3)	0.240(1)	0.241(5)	0.234(1)
Occupancy	Ca1/M1	0.75(1)	0.73(1)	0.55(1)	0.72(2)	0.95(1)	0.89(1)	0.92(2)	0.97(3)	0.98(2)
	M2/Ca2	0.25(1)	0.27(1)	0.45(1)	0.28(2)	0.05(1)	0.11(1)	0.08(2)	0.03(3)	0.02(2)
$B_{iso}(^2)$	Sb	0.98(1)	0.98(2)	0.99(2)	1.05(1)	1.10(1)	1.02(4)	1.04(2)	1.01(1)	1.00(1)
	O1, O2, O3	1.10(1)	1.15(2)	1.16(1)	1.12(4)	1.21(1)	1.34(2)	1.21(1)	1.410(7)	1.32(1)
Cell parameters	a(Å)	5.6310 (1)	5.5932(2)	5.5895(3)	5.5886(1)	5.5979(1)	5.5908(1)	5.5867(1)	5.5846(1)	5.5802(1)
	b(Å)	5.8685 (1)	5.8538(2)	5.8530(3)	5.8239(1)	5.7996(1)	5.8007(1)	5.7904(1)	5.7756(1)	5.7622(1)
	c(Å)	8.1199 (2)	8.0887(3)	8.0872(5)	8.0690(1)	8.0516(1)	8.0500(1)	8.0366(1)	8.0205(1)	8.0083(1)
	$\beta(^\circ)$	89.9(1)	89.8(2)	89.8(1)	89.6(6)	89.7(1)	89.5(1)	89.5(7)	89.4(7)	89.3(2)
	V(Å^3)	268.33(1)	264.83(1)	264.57(2)	262.62(4)	261.40(6)	261.07(7)	260.30(7)	258.70(7)	257.50(6)
Modes amplitudes	GM^{4+}	1.55(1)	1.58(2)	1.64(2)	1.64(2)	1.65(1)	1.66(2)	1.68(1)	1.69(4)	1.75(2)
	X^{3+}	0.72(2)	0.76(4)	0.75(1)	0.86(1)	0.90(5)	0.91(2)	0.88(2)	0.93(7)	1.01(1)
	X^{5+}	0.60(1)	0.58(7)	0.53(6)	0.57(1)	0.59(4)	0.60(3)	0.61(1)	0.59(3)	0.72(2)

Compositional uniformity as driving force of patterned orderings: Nano-chessboards NaLnMM'O_6

Some materials are subjected to spontaneous non-patterning and exhibit so-called chessboard arrangements. This self-patterning at the nanoscale can be of interest for potential applications, especially if it could be tuned (ex. Multiferroics) Nano-chessboards arrangements have been known for a long time, and appear in many compositionally flexible ordered phases.

Recently, the observation of alternative two dimensional ordered chessboard-like patterns in different compounds, as simple and double perovskites, has thrown a new light and rekindled interest in this phenomenon. These two-dimensional nano-patterns have been interpreted as the signature of some kind of phase segregation of spinodal decomposition.

In our case, in relation to these kind of orderings, the main idea was to go a step further in the analysis of double perovskites. Materials with the general formula NaLnMM'O_6, but in which a layer ordering scheme of the A and A' site cations, having very different size and charge, gives rise to a different set of possible structural symmetries. With this kind of ordering, it can be demonstrated that the prototype symmetry is described by the space group $P4/nmm$, and one of the subgroups of that tetragonal is a the polar (which has no inversion) $P2_1$ (Figure 10.16), so that ferroelectricity could be present. At the same time, placing a magnetic cation (for instance Co or Mn), could give rise to magnetic properties that eventually can couple to the electric ones, giving rise to the multiferroic magnetoelectric properties. Theoretically, these materials are good candidates to show the coexistence of ferroelectricity and ferromagnetism (multiferroic behavior).

The series NaLnMM'O_6 (Ln= La, Nd, Pr; M= Co, Mn and M'= W, Te) has synthesized and analyzed by preliminary XRD and the data show a pure samples with high crystallinity. While the room temperature NPD data has shown many extra peaks. In order to have a view on the microscopical structures of the materials, SEM analysis have been carried out, and the results have shown that the samples are highly pure and homogeneous. Following

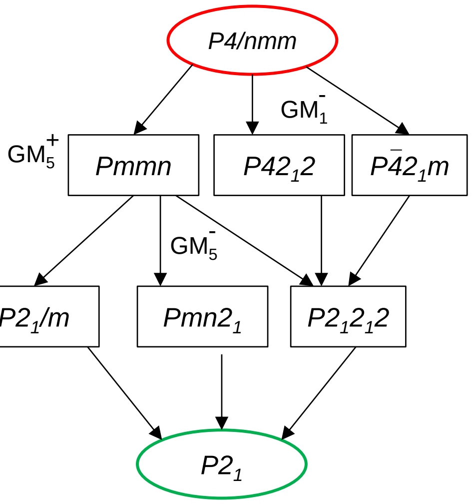

Figure 10.16: Group-subgroup tree connecting the paraelectric $P4/nmm$ phase to the ferroelectric $P2_1$ phase

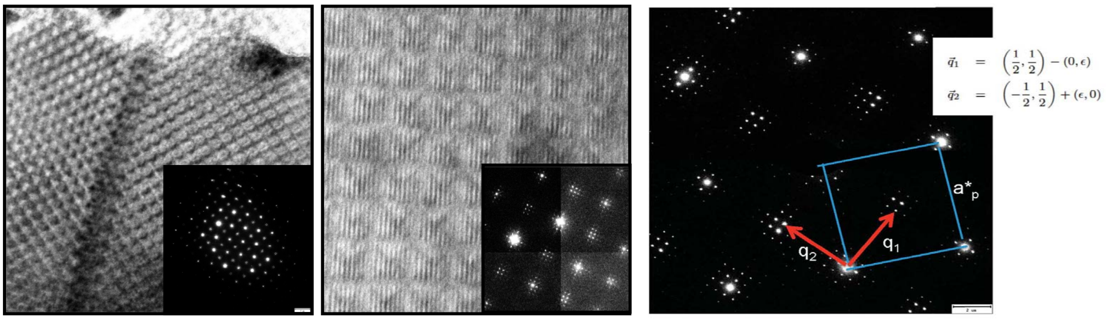

Figure 10.17: Images in the real space and in the reciprocal space, showing clearly the Nano-Chessboard structure.

some the work done by some research groups on this kind of materials, TEM measurements have been done and the results show the existence of satellites, which are responsible of the new set of peak we were observing in the NPD data (Figure 10.17).

Based on the Electron Microscopy diffraction images, a 'toy model' was prepared, which describes those observed structures in TEM measurements (Figure 10.18). An approximate cell parameters were calculated from the diffraction spots, giving a kind of big cells $\simeq 8.a_{2p} \simeq 45$ Å. The cell parameters calculated from those reflections, have described perfectly the pattern we collected including the new set of small reflections.

A theoretical model has been prepared (based on two q-vectors modulation vectors), which serves to explain some kind of similar diffraction images (Figure 10.17).

The model describes perfectly the patterns we have obtained, assumes a non-fixed

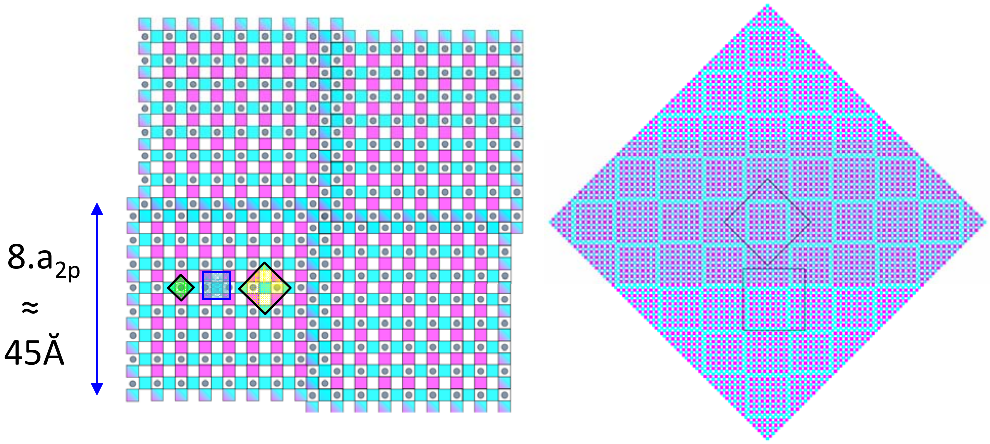

Figure 10.18: Theoretical models describing the Nano-Chessboards structure.

stoichiometry that shows a long range ordering. In this model, even in the same preparation of the material, different crystallites could show a different long range order.

The key point in our view is that all the materials we have analyzed show the multiplication of the standard double perovskite cell. This multiplication scheme can be described by a bi-dimensional modulation vector, which is different in modulus and direction from one to the other. As mentioned previously, we want to prove that the modulation vector is different also from one crystallite to another one in different samples of the same preparation for the same material.

These two-dimensional square-like 'Nano-Patterns' have been interpreted as the signature of some kind of phase segregation or synodal decomposition, but subjected to some unknown ordering constraints. We have recently shown, however, that these patterns may be explained, instead, as a single coherent phase, where some minority compositional motif becomes long-range ordered in response to an intrinsic drive to maximal uniformity. In fact, a simple two dimensional lattice that simulates a binary system in which the dilution of the minority component is energetically privileged, is sufficient to generate a hierarchy of ordered arrangements similar to the observed 'Nano-Chessboards' and 'Nano-Striped' patterns. Thus, according to these results, these configurations would be long-period limiting case of composition-dependent ordered superstructures, stabilized by the quest for maximal compositional dilution.

Raman scattering and high temperatures studies on double perovskites

The information obtained from well done Raman experiments is very valuable and good complementary technique for the structural and phase-transitions studies.

The idea is to complete the studies we have doing, on the perovskites we have being analyzing, by performing Raman experiments at low-temperature (LT), room-temperature (RT) and high-temperature (HT) for a very large series of materials, with different combinations of cations, having different symmetries at RT and showing different phase-transitions sequences.(see Table 10.7).

The main objectives of those experiments is to perform a systematic study, in order to extract:

1- The band distributions in the Raman shift axis (this is obvious from previous studies)

2- The statistics for the present bands in the phases with the same symmetry: One point is the active Raman modes, which give rise to observable bands, although, perhaps, not all of them observable, for several reasons some reasons could be related to the type of material (a perovskite, in our case, ordered, with a known set of cations) and to the symmetry of the phase we could try to extract some conclusions about the symmetry just counting the observed bands.

3- If the distribution of these band is irrespective of the temperature: Many phases show the same symmetry but at different temperatures, the point is to see if for the same symmetry, the same bands are going to be present.

4- Does it happen for different phase-transition sequences?

5- Can we infer something from the evolution of the present bands in temperature? and in the different phase-transition sequences?

6- Are there common features in the evolution of the bands, just because of the

Table 10.7: The possible materials and their corresponding phase-transitions sequences.

Sr2MSbO$_6$	
Co	$P2_1/n \rightarrow R\bar{3}$
Al	$Fm\bar{3}m$
Cr	$P2_1/n \rightarrow I4/m \rightarrow Fm\bar{3}m$
Nd, Eu, Sm, La	$P2_1/n \rightarrow R\bar{3} \rightarrow Fm\bar{3}m$
Fe, Ga,	$P2_1/n \rightarrow I4/m \rightarrow Fm\bar{3}m$
Sc, In	$P2_1/n \rightarrow I2/m \rightarrow I4/m \rightarrow Fm\bar{3}m$
Mn	$I4/m \rightarrow Fm\bar{3}m$
Na$_{0.5}$K$_{0.5}$NbO$_3$	$P2_1/n \rightarrow Bmm2 \rightarrow P4mm \rightarrow Pm\bar{3}m$
Ca$_2$MSbO$_6$	$P2_1/n$
Sr2MTeO$_6$	
Sr2Co$_{1-x}$Mn$_x$TeO$_6$	$P2_1/n \rightarrow I2/m \rightarrow I4/m \rightarrow Fm\bar{3}m$
Sr2Co$_{1-x}$MFe$_x$TeO$_6$	$P2_1/n \rightarrow I2/m \rightarrow I4/m \rightarrow Fm\bar{3}m$
Sr2Co$_{1-x}$Mg$_x$TeO$_6$	$P2_1/n \rightarrow I2/m \rightarrow I4/m \rightarrow Fm\bar{3}m$
Sr2Ni$_{1-x}$Mg$_x$TeO$_6$	$P2_1/n \rightarrow I4/m \rightarrow Fm\bar{3}m$
Sr2Mn$_{1-x}$Mg$_x$TeO$_6$	$P2_1/n \rightarrow I2/m \rightarrow I4/m \rightarrow Fm\bar{3}m$
Sr2Fe$_{1-x}$Mg$_x$TeO$_6$	$P2_1/n \rightarrow I4/m \rightarrow Fm\bar{3}m$
SrNdMRuO$_6$	$P2_1/n \rightarrow P42/n \rightarrow Fm\bar{3}m$
SrPrMRuO$_6$	$P2_1/n \rightarrow R\bar{3} \rightarrow Fm\bar{3}m$
SrLaMRuO$_6$	$P2_1/n \rightarrow R\bar{3}$
SrPrFeRuO$_6$	$Pbnm \rightarrow R\bar{3}$

symmetry change?

After all this, perhaps, a "simple" test by Raman could clarify the position of the material in a classifying table of double perovskites. Simple, means there are no misprize at all: referring to a preliminary readily performable inexpensive test, which could place the material in the general context of the double perovskites.

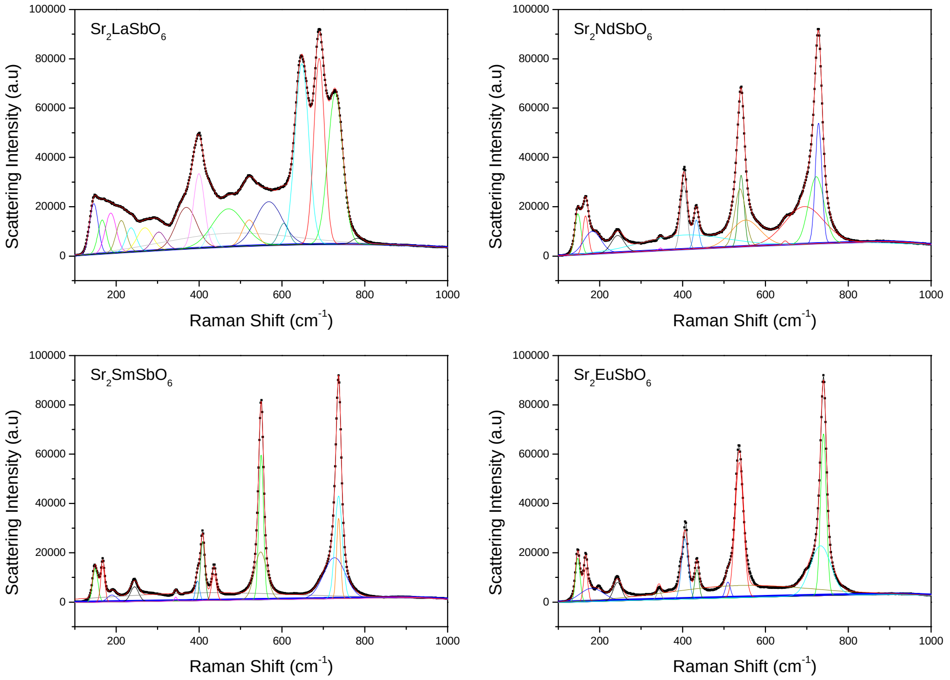

Figure 10.19: Raman spectra of the monoclinic Sr_2MSbO_6 (M=La, Nd, Sm and Eu) measured at room temperature. Experimental data are in open circles, while the fitted curves are in colored lines.

Appendices

Appendix A

Symmetry-mode decomposition of the structures

For the symmetry mode analysis, many mode decompositions have been done for different materials, some of them are mainly the purposes of the thesis, and some others have been in our work for a comparative purpose. In order not to lose all the calculations and for a future need for other users, all the information is collected in the following pages. All the information is given in the ’Bilbao Crystallographic Server’ format, ready to be used for all the programs.

A.1 Symmetry-mode decomposition of perovskite structures

A.1.1 $Fm\bar{3}m$ (ITA No. 225) $\rightarrow$ $P2_1/n$ (ITA No. 14)

```
High symmetry structure
Setting used: FM-3M

225
8.3259 8.3259 8.3136 90 90 90
4
M   1  4a  0.0000  0.0000  0.0000
Sb  1  4b  0.5000  0.0000  0.0000
Ca  1  8c  0.2500  0.7500  0.2500
O   1  24e 0.5000  0.7708  0.0000

# Transformation matrix (Setting P121/n1)
[   1/2   1/2     0 ] [   -1/4]
[  -1/2   1/2     0 ] [    1/4]
[     0     0     1 ] [      0]
```

```
Low symmetry structure
Setting used: P121/N1

#Ca2SmSbO6
14
5.6820 5.8729 8.1676 90. 89.98 90.
6
Sb  1  2c  0.0000  0.5000  0.0000
M   1  2d  0.5000  0.0000  0.0000
Ca  2  4e  0.0150  0.0569  0.2466
O   1  4e  0.3310  0.2930  0.0690
O   2  4e  0.2890  0.3180  0.4530
O   3  4e  0.8810  0.4430  0.2690

#Ca2LaSbO6
14
5.6820 5.8729 8.1676 90. 89.98 90.
6
Sb  1  2c  0.0000  0.5000  0.0000
La  1  2d  0.5000  0.0000  0.0000
Ca  1  4e  0.0108  0.0496  0.2486
O   1  4e  0.3260  0.2950  0.0640
O   2  4e  0.2950  0.3110  0.4510
O   3  4e  0.8990  0.4570  0.2630

#Ca1.5Sr0.5SmSbO6
14
5.6535 5.8692 8.1375 90. 90.07 90.
6
Sb  1  2c  0.0000  0.5000  0.0000
Sm  1  2d  0.5000  0.0000  0.0000
Ca  2  4e  0.0134  0.0536  0.2473
O   1  4e  0.3070  0.2960  0.0450
O   2  4e  0.3050  0.2950  0.4360
O   3  4e  0.8910  0.4520  0.2420

#Ca1.5Sr0.5LaSbO6
14
5.703 5.8864 8.2065 90. 89.93 90.
6
Sb  1  2c  0.0000  0.5000  0.0000
La  1  2d  0.5000  0.0000  0.0000
Ca  1  4e  0.0114  0.0467  0.2491
O   1  4e  0.3090  0.2990  0.0580
O   2  4e  0.3060  0.2980  0.4510
O   3  4e  0.9030  0.4650  0.2490
```

```
#CaSrSmSbO6
14
5.7110 5.8856 8.1932 90. 90.07 90.
6
Sb  1  2c  0.0000  0.5000  0.0000
Sm  1  2d  0.5000  0.0000  0.0000
Ca  2  4e  0.0147  0.0487  0.2489
O   1  4e  0.3010  0.2590  0.0710
O   2  4e  0.2750  0.3060  0.4450
O   3  4e  0.8930  0.4540  0.2650
```

```
#CaSrLaSbO6
14
5.7756 5.9020 8.2448 90. 89.86 90.
6
Sb  1  2c  0.0000  0.5000  0.0000
Sm  1  2d  0.5000  0.0000  0.0000
Ca  1  4e  0.0103  0.0442  0.2498
O   1  4e  0.3050  0.2760  0.0550
O   2  4e  0.2780  0.3020  0.4520
O   3  4e  0.9000  0.4690  0.2620
```

```
#Sr2CoTeO6
14
5.6437 5.6096 7.9271 90.00 90.06 90.00
6
Te  1  -  0.0000  0.5000   0.0000
Co  1  -  0.0000  0.0000  -0.5000
Sr  1  -  0.4999  0.0066  -0.2507
O   1  -  0.9499  0.0028   0.2376
O   2  -  0.2751  0.2452   0.4721
O   3  -  0.7536  0.2727  -0.4776

#Sr2Co0.9Mg0.1TeO6
14
5.6424 5.6088 7.9240 90.00 90.06 90.00
6
Sr  1  -  0.5003  0.0043  -0.2503
Co  1  -  0.0000  0.0000  -0.5000
Te  1  -  0.0000  0.0000   0.0000
O   1  -  0.9509  0.0031   0.2381
O   2  -  0.2717  0.2473   0.4727
O   3  -  0.7510  0.2704  -0.4783
```

```
Symmetry Modes Summary
Atoms WP Modes
O1  24e GM1+(1) GM3+(1) GM4+(1) GM5+(2) X2+(1) X3+(1) X5+(2)
Ca1 8c  GM5+(2) X5+(1)

Summary of Amplitudes
K-vector Irrep Direction Isotropy Subgroup Dimension
(0,0,0) GM1+ (a)             Fm-3m (225)    1
(0,0,0) GM3+ (a,0)           I4/mmm (139)   1
(0,0,0) GM4+ (a,a,0)         C2/m (12)      1
(0,0,0) GM5+ (-b,a,-a)       C2/m (12)      4
(0,1,0) X2+  (0,a,0)         P4_2/mnm (136) 1
(0,1,0) X3+  (0,a,0)         P4/mnc (128)   1
(0,1,0) X5+  (a,a,0,0,a,-a)  Pnnm (58)      3
```

```
High symmetry structure
Setting used: FM-3M

225
7.920942 7.920942 7.920942 90.00 90.00 90.00
4
Ru  1  4a   0.0000  0.0000  0.0000
M   1  4b   0.5000  0.5000  0.5000
Ca  1  8c   0.2500  0.2500  0.2500
O   1  24e  0.2471  0.0000  0.0000

# Transformation matrix (Setting P121/n1)
[   1/2   1/2     0 ] [      0]
[  -1/2   1/2     0 ] [      0]
[     0     0     1 ] [      0]
```

```
Low symmetry structure
Setting used: P121/N1

#Ca2LaRuO6
14
5.6300 5.7170 8.2400 90.00 90.25 90.00
6
Ca  1  -  0.5127   0.0536  -0.2488
La  2  -  0.0000   0.0000  -0.5000
Ru  1  -  0.5000  -0.5000  -0.5000
O   1  -  0.2164  -0.3190  -0.5465
O   2  -  0.3232   0.2193  -0.5603
O   3  -  0.3935  -0.5423  -0.2693

#Ca2NdRuO6
14
5.5564 5.8296 8.0085 90.00 90.07 90.00
6
Ca  1  -  0.5145   0.0590  -0.2455
Nd  2  -  0.0000   0.0000  -0.5000
Ru  1  -  0.5000  -0.5000  -0.5000
O   1  -  0.2131  -0.3238  -0.5514
O   2  -  0.3280   0.2198  -0.5664
O   3  -  0.3882  -0.5494  -0.2709

#Ca2HoRuO6
14
5.4991 5.7725 7.9381 90.00 90.18 90.00
6
Ca  1  -  0.5167   0.0620  -0.2445
Ho  2  -  0.0000   0.0000  -0.5000
Ru  1  -  0.5000  -0.5000  -0.5000
O   1  -  0.2123  -0.3212  -0.5545
O   2  -  0.3277   0.2182  -0.5678
O   3  -  0.3835  -0.5518  -0.2697

#Ca2YRuO6
14
5.5239 5.7770 7.9637 90.00 90.23 90.00
6
Ca  1  -  0.5150   0.0584  -0.2466
Y   2  -  0.0000   0.0000  -0.5000
Ru  1  -  0.5000  -0.5000  -0.5000
O   1  -  0.2129  -0.3203  -0.5536
O   2  -  0.3260   0.2176  -0.5661
O   3  -  0.3860  -0.5490  -0.2686
```

```
#Ca2YbRuO6
14
5.5153 5.7011 7.9059 90.00 90.31 90.00
6
Ca  1  -  0.5156   0.0561  -0.2500
Yb  2  -  0.0000   0.0000  -0.5000
Ru  1  -  0.5000  -0.5000  -0.5000
O   1  -  0.2138  -0.3134  -0.5520
O   2  -  0.3179   0.2175  -0.5580
O   3  -  0.3957  -0.5404  -0.2659

#Ca2LuRuO6
14
5.5200 5.5910 8.0610 90.00 90.21 90.00
6
Ca  1  -  0.5151   0.0556  -0.2492
Lu  2  -  0.0000   0.0000  -0.5000
Ru  1  -  0.5000  -0.5000  -0.5000
O   1  -  0.2194  -0.3078  -0.5552
O   2  -  0.3167   0.2184  -0.5580
O   3  -  0.3976  -0.5375  -0.2642
```

```
Symmetry Modes Summary
Atoms WP Modes
O1  24e GM1+(1) GM3+(1) GM4+(1) GM5+(2) X2+(1) X3+(1) X5+(2)
Ca1 8c  GM5+(2) X5+(1)

Summary of Amplitudes
K-vector Irrep Direction Isotropy Subgroup Dimension
(0,0,0) GM1+ (a)             Fm-3m (225)    1
(0,0,0) GM3+ (a,0)           I4/mmm (139)   1
(0,0,0) GM4+ (a,a,0)         C2/m (12)      1
(0,0,0) GM5+ (-b,a,-a)       C2/m (12)      4
(0,1,0) X2+  (0,a,0)         P4_2/mnm (136) 1
(0,1,0) X3+  (0,a,0)         P4/mnc (128)   1
(0,1,0) X5+  (a,a,0,0,a,-a)  Pnnm (58)      3
```

```
High symmetry structure
Setting used: FM-3M

225
7.920942 7.920942 7.920942 90.00 90.00 90.00
4
Mn  1  4a  0.0000  0.0000  0.0000
M   1  4b  0.5000  0.5000  0.5000
Ln  1  8c  0.2500  0.2500  0.2500
O   1  24e 0.2471  0.0000  0.0000

# Transformation matrix (Setting P121/n1)
[   1/2   1/2     0 ] [      0]
[  -1/2   1/2     0 ] [      0]
[     0     0     1 ] [      0]
```

```
#Sm2NiMnO6
14
5.3524 5.5119 7.6103 90.00 90.03 90.00
6
Sm  1  -  0.4872  0.0542  0.2483
Ni  1  -  1.0000  0.0000  0.5000
Mn  1  -  1.0000  0.0000  0.0000
O   1  -  0.5925  0.4732  0.2724
O   2  -  1.2180  0.2740  0.0323
O   3  -  1.2066  0.2986  0.4408

#Lu2NiMnO6
14
5.1638 5.5467 7.4153 90.00 89.67 90.00
6
Lu  1  -  1.0208  0.5787  0.2499
Co  1  -  0.5000  0.5000  0.0000
Mn  1  -  1.0000  0.0000  0.0000
O   1  -  0.8841  0.9585  0.2411
O   2  -  0.6971  0.1957 -0.0575
O   3  -  0.8228  0.6953 -0.0593

#Nd2CoMnO6 #Physica Status Solidi, Sectio B: Basic Research (2007) 244, 3367-3376
14
5.4104 5.5405 7.6613 90.00 90.01 90.00
6
Nd  1  -  1.4910  0.0496  0.2506
Co  1  -  0.5000  0.5000  0.0000
Mn  1  -  1.0000  0.0000  0.0000
O   1  -  0.5833  0.4795  0.2531
O   2  -  1.2159  0.3020  0.4600
O   3  -  1.1938  0.2898  0.0438

#Nd2CoMnO6 #Journal of Magnetism and Magnetic Materials (2006) 302, 443-447
14
5.4260 5.5390 7.6580 90.00 90.23 90.00
6
Nd  1  -  1.4850  0.0450  0.2410
Co  1  -  0.5000  0.5000  0.0000
Mn  2  -  1.0000  0.0000  0.0000
O   1  -  0.5750  0.4790  0.2680
O   2  -  1.1860  0.3030  0.0450
O   3  -  1.2240  0.2790  0.4570
```

```
#La2VMnO6
14
5.6130 5.5679 7.8864 90.00 90.04 90.00
6
La  1  -  1.4935  0.0375  0.2492
Mn  1  -  1.0000  0.0000  0.0000
V   1  -  0.5000  0.5000  0.0000
O   1  -  0.7030  0.2250  0.9530
O   2  -  0.7290  0.1990  0.5290
O   3  -  1.0780  0.0120  0.7400

#Tb2NiMnO6
14
5.2740 5.5417 7.5302 90.00 89.81 90.00
6
Tb  1  -  0.4849  0.0658  0.2526
Ni  1  -  1.0000  0.0000  0.5000
Mn  1  -  1.0000  0.0000  0.0000
O   1  -  0.5917  0.4680  0.2577
O   2  -  1.1935  0.2779  0.0454
O   3  -  1.2012  0.3066  0.4468

#Y2NiMnO6
14
5.2258 5.5573 7.4824 90.00 89.76 90.00
6
Y   1  -  0.4818  0.0734  0.2484
Ni  1  -  1.0000  0.0000  0.5000
Mn  2  -  1.0000  0.0000  0.0000
O   1  -  0.6018  0.4670  0.2549
O   2  -  1.1830  0.2935  0.0543
O   3  -  1.2006  0.3170  0.4480

#Bi2NiMnO6
14
5.4039 5.5668 7.7330 90.00 90.17 90.00
6
Bi  1  -  0.0049  0.5468  0.2510
Ni  1  -  0.5000  0.5000  0.0000
Mn  1  -  0.0000  1.0000  0.0000
O   1  -  0.2800  0.7790  0.4770
O   2  -  0.2810  0.7810  0.0530
O   3  -  0.5940  0.4780  0.2520
```

```
#Ho2NiMnO6
14
5.244 5.593 7.515 90. 90.078 90.
6
Ho  1  -  0.0183  0.4277  0.7499
Ni  1  -  0.0000  0.0000  0.5000
Mn  2  -  0.0000  0.0000  0.0000
O   1  - -0.1054  0.0322  0.7498
O   2  -  0.1918  0.6965  0.5541
O   3  -  0.3081  0.1937  0.5546

#In2NiMnO6
14
5.1352 5.3372 7.5455 90.00 90.13 90.00
6
Mn  1  -  0.0000  0.0000  0.0000
Ni  1  -  1.0000  0.0000  0.5000
In  1  -  1.4804  0.0611  0.7525
O   1  -  0.8804  0.9363  0.7621
O   2  -  0.6992  0.1844  1.0626
O   3  -  1.1784  0.2914  0.9313

#La2CoMnO6 #Journal of Physics: Condensed Matter (2003) 15, 4927-4936
14
5.5252 5.4876 7.7787 90.00 89.95 90.00
6
La  1  -  0.5072  0.0239  0.2444
Co  1  -  0.5000  0.5000  0.0000
Mn  2  -  1.0000  0.0000  0.0000
O   1  -  0.7893  0.2654  0.0347
O   2  -  0.7645  0.2753  0.4631
O   3  -  1.0702 -0.0019  0.2436

#La2CoMnO6 #Journal of Experimental and Theoretical Physics (2004) 99, 363-369
14
5.5131 5.4624 7.7559 90.00 90.03 90.00
6
La  1  -  0.9895  0.5256  0.2390
Co  1  -  0.5000  0.5000  0.0000
Mn  1  -  0.0000  0.0000  0.0000
O   1  -  0.0553  0.9937  0.2544
O   2  -  0.7127  0.7708  0.0220
O   3  -  0.7442  0.7857  0.4660
```

```
#La2CoMnO6 #Barcelona
14
5.5123 5.4794 7.7600 90.00 89.92 90.00
6
La  1  - -0.0030  0.5223  0.2520
Co  1  -  0.5000  0.5000  0.0000
Mn  1  -  0.0000  0.0000  0.0000
O   1  -  0.0669  0.9907  0.2400
O   2  -  0.7370  0.7810  0.0369
O   3  -  0.7120  0.7710  0.4650

#La2NiMnO6 #Bull, Journal of Physics: Condensed Matter (2003) 15, 4927-4936
14
5.4670 5.5105 7.7512 90.00 90.12 90.00
6
La  1  -  0.5021  0.0522  0.2629
Ni  1  -  0.5000  0.5000  0.0000
Mn  2  -  0.0000  0.0000  0.0000
O   1  -  0.7505  0.2347  0.0231
O   2  -  0.7943  0.2928  0.4747
O   3  -  1.0434  0.0360  0.2430
```

```
Symmetry Modes Summary
Atoms WP Modes
O1   24e GM1+(1) GM3+(1) GM4+(1) GM5+(2) X2+(1) X3+(1) X5+(2)
Ln1 8c  GM5+(2) X5+(1)

Summary of Amplitudes
K-vector Irrep Direction Isotropy Subgroup Dimension
(0,0,0) GM1+ (a)             Fm-3m (225)    1
(0,0,0) GM3+ (a,0)           I4/mmm (139)   1
(0,0,0) GM4+ (a,a,0)         C2/m (12)      1
(0,0,0) GM5+ (-b,a,-a)       C2/m (12)      4
(0,1,0) X2+  (0,a,0)         P4_2/mnm (136) 1
(0,1,0) X3+  (0,a,0)         P4/mnc (128)   1
(0,1,0) X5+  (a,a,0,0,a,-a)  Pnnm (58)      3
```

A.1.2 $Fm\bar{3}m$ (ITA No. 225) $\rightarrow$ $R\bar{3}$ (ITA No. 148)

```
High symmetry structure
Setting used: FM-3M

225
7.920942 7.920942 7.920942 90.00 90.00 90.00
4
Ru  1  4a  0.0000  0.0000  0.0000
M   1  4b  0.5000  0.5000  0.5000
Sr  1  8c  0.2500  0.2500  0.2500
O   1  24e 0.2471  0.0000  0.0000

# Transformation matrix (Setting R-3 hexagonal)
[  -1/2     0     1 ] [      0]
[   1/2  -1/2     1 ] [      0]
[     0   1/2     1 ] [      0]


Low symmetry structure
Setting used: R-3:H

# SrPrMgRuO6 #E. Iturbe-Zabalo et al./ http://dx.doi.org/10.1088/0953-8984/25/20/205401
148
5.61494 5.61494 13.7096 90.00 90.00 120.00
4
Ru  1  3a  0.0000  0.0000  0.0000
Mg  1  3b  0.0000  0.0000  0.5000
Sr  1  6c  0.0000  0.0000  0.2467
O   1  18f 0.6645  0.8735  0.0781



Symmetry Modes Summary
Atoms WP Modes
O1  24e GM1+(1) GM4+(1) GM5+(1)
Sr1 8c  GM5+(1)
Note: The primary mode is written in bold letters

Summary of Amplitudes
K-vector Irrep Direction Isotropy Subgroup Dimension
(0,0,0)  GM1+  (a)         Fm-3m (225)      1
(0,0,0)  GM4+  (a,a,a)     R-3 (148)        1
(0,0,0)  GM5+  (a,a,a)     R-3m (166)       2
```

A.1.3 $Fm\bar{3}m$ (ITA No. 225) $\rightarrow$ $I2/m$ (ITA No. 12)

```
High symmetry structure
Setting used: FM-3M

225
7.920942 7.920942 7.920942 90.00 90.00 90.00
4
C 1 4a  0.0000 0.0000 0.0000
B 1 4b  0.5000 0.5000 0.5000
A 1 8c  0.2500 0.2500 0.2500
O 1 24e 0.2471  0.0000 0.0000

# Transformation matrix (Setting I12/m1)
[   1/2   1/2     0 ] [      0]
[  -1/2   1/2     0 ] [      0]
[     0     0     1 ] [      0]

Low symmetry structure
Setting used: I12/M1

#Sr2CrSbO6 # A. Faik et al./ http://dx.doi.org/10.1016/j.jssc.2009.04.014
012
5.5574 5.5782 7.8506 90.00 90.06 90.00
5
C 1  -  0.0000  0.0000  0.0000
B 1  -  0.0000  0.0000  0.5000
A 1  -  0.4999  0.0000  0.2504
O 1  - -0.0390  0.0000  0.2490
O 2  -  0.2460  0.2490  0.0150
```

```
Low symmetry structure
Setting used: I12/M1

#Sr2Co0.8Mg0.2TeO6
12
5.6380 5.6062 7.9176 90.00 89.93 90.00
5
Sr  1  - -0.4990  0.0000  0.7490
Co  1  - -0.5000  0.5000  0.0000
Te  1  -  0.0000  0.0000  0.0000
O   1  - -0.0490  0.0000  0.7540
O   2  - -0.2360  0.2470  0.0190

#Sr2Co0.5Mg0.5TeO6
12
5.6286 5.6013 7.9114 90.00 89.93 90.00
5
Sr  1  - -0.4990  0.0000  0.7498
Co  1  - -0.5000  0.5000  0.0000
Te  1  -  0.0000  0.0000  0.0000
O   1  - -0.0580  0.0000  0.7480
O   2  - -0.2420  0.2440  0.0220
```

```
Symmetry Modes Summary
Atoms WP Modes
O1  24e GM1+(1) GM3+(1) GM4+(1) GM5+(2)
A1 8c  GM5+(2)
Note: The primary mode is written in bold letters

Summary of Amplitudes
K-vector Irrep Direction Isotropy Subgroup Dimension
(0,0,0)  GM1+  (a)        Fm-3m (225)         1
(0,0,0)  GM3+  (a,0)      I4/mmm (139)       1
(0,0,0)  GM4+  (a,a,0)    C2/m (12)          1
(0,0,0)  GM5+  (-b,a,-a)  C2/m (12)          4
```

A.1.4 $Fm\bar{3}m$ (ITA No. 225) → $I4/m$ (ITA No. 87)

```
High symmetry structure
Setting used: FM-3M

225
7.920942 7.920942 7.920942 90.00 90.00 90.00
4
C  1  4a  0.0000  0.0000  0.0000
B  1  4b  0.5000  0.5000  0.5000
A  1  8c  0.2500  0.2500  0.2500
O  1  24e 0.2471  0.0000  0.0000

# Transformation matrix
[   1/2   1/2     0 ] [      0]
[  -1/2   1/2     0 ] [      0]
[     0     0     1 ] [      0]

Low symmetry structure
Setting used: I4/M

# A. Faik et al./J. Solid State Chemistry 182 (2009) 1717-1725
087
5.5668 5.5668 7.8899  90.00  90.00  90.00
5
C  1  2a  0.0000  0.0000  0.0000
B  1  2b  0.0000  0.0000  0.5000
A  1  4d  0.0000  0.5000  0.2500
O  1  4e  0.0000  0.0000  0.2431
O  2  8h  0.2825  0.2053  0.0000

Symmetry Modes Summary
Atoms WP Modes
O1 24e GM1+(1) GM3+(1) GM4+(1)
Note: The primary mode is written in bold letters

Summary of Amplitudes
K-vector Irrep Direction Isotropy Subgroup Dimension
(0,0,0)  GM1+  (a)         Fm-3m (225)      1
(0,0,0)  GM3+  (a,0)       I4/mmm (139)     1
(0,0,0)  GM4+  (0,0,a)     I4/m (87)        1
```

A.1.5 $Pm\bar{3}m$ (ITA No. 221) → $Amm2$ (ITA No. 38)

```
High symmetry structure
Setting used: PM-3M

221
4.0054 4.0054 4.0054 90.00 90.00 90.00
3
Na  1  1a  0.0000  0.0000  0.0000
Nb  1  1b  0.5000  0.5000  0.5000
O   1  3c  0.5000  0.0000  0.5000

# Transformation matrix (Setting Amm2)
[     0     1     1 ] [      0]
[     0    -1     1 ] [      0]
[     1     0     0 ] [      0]

Low symmetry structure
Setting used: AMM2

#Na0.5K0.5NbO3 #N. Ishizawa et al./ http://dx.doi.org/10.1016/j.jssc.2010.09.018
38
3.9710 5.6970 5.7210 90.00 90.00 90.00
4
Na  1  2a  0.0000  0.0000  -0.0010
Nb  1  2b  0.5000  0.0000  -0.5000
O   1  2a  0.0000  0.0000  -0.4613
O   2  4e  0.5000  0.2488  -0.2180

Symmetry Modes Summary
Atoms WP Modes
O1  3d GM4-(2) GM5-(1)
A1  1b GM4-(1)
B1  1a GM4-(1)
Note: The primary mode is written in bold letters

Summary of Amplitudes
K-vector Irrep Direction Isotropy Subgroup Dimension
(0,0,0)  GM4-  (a,a,0)    Amm2 (38)        4
(0,0,0)  GM5-  (0,a,-a)   Amm2 (38)        1
```

A.1.6 $Pm\bar{3}m$ (ITA No. 221) → $P4mm$ (ITA No. 99)

```
High symmetry structure
Setting used: PM-3M

221
4.0054 4.0054 3.9551 90.00 90.00 89.85
3
Na  1  1a  0.0000  0.0000  0.0000
Nb  1  1b  0.5000  0.5000  0.5000
O   1  3c  0.5000  0.0000  0.5000

# Transformation matrix
[     1     0     0 ] [      0]
[     0     1     0 ] [      0]
[     0     0     1 ] [      0]

Low symmetry structure
Setting used: P4MM

#PbVO3 #Alexei A. Belik et al./ http://dx.doi.org/10.1021/cm048387i
99
3.9551 3.9551 3.9551 90.00 90.00 90.00
4
Na  1  1a  0.0000  0.0000  0.0000
Nb  1  1b  0.5000  0.5000  0.5677
O   1  1b  0.5000  0.5000  0.2087
O   2  2c  0.5000  0.0000  0.6919

Symmetry Modes Summary
Atoms WP Modes
O1 3c GM4-(2)
Nb1 1b GM4-(1)
Na1 1a GM4-(1)
Note: The primary mode is written in bold letters

Summary of Amplitudes
K-vector Irrep Direction Isotropy Subgroup Dimension
(0,0,0)  GM4-   (0,0,a)     P4mm (99)        4
```

A.1.7 $Pm\bar{3}m$ (ITA No. 221) $\rightarrow$ $R3c$ (ITA No. 161)

```
High symmetry structure
Setting used: PM-3M

221
4.0054 4.0054 4.0054 90.00 90.00 90.00
3
Na  1  1a  0.5000  0.5000  0.5000
Nb  1  1b  0.0000  0.0000  0.0000
O   1  3c  0.5000  0.0000  0.0000

# Transformation matrix
[    -1     0     2 ] [      0]
[     1    -1     2 ] [      0]
[     0     1     2 ] [      0]



Low symmetry structure
Setting used: R3C:H

#K0.3Na0.7NbO3 # N. Zhang et al./http://dx.doi.org/10.1107/S0108768109011057
161
5.59447 5.59447 13.8429 90 90 120
3
Na 1  -  0.0000  0.0000  0.2724
Nb 1  -  0.0000  0.0000  0.0160
O  1  -  0.1061  0.3369  0.0833

Symmetry Modes Summary
Atoms WP Modes
O1 3d GM4-(2) R4+(1)
Na1 1b GM4-(1)
Nb1 1a GM4-(1)


Note: The primary mode is written in bold letters

Summary of Amplitudes
K-vector     Irrep    Direction Isotropy Subgroup Dimension
(0,0,0) GM4- (a,a,a) R3m (160) 4
(1/2,1/2,1/2) R4+ (a,a,a) R-3c (167) 1
```

A.1.8 $Pm\bar{3}m$ (ITA No. 221) $\rightarrow$ $R3m$ (ITA No. 160)

```
High symmetry structure
Setting used: PM-3M

221 4.0054 4.0054 3.9551 90.00 90.00 89.85
3
Na  1  1a  0.0000  0.0000  0.0000
Nb  1  1b  0.5000  0.5000  0.5000
O   1  3c  0.5000  0.0000  0.5000

# Transformation matrix
[     1     0     1 ] [      0]
[    -1     1     1 ] [      0]
[     0    -1     1 ] [      0]



Low symmetry structure
Setting used: R3M
160
5.5945 5.5945 6.9215 90.00 90.00 120.00
3
Na  1  -  0.0000  0.0000  0.0000
Nb  1  -  0.0000  0.0000  0.4830
O   1  -  0.1770  0.8230  0.3420

Symmetry Modes Summary
Atoms WP Modes
O1 3c GM4-(2)
Nb1 1b GM4-(1)
Na1 1a GM4-(1)


Note: The primary mode is written in bold letters

Summary of Amplitudes
K-vector     Irrep    Direction Isotropy Subgroup Dimension
(0,0,0) GM4-(a,a,a) R3m (160) 4
```

Appendix B

Instrumentation

Synthesis equipements

The synthesis of the different materials presented in this memory was done using several tubular furnaces with horizontal temperature gradient (the majority of them Lenton furnaces) as shown in Figure B.1 and Figure B.2. In some case those furnaces where equipped with a Quartz tube for the synthesis needed to be done under a controlled atmosphere. In the most case, inert atmosphere of Ar and/or N_2 was used.

Depending on the calefactory resistance, the furnaces can overcome 1700 K. Another furnace B.3type was used for treatments lowed than 1370K. During the synthesis process and before the final treatments, the samples where pressed in a hydraulic MEGA-KSC-15 press B.4.

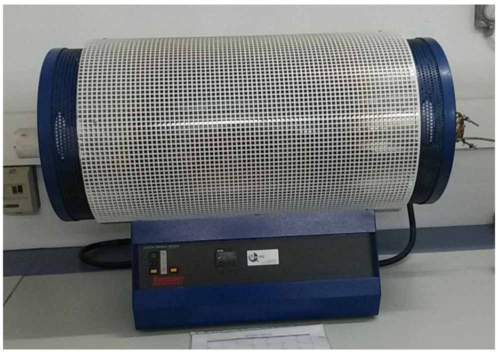

Figure B.1: Lenton tube furnace *(UPV/EHU: Inorganic Chemistry department)*

Figure B.2: AGNI Ceram-Aix RHT 175-50-300-1H furnace *(UPV/EHU: Applied Physics II department)*

Figure B.3: Heraeus furnace *(UPV/EHU: Applied Physics II department)*

Figure B.4: MEGA KSC-15 press, with a capacity of 15*t* *(UPV/EHU: Inorganic Chemistry department)*

X-ray powder diffractometers

Stoe STADI-P

Place	Applied Physics II and Condensed Matter Physics dept.	Leioa (Spain)
Radiation type	Laboratory X-rays	Cu tube
Monochromator	Ge(111)	$\lambda_{K\alpha1} = 1.5406$ Å
Detector	PSD	2θ=-70$-$135°
Sample environment	Heater	
Characteristics	Bragg-Brentano geomety	

Figure B.5: Stoe STADI-P laboratory X-ray powder diffractometer.

Philips X'Pert PRO

Place	UPV/EHU general services (SGIker)	Leioa (Spain)
Radiation type	Laboratory X-rays	Cu tube
Monochromator	Graphite secondary	$\lambda_{K\alpha} = 1.54187$ Å
Detector	Pixcel, 255 channels	2θ=1−110°
Sample environment	Anton Paar HTK16	RT−1273 K (vacuum)
Characteristics	Bragg-Brentano geometry	$\theta - \theta$
	Sample changer	3x15 positions

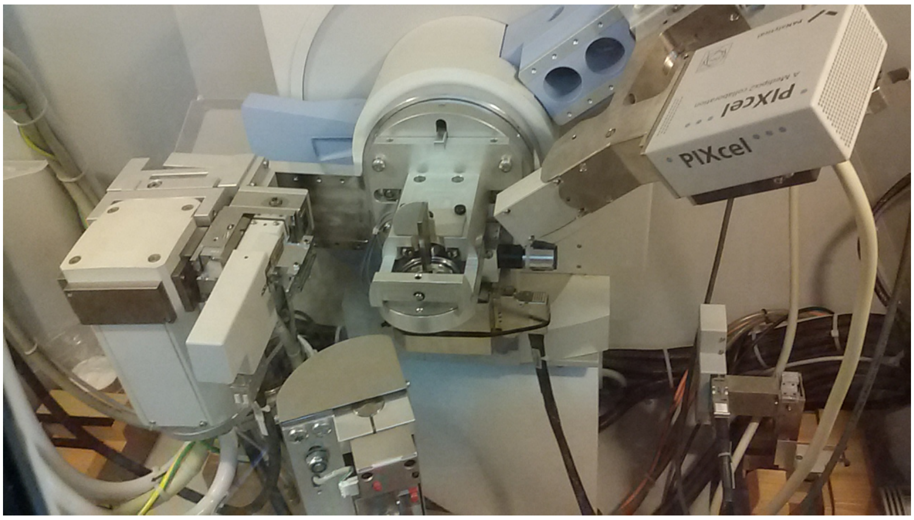

Figure B.6: Philips X'Pert PRO laboratory X-ray powder diffractometer.

Bruker Advance D8 Vårio

Place	UPV/EHU general services (SGIker)	Leioa (Spain)
Radiation type	Laboratory X-rays	Cu tube
Monochromator	Primary Vårio, Ge	$\lambda_{K\alpha1} = 1.5406$ Å
Detector	Sol-X energy dispersive	2θ=0.4−155°
Sample environment		RT
Characteristics	Bragg-Brentano geometry	$\theta - 2\theta$
	Window to avoid fluorescence	
	Sample changer	Plain samples
		Transmission configuration

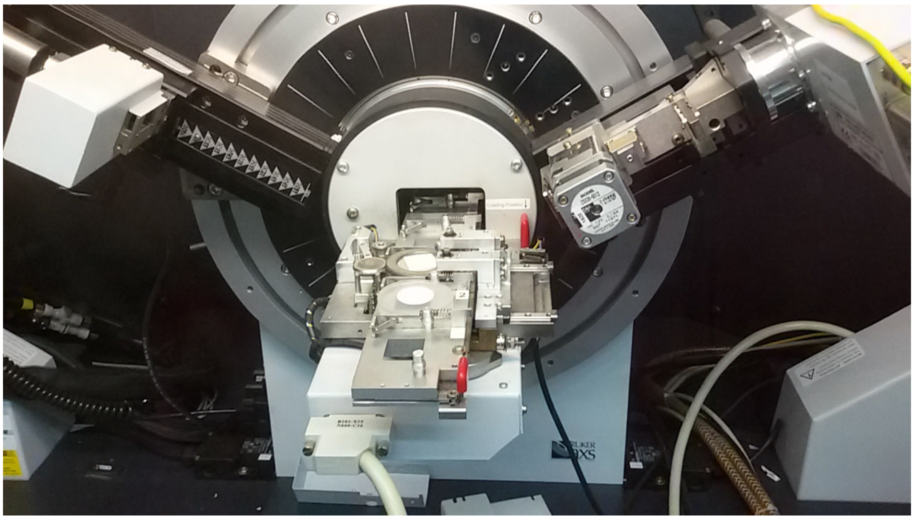

Figure B.7: Bruker Advance D8 Vårio laboratory X-ray powder diffractometer.

Bruker Advance D8 Vantec

Place	UPV/EHU general services (SGIker)	Leioa (Spain)
Radiation type	Laboratory X-rays	Cu tube
Monochromator	—	$\lambda_{K\alpha} = 1.54187$ Å
Detector	One dimension Våntec detector	2θ=5−140°
Sample environment	Anton Paar HTK2000	RT−1873 K (vacuum)
	MRI-TC wide	100−500 K
Characteristics	Bragg-Brentano geometry	$\theta - \theta$
	High temperature	Platinum sample-holder
	Low temperature	Ni sample-holder

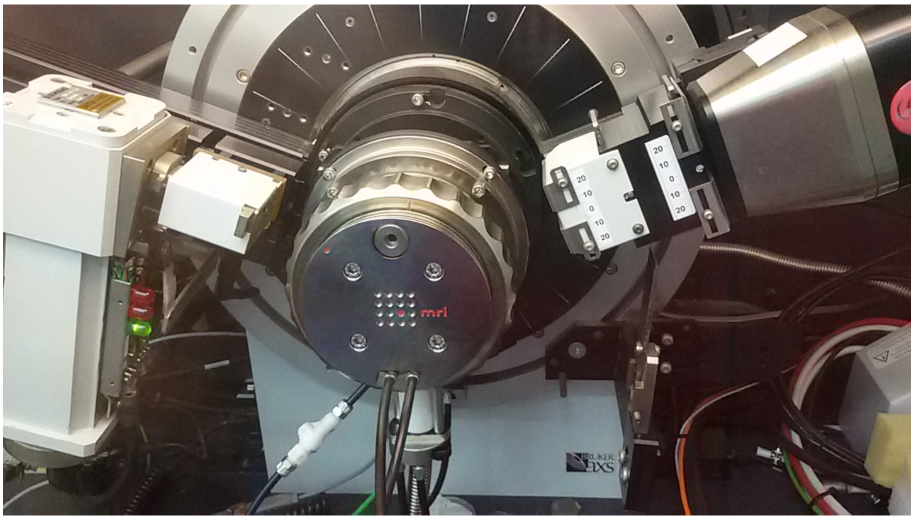

Figure B.8: Bruker Advance D8 Vantec laboratory X-ray powder diffractometer.

Synchrotron radiation powder diffractometers

BM-25-Brach A [192]

Place	Spline, ESRF	Grenoble (France)
Radiation type	Synchrotron radiation	Bending magnet
Monochromator	Pseudo channel-cut type Si(111) or Si(311)	0.28−2.48 Å
Detector	Si(Li)	13 elements
Sample environment	Low temperature	80 K
	High temperature	1000 K
Characteristics	Capillary	
	Flat samples	
	Angular resolution	0.0001°

Figure B.9: Powder diffractometer from BM25-Branch A line in ESRF.

Neutron powder diffractometers

HRPT [193]

Place	SINQ-PSI	Villigen (Swiss)
Radiation type	Neutrons	Thermal
Monochromator	Take-off angle	120°
	Ge(311)	2.4097 Å
	Ge(511)	1.5384 Å
	Take-off angle	90°
	Ge(511)	1.886 Å
	Ge(533)	1.494 Å
	Ge(822)	1.154 Å
Detector	^{3}He, 1600 wires	$2\theta=0-160^\circ$
Sample environment	Closed cycle refrigerator	4−325 K
	Helium cryostat	1.5 K<
	Dilution cryostat	50 mK<
	Small furnace	350−700 K
	Tantalum furnace	375−1400 K
	ILL-type furnace	500−1800 K
	Magnet	<4 T
	Supraconducting magnet	<15 T
	Pressure device	<14, <100 kbar
Characteristics	Oscillating radial collimator	Removes sample environment contamination
	Sample changer	Room temperature, 8 sample 1.5−315 K, 4 sample

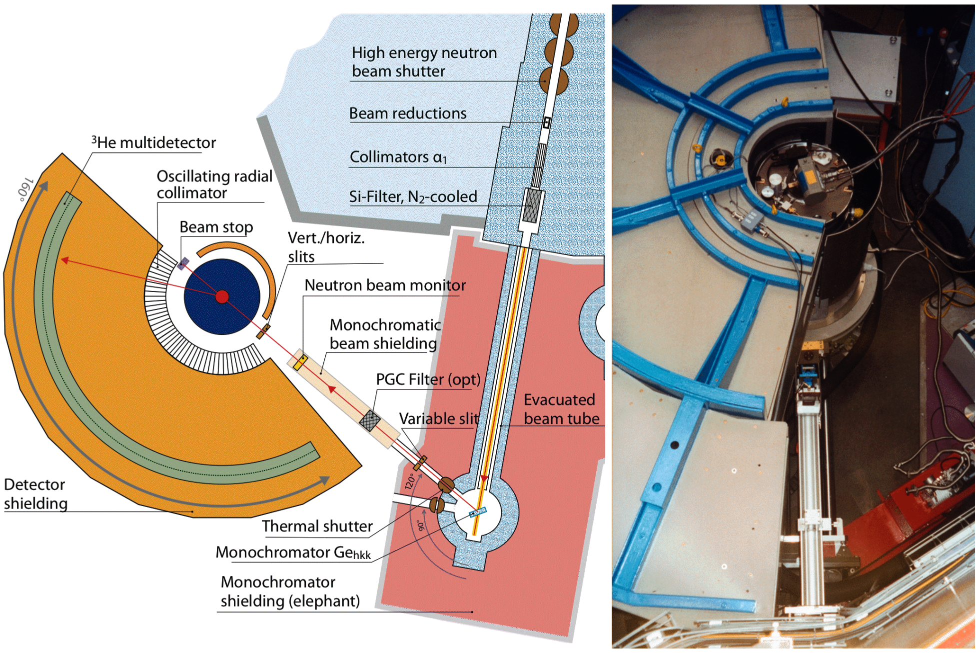

Figure B.10: HRPT neutron powder diffractometer.

D2B

Place	ILL	Grenoble (France)
Radiation type	Neutrons	Thermal
Monochromator	Take-off angle	135°
	Ge(557) Ge(337) Ge(551)	$\lambda = 1.051$ Å $\lambda = 1.28$ Å $\lambda = 1.464$ Å
	Ge(335) Flux at sample	$\lambda = 1.594$ Å (optimum) 10^6 n cm^{-2}s^{-1} (HR [1]) 10^7 n cm^{-2}s^{-1} (HI [2])
	Ge(331) Ge(113)	$\lambda = 2.398$ Å $\lambda = 3.152$ Å
Detector	^{3}He, 128 tubes	2θ=5−165°
Sample environment	Cryostat Cryocooler Dilution cryostat	1.5−300 K 3.5−700 K 50−4000 mK
	Cryofurnace	1.5−525 K
	Furnace	200−1000 K
	Pressure device	2 GPa (4−300 K)
	Cryomagnet	
Characteristics	Environment changer	6 positions (ex.: furnace, displex, 4 room temperature positions)

[1]High resolution; [2]High intensity

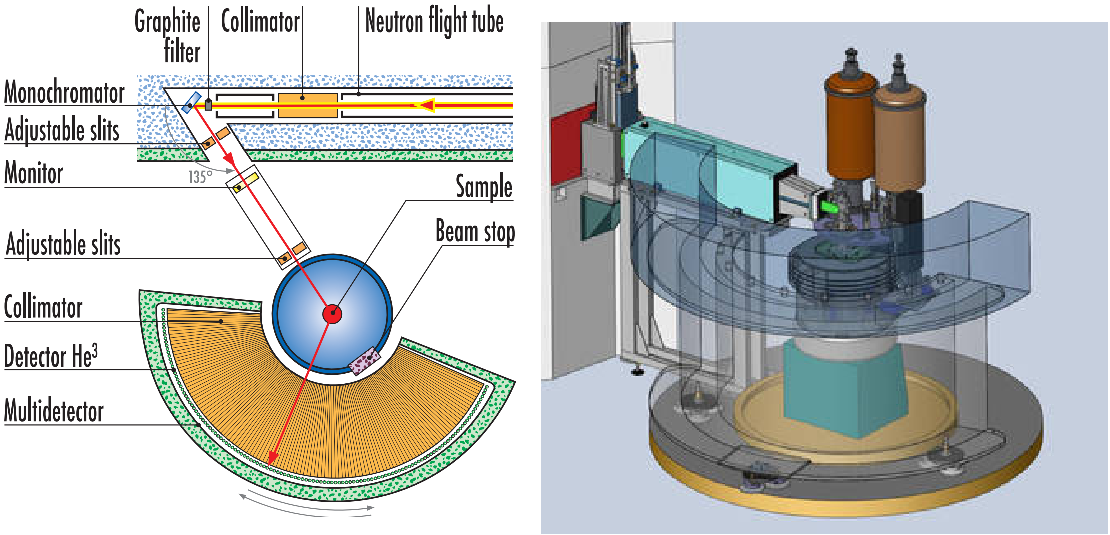

Figure B.11: D2B neutron powder diffractometer.

D1B

Place	ILL	Grenoble (France)
Radiation type	Neutrons	Thermal
Monochromator	Take-off angle	44,22°
	Pyrolytic graphite (002)	$\lambda = 2.52$ Å
	Flux at sample	6.5×10^6 n cm^{-2}s^{-1}
	Ge(331)	$\lambda = 1.28$ Å
	Flux at sample	0.4×10^6 n cm^{-2}s^{-1}
Detector	^{3}He, 1280 cells	2θ=0−128°
Sample environment	Cryostat	1.7−300 K
	Furnace	<800 °C
		<2500 °C
	Electromagnet	1 T (vertical or horizontal gap)
	Eulerian cradle	Texture analysis
Characteristics	Radial oscillating collimator	Removes sample environment contamination

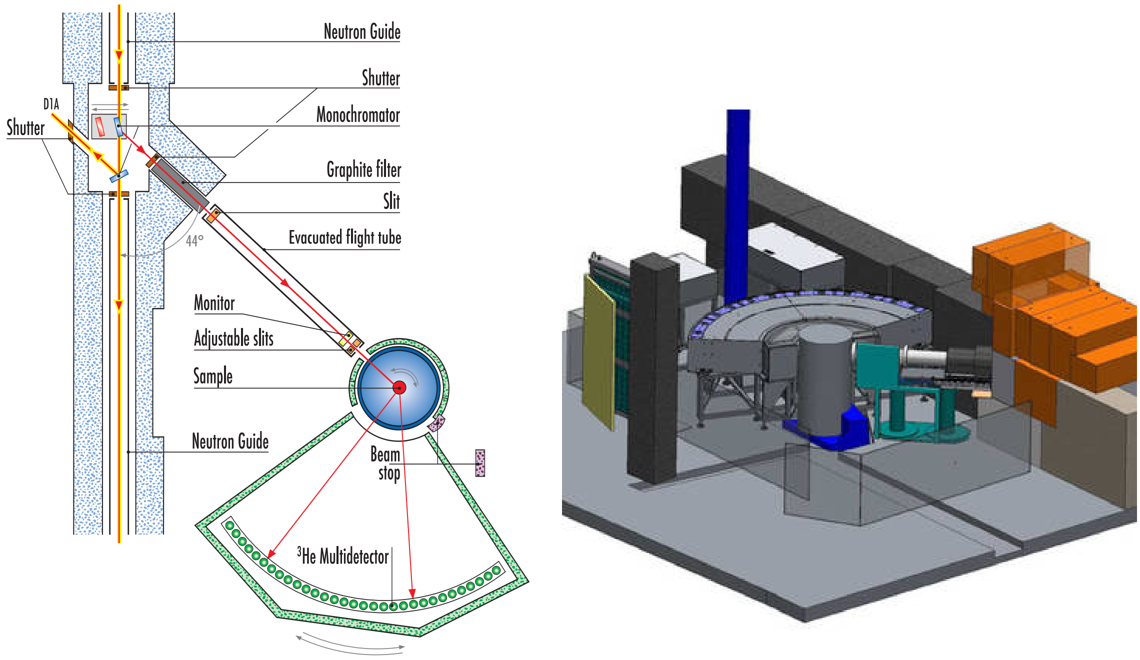

Figure B.12: D1B neutron powder diffractometer.

Scanning electron microscope (SEM)

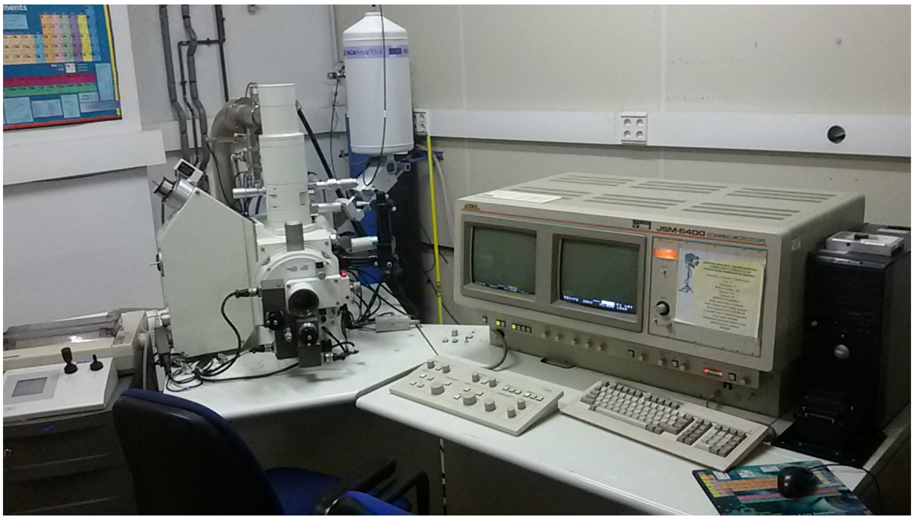

Figure B.13

Transmission electron microscope (TEM)

Figure B.14

Bibliography

[1] M. Gateshki. *Estudio, mediante métodos de difracción, de la estructura y las transiciones de fase en las perovskitas dobles* Sr_2MWO_6 *(M=Mn,Cu,Ni,Co,Fe,Zn,Mg) Y* La_2NiRuO_6. PhD thesis. Universidad del País Vasco/Euskal Herriko Unibertsitatea, 2003. (see p. III)

[2] A. Faik. *Estudio de las estructuras y de las transiciones de fase en nuevos materiales de wolframio (*$Sr_2M^{2+}W^{6+}O_6$*) y de antimonio (*$A_2M^{3+}Sb^{5+}O_6$*) con estructuras de perovskita doble*. PhD thesis. Universidad del País Vasco/Euskal Herriko Unibertsitatea, 2009. (see p. III)

[3] E. Iturbe Zabalo. *Crystal structure and phase transition studies in perovskite-type oxides using powder-diffraction techniques and symmetry-mode analysis.* $SrLnMRuO_6$ *(Ln=La,Pr,Nd; M=Zn,Co,Mg,Ni,Fe) and* $ALn_2CuTi_2O_9$ *(A=Ca,Ba; Ln=La,Pr,Nd,Sm)*. PhD thesis. Universidad del País Vasco/Euskal Herriko Unibertsitatea, 2012. (see p. III)

[4] T. Fukushima, A. Stroppa, S. Picozzi, and J. M. Perez-Mato. *Phys. Chem. Chem. Phys.*, **13**: 12186–12190, 2011. DOI: `10.1039/C1CP20626E` (see pp. IV, 66)

[5] L. Ortega San Martín. *Óxidos mixtos* $Sr_2B_{1-x}Mg_xO_6$ *(B =* Co^{2+}*,* Ni^{2+} Mn^{2+} *and* Fe^{3+}*) con estructura tipo perovskita doble. Estudio estructural, espectroscópico y magnético*. PhD thesis. Universidad del País Vasco/Euskal Herriko Unibertsitatea, 2005. (see pp. V, 16, 28)

[6] B. Kocsis, J. M. Perez-Mato, E. S. Tasci, G. de la Flor, and M. I. Aroyo. *Journal of Applied Crystallography*, **47**: 1165–1179, 2014. DOI: `10.1107/S1600576714010693` (see pp. VI, 41, 45, 49, 51, 59, 61, 64–66, 80, 106)

[7] G. Rose. *De novis quibusdam fossilibus, quae in montibus uraliis inveniuntur*. Scripsit. Ann. Phys., 1839. (see p. 3)

[8] V. M. Goldschmidt. *Naturwissenschaften*, **14**: 477–485, 1926. DOI: `10.1007/BF01507527` (see pp. 3, 9)

[9] W. Hönle, G. Miller, and A. Simon. *Journal of Solid State Chemistry*, **75**: 147–155, 1988. DOI: `10.1016/0022-4596(88)90312-X` (see p. 4)

[10] V. Luaña, A. Costales, and A. M. Pendás. *Physical Review B*, **55**: 4285–4297, 1997. DOI: `10.1103/PhysRevB.55.4285` (see p. 4)

[11] A. Clearfield. *Acta Crystallographica*, **16**: 135–142, 1963. DOI: `10.1107/S0365110X6300030X` (see p. 4)

[12] F. Gingl, T. Vogt, E. Akiba, and K. Yvon. *Journal of Alloys and Compounds*, **282**: 125–129, 1999. DOI: `10.1016/S0925-8388(98)00834-2` (see p. 4)

[13] H. Sreemoolanadhan, R. Ratheesh, M. T. Sebastian, and P. Mohanan. *Materials Letters*, **33**: 161–165, 1997. DOI: `10.1016/S0167-577X(97)00100-6` (see p. 5)

[14] R. J. Cava et al. *Physical Review Letters*, **58**: 1676–1679, 1987. DOI: `10.1103/PhysRevLett.58.1676` (see p. 5)

[15] S. M. Rao et al. *Applied Physics Letters*, **89**: 232509–3, 2006. DOI: `10.1063/1.2402902` (see p. 5)

[16] B. B. Karki et al. *American Mineralogist*, **82**: 635–638, 1997. DOI: `0003âĂŞ004X/97/0506âĂŞ0635` (see p. 5)

[17] C. Michel, L. Er-Rakho, and B. Raveau. *Materials Research Bulletin*, **20**: 667–671, 1985. DOI: `10.1016/0025-5408(85)90144-8` (see p. 5)

[18] D. E. Cox et al. *Applied Physics Letters*, **79**: 400–402, 2001. DOI: `10.1063/1.1384475` (see p. 5)

[19] K-I. Kobayashi, T. Kimura, H. Sawada, K. Terakura, and Y. Tokura. *Nature*, **395**: 677–680, 1998. DOI: `10.1038/27167` (see pp. 5, 105)

[20] Y. N. Lee, R. M. Lago, J.-L. G. Fierro, and J. González. *Applied Catalysis, A-General*, **215**: 245–256, 2001. DOI: `10.1016/S0926-860X(01)00536-1` (see p. 5)

[21] C. H. Kim, G. Qi, K. Dahlberg, and W. Li. *Science*, **327**: 1624–1627, 2010. DOI: `10.1126/science.1184087` (see p. 5)

[22] K. Ueda, H. Tabata, and T. Kawai. *Science*, **280**: 1064–1066, 1998. DOI: `10.1126/science.280.5366.1064` (see p. 5)

[23] J.B. Goodenough. *Reports on Progress in Physics*, **67**: 1915–1993, 2004. DOI: `10.1007/BF01507527` (see p. 5)

[24] R. H. Mitchell. *Perovskites Modern and Ancient*. Almaz Press Inc., 2002. (see pp. 5, 95)

[25] K. Leinenweber and J. Parise. *Journal of Solid State Chemistry*, **114**: 277–281, 1995. DOI: `10.1006/jssc.1995.1040` (see p. 6)

[26] P. M. Woodward, D. E. Cox, T. Vogt, C. N. R. Rao, and A. K. Cheetham. *Chemistry of Materials*, **11**: 3528–3538, 1999. DOI: `10.1021/cm990281d` (see p. 6)

[27] T. Sekiya, T. Yamamoto, and Y. Torii. *Bulletin of the Chemical Society of Japan.*, **57**: 1859–1862, 1984. DOI: `10.1246/bcsj.57.1859` (see p. 6)

[28] K. R. Poeppelmeier et al. *Physica C*, **185-189**: 525–526, 1991. DOI: `10.1016/0921-4534(91)92065-J` (see p. 6)

[29] M. C. Knapp and P. M. Woodward. *Journal of Solid State Chemistry*, **179**: 1076–1085, 2006. DOI: `10.1016/j.jssc.2006.01.005` (see p. 6)

[30] Graham King and Patrick M. Woodward. *Journal of Materials Chemistry*, **20**: 5785–5796, 2010. DOI: `10.1039/B926757C` (see p. 6)

[31] A. Faik et al. *Journal of Solid State Chemistry*, **181**: 1759–1766, 2008. DOI: `10.1016/j.jssc.2008.03.029` (see pp. 7, 8, 14, 107, 117)

[32] J. B. Goodenough and R. I. Dass. *International Journal of Inorganic Matererials*, **2**: 3–9, 2000. DOI: `10.1016/S1466-6049(99)00069-0` (see p. 7)

[33] J. Lindén, M. Karppinen, T. Shimada, Y. Yasukawa, and H. Yamauchi. *Physical Review B*, **68**: 174415–5, 2003. DOI: `10.1103/PhysRevB.68.174415` (see p. 7)

[34] M. T. Anderson, K. B. Greenwood, G. A. Taylor, and K. R. Poeppelmeier. *Progress in Solid State Chemistry*, **22**: 197–233, 1993. DOI: `10.1016/0079-6786(93)90004-B` (see pp. 7, 8)

[35] A. K. Azad et al. *Materials Research Bulletin*, **37**: 1797–1813, 2002. DOI: `10.1016/S0025-5408(02)00872-3` (see p. 8)

[36] E. J. Cussen, J. F. Vente, P. D. Battle, and T. C. Gibbb. *Journal of Materials Chemistry*, **7**: 459–463, 1997. DOI: `10.1039/a607083c` (see p. 8)

[37] A. Faik, J. M. Igartua, E. Iturbe-Zabalo, and G. J. Cuello. *Journal of Molecular Structure*, **963**: 145–152, 2010. DOI: `10.1016/j.molstruc.2009.10.027` (see p. 8)

[38] P. D. Battle, T. C. Gibb, C. W. Jones, and F. Studer. *Journal of Solid State Chemistry*, **78**: 281–293, 1989. DOI: `10.1016/0022-4596(89)90109-6` (see p. 8)

[39] P. W. Barnes, M. W. Lufaso, and P. Woodward. *Acta Crystallographica B*, **62**: 384–396, 2006. DOI: `10.1107/S0108768106002448` (see p. 8)

[40] A. Faik, D. Orobengoa, E. Iturbe-Zabalo, and J. M. Igartua. *Journal of Solid State Chemistry*, **192**: 273–283, 2012. DOI: `10.1016/j.jssc.2012.04.019` (see pp. 8, 45, 51, 76, 131, 132, 137, 154)

[41] M. W. Lufaso, P. M. Woodward, and J. Goldberger. *Journal of Solid State Chemistry*, **177**: 1615–1659, 2004. DOI: `10.1016/j.jssc.2003.12.020` (see pp. 8, 9)

[42] P. M. Woodward. *Structural distortion, phase transitions, and cation ordering in the perovskite and tungsten trioxide structures*. PhD thesis. Oregon State University, 1996. (see p. 8)

[43] P. Woodward, R. D. Hoffmann, and A. W. Sleight. *Journal of Materials Research*, **9**: 2118–2127, 1994. DOI: `10.1557/JMR.1994.2118` (see p. 8)

[44] T. K. Mandal, V. V. Poltavets, M. Croft, and M. Greenblatt. *Journal of Solid State Chemistry*, **181**: 2325–2331, 2008. DOI: `10.1016/j.jssc.2008.04.038` (see pp. 9, 117)

[45] A. M. Glazer. *Acta Crystallographica B*, **28**: 3384–3392, 1972. DOI: `10.1107/S0567740872007976` (see pp. 9, 10, 75, 105)

[46] A. M. Glazer. *Acta Crystallographica A*, **31**: 756–762, 1975. DOI: `10.1107/S0567739475001635` (see p. 9)

[47] H. D. Megaw. *Crystal Structures - A working Approach*. Philadelphia: W.B. Saunders, 1973. (see p. 9)

[48] R. D. Shannon. *Acta Crystallographica Section A*, **32**: 751–767, 1976. DOI: `10.1107/S0567739476001551` (see p. 9)

[49] J. B. Philipp et al. *Physical Review B*, **68**: 144431–13, 2003. DOI: `10.1103/PhysRevB.68.144431` (see p. 10)

[50] K. S. Alexandrov, B. V. Besnosikov, and L. A. Posdnjakova. *Ferroelectrics*, **12**: 197–198, 1976. DOI: `10.1080/00150197608241424` (see p. 10)

[51] P. M. Woodward. *Acta Crystallographica B*, **53**: 32–43, 1997. DOI: `10.1107/S0108768196010713` (see p. 10)

[52] D. Reinen and H. Weitzel. *Zeitschrift für anorganische und allgemeine Chemie*, **424**: 31–38, 1976. DOI: `10.1002/zaac.19764240107` (see p. 10)

[53] C. J. Howard and H. T. Stokes. *Acta Crystallographica B*, **54**: 782–789, 1998. DOI: `10.1107/S0108768198004200` (see pp. 11, 26, 105, 106)

[54] H. M. Rietveld. *Journal of Applied Crystallography*, **2**: 65–71, 1969. DOI: `10.1107/S0021889869006558` (see pp. 23, 130)

[55] J. Rodríguez-Carvajal. *Physica B*, **192**: 55–69, 1993. DOI: `10.1016/0921-4526(93)90108-I` (see pp. 23, 130)

[56] H. T. Stokes, D. M. Hatch, and J. D. Wells. *Physical Review B*, **43**: 11010–11018, 1991. DOI: `10.1103/PhysRevB.43.11010` (see pp. 25, 106)

[57] M. I. Aroyo and J. M. Perez-Mato. *Phase Transitions*, **63**: 235–255, 1997. DOI: `10.1080/01411599708228797` (see pp. 25, 106)

[58] M. I. Aroyo and J. M. Perez-Mato. *Acta Crystallographica A*, **54**: 19–30, 1998. DOI: `10.1107/S0108767397010106` (see pp. 25, 106)

[59] D. Orobengoa, C. Capillas, M. I. Aroyo, and J. M. Perez-Mato. *Journal of Applied Crystallography*, **42**: 820–833, 2009. DOI: `10.1107/S0021889809028064` (see pp. 25, 74, 97, 106, 108, 130, 131, 154)

[60] D. Orobengoa. *Desarrollo de bases de datos cristalográficos on-line y de herramientas para el estudio grupo-teórico de materiales ferróicos y multiferróicos*. PhD thesis. Universidad del País Vasco/Euskal Herriko Unibertsitatea, 2010. (see p. 25)

[61] B. J. Campbell, H. T. Stokes, D. E. Tanner, and D. M. Hatch. *Journal of Applied Crystallography*, **39**: 607–614, 2006. DOI: `10.1107/S0021889806014075` (see p. 25)

[62] M. I. Aroyo et al. *Zeitschrift Für Kristallographie*, **221**: 15–27, 2006. DOI: `10.1524/zkri.2006.221.1.15` (see pp. 25, 106, 130)

[63] M. I. Aroyo, A. Kirov, C. Capillas, J. M. Perez-Mato, and H. Wondratsechek. *Acta Crystallographica A*, **62**: 115–128, 2006. DOI: `10.1107/S0108767305040286` (see pp. 25, 106, 130)

[64] C. J. Howard, B. J. Kennedy, and P. M. Woodward. *Acta Crystallographica B*, **59**: 463–471, 2003. DOI: `10.1107/S0108768103010073` (see pp. 26, 106)

[65] C. J. Howard and H. T. Stokes. *Acta Crystallographica B*, **60**: 674–684, 2004. DOI: `10.1107/S0108768104019901` (see pp. 26, 105, 106)

[66] C. J. Howard and H. T. Stokes. *Acta Crystallographica A*, **61**: 93–111, 2005. DOI: `10.1107/S0108767304024493` (see pp. 26, 106)

[67] C. Capillas et al. *Zeitschrift Für Kristallographie*, **226(2)**: 186–196, 2011. DOI: `10.1524/zkri.2011.1321` (see pp. 27, 108)

[68] J. M. Perez-Mato, D. Orobengoa, and M. I. Aroyo. *Acta Crystallographica A*, **66**: 558–590, 2010. DOI: `10.1107/S0108767310016247` (see pp. 36, 45, 48, 51, 60, 61, 106)

[69] M. Li et al. *Nature Materials*, **13**: 31–35, 2014. DOI: `10.1038/nmat3782` (see p. 43)

[70] S. Wada et al. *Journal of Applied Physics*, **108**: 094–114, 2010. DOI: `10.1063/1.3481390` (see p. 43)

[71] T. Tani and T. Kimura. *Advances in Applied Ceramics*, **105**: 55–65, 2006. DOI: `10.1179/174367606X81650` (see p. 43)

[72] E. Cross. *Nature*, **432**: 24–25, 2004. DOI: `10.1038/nature03142` (see p. 43)

[73] G. A. Samara. *Journal of Physics-Condensed Matter*, **15**: R367, 2003. DOI: `10.1088/0953-8984/15/9/202` (see p. 43)

[74] M. Kosec et al. *Journal of Materials Research*, **19**: 1849–1853, 2004. DOI: `10.1557/JMR.2004.0229` (see p. 43)

[75] J. Yoo, D. Oh, Y. Jeong, J. Hong, and M. Jung. *Materials Letters*, **58**: 3831–3835, 2004. DOI: `10.1016/j.matlet.2004.08.011` (see p. 43)

[76] R. J. Zeches et al. *Science*, **326**: 977, 2009. DOI: `10.1126/science.1177046` (see p. 44)

[77] H. Maiwa, N. Lizawa, D. Togawa, and T. Hayashi. *Applied Physics Letters*, **82**: 1760–1762, 2003. DOI: `10.1063/1.1560864` (see p. 44)

[78] J.X. Zhang et al. *Nature Nanotechnology*, **6**: 98–102, 2011. DOI: `10.1038/nnano.2010.265` (see p. 44)

[79] M. S. Kim, S. J. Jeong, and J.S. Song. *Journal of The American Ceramic Society*, **90**: 3338–3340, 2007. DOI: `10.1111/j.1551-2916.2007.01893.x` (see p. 44)

[80] D. S. Tinberg and S. Trolier-Mckinstry. *Journal of Applied Physics*, **101**: 024112, 2007. DOI: `10.1063/1.2430627` (see p. 44)

[81] P. Wang, Y. Li, and Y. Lu. *Journal of The European Ceramic Society.*, **31**: 2005–2012, 2011. DOI: `10.1016/j.jeurceramsoc.2011.04.023` (see p. 44)

[82] J. Kling et al. *Journal of The American Ceramic Society*, **93**: 2452–2455, 2010. DOI: `10.1111/j.1551-2916.2010.03778.x` (see p. 44)

[83] C. Ma, H. Guo, S. P. Beckman, and X. Tan. *Physical Review Letters*, **109**: 107602, 2012. DOI: `10.1103/PhysRevLett.109.107602` (see p. 44)

[84] D. Fu, K. Suzuki, K. Kato, and H Suzuki. *Applied Physics Letters*, **82**: 2130, 2003. DOI: `10.1063/1.1565502` (see p. 44)

[85] P. Baettig, C. F. Schelle, R. LeSar, U. W. Waghmare, and N.A. Spaldin. *Chemistry of Materials*, **17**: 1376–1380, 2005. DOI: `10.1021/cm0480418` (see p. 44)

[86] N. Zhang, A. M. Glazer, D. Baker, and P. A. Thomas. *Acta Crystallographica B*, **65**: 291–299, 2009. DOI: `10.1038/nnano.2010.265` (see pp. 44, 51)

[87] T. Sakakura, J. Wang, N. Ishizawa, Y. Inagaki, and K. Kakimoto. *IOP Conference Series: Materials Science and Engineering*, **18**: 022006, 2011. DOI: `10.1088/1757-899X/18/2/022006` (see p. 44)

[88] Y. P. Guo, K. Kakimoto, and H. Ohsato. *Applied Physics Letters*, **85**: 4121–3, 2004. DOI: `10.1063/1.1813636` (see p. 44)

[89] D. W. Baker, P. A. Thomas, N. Zhang, and A. M. Glazer. *Acta Crystallographica B*, **65**: 22–28, 2009. DOI: `10.1107/S0108768108037361` (see pp. 44, 53)

[90] V. A. Shuvaeva, Y. Azuma, K. Yagi, K. Sakaue, and H. Terauchi. *Journal of Synchrotron Radiation*, **8**: 833, 2001. DOI: `10.1107/S0909049500018069` (see p. 44)

[91] J. Chen and D. Feng. *Physica Status Solidi A.*, **109**: 427–434, 1988. DOI: `10.1002/pssa.2211090208` (see p. 44)

[92] A. Avogadro, G. Bonera, F. Borsa, and A. Rigamont. *Physical Review B*, **9**: 3905, 1974. DOI: `10.1103/PhysRevB.9.3905` (see p. 44)

[93] G. D. Ariano, S. Aldrovandi, and A. Rigamonti. *Physical Review B*, **25**: 7044, 1982. DOI: `10.1103/PhysRevB.25.7044` (see p. 44)

[94] S. E. Ashbrook, L. Le Polles, R. Gautier, C. J. Pickard, and R. I Walton. *Physical Chemistry. Chemical Physics*, **8**: 3423, 2006. DOI: `10.1039/B604520K` (see p. 44)

[95] K. K. Mishra, V. Sivasubramanian, and A. K. Arora. *Journal of Raman Spectroscopy*, **42**: 517–521, 2011. DOI: `10.1002/jrs.2706` (see p. 44)

[96] L. Liu et al. *Materials Letters*, **68**: 300–302, 2012. DOI: `10.1016/j.matlet.2011.10.103` (see p. 44)

[97] N. Ishizawa, J. Wang, T. Sakakura, Y. Inagaki, and K. Kakimoto. *Journal of Solid State Chemistry*, **183**: 2731–2738, 2010. DOI: `10.1016/j.jssc.2010.09.018` (see pp. 44, 45, 50, 51, 58, 65, 66)

[98] Germany Fachin formations zentrum Karlsruhe. *ICSD (Inorganic Crystal Structure Database)*. 2010. (see p. 45)

[99] A. Faik, J. M. Igartua, M. Gateshki, and G. J. Cuello. *Journal of Solid State Chemistry*, **182**: 1717–1725, 2009. DOI: `10.1016/j.jssc.2009.04.014` (see pp. 45, 51, 128, 131)

[100] E. Iturbe-Zabalo et al. *Journal of Solid State Chemistry*, **198**: 24–38, 2013. DOI: `10.1016/j.jssc.2012.09.007` (see pp. 45, 51, 76, 79, 80, 108, 110, 151)

[101] E. Iturbe-Zabalo et al. *Journal of Physics-Condensed Matter*, **25**: 205401, 2013. DOI: `10.1088/0953-8984/25/20/205401` (see pp. 45, 51, 76, 80, 108, 110, 154)

[102] E. Iturbe-Zabalo, J. M. Igartua, and M. Gateshki. *Journal of Applied Crystallography*, **46**: 1085–1093, 2013. DOI: `10.1107/S0021889813013253` (see pp. 45, 76, 80)

[103] A. Gómez-Pérez et al. *Journal of Applied Crystallography*, **47**: 745–754, 2014. DOI: `10.1107/S1600576714004907` (see p. 45)

[104] R. Gaur, K. C. Singha, and R Laishram. *Ceramics International*, **41**: 1413–1420, 2015. DOI: `10.1016/j.ceramint.2014.09.074` (see p. 45)

[105] H. E. Mgbemere and G. A. Schneider. *Functional Materials Letters*, **3**: 25–28, 2010. DOI: `10.1142/S1793604710000841` (see p. 45)

[106] L. Katz and H. D. Megaw. *Acta Crystallographica*, **22**: 639–648, 1967. DOI: `10.1107/S0365110X6700129X` (see p. 50)

[107] M. Ahtee and A. M. Glazer. *Acta Crystallographica A*, **32**: 434, 1976. DOI: `10.1107/S0567739476000983` (see p. 51)

[108] M. Ahtee and A. W. Hewat. *Acta Crystallographica A*, **34**: 309–317, 1978. DOI: `10.1107/S056773947800056X` (see p. 51)

[109] D. W. Baker, P. A. Thomas, N. Zhang, and A. M. Glazer. *Appl. Phys. Lett.*, **95**: 091903, 2009. DOI: `10.1063/1.3212861` (see p. 51)

[110] E. Lines and A. Glass. *Principles and Applications of Ferroelectrics and Related Materials*. OUP, 1977. (see p. 59)

[111] D. Orobengoa, C. Capillas, M. I. Aroyo, and J. M. Perez-Mato. *Acta Crystallographica*, **42**: 820–833, 2010. DOI: `10.1107/S0021889809028064` (see pp. 59, 61)

[112] H. Stokes, D. Hatch, and B. Campbell. iso.byu.edu. (see p. 61)

[113] D. Di Sante, A. Stroppaa, and S. Picozzi. *Phys. Chem. Chem. Phys.*, 14673–14681, 2012. DOI: `10.1039/C2CP42127E` (see p. 66)

[114] R. I. Dass and J. B. Goodenough. *Physical Review B*, **67**: 014401, 2003. DOI: `10.1103/PhysRevB.67.014401` (see p. 71)

[115] C. L. Bull, D. Gleeson, and K. S. Knight. **15**: 4927, 2003. DOI: `10.1088/0953-8984/15/29/304` (see pp. 72, 78, 80, 88)

[116] I. O. Troyanchuk, A. P. Sazonov, H. Szymczak, D. M. Többens, and H. Gamari-Seale. *Journal of Experimental and Theoretical Physics*, **99**: 363–369, 2004. DOI: `10.1134/1.1800193` (see p. 72)

[117] A. P. Sazonov, I. O. Troyanchuk, V. V. Sikolenko, H. Szymczak, and K. Bärner. *Physica Status Solidi B.*, **244**: 3367–3376, 2007. DOI: `10.1002/pssb.200642481` (see p. 72)

[118] R. J. Booth et al. *Materials Research Bulletin*, **44**: 1559 –1564, 2009. DOI: `10.1016/j.materresbull.2009.02.003` (see pp. 72, 78, 80, 88)

[119] A. J. Barán-González, C. Frontera, J. L. García-Muõz, B. Rivas-Murias, and J. Blasco. *Journal of Physics-Condensed Matter*, **23**: 496003, 2011. DOI: `10.1088/0953-8984/23/49/496003` (see pp. 72, 74, 78, 80, 88)

[120] S. Yañez Vilar et al. *Physical Review B*, **84**: 134427, 2011. DOI: `10.1103/PhysRevB.84.134427` (see p. 72)

[121] Z. Ganghua et al. *Journal of Crystal Growth*, **327**: 262 –266, 2011. DOI: `S0022024811005033` (see p. 72)

[122] Christopher J. Howard and Harold T. Stokes. *Acta Crystallographica A*, **61**: 93–111, 2005. DOI: `10.1107/S0108767304024493` (see pp. 75, 105, 106)

[123] K. Asai et al. *Journal of the Physical Society Japan*, **67**: 4218–4228, 1998. DOI: `10.1143/JPSJ.67.4218` (see p. 75)

[124] T. I. Milenov et al. *Mater. Sci. Eng: B*, **172**: 80 –84, 2010. DOI: `10.1016/j.mseb.2010.04.021` (see p. 75)

[125] E. Kroumova et al. *Journal of Applied Crystallography*, **34**: 783–784, 2001. DOI: `10.1107/S0021889801011852` (see p. 76)

[126] C. Capillas et al. *Zeitschrift Für Kristallographie*, **226(2)**: 477–485, 2011. DOI: `10.1524/zkri.2011.1321` (see p. 76)

[127] U. Petralanda and I. Etxebarria. *Physical Review B*, **89**: 064107, 2014. DOI: `10.1103/PhysRevB.89.064107` (see p. 77)

[128] S. Yáñez Vilar et al. *Physical Review B*, **84**: 134427, 2011. DOI: `10.1103/PhysRevB.84.134427` (see pp. 78, 80, 88)

[129] A. P. Sazonov, I. O. Troyanchuk, V. V. Sikolenko, H. Szymczak, and K. Bärner. *Physica Status Solidi B.*, **244**: 2007. DOI: `10.1002/pssb.200642481` (see pp. 78, 80, 88)

[130] A. P. Sazonov, I. O. Troyanchuk, D. P. Kozlenko, A. M. Balagurov, and V. V. Sikolenko. *Journal of Magnetism and Magnetic Materials*, **302**: 443 –447, 2006. DOI: `10.1016/j.jmmm.2005.10.004` (see pp. 78, 80, 88)

[131] G. Zhang et al. *Journal of Crystal Growth*, **327**: 262 –266, 2011. DOI: `10.1016/j.jcrysgro.2011.06.002` (see pp. 78, 80, 88)

[132] M. Mouallem-Bahout et al. (see pp. 78, 80, 88)

[133] K. Takata, M. Azuma, Y. Shimakawa, and M. Takano. *Funtai Oyobi Funmatsu Yakin*, **52**: 913–917, 2005. DOI: `10.2497/jjspm.52.913` (see pp. 78, 80, 88)

[134] W. Z. Yang, X. Q. Liu, Y. Q. Lin, and X. M. Chen. *Journal of Applied Physics*, **111**: 084106, 2012. DOI: `http://dx.doi.org/10.1063/1.4704392` (see p. 80)

[135] W. Z. Yang, X. Q. Liu, H. J. Zhao, Y. Q. Lin, and X. M. Chen. *Journal of Applied Physics*, **112**: 064104, 2012. DOI: `http://dx.doi.org/10.1063/1.4752262` (see p. 80)

[136] B. Orayech, A. Faik, G. A. López, O. Fabelo, and J. M. Igartua. *Journal of Applied Crystallography*, **48**: 318–333, 2015. DOI: `10.1107/S1600576715000941` (see pp. 80, 111, 128, 151)

[137] A. Faik, E. Iturbe-Zabalo, I. Urcelay, and J. M. Igartua. *Journal of Solid State Chemistry*, **182**: 2656–2663. DOI: `10.1016/j.jssc.2009.07.021` (see pp. 88, 89, 107, 117, 119, 120)

[138] A. Faik, J. M. Igartua, Gateshki M., and G. J. Cuello. *Journal of Solid State Chemistry*, **V182**: 1717–1725, 2009. DOI: `10.1016/j.jssc.2009.04.014` (see pp. 89, 107, 117)

[139] A. Faik, J. M. Igartua, E. Iturbe-Zabalo, and G. J. Cuello. *J. Molecular Structure*, **963**: 145–152, 2010. DOI: `10.1016/j.molstruc.2009.10.027` (see pp. 89, 107, 117, 128, 183, 188)

[140] A. Faik, I. Urcelay, E. Iturbe-Zabalo, and J.M. Igartua. *journal of Molecular Structure*, **977**: 137–144, 2010. DOI: `10.1016/j.molstruc.2010.05.024` (see pp. 89, 107, 128, 183, 188)

[141] A. Faik, D. Orobengoa, E. Iturbe-Zabalo, and J.M. Igartua. *Journal of Solid State Chemistry*, **192**: 273–283, 2012. DOI: `10.1016/j.jssc.2012.04.019` (see pp. 89, 107, 117)

[142] Brendan J. Kennedy, Christopher J. Howard, and Bryan C. Chakoumakos. *Physical Review B*, **59**: 4023–4027, 1999. DOI: `10.1103/PhysRevB.59.4023` (see pp. 91, 120, 159)

[143] E. K. H. Salje. *Phase Transitions in Ferroelastic and Co-elastic Crystals*. The Pitt Building, Trumpington Street, Cambridge CB2 1RP: Cambridge Topics in Mineral Physics and Chemistry Vol. 1, ed., Cambridge University Press, 1990. (see pp. 92, 120)

[144] Th. Hahn. *International Tables for Crystallography Volume A: Space-group symmetry*. The International Union of Crystallography and Kluwer Academic Publishers: Dordrecht, Holland., 1992. (see pp. 96, 129, 130)

[145] Sebastián A. Larrégola et al. *Inorganic Chem.*, **53**: 5609–5618, 2014. DOI: `10.1021/ic500278y` (see p. 105)

[146] Javier Sánchez-Benítez et al. *The Journal of Physical Chemistry C*, **118**: 9652–9658, 2014. DOI: `10.1021/jp500562e` (see p. 105)

[147] M. DeMarco et al. *Phys. Rev. B*, DOI: `10.1103/PhysRevB.62.14297` (see p. 105)

[148] E. J. Cussen, J. F. Vente, P. D. Battle, and T. C. Gibbb. *Journal of Materials Chemistry*, **7**: 459–463, 1997. DOI: `10.1039/a607083c` (see pp. 105, 107)

[149] H. T. Stokes, E. H. Kisi, D. M. Hatch, and C. J. Howard. *Acta Crystallographica B*, **58**: 934–938, 2002. DOI: `10.1107/S0108768102015756` (see pp. 105, 106)

[150] M. A Cheah, P.J. Saines, and B.J. Kennedy. *Journal of Solid State Chemistry*, DOI: `10.1016/j.jssc.2006.03.013` (see p. 105)

[151] C. J. Howard and H. T. Stokes. *Acta Crystallographica B*, **54**: 782–789, 1998. DOI: `10.1107/S0108768198004200` (see pp. 106, 129)

[152] N. Kashima, K. Inoue, T. Wada, and Y. Yamaguchi. *Applied Physica A*, DOI: `10.1007/s003390201362` (see p. 107)

[153] H. Karunadasa, Q. Huang, B. G. Ueland, P. Schiffer, and R. J. Cava. *PNAS*, **V100**: 8097–8102, 2003. (see p. 107)

[154] V. Primo-Martín and M. Jansen. *Journal of Solid State Chemistry*, **157**: 76–85, 2001. DOI: `10.1006/jssc.2000.9041` (see p. 107)

[155] A. Tauber, S.C. Tidow, R. D. Finnegan, and W. D. Wilber. *Physica C*, DOI: `10.1016/0921-4534(95)00661-3` (see p. 107)

[156] W. T. Fu and D. J. W. Ijdo. *Solid State Communications*, (see p. 107)

[157] M.W. Lufaso, R.B. Macquart, Lee Yong Jae, T. Vogt, and H.C. zur Loye. *Journal of Physics-Condensed Matter*, DOI: `10.1088/0953-8984/18/39/008` (see p. 107)

[158] S. A. Ivanov, P. Nordblad, R. Tellgren, and A. Hewat. *Materials Research Bulletin*, DOI: `10.1016/j.materresbull.2008.09.017` (see p. 107)

[159] C. Bharti and T. P. Sinha. *Solid State Sciences*, DOI: `10.1016/j.solidstatesciences.2009.12.014` (see p. 107)

[160] H. Karunadasa, Q. Huang, B. G. Ueland, P. Schiffer, and R. J. Cava. *Proceedings of the National Academy of Sciences of the United States of America*, **V100**: 8097–8102, 2003. (see pp. 107, 108)

[161] W. T. Fu and D. J. W. Ijdo. *Solid State Communications*, **134**: 177–181, 2005. DOI: `10.1016/j.ssc.2005.01.018` (see pp. 107, 108)

[162] O. Ortiz-Diaz, M. J. A. Rodríguez, F. Fajardo, D.A. Landínez Téllez, and J. Roa-Rojas. *Physica B*, DOI: `10.1016/j.physb.2007.04.077` (see pp. 107, 108)

[163] R. D. Shannon. *Acta Crystallographica Section A*, **32**: 751–767, 1976. DOI: `10.1107/S0567739476001551` (see pp. 110, 183)

[164] R. Shaheen and J. Bashir. *Solid State Sciences*, DOI: `10.1016/j.solidstatesciences.2010.01.011` (see p. 117)

[165] M. Retuerto et al. *Journal of Materials Chemistry*, DOI: `10.1039/B705797K` (see p. 117)

[166] E.J. Cussen, J.F. Vente, P.D. Battle, and T.C. Gibb. *Journal of Materials Chemistry*, **7**: 459–463, 1997. DOI: `10.1039/a607083c` (see p. 117)

[167] N. Kashima, K. Inoue, T. Wada, and Y. Yamaguchi. *Applied Physica A*, DOI: `10.1007/s003390201362` (see p. 117)

[168] M.W. Lufaso, R.B. Macquart, Y. Lee, T. Vogt, and H.C. Loye. *Journal of Physics-Condensed Matter*, DOI: `10.1088/0953-8984/18/39/008` (see p. 117)

[169] A. Tauber, S.C. Tidow, R.D. Finnegan, and W.D. Wilber. *Physica C*, DOI: `10.1016/0921-4534(95)00661-3` (see p. 117)

[170] B. Orayech, A. Faik, and J. M. Igartua. *Paper in process, A. Sr_2GaSbO_6, Sr_2MnSbO_6*, 2015. (see p. 117)

[171] M. Cheah, P. J. Saines, and B. J. Kennedy. *Journal of Solid State Chemistry*, DOI: `10.1016/j.jssc.2006.03.013` (see p. 117)

[172] Z.Q. Deng et al. *Chemistry of Materials*, **21**: 5154–5162, 2009. DOI: `10.1021/cm902094q` (see p. 127)

[173] A. Gómez-Pérez et al. *journal of Power Sources*, **227**: 309 –317, 2013. DOI: `10.1016/j.jpowsour.2012.11.066` (see p. 127)

[174] R. Mathieu, S. A. Ivanov, R. Tellgren, and P. Nordblad. *Physical Review B*, **83**: 174420, 2011. DOI: `10.1103/PhysRevB.83.174420` (see p. 127)

[175] M. S. Augsburger et al. Preparation, crystal and magnetic structures of two new double perovskites: Ca2CoTeO6 and Sr2CoTeO6. *Journal of Materials Chemistry*, **15**: 993–1001, 2005. DOI: `10.1039/B413976C` (see p. 127)

[176] S. A. Ivanov, P. Nordblad, R. Mathieu, R. Tellgren, and C. Ritter. *Dalton Transactions.*, **39**: 5490–5499, 2010. DOI: `10.1039/B927498G` (see p. 127)

[177] L. Ortega-San Martín et al. *Journal of Materials Chemistry*, **15**: 183–193, 2005. DOI: `10.1039/B413341B` (see pp. 127, 157)

[178] S. A. Ivanov, P. Nordblad, R. Mathieu, R. Tellgren, and C. Ritter. *Dalton Transactions*, **39**: 11136–11148, 2010. DOI: `10.1039/C0DT00558D` (see p. 127)

[179] W. D. J. Evans. *Transactions and Journal of the British Ceramic Society*, **67**: 397–419, 1968. (see p. 127)

[180] Yu. N. Venevtsev, E. D. Politova, and G. S. Zhdanov. *Ferroelectrics*, **8**: 489–490, 1974. DOI: `10.1080/00150197408234136` (see p. 127)

[181] P. Köhl, E. Schultze-Rhonhof, and D. Reinen. *Zeitschrift für anorganische und allgemeine Chemie*, **378**: 129–143, 1970. DOI: `10.1002/zaac.19703780202` (see p. 127)

[182] L. Ortega-San Martín et al. *Zeitschrift für anorganische und allgemeine Chemie*, **631**: 2127–2130, 2005. DOI: `10.1002/zaac.200570028` (see p. 128)

[183] Rick Ubic, Steven Letourneau, Sherin Thomas, G. Subodh, and M. T. Sebastian. *Chemistry of Materials*, **22**: 4572–4578, 2010. DOI: `10.1021/cm100486r` (see pp. 128, 130)

[184] R. Ubic, S. Letourneau, and S. Thomas. *Journal Of The Australasian Ceramic Society*, **47**: 49, 2011. (see p. 128)

[185] E. Iturbe-Zabalo et al. *Journal of Physics-Condensed Matter*, **25**: 205401, 2013. DOI: `10.1088/0953-8984/25/20/205401` (see p. 131)

[186] E. Iturbe-Zabalo et al. *Journal of Solid State Chemistry*, **198**: 24–38, 2013. DOI: `10.1016/j.jssc.2012.09.007` (see pp. 131, 132)

[187] R. B. Macquart, B. J. Kennedy, and M. Avdeev. *Journal of Solid State Chemistry*, **183**: 2400–2405, 2010. DOI: `10.1016/j.jssc.2010.08.001` (see p. 131)

[188] V. A. Koptsik. *Shubnikov Groups. Handbook on the Symmetry and Physical Properties of Crystal Structures*. translated by Kopecky, J. and Loopstra, B. O. Fysica Memo 175, Stichting, Reactor Centrum Nederlands, 1971. (see p. 138)

[189] C. J. Bradley and A. P. Cracknell. *The mathematical theory of symmetry in solids : representation theory for point groups and space groups*. Oxford : Clarendon Press, 1972. (see p. 138)

[190] J.M. Perez-Mato et al. *Annual Review of Materials Research*, **45**: 1–30, 2015. DOI: `10.1146/annurev-matsci-070214-021008` (see p. 138)

[191] C. Sakai, Y. Doi, and Y. Hinatsu. *Journal of Alloys and Compounds*, DOI: `10.1016/j.jallcom.2004.12.068` (see pp. 188, 189)

[192] G. R. Castro. *Journal Of Synchrotron Radiation*, **5**: 657–660, 1998. DOI: `10.1107/S0909049597019079` (see p. 234)

[193] P. Fischer et al. *Physica B*, **276-278**: 146–147, 2000. DOI: `10.1016/S0921-4526(99)01399-X` (see p. 235)